

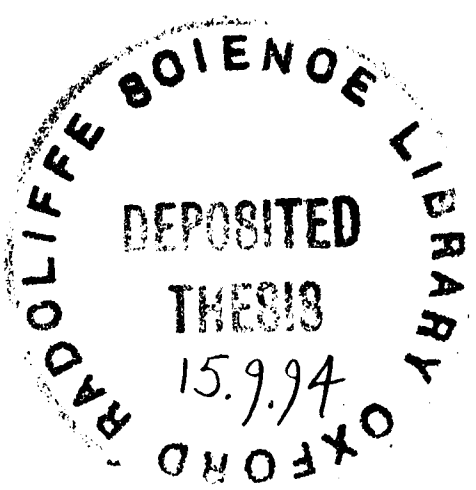
Shear Wave Heterogeneity in the Lower Mantle from Seismic Tomography

Thesis submitted in support of an application for leave to supplicate for the degree of Doctor of Philosophy

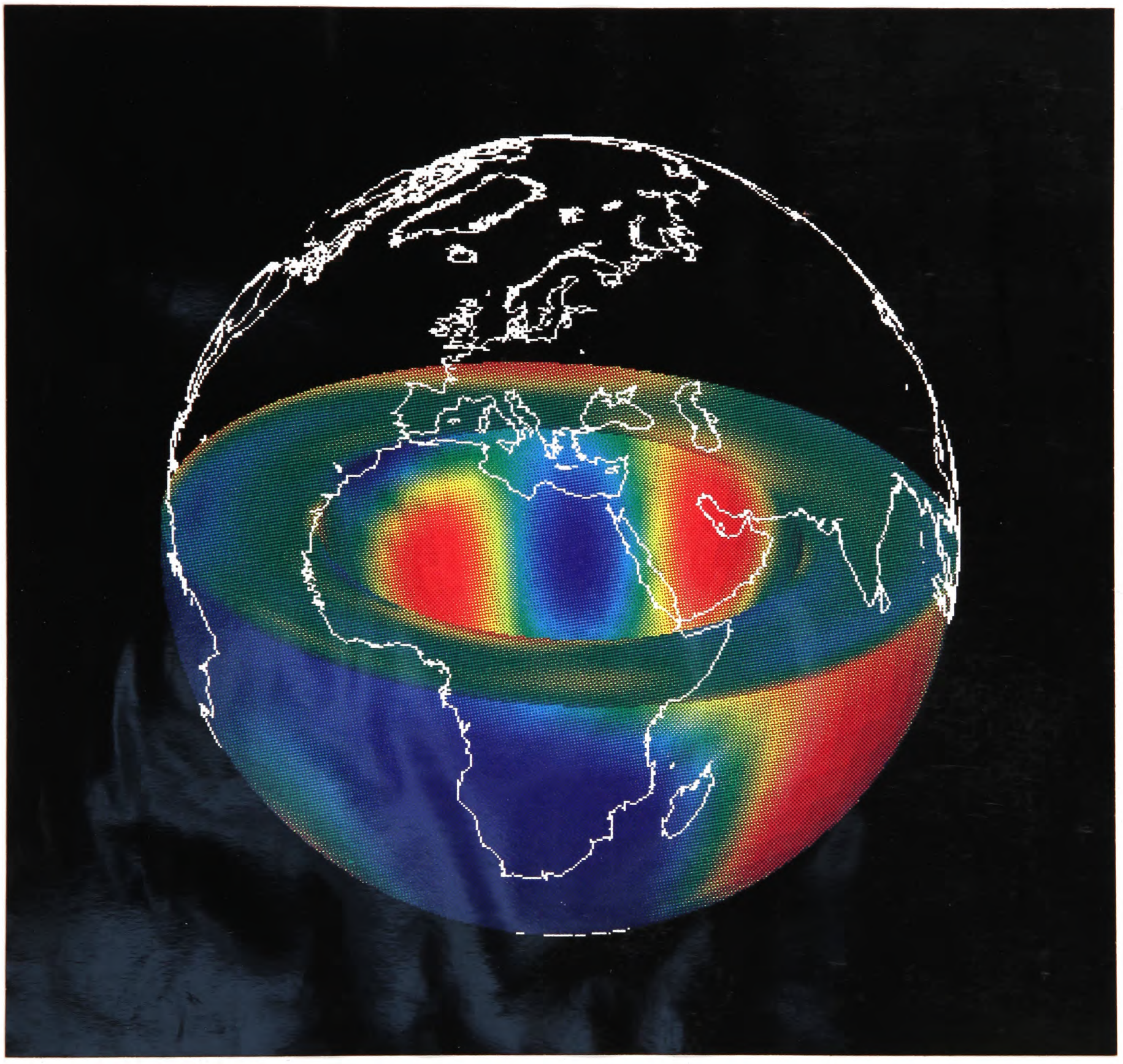
by

Graham Scott Robertson

Department of Earth Sciences
and
St Cross College
University of Oxford
Trinity, 1994



Supervisor: Prof. J. H. Woodhouse



AVS image of the S heterogeneity in the lower mantle, sliced through the equator. Red areas correspond to slower than average velocities, and blue areas correspond to faster than average velocities.

Shear Wave Heterogeneity in the Lower Mantle from Seismic Tomography

Graham S. Robertson
Department of Earth Sciences and St. Cross College
University of Oxford
Trinity, 1994

Abstract

To date, most shear velocity heterogeneity models in the lower mantle have been derived using long period data. Comparatively little use has been made of the vast ISC database of shear wave arrival times, which covers the years 1964 to 1991. The aim of this study is to use this database to construct global models of shear wave heterogeneity in the lower mantle and compare it with existing P models using similar period data in order to evaluate the hypothesis that P and S heterogeneity are proportional.

In order to reproduce the resolution operator inherent in these existing models, the same parameterization has been employed; lateral dependence is in terms of spherical harmonics up to degree and order 6, and radial dependence in terms of a quartic polynomial. The inversion uses data from over 4500 events selected according to criteria which minimize the bias introduced by uneven source receiver coverage. Despite having approximately one sixth of the amount of data the model correlates well with a P wave model computed using data from the same events, and this in turn is almost identical to models computed by other authors using similar inversion methods.

Assuming proportionality of P and S heterogeneity, a joint inversion of the P and S data has been performed. The resultant model correlates extremely well with the P model of this study, and similar variance reductions are obtained for both the P and S datasets as were found in the original inversions. Several model parameterizations have been used to try to investigate the dependence of the model expansion on the results. Consequently, taking into account results from synthetic experiments and from experiments into trade–offs with other inversion parameters, the average ratio of relative S to P heterogeneity $\frac{d\ln v_s}{d\ln v_p}$ throughout the lower mantle is constrained to be in the interval (1.8,2.1) with emphasis on higher values within these bounds. This value is in agreement with other studies using similar period data, and the upper bound is close to the optimum value of 2.27 obtained by Li *et al.*, 1991 from normal mode data, suggesting that the ratio is at least only weakly dependent on frequency. In addition evidence is presented that the ratio is increasing with depth although attempts to extract specific gradients have failed because of the very poor distribution of S rays in the deepest mantle.

Shear Wave Heterogeneity in the Lower Mantle from Seismic Tomography

Graham S. Robertson

Extended Abstract

International Seismological Centre (ISC) data from the years 1966 to 1990 has been used to construct shear and compressional wave models of the lower mantle with expansions to degree $l = 6$ laterally in terms of spherical harmonics, and with Legendre polynomials to degree $n = 4$ for depth variation. The resulting P and S models can be used to evaluate the hypothesis that P and S heterogeneity are proportional, as might be expected if both are due, for example, to temperature variations. Furthermore, the ratio of S to P heterogeneity is an important parameter in constraining the physics of mantle rocks, and the simultaneous use of P and S data sets, sampling the mantle in a similar way, provides an opportunity to constrain this ratio at short periods.

Several problems are encountered with the shear wave data. The ISC does not publish as 'S' any arrival which has a residual greater than 7.5 seconds in magnitude with respect to JB tables. In order to circumvent this problem data which lies within 11s of the expected PREM arrival time, and which is reported by a station which does not have an ISC published 'S' arrival for a given event, is additionally used. Furthermore there is considerable contamination of the data by SKS between 80° and 90° epicentral distance, and this is removed.

Shallow events from the ISC catalogue with $m_b \geq 4.0$ are relocated in PREM using both compressional and shear phases to avoid a compressional bias in the S model. The choice of events is governed by the number and azimuthal distribution of arrivals. Further event selection is then performed in order to minimize the effects of the biased source and receiver coverage worldwide.

As well as the determination of the model, the inversion involves the additional calculation of approximately 2800 P and 900 S static station corrections, and the location of over 18 000 events. The process is carried out iteratively because of the prohibitive number of parameters involved. Variance reductions abtained from the incorporation of large scale lower mantle heterogeneous models are ≈13% and 9% for the P and S datasets respectively.

Several problems are encountered because of the differential weighting of the P and S phases in the relocation and inversion. Experiments to investigate the possible effects of trade–offs between the model, event depths, and station corrections, show that the P and S models are affected differently. Choices of the P and S models are based on these findings.

The shear wave model has to be damped because of the relatively small amount of data that samples the lower mantle at depths greater than ≈2000km. As a result of this damping, comprehensive resolution and variance analysis of the models is also performed. These describe quantatively what qualitative inferences can be made about the data coverage in the lower mantle. In particular they highlight the effects of the missing data window between 80° and 90° epicentral angle.

An experiment has also been conducted into what differences between the P and S models can be attributed to the different coverages of the two datasets in the lower mantle. This involves the calculation of a P model using only those P arrivals from which an S arrival has been recorded on the same seismogram. In general this model correlates with the S model only slightly better than the P model above 2000km depth, showing that in this region there are few data coverage dependent differences in the compressional and shear wave models. Below this depth the test model correlates worse with the S model than does the P model. This result is attributed to the restricted P dataset having 26% fewer arrivals at epicentral angles greater than 80° compared to the S dataset.

Comparison of the P and S models from this study shows that correlation is good where resolution of the S model is good. In these areas the S model correlates as well with pre–existing S models from different datasets as these models do with eachother showing that the ISC short period shear wave dataset contains information about the interior of the earth which is consistent with other seismic datasets with different coverages and resolving powers, and opens up possibilities for their joint use in the future to make more accurate tomographic models. Similarly the P model correlates well with other short period compressional models which have different representations of the upper mantle and core mantle boundary.

Several higher parameterized models have also been calculated and their resolution investigated. In areas where resolution is good and variance is low, in particular around 1300km depth, these models are similar to eachother and display in greater detail many of the prominent features of the P and S models already derived.

These higher parameterized models have also been truncated to $n = 4, l = 6$ in order to investigate the effects of spectral leakage or aliasing on the results of the main inversion. The resultant P model correlates very well with the P model inverted to $n = 4, l = 6$. Correlation of the equivalent S models is only good at shallow depths. Differences in depth are attributable to insufficient damping of the original S model rather than to the effects of aliasing.

Assuming proportionality of P and S heterogeneity, a joint inversion of the P and S data has been performed. As a result a P model of the lower mantle has been derived with a ratio of S to P heterogeneity.

The resultant model correlates extremely well with the P model of this study, and similar variance reductions are obtained for both the P and S datasets as were found in the original inversions. Several model parameterizations have been used to investigate the dependence of the model expansion on the results. Consequently, taking into account results from synthetic experiments and from experiments into trade–offs with other inversion parameters, the average ratio of relative S to P heterogeneity $\frac{d\ln v_s}{d\ln v_p}$ throughout the lower mantle is constrained to be in the interval (1.8,2.1) with emphasis on higher values within these bounds. This value is in agreement with other studies using similar period data, and the upper bound is close to the optimum value of 2.27 obtained by Li *et al.*, 1991 from normal mode data, suggesting that the ratio is at least only weakly dependent on frequency. In addition evidence is presented that the ratio is increasing with depth although attempts to extract specific gradients have failed because of the very poor distribution of S rays in the deepest mantle.

Acknowledgements

I would like to thank Steve and Martin for the reliability of the computer network in Earth Sciences, and for their help which has always been freely available. In addition I am sure that my efforts with AVS would not have met with the same degree of success had it not been for the enthusiasm of Keith. Geoff Pegler's program *xzplot* was used to generate most of the diagrams in chapter 4, and his help is greatly appreciated.

Thanks also go to John, whose encouragement and diplomatic criticism has always kept me pointing in the right direction.

College life, and specifically college lunch, has always provided welcome relief from work. For this I would like to acknowledge Becca, Marco, Beccy, Charlie, Sharon, and Tom.

My survival over the last three years has also been aided by the companionship of my fellow classmates of 1990, namely Cath, Halcyon, and in particular, Andy Curtis and Pete. These latter characters have always kept me from straying onto the straight and narrow.

My acknowledgements would not be complete without expressing my gratitude to Andy Bingham, who entertained me for most of my time in Oxford, and nursed my emotions through the American Presidential debates of 1992. In connection, I am indebted to Christine for her unselfishness and sensitivity over the last 18 months.

Most of all, thanks go to my mother and father who were there when I really needed them.

Contents

Abstract Extended abstract Acknowledgements

1 Introduction **2**

1.1 Seismic datasets 3

1.2 Deterministic mantle models using short period arrival time data 5

1.3 History of short period deterministic mantle models 7

1.4 Motivation for this study 8

2 Data **10**

2.1 Event distribution and selection 10

2.2 Fundamental problems 11

2.3 Travel time residuals 12

2.3.1 Reference earth models 12

2.4 S wave data 13

2.4.1 S residuals 13

2.4.2 S wave cutoff 14

2.5 P wave data 15

2.5.1 P residuals 15

2.5.2 P wave cutoff 15

2.6 Implications for global models. 15

3 Methodology **29**

3.1 The tomographic inverse problem 29

3.2 Time-term analysis 31

3.2.1 Source term 32

3.2.2 Receiver term . . . 32
3.2.3 Ellipticity corrections . . . 32
3.3 Iterative time term inversion . . . 33
3.4 Fermat's principle and travel time tomography . . . 34
3.5 Spherical harmonic expansions . . . 35
3.6 Lower mantle model inversion theory . . . 35
3.6.1 Lower mantle representation . . . 38
3.7 Discussion . . . 38
3.7.1 Physical meaning of the perturbation integrals . . . 39
3.8 Transformation of model coefficients . . . 39
3.9 Conclusion . . . 40

4 Relocation 44
4.1 Why relocate? . . . 44
4.2 Overview . . . 45
4.3 Choice of seismic phases to be used in the relocations . . . 45
4.4 Relocation theory . . . 46
4.5 Algorithm testing . . . 47
4.6 Conclusions . . . 51

5 Lower Mantle Models 57
5.1 Data weighting in the inversions . . . 57
5.2 Model parameterization . . . 58
5.3 Procedure for the zeroth iteration . . . 58
5.4 Model analysis. Question of damping . . . 59
5.5 Results from the zeroth iteration . . . 60
5.5.1 Hypocentre locations and depths . . . 60
5.5.2 Station corrections . . . 60
5.5.3 Models . . . 61
5.6 Subsequent iterations . . . 63
5.6.1 One step models . . . 64
5.7 Iteration statistics . . . 64

5.7.1 Discussion . . . 65
5.7.2 Changes in models . . . 68
5.7.3 Relocation vectors . . . 68
5.7.4 Depth changes . . . 69
5.7.5 Station corrections . . . 70
5.8 Trade-off experiments . . . 71
5.8.1 Experiment 1: Fixed depth iterations . . . 72
5.8.2 Experiment 2: Fixed station correction iterations . . . 75
5.9 Conclusions: Choice of lower mantle models . . . 77
5.10 Further work . . . 79

6 Resolution and variance 118
6.1 Resolution tests . . . 118
6.1.1 Test model . . . 119
6.1.2 Central Asia input spike . . . 121
6.1.3 Central Pacific input spike . . . 121
6.2 Model variance . . . 121
6.3 P_S : P with S paths model . . . 122
6.3.1 Calculation of the model . . . 123
6.3.2 Comparison of the P_S model and P model . . . 124
6.3.3 Comparison of the P_S model and S model . . . 124
6.3.4 Correlation coefficients . . . 125
6.3.5 P_S model variance . . . 126
6.3.6 P_S model resolution . . . 126
6.4 Conclusions . . . 127

7 Further parameterizations 152
7.1 Calculation of models . . . 153
7.2 Resolution . . . 153
7.3 Variance . . . 154
7.4 Comparison of the models . . . 155
7.4.1 6A . . . 155

7.4.2 8C . . . 156
7.4.3 Correlation coefficients . . . 156
7.5 Aliasing . . . 157
7.5.1 S . . . 157
7.5.2 P . . . 158
7.5.3 Variance reductions . . . 159
7.6 Conclusions . . . 159

8 Model analysis 181
8.1 Pre-existing models . . . 181
8.2 RMS amplitude . . . 184
8.3 Correlation coefficients . . . 186
8.3.1 P . . . 186
8.3.2 S . . . 187
8.4 Comparison of features . . . 188
8.5 Comparisons of further parameterized models . . . 190
8.6 Discussion and conclusions . . . 192

9 Ratio of relative S to P model perturbations 202
9.1 Importance of the ratio . . . 203
9.2 Chapter outline . . . 204
9.3 Experiment 1: Fixed P model . . . 205
9.3.1 Methodology . . . 205
9.3.2 Synthetic experiments . . . 206
9.3.3 Results . . . 208
9.4 Experiment 2: Joint inversion of P and S datasets . . . 211
9.4.1 Calculation of model perturbations . . . 212
9.4.2 Depth independent ratio . . . 212
9.4.3 Depth independent ratio with fixed depths . . . 219
9.4.4 Depth dependent ratio . . . 222
9.5 Discussion and conclusions . . . 223

10 Conclusions and further work **244**

10.1 Further work 245

References **247**

Appendices

A Transformation of model coefficients **253**

B Derivation of mean square amplitude **255**

C Model coefficients **256**

List of Figures

1.1 P wave ray geometries through the spherically symmetric reference model PREM 10

2.1 Distribution of sources and receivers per 5 degree cell. 17

2.2 Jeffreys-Bullen travel time tables. 18

2.3 ISC 'S' travel time residuals. 19

2.4 PREM residuals for those arrivals which lie within 25s of the expected S arrival time from PREM but are not identified as S by the ISC. 20

2.5 ISC published residuals for those arrivals which lie within 25s of the expected S arrival time from PREM but are not identified as S by the ISC. See text for details. 21

2.6 Explanation of the shape of misidentified arrivals on raw residual plots. See text for details. 22

2.7 S residuals with respect to PREM. This plot is a combination of the S PREM residuals and the 'unidentified' S PREM residuals. 23

2.8 S residuals with respect to PREM including cutoffs. 24

2.9 Statistical analysis of the final S data. 25

2.10 ISC 'P' travel time residuals. 26

2.11 P travel time residuals calculated with respect to PREM. 27

2.12 Statistical analysis of the P data of the final P data. 28

3.1 The bending of a seismic ray through a velocity anomaly. 34

3.2 The three Euler angles Φ, Θ and Ψ. 37

3.3 Examples of the S perturbation integrals. 41

3.4 Examples of the P perturbation integrals. 42

3.5 Examples of the variation in P perturbation integral with depth. 43

4.1 AVS image of the events in the Tonga dataset viewed from a north-northwesterly direction. 52

4.2 Map and cross section of ISC locations in Tonga region. 53

4.3 Map with ISC locations and cross section relocated with P arrivals only. 54

4.4 Cross sections and confidence ellipses for relocations with P and S, and all phases. . . . 55

4.5 Cross sections showing only the hypocentres for events relocated including three dimensional models. 56

5.1 Analysis of the mean P and S residual versus epicentral angle before and after inversion. 67

5.2 Binned depths for the relocated events contributing to the iteration 0 models 80

5.3 Average relocation vectors for events at the end of the zeroth iteration 81

5.4 Average P station corrections at the end of the zeroth iteration 82

5.5 Average S station corrections at the end of the zeroth iteration 83

5.6 Zeroth iteration S model constructed from the complete eigenvalue spectrum. 84

5.7 Zeroth iteration P model constructed from the complete eigenvalue spectrum. 85

5.8 Eigenvalue analysis for zeroth iteration models. 86

5.9 Zeroth iteration damped shear wave model constructed using 230 out of 245 eigenvalues and eigenvectors. 87

5.10 First iteration P model. 88

5.11 Second iteration P model. 89

5.12 Third iteration P model. 90

5.13 Final iteration P model. 91

5.14 First iteration S model using only 230 eigenvalues and eigenvectors. 92

5.15 Second iteration S model using only 230 eigenvalues and eigenvectors. 93

5.16 Third iteration S model using only 230 eigenvalues and eigenvectors. 94

5.17 Final iteration S model using only 230 eigenvalues and eigenvectors. 95

5.18 Average relocation vectors between the 0^{th} and 1^{st} iterations. 96

5.19 Average relocation vectors between the 1^{st} and 2^{nd} iterations. 97

5.20 Average relocation vectors between the 2^{nd} and 3^{rd} iterations. 98

5.21 Average relocation vectors between the 3^{rd} and 4^{th} iterations. 99

5.22 Average changes in depths between the 0^{th} and 1^{st} iterations. 100

5.23 Average changes in depths between the 1^{st} and 2^{nd} iterations. 101

5.24 Average changes in depths between the 2^{nd} and 3^{rd} iterations. 102

5.25 Average changes in depths between the 3^{rd} and 4^{th} iterations. 103

5.26 Average depths per 5° cell at the end of the 4^{th} iteration. 104

5.27 ISC average depths per 5° cell. 105

5.28 Origin time versus change in depth plots for the complete dataset at iterations 0 and 4. 106

5.29 Average station corrections for each iteration for the four zones chosen for study. 107

5.30 Fourth iteration P model from the experiment in which the depths were fixed after the first iteration. 108

5.31 Fourth iteration S model using only 230 eigenvectors from the experiment in which the depths were fixed after the first iteration. 109

5.32 Comparison of average station corrections between the reference and fixed depth iterations for the stations around Hawaii and Japan. 110

5.33 Fourth iteration P model from the experiment in which the station corrections were fixed after the first iteration. 111

5.34 Fourth iteration S model using only 230 eigenvectors from the experiment in which the station corrections were fixed after the first iteration. 112

5.35 Average relocation vectors between the fourth reference iteration and the fourth iteration with station corrections fixed. 113

5.36 P model norm plots versus cumulative eigenvalue number for reference (bottom), fixed depth (middle), and fixed station correction (top) experiments. 114

5.37 S model norm plots versus cumulative eigenvalue number for reference (bottom), fixed depth (middle), and fixed station correction (top) experiments. 115

5.38 Third iteration P model from the experiment in which the depths were fixed after the first iteration. 116

5.39 Third iteration S model from the experiment in which the depths were fixed after the first iteration. 117

6.1 Normalized Legendre polynomials to n=4. 120

6.2 Synthesis of a delta function from 5 Legendre polynomial coefficients for the four standard model plotting depths. 120

6.3 Difference in bottoming depths between a P ray and an S ray for the same source and receiver from PREM. 123

6.4 Model norm and variance reduction graphs for the PS model. 123

6.5 Correlation coefficients of the 4_6 models of this study with depth. 125

6.6 Comparison of the number of arrivals at a given epicentral angle for the S dataset and the PS dataset. 126

6.7 Test model with delta function placed in central Asia at 680km depth. 128

6.8 Test model with delta function placed in central Asia at 1300km depth. 129

6.9 Test model with delta function placed in central Asia at 2000km depth. 130

6.10 Test model with delta function placed in central Asia at 2700km depth. 131

6.11 Test model with delta function placed in central Pacific at 680km depth. 132

6.12 Test model with delta function placed in central Pacific at 1300km depth. 133

6.13 Test model with delta function placed in central Pacific at 2000km depth. 134

6.14 Test model with delta function placed in central Pacific at 2700km depth. 135

6.15 Resolution model to be compared with delta function placed in central Asia at 680km depth. 136

6.16 Resolution model to be compared with delta function placed in central Asia at 1300km depth. 137

6.17 Resolution model to be compared with delta function placed in central Asia at 2000km depth. 138

6.18 Resolution model to be compared with delta function placed in central Asia at 2700km depth. 139

6.19 Resolution model to be compared with delta function placed in central Pacific at 680km depth. 140

6.20 Resolution model to be compared with delta function placed in central Pacific at 1300km depth. 141

6.21 Resolution model to be compared with delta function placed in central Pacific at 2000km depth. 142

6.22 Resolution model to be compared with delta function placed in central Pacific at 2700km depth. 143

6.23 Velocity perturbation variance of the P model. 144

6.24 Velocity perturbation variance of the S model. 145

6.25 PS model using 220 out of the possible 245 eigenvalues. 146

6.26 Velocity perturbation variance of the PS model constructed from 220 eigenvalues. 147

6.27 PS resolution model to be compared with delta function placed in central Pacific at 680km depth. 148

6.28 PS resolution model to be compared with delta function placed in central Pacific at 1300km depth. 149

6.29 PS resolution model to be compared with delta function placed in central Pacific at 2000km depth. 150

6.30 P-S resolution model to be compared with delta function placed in central Pacific at 2700km depth. 151

7.1 Correlation coefficients of the P and S models with all parameterizations 157

7.2 Correlation coefficients of the truncated models of this chapter and the 4_6 models of chapter 5. 158

7.3 Model norm and variance plots for the larger parameterized P and S models. 160

7.4 $n, l = 6, 10$ S model constructed using the best known 600 eigenvalues and eigenvectors of the inner product matrix. 161

7.5 $n, l = 6, 10$ P model constructed using the best known 770 eigenvalues and eigenvectors of the inner product matrix. 162

7.6 $n, l = 8, 12$ S model constructed using the best known 1030 eigenvalues and eigenvectors of the inner product matrix. 163

7.7 $n, l = 8, 12$ P model constructed using the best known 1280 eigenvalues and eigenvectors of the inner product matrix. 164

7.8 Resolution maps for the 2% amplitude input delta function (top) in central Asia at 1300km depth. 165

7.9 Resolution maps for the 2% amplitude input delta function (top) in central Asia at 2700km depth. 166

7.10 Resolution maps for the 2% amplitude input delta function (top) in central Pacific at 1300km depth. 167

7.11 Resolution maps for the 2% amplitude input delta function (top) in central Pacific at 2700km depth. 168

7.12 Resolution maps for the 2% amplitude input delta function (top) in central Asia at 680km depth. 169

7.13 Resolution maps for the 2% amplitude input delta function (top) in central Asia at 2000km depth. 170

7.14 Resolution maps for the 2% amplitude input delta function (top) in central Pacific at 680km depth. 171

7.15 Resolution maps for the 2% amplitude input delta function (top) in central Pacific at 2000km depth. 172

7.16 Variance of the 6A S model. 173

7.17 Variance of the 6A P model. 174

7.18 Variance of the 8C S model. 175

7.19 Variance of the 8C P model. 176

7.20 6A S model truncated to $n = 4, l = 6$. 177

7.21 8C S model truncated to $n = 4, l = 6$. 178

7.22 6A P model truncated to $n = 4, l = 6$. 179

7.23 8C P model truncated to $n = 4, l = 6$. 180

8.1 RMS amplitudes for the compressional models. 184

8.2 RMS amplitudes for the shear models. 185

8.3 Correlation coefficients as a function of depth for the P models. 186

8.4 Shear wave model correlation coefficients. ULSH is short for U84L85/SH 187

8.5 Correlation of SH8WM13 with the 6A S model and the P and S 8C models to degree 8. 191

8.6 Maps of P, l02.56, and V3.i at 1300km depth. 193

8.7 Maps of P, l02.56, and V3.i at 2000km depth. 194

8.8 Maps of P, l02.56, and V3.i at 2700km depth. 195

8.9 Maps of S, U84L85/SH , MDLSH, and SH8WM13 at 1400km depth. 196

8.10 Maps of S, U84L85/SH , MDLSH, and SH8WM13 at 1950km depth. 197

8.11 Maps of S, U84L85/SH , MDLSH, and SH8WM13 at 2760km depth. 198

8.12 Maps of SH8WM13, 6A S model, and 8C S and P models at 1300km depth. 199

8.13 Maps of SH8WM13, 6A S model, and 8C S and P models at 2700km depth. 200

8.14 Maps of SH8WM13, 6A S model, and 8C S and P models at 2700km depth. 201

9.1 Distribution of seismic velocities and density within the spherically symmetric model PREM. 204

9.2 The results of the synthetic experiment to investigate the effects of weighting in the ratio inversion. 207

9.3 Number of S arrivals per bottoming depth bin for the dataset contributing towards the final S model, and the models of this section. 208

9.4 Correlation coefficients of the compressional models P, PS , and V3.i with the S model of this study. 210

9.5 Comparison of the RMS amplitudes of the model perturbations throughout the joint inversion of the P and S datasets. 216

9.6 Comparison of the depth independent ratio models with the linear P model. 221

9.25 Average change in the S station corrections between the third iterations of the reference joint inversion and the joint inversion in which the depths of the events were fixed after the second iteration. 242

9.26 The third iteration joint inversion P model for a depth dependent ratio. 243

Chapter 1

Introduction

Since the evolution of the theory of plate tectonics throughout the 1960s, the nature of the dynamic earth has been in the forefront of geophysical research. The plates themselves can be thought of as simply the cooled boundary layer of the mantle, and their motion is the surface manifestation of convection in the Earth's mantle.

This convection within the earth is linked to the existence of mantle heterogeneity, the departure from the spherical average of its physical properties. Convection patterns arise when there exist simultaneously upwellings of hot, lighter material and cold, dense material. While the existence of hotspots is evidence of localized plumes, mid ocean ridges represent large scale mantle upwellings which can constrain the locations of convective cells. Ultimately the material deposited at these ridges is transported across the ocean floor, cooling and thickening in the process, until it forms a subduction zone, where the plate descends to depths of at least 700km.

In addition to volumetric heterogeneity, convection also causes changes to the shape of the boundaries within the earth. In the most obvious case, the core mantle boundary (CMB), where the fluid iron alloy outer core meets the viscous lower mantle, perturbations to the boundary will result from density heterogeneity as well as from the dynamic forces of the upwelling and downwelling mantle. Recent maps have also been produced of the boundary between the upper and lower mantle.

Changes in temperature, density, and chemical composition of mantle material all affect the velocity of seismic waves, and so by determining the velocity heterogeneity within the mantle it is possible to infer changes to rock properties. The technique used by seismologists to do this is called tomography, and it is the only method that can retrieve information about the earth's deep interior with enough resolution to be informative to geophysicists studying the dynamics of the planet.

1.1 Seismic datasets

To date seismologists have used vastly different types of data covering the entire seismic spectrum from 1Hz to 0.5mHz in order to retrieve detail of the three dimensional earth.

Each seismic frequency has the ability to resolve mantle heterogeneity in different ways. In other words, the different frequencies have the effect of filtering the earth in different ways. A thorough review of the techniques can be found in Woodhouse & Dziewonski, 1989. In order of increasing frequency, seismic studies on a global scale use data which fall into the following categories.

- Free oscillations of the earth

  Benioff, 1958 was the first to notice a wave of period around 57 minutes from an event in Kamchatka and associate it with standing waves, or free oscillations of the earth. Since then the periods of both toroidal and spheroidal modes have been measured from seismograms and calculated theoretically to a high degree of accuracy. Analysis of mantle heterogeneity from free oscillations has arisen from the theory of degenerate splitting (Dahlen, 1968; Woodhouse & Dahlen, 1978; Woodhouse & Girnius, 1982) and is analogous to the Zeeman effect in atomic physics. Three dimensional velocity models have been derived using *splitting functions* (Woodhouse & Giardini, 1985; Giardini *et al.*, 1987; Giardini *et al.*, 1988; Woodhouse *et al.*, 1986) – functions defined on the surface of a sphere which describe the dependence on the earth structure of an isolated mode.

  Free oscillations have wavelengths of the order of the radius of the earth, and are therefore sensitive to only the largest scale lengths of heterogeneity. As a result they contain information down to the centre of the earth, albeit with restricted resolution. This property means that they are insensitive not only to the small scale structure of the earth (which can contaminate studies of large scale structure constructed with higher frequency datasets), but they are also insensitive to source mislocation.

  Free oscillation data relies on measurements being taken over complete great circle paths since they are in fact standing waves within the earth. Backus, 1964, however, pointed out that these measurements only give information about heterogeneity which is symmetric under reflection through the centre of the earth, and so free oscillations can only describe the even degree harmonic heterogeneity.

  Although this dataset is predominantly sensitive to shear velocity, some modes do show some sensitivity to v_p, and as a result, both shear and compressional models have been constructed (*e.g.* Giardini *et al.*, 1987; Li *et al.*, 1991).

- Surface waves

  Free oscillations can be thought of as the interference pattern of traveling waves (Garland, 1971). The computation of mantle structure using great circle phase velocities of long period surface waves is equivalent to the method involving observations of eigenperiods of fundamental spheroidal

modes, as used by Masters *et al.*, 1982. For this reason some global studies using surface waves suffer from the same inherent problems as free oscillation studies. The frequency of these waves is higher, so smaller features can be resolved using this dataset, but harmonic expansions are still limited to even degrees. However, if the source parameters are known, or are treated as inversion parameters, both minor and major arc phase velocities can be determined and thus odd structure can also be retrieved.

Woodhouse & Dziewonski, 1984 were able to compute a map of upper mantle S heterogeneity with an expansion in both even and odd harmonics laterally to degree 8, and with a cubic polynomial in depth. in order to do this they derived a new technique of whole waveform inversion using synthetic seismograms and a least squares fitting procedure. The data used in this study are long period *mantle waves* – Rayleigh and Love waves which travel along great circle paths and are predominantly sensitive to upper mantle structure.

- Long period body waves

  This dataset consists of two differently polarized waveforms – horizontally polarized SH and vertically polarized P–SV. These have periods greater than or equal to 45 seconds and consist of deep turning multiple reflections of S at the free surface. The modeling technique used with this dataset is the same as that used in Woodhouse & Dziewonski, 1984 for the mantle wave data.

  Several studies have used the SH subset of this data. The first, a model of separate upper and lower mantle S heterogeneity expanded in terms of spherical harmonics to degree 8 and Legendre polynomials for their depth variation, was derived by Woodhouse, and is reported in several papers, Woodhouse & Dziewonski, 1986; Dziewonski & Woodhouse, 1987; Woodhouse & Dziewonski, 1989. Tanimoto, 1990 used this dataset along with longer period Love waves to derive a whole mantle model with spherical harmonics to degree 6 and discrete depth layers. The most recent model is SH8WM13 of Woodward *et al.*, 1992 who use long period body waves in addition to mantle waves and several short period datasets. This model is expanded throughout the entire mantle to spherical harmonic degree 8 and with Chebychev polynomials to degree 13 to represent the depth variation.

  Some authors have used waveform correlation techniques to derive absolute and differential arrival times from long period data (20 – 60 second period). For example Woodward & Masters, 1991a; Woodward & Masters, 1991b cross correlate direct S with SS waveforms from the same seismograms to obtain differential travel times as the raw data in their inversions. Differential travel times involving surface reflections, SS-S and PP-P, have been shown to correlate very well with the heterogeneity at the bounce point of the reflected phase because the ray paths elsewhere are similar. Hence these data can be used to construct models of the upper mantle. Similarly PcP-P and ScS-S measurements, which involve reflected phases from the CMB are sensitive to structure in the lowermost mantle.

- Short period body waves

  This dataset consists of compressional and shear waves which have a dominant period of order 1 second. Their short wavelength (≈10km) means that they are sensitive to the smallest scale lengths of heterogeneity and hence their potential to retrieve structural detail is far greater than that of any of the datasets considered above. However this sensitivity means that they are affected to a far greater extent by the very thin but extremely heterogeneous outer regions of the earth.

  Since 1964 these arrival times have been recorded at seismic observatories worldwide and sent to the International Seismological Centre who publish them in regular bulletins. Seismic studies using this dataset fall into two categories – stochastic, and deterministic. Stochastic models, *e.g.* Gudmundsson *et al.*, 1990; Davies *et al.*, 1992, abandon information governing the positional nature of velocity anomalies, and instead use a statistical formulation to derive the scale lengths and power in harmonic degrees of the heterogeneity down to very small wavelengths. Deterministic studies derive maps of velocity perturbations but only consider the very largest scales because of restrictions in data coverage. Where the models from these two categories can be compared, for example in their amplitude distribution with depth, the results are consistent with each other. Deterministic models, the subject of this study, will be discussed in detail in the next section.

  Both types of study suffer from the same fundamental problems associated with the unevenness of the distribution of the seismic sources and receivers, as well as the errors associated with each arrival time reading (see chapter 2).

1.2 Deterministic mantle models using short period arrival time data

The previous sections have considered the motivation for the construction of global velocity maps of the earth's mantle, and what datasets can be employed. The object of this section is to give a brief explanation into how this is done.

The ray paths of compressional P waves from an event through a two dimensional slice of the spherically symmetric reference earth model PREM (Dziewonski & Anderson, 1981) is shown in figure 1.1 at the end of this chapter. Within ray theory, an arrival time measurement constitutes an integral average of slowness along a ray path. One of the fundamental assumptions in tomography involves the use of Fermat's principle, which in this case means that to first order, this integral is insensitive to small deviations in the path of integration – the ray path. Hence the change in travel time between the time that a seismic wave actually takes through the earth and that predicted by a spherically symmetric model is simply obtained by integrating the travel time perturbations along the ray path through the reference model. The use of Fermat's principle linearizes the whole travel time inversion by making it unnecessary to consider the effects of the heterogeneity on the ray path.

For these velocity variations to be positioned uniquely, the path taken by a seismic ray from the source to the receiver must also be unique. Figure 1.1 shows that at small epicentral distances a station can record a reflected as well as a refracted ray, which destroys the uniqueness of the travel time curve. For this reason most tomographic models of the mantle from arrival times use data for epicentral distances beyond 25° . At epicentral angles greater than this and up to ≈100° stations can record refracted arrivals that have traveled through the mantle and arrivals which have been reflected from various boundaries, most notably the CMB. However the difference in arrival times between the refracted and reflected phases is large enough to avoid confusion. As epicentral distances approach 100° the refracted arrivals disappear as they are transmitted into the core. The rays which penetrate the core and then re–emerge into the mantle at distances greater than ≈ 140° are not used in most tomographic models because they have far more complex paths. These arrivals have been used in studies which also include parameterizations of the inner core and topography on the CMB.

The choice of parameterization of a mantle model is extremely important because one of the largest sources of uncertainty originates from possible deficiencies in the model expansion (Morelli & Dziewonski, 1991). Careful analysis of the region that is to be modeled and the data with which this is to be done is necessary. For example, from figure 1.1 it is clear that the ray paths through the upper mantle within the teleseismic range 25° to 100° are predominantly vertical and so any model of this region will suffer from poor vertical resolution. However the lower mantle has dense ray coverage both radially and laterally in all regions apart from the deepest, where ray paths are tangential to the CMB. It is for this reason that models of the earth's mantle from arrival time data are restricted to the lower mantle.

The choice of basis functions for the model expansion is equally important. These fall into two main categories:

1. Smoothly varying functions for lateral and/or depth variation.
2. Blocks

There has been considerable debate in the literature over which is best, and no firm conclusion has been reached. Current models using both of these expansions exist. The principal arguments for using smoothly varying functions such as spherical harmonics are:

- For the same smoothness, block parameterized models have more parameters which often require iterative inversion routines.
- The results are easily compared with existing gravity, magnetic, and mantle convection models, which also use this representation.

In favour of block parameterized models these arguments can be answered by:

- Different block sizes can be used in different areas in accordance with the data distribution, hence cutting down the number of parameters used.

- It is possible to compute spherical harmonic expansions of block parameterized models.

In this study smooth functions are chosen in order to be consistent with the majority of global models that exist. The maximum expansion that can be achieved is governed by a more practical consideration – the data distribution. In other words, it is dependent on the locations of the seismic sources – the earthquakes – and the receivers. Both of these occur in specific regions and are not evenly spread. In chapter 2 it will be shown that there is excellent data coverage under the continents because seismic observatories are generally land based. This means that there is far better sampling of the lower mantle in the northern hemisphere, and that the upper parts of the lower mantle under oceanic areas are almost devoid of coverage.

Once the maximum expansion has been chosen, it is important to consider whether the nature of heterogeneity is going to be accurately described by the expansion. In other words, is the structure of the lower mantle dominated by heterogeneity that has too small wavelengths to be incorporated into the smallest features of the model? In theory, if the distribution of data throughout the lower mantle is optimal, the use of orthonormal functions in the model expansion should mean that small scale structure is not mapped into the large scale structure described by the model. However real data is far from ideal, and spectral leakage, or aliasing, is a possibility. The pioneers of mantle tomography knew very little about the nature of the heterogeneity, but recent stochastic analysis (Gudmundsson *et al.*, 1990) has shown that the lower mantle is dominated by large scale features with characteristic wavelengths of $\approx$1000km, corresponding to a spectral band width of $l \approx 7$.

As a result of the very limited expansions that are possible using tomographic techniques, it is quite often the inadequacies in the parameterization of the models that are the sources of the largest errors. This is difficult to quantify by standard techniques, but can be investigated by examining the similarities of models computed using different theories and expansions.

1.3 History of short period deterministic mantle models

Regional differences in travel time arrivals were first studied by Gutenberg, 1953, and subsequently their effects on hypocentre locations were reported by Herrin & Taggart, 1962. At that time the strong heterogeneity of the crust and upper mantle were well known, but it was not until 1967 that Toksöz *et al.* also found evidence of heterogeneity in the lower mantle. Work using seismic arrays (Davies & Sheppard, 1972) confirmed this observation, and then Julian & Sengupta, 1973 using travel time data showed that not only is the whole of the lower mantle heterogeneous, but that the deepest regions are more heterogeneous than the middle mantle – a feature common to all current lower mantle models. The first three dimensional analysis of the entire mantle was conducted by Sengupta & Toksoz, 1976, who presented a model of the variation of the root mean square amplitude of heterogeneity with depth. Subsequent work by Dziewonski *et al.*, 1977 used ISC P data from the years 1967-1973 to conduct a

tomographic analysis of the mantle with a lateral expansion to spherical harmonic degree 3 and five shells for its radial variation. Depths of up to 1100km, including the upper mantle, were found to be unstable, but long wavelength anomalies were found below this. In a subsequent study, using far more data and a continuous depth parameterization using Legendre polynomials, Dziewonski, 1984 computed a lower mantle model of P heterogeneity to degree 6. Since this time, several authors have computed heterogeneous models of the mantle using the ISC P wave data. Separating these into the two types of parameterizations used, these include:

- **blocks:** Clayton & Comer, 1983; Hager & Clayton, 1989; Davies & Clayton, 1986; Inoue *et al.*, 1990
- **spherical harmonics:** Dziewonski, 1984; Morelli & Dziewonski, 1991

This last study has derived simultaneously models of lower mantle of P heterogeneity, CMB topography, and heterogeneity of the outer core, which in theory at least frees the lower mantle model of contamination by CMB topography. Some of these models and modeling techniques will be discussed in detail in chapter 8 when they will be compared to the models of this study.

1.4 Motivation for this study

To date almost all models of the lower mantle from arrival time data have used P waves alone because this phase is relatively free from contamination from other arrivals. There is currently only one global mantle model of shear wave heterogeneity in existence, that of Davies & Clayton, 1986. This uses ISC published 'S' residuals and is parameterized using 48 604 blocks with 29 layers radially. This study has shown that in areas where resolution is good, the S model correlates well with a similarly parameterized P model. However events were not relocated in this study and as a result it is possible that the final model could be biased by using event locations derived entirely from compressional data. The true worth of the enormous ISC database of shear wave arrival times is still relatively unknown.

Hence the purpose of this study is to re–examine the shear wave arrivals in the ISC bulletins and compute a lower mantle model of S heterogeneity in order to establish the value of this dataset to tomographic studies. In addition an identically parameterized P model will be simultaneously calculated so that comparisons between the two should be devoid of differences in the way the models are derived.

The resulting P and S models can be used to evaluate the hypothesis that P and S heterogeneity are proportional, as might be expected if both are due, for example, to temperature variations. Furthermore, the ratio of S to P heterogeneity is an important parameter in constraining the physics of mantle rocks, and the simultaneous use of P and S data sets, sampling the mantle in a similar way, provides an opportunity to constrain this ratio at short periods.

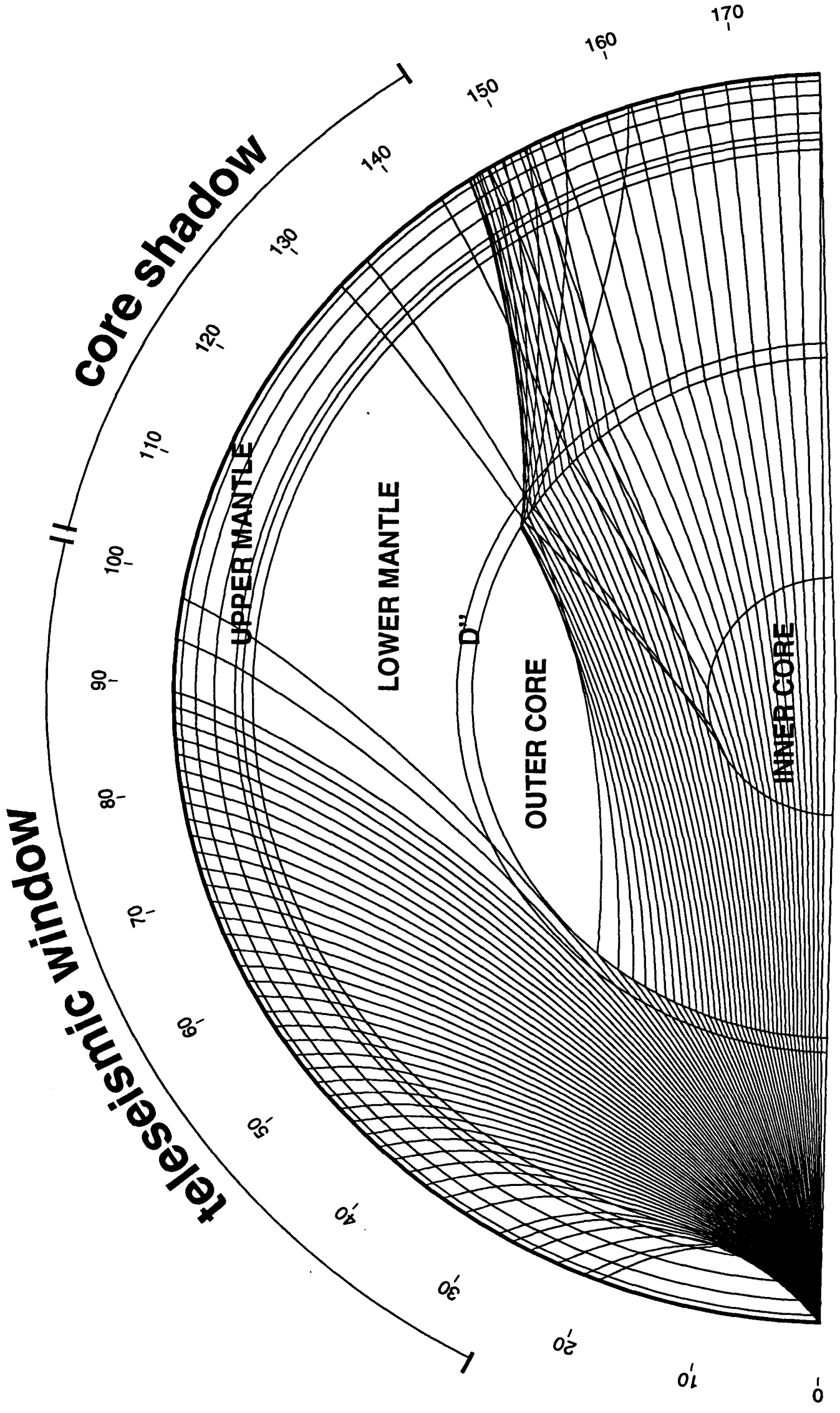


Figure 1.1: P wave ray geometries through the spherically symmetric reference model PREM

Chapter 2

Data

The Bulletins of the International Seismological centre (ISC) are published monthly in the form of written catalogues and issued on a more infrequent basis on computer tape. They consist of arrival times of seismic phases from a global network of stations plus their own estimates of hypocentre locations and origin times.

2.1 Event distribution and selection

In any inversion of a dataset, the distribution of the original data is intrinsically related to the final model. Global seismic tomography is no exception, with the distribution of sources (the earthquake or explosion) and receivers (the seismic observatory or station) being of vital importance. The latter, plotted at the top of figure 2.1, are land based and are therefore restricted mainly to the continents. In large oceanic areas, for example the Pacific Ocean, coverage is restricted to the sparsely distributed island stations. Similarly, earthquakes large enough to be recorded occur mainly in subduction zones and mid ocean ridges. Hence a seismic dataset consisting of source receiver paths suffers from being unevenly distributed and can be considerably biased in some regions. The whole procedure of data selection, processing, and inversion has to attempt to minimize this bias while at the same time using the maximum amount of data to enhance the signal to noise ratio.

At this stage the choice of events used is very important. Firstly, given the subject of the study, we only use events with at least one S arrival. Secondly, small events are not constrained well in the location procedure so, from experimentation, we have chosen to use events with $m_b \geq 4.0$. Also earthquakes occurring deeper than the thickness of a plate $\approx$ 50km will predominantly be subduction related and will therefore introduce bias. Several authors (Davies & McKenzie, 1969; Dziewonski & Anderson, 1981) have noted that the travel time curves of these deeper events are markedly different than those from shallow events, and this has been attributed to their systematic mislocation. This occurs because

rays become channelled in a plate (Bott, 1980) where the seismic velocity is much higher than that given by a spherical earth model at the equivalent depth.

Restricting to events having depths less than 50km and $m_b \geq 4.0$ gives a total of approximately 19000 events.

2.2 Fundamental problems

The reliability of the ISC dataset is often questioned because there is no standard way of picking an arrival time. The stations have a variety of instruments, and even if they all had the same instruments, there are several other parameters, for example gain, that can be changed. Furthermore the personnel that report arrival times to the ISC may have vastly different amounts of experience. Picking an S arrival is harder than picking a P arrrival because it is far less impulsive, having approximately four times the period. Duda, 1971 has also found evidence of operators biasing onsets of P and PP by the expected arrival time from Jeffreys Bullen travel time tables.

Often the seismic waveform is complex, especially if the source is shallow, when several direct and reflected phases can interfere. The gain of a seismometer is often determined by the tectonic province of its location. Tectonically active regions have high ambient seismicity, and so station amplification factors are low (Hager & Clayton, 1989). This may mean that the arrivals are picked late, and could result in an artificial correlation of residual with tectonic region. Grand, 1990 has conducted a survey into this and found that there may be a 0.4 to 0.5 second bias in travel time with a factor of 10 in gain, although there is considerable scatter in the data. Contamination of the datasets by this method is systematic and is a cause of major problems in inversion schemes for the retrieval of earth structure.

The ISC data is widely known to be noisy. Stochastic analyses of the ISC published P and S residuals use summary rays, which are bundles of rays from one source cell to a receiver cell. The size of these cells determines the scale length of the heterogeneity to which they are sensitive. When these summary rays become asymptotically thin, the variance within the bundles tends to the variance in the dataset which is independent of structure – random noise. Estimates of this in the datasets are derived from deep events because they will be less affected by the strong heterogeneity in the upper mantle. For P waves this is reckoned to be $\approx 0.25s^2$ (Gudmundsson *et al.*, 1990) and for S waves the value is over an order of magnitude greater at $\approx 4s^2$ (Davies *et al.*, 1992). Estimates of the signal to noise ratios vary depending on the method of extrapolation used to calculate the interception point on the variance axis of an infinitessimally thin summary ray. Using linear extrapolations the signal to noise ratios for the ISC P and S datasets are 2 and 1.4 respectively.

There is also evidence that the ISC 'S' arrival times are reported only to the nearest second, but with variances of the order of $10s^2$ to be explained it does seem that there is considerable signal to be modelled.

The S travel time curve within the teleseismic window is far more complicated than the P equivalent because it is either crossed or is asymptotic to at least four other seismic phases (see figure 2.2). In the vicinity of these crossings correct identification of the seismic phase is extremely difficult.

2.3 Travel time residuals

The most basic data element used in seismic tomography is the travel time residual – the difference between the actual travel time of a seismic phase and the theoretical travel time predicted from a reference earth model. Of course the actual travel time of a ray is unknown since the hypocentre location and origin time are not precisely known. To obtain a location the ISC uses the arrival times it receives from the global network of stations and an initial guess at the hypocentre and utilizes a relocation procedure similar to the one in chapter 4 to iterate towards the best fitting solution. During this process the ISC can refine the phase identifications linked to an arrival time by the operators at the seismic station, governed by the size of the residual with respect to standard travel time tables.

2.3.1 Reference earth models

Given this location the epicentral angle between the source and a receiver can be used to compute a theoretical travel time. The ISC uses Jeffreys Bullen (JB, Jeffreys & Bullen, 1940) tables as its reference model. The problems associated with JB tables have been well documented (see below), but they are adequate for their purpose at this stage. The travel times that will be used extensively as reference curves in these studies are computed from the Preliminary Reference Earth Model (PREM) (Dziewonski & Anderson, 1981) by ray tracing. Agreement between PREM P residuals and JB P residuals is very good if the JB tables are corrected with -1.88s baseline and -0.0085s deg^{-1} slope (see figure 2.11). We have decided to treat PREM as isotropic, despite being anisotropic in the original model. This is because anisotropy was introduced in order to reconcile differences between Love and Rayleigh wave data at short epicentral distances ($< 20°$), corresponding to depths around 200km. Hence anisotropy need not be considered in studying short period ($\approx 1s$) arrivals alone. In any case, the mantle deeper than 200km was not required to be anisotropic, so this should enable direct comparisons between P and S models.

The version of PREM that is used has no oceanic layer so ray tracing an S wave through the outermost layers is possible. The choice of whether to use horizontally polarized SH or vertically polarized SV velocities when ray tracing through PREM is arbitrary since it will result only in differences in the degree zero, or spherical part of the heterogeneous models. Ultimately it is the aspherical deviations from the spherical that are of interest in this study. In this instance we have chosen to average the polarization direction velocities for both P and S cases.

2.4 S wave data

2.4.1 S residuals

Figure 2.3 is a plot of all the data identified by the ISC as S between the years 1964 and 1990 inclusive. The Y axis is the published travel time residual with respect to JB tables at the given epicentral angle on the X axis. The horizontal lineations occur because the times are only given to the nearest 0.1 seconds. Several features are apparent:

1. The windowing of the data at $\Delta > 80°$. On inspection of figure 2.2 it can be seen that the S travel time curve is crossed or asymptotic to several other phases – ScS, SKS, SKKS, PS, PcP, etc.

2. The cutoff in the data at ± 7.5 seconds. It is clear that the ISC do not give S identification to any arrival with a residual with respect to the JB S travel time curve with an absolute residual greater than 7.5s. The sharpness of the cutoff means that there is undoubtedly signal beyond these limits.

3. The average of the data from visual inspection seems to be greater than zero, and in fact turns out to be 1.7s.

The remaining S wave data with absolute residuals greater than 7.5s has to be found before any analysis can continue. In order to do this, for every station not recording an ISC identified S, every arrival was assumed to be S and its residual calculated. In cases where there was more than one arrival at a given station for an event lying within 20s of the expected travel time, the one with the smallest absolute residual was chosen. These residuals, calculated with respect to PREM are plotted in the same way in figure 2.4. Again several features are immediately apparent.

1. The lighter region at all epicentral angles in the centre of the plot representing the ISC S window of absolute value < 7.5s

2. The denser regions of the plot at $\pm$ 7.5s representing the missing large residual S data.

3. The differences between PREM and JB models at epicentral angles less than $\approx 40°$ in the ISC identified S window.

4. The appearance of PcS arrivals at $\Delta \approx 40°$ and the missing windows of data beyond 80°.

It is also useful to examine the ISC published residuals for those arrivals plotted in figure 2.4. Figure 2.5 does this, and shows quite clearly the various data windows chosen by the ISC. The PcS streak of data at all Y values at around 40° in figure 2.4 have been identified on this diagram as PcS and not S and the residuals have collapsed much nearer to zero. This also occurs with the ScS and SKS data at

$\Delta > 80°$. However there are several instances where there are gaps in the areas where large residual S arrivals might be expected to occur, for example at large positive values between 45° and 60° and 80° to 100° at both positive and negative values. Because the edges of the ISC 'unidentified' S window in fig 2.4 are very clear, these gaps are most likely to be misidentifications of large residual S arrivals. Figure 2.6 explains some of the patterns seen in this plot. It has to be remembered that all the points in figures 2.4 and 2.5 represent arrivals at stations where there has been no S arrival published by the ISC, which means for example that there are many more PcS arrivals between 45° and 60° that are not plotted in these figures.

2.4.2 S wave cutoff

Now that all the possible S arrivals have been identified, the extents of the S window have to be established and a cutoff applied. This cannot be done using figure 2.5 because the residuals on this plot that are lying at about zero are in general not S residuals and may have true S residuals anywhere within ± 20 seconds. Hence a plot like figure 2.4 must be used, and from this it is apparent that the background level of residuals seems to increase towards the top of the plot so care must be taken not to make the absolute cutoff point too large otherwise there could be a significant positive bias introduced. This can ultimately affect the degree zero terms of the model. It is much easier to see where the cutoff should be from figure 2.7 which is a combination of figures 2.4 and the PREM calculated residuals of the data in figure 2.3. The positive average is clearly seen to be around 2s, and the lower and upper bounds of the data window are estimated to be -9 and 13 seconds respectively.

Any cutoff should be independent of epicentral angle so that there is no average positive or negative bias in the average residual at a given delta. However, because the residuals in this plot are calculated with respect to PREM and not JB tables, the differences in the shapes of the travel time curves are distance dependent so the cutoff has to be distance dependent. The only range where this is a problem is between 25° and 35° where the curves differ greatly, as indicated by the dipping ISC S window in figure 2.4. This is accounted for by tapering down the cutoff value going from 35° to 25° at both 13 s and -9 s.

The considerable data contamination of S by SKS has to be removed, so it was decided to omit all residuals lying between 80° and 90° between the upper and lower residual bounds. This corresponds to the choice of 83° as the cutoff by Davies & Clayton, 1986 and 75° by Davies *et al.*, 1992. However neither of these studies reintroduce data past 90°. This is deemed a necessity in this study in order to obtain a similarly parameterized model to the one derived from the P dataset. If the data at these large epicentral angles is badly contaminated the model will not correlate well with other lower mantle models at this depth.

The effect of correct PcS identifications where there has been no S arrival can still be seen at $\Delta \approx 40°$ in figure 2.5. A delta independent window removing this area would extend from about 37° to 41° and

eliminate a large amount of usable data, much of which would be S residuals of large absolute value which are particularly important in determining the size of the model. Therefore, since the number of legitimate PcS arrivals seems to be minimal compared with the total number of S data, it was decided to include them, expecting that they will not have a large effect. The finalized raw data is plotted in figure 2.8 and is analyzed in figure 2.9.

2.5 P wave data

2.5.1 P residuals

The equivalent plot to figure 2.3 for P waves is shown in figure 2.10. As a result of the size of the dataset, only one arrival in 20 is plotted. From the travel time curve it is clear that the only identification problems that might occur are at large epicentral angles where the much weaker core reflected PcP becomes asymptotic to P. Nevertheless figure 2.10 shows none of the problems inherent in figure 2.3. The PREM residual equivalent plot, figure 2.11, illustrates some of the differences between the two reference models. Firstly PREM has a clear positive bias of about 2s over JB, and there seems to be a slight increase in the average towards larger epicentral angles – in agreement with section 2.3.1. The statistical analysis of this raw P data from figure 2.11 is shown in figure 2.12.

2.5.2 P wave cutoff

Again this is much clearer than the case for S waves. There seems to be very little signal outside 4 seconds of the mean value, so a cutoff of $\pm$ 4 seconds can be applied to figure 2.10. This agrees well with Gudmundsson *et al.*, 1990 who suggest that the maximum feasible signal is contained in $\pm$ 4 – 5 seconds. Bolton & Masters, 1991 have found signal to $\pm$6s, and Darragh, 1985 has excluded signal past $\pm$6.75s. The primary use of P waves in ISC studies to date is understandable given the unproblematic nature of the data.

2.6 Implications for global models.

From examination of the data alone, several insights into the outcome of the final model can be made:

- It is the combination of the source and receiver coverage in figure 2.1 that determines the maximum lateral resolution of any mantle model – in this case the large gap across the Pacific Ocean bridged only by a handful of sources and stations around Hawaii. Hence a complete eigenvalue inversion for a model beyond about degree 6, corresponding to a half wavelength of 30° is unjustified (Dziewonski, 1984).

- The complete absence of shear wave data between 80° and 90° epicentral distance is ultimately going to be a significant limiting factor in the resolution of the final S model. From PREM, a ray traveling 80° bottoms out at approximately 2100km depth, so at greater depths the model is going to be constrained by very little data. The only reliable way to obtain S arrival times in this region and possibly deeper is to take the original seismograms and cross correlate them with synthetic wave forms.

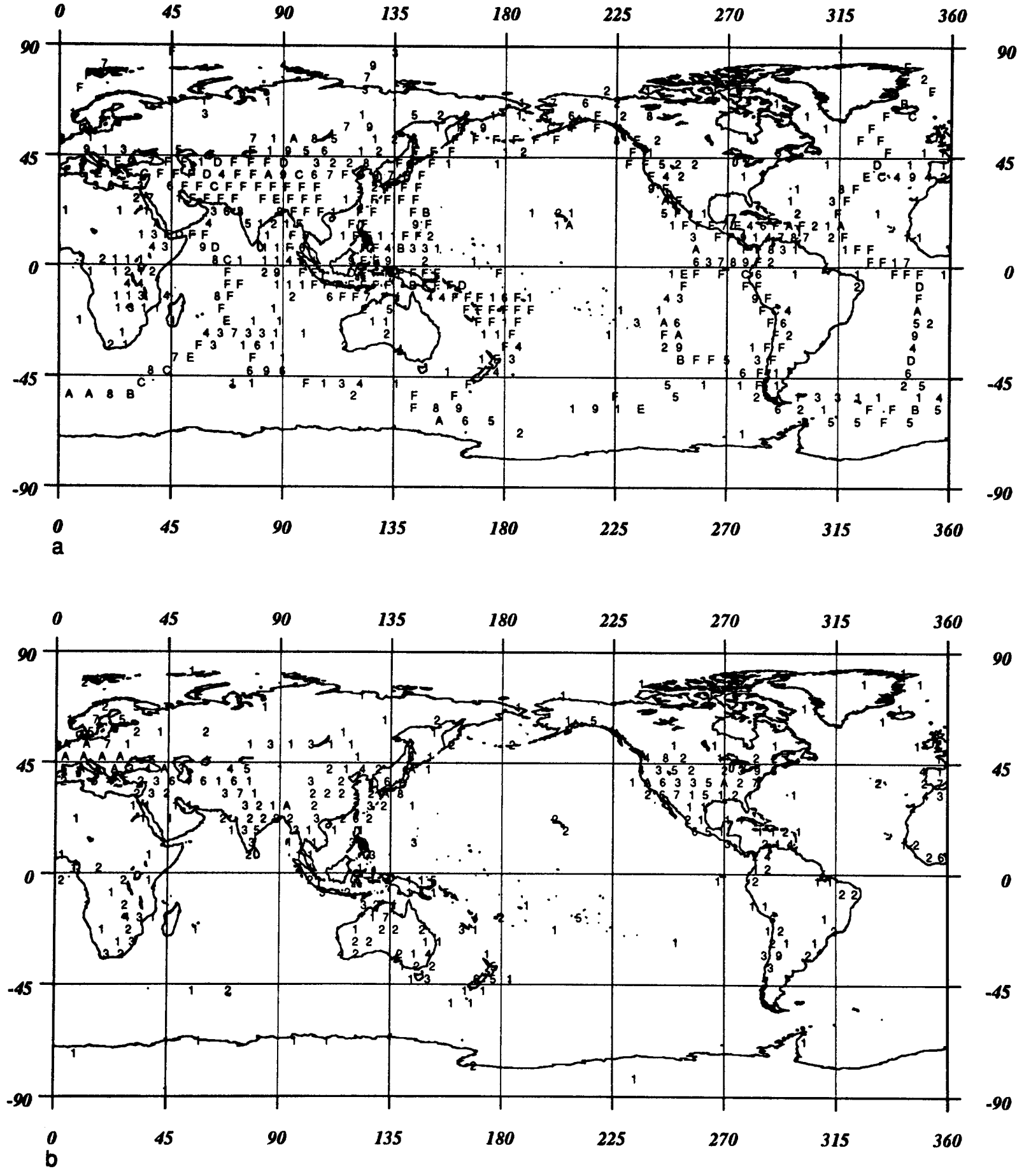


Figure 2.1: Distribution of sources (top) and receivers (bottom). The numbers represent a count in a 5° by 5° cell. The letters A to E represent the numbers 10 to 14, and F represents 15 or more counts.

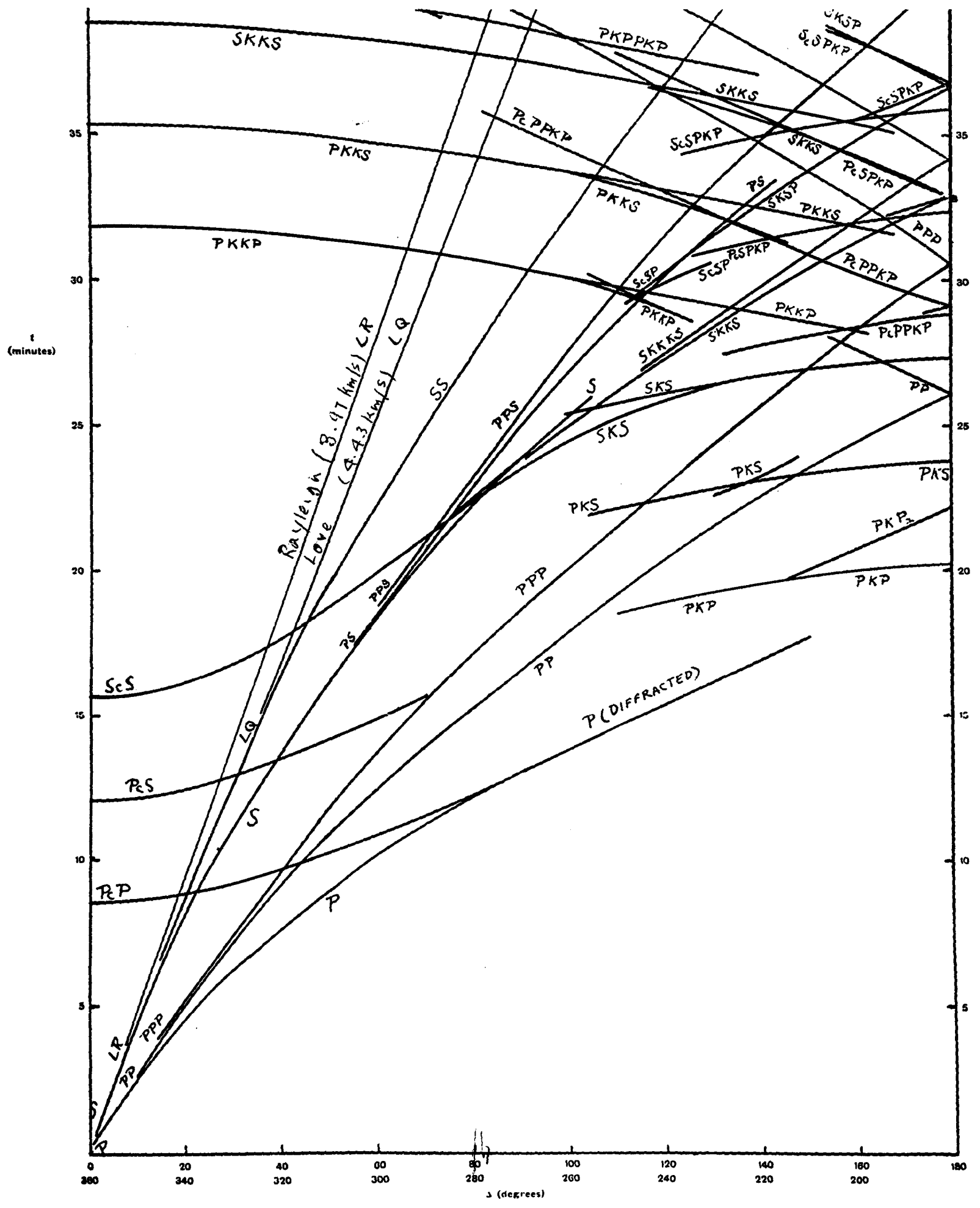


Fig. 5.—Travel times for a surface focus.

Harold Jeffreys, The Times of the Core Waves.

Figure 2.2: Jeffreys-Bullen travel time tables.

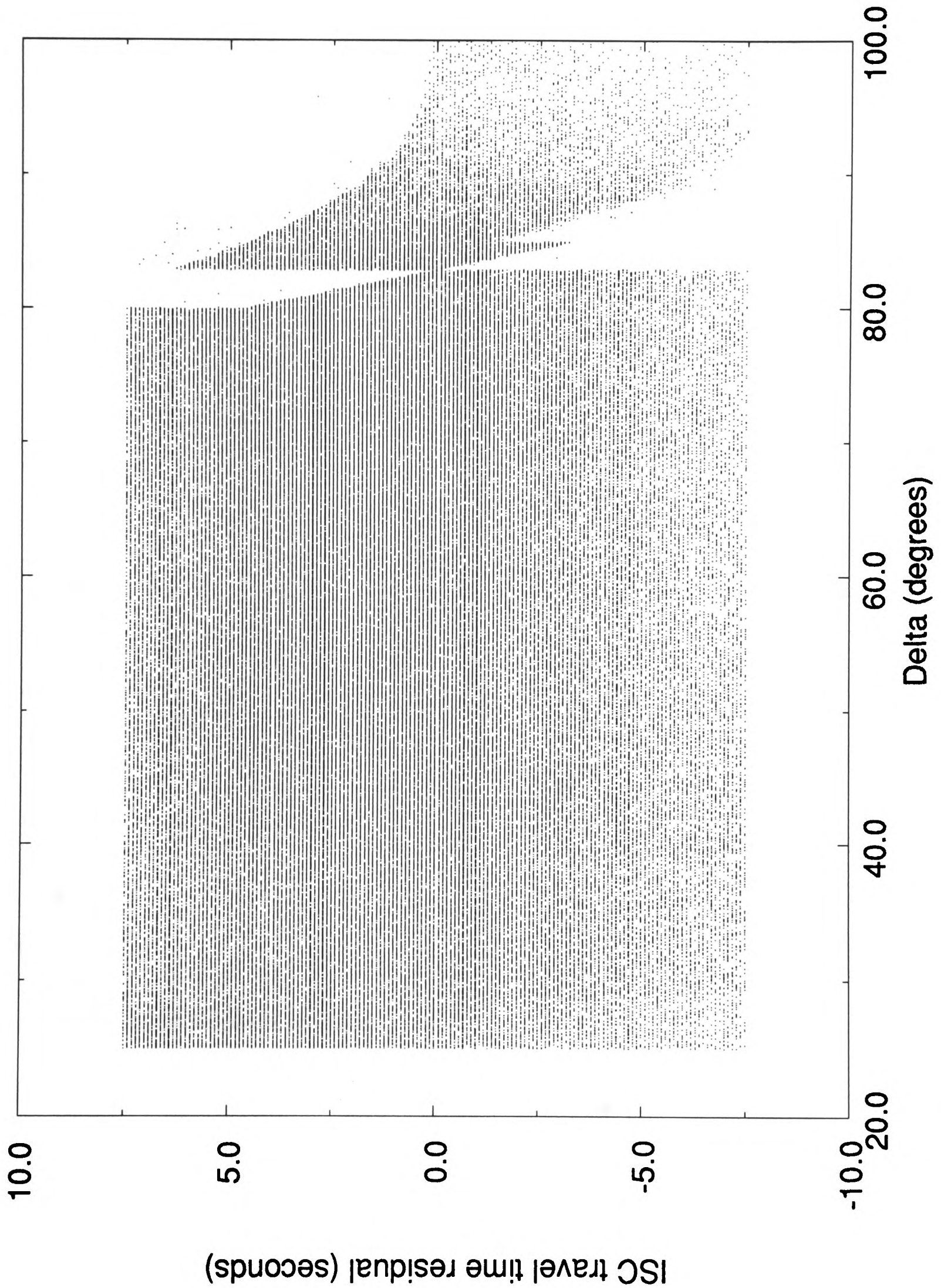


Figure 2.3: ISC 'S' travel time residuals.

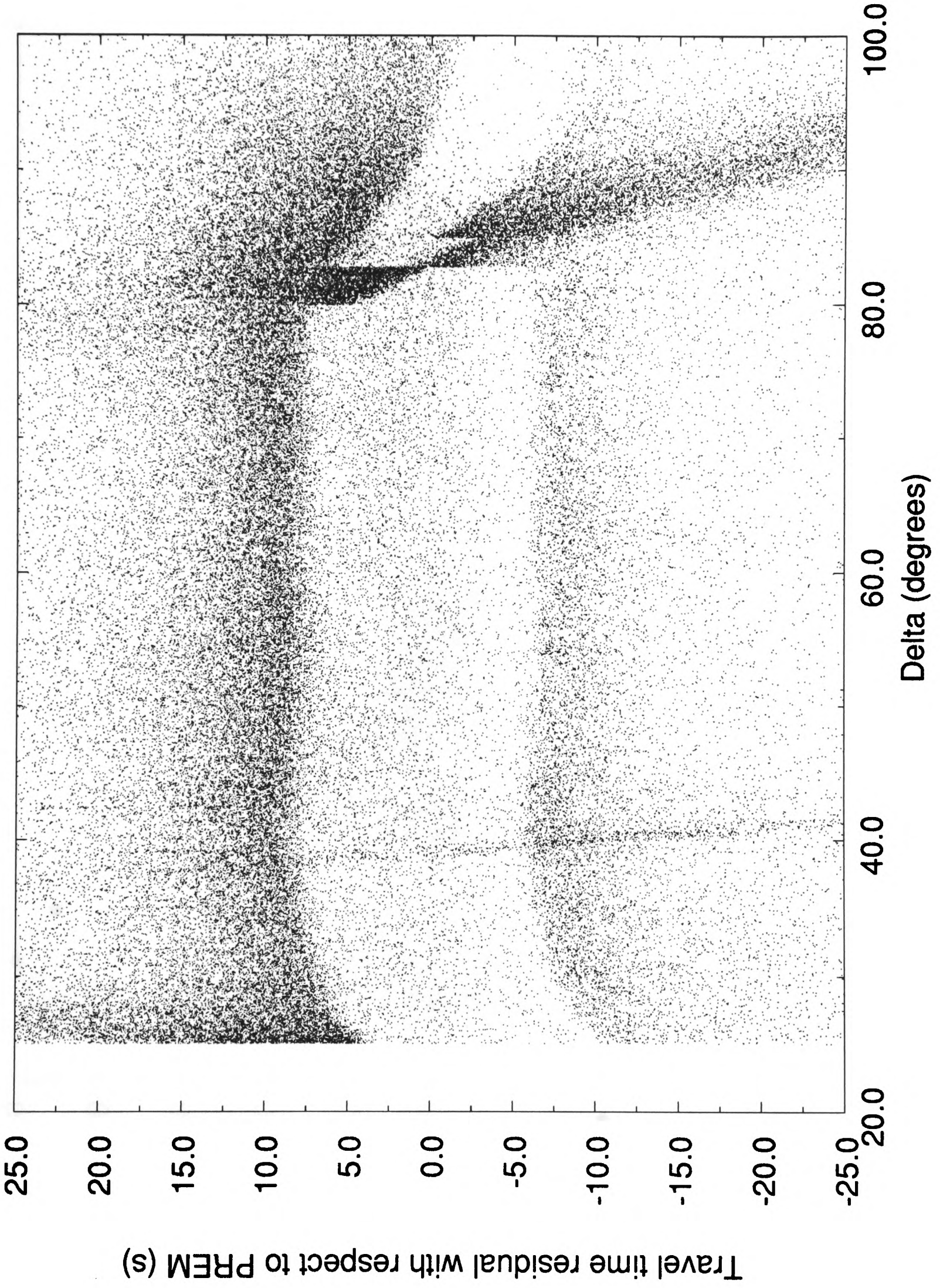


Figure 2.4: PREM residuals for those arrivals which lie within 25s of the expected S arrival time from PREM but are not identified as S by the ISC. These are the 'unidentified' S travel time residuals. See text for details

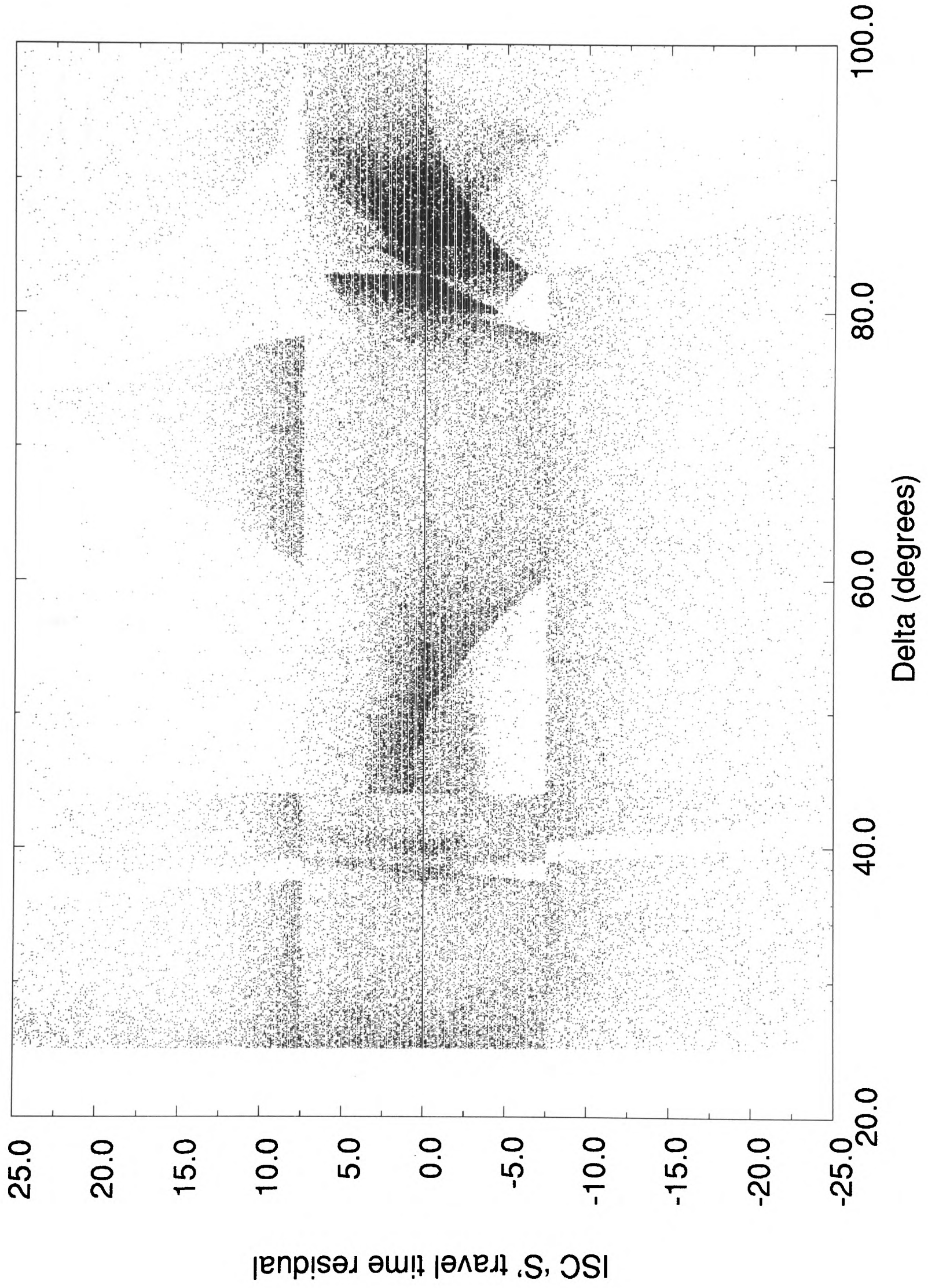


Figure 2.5: ISC published residuals for those arrivals which lie within 25s of the expected S arrival time from PREM but are not identified as S by the ISC. See text for details.

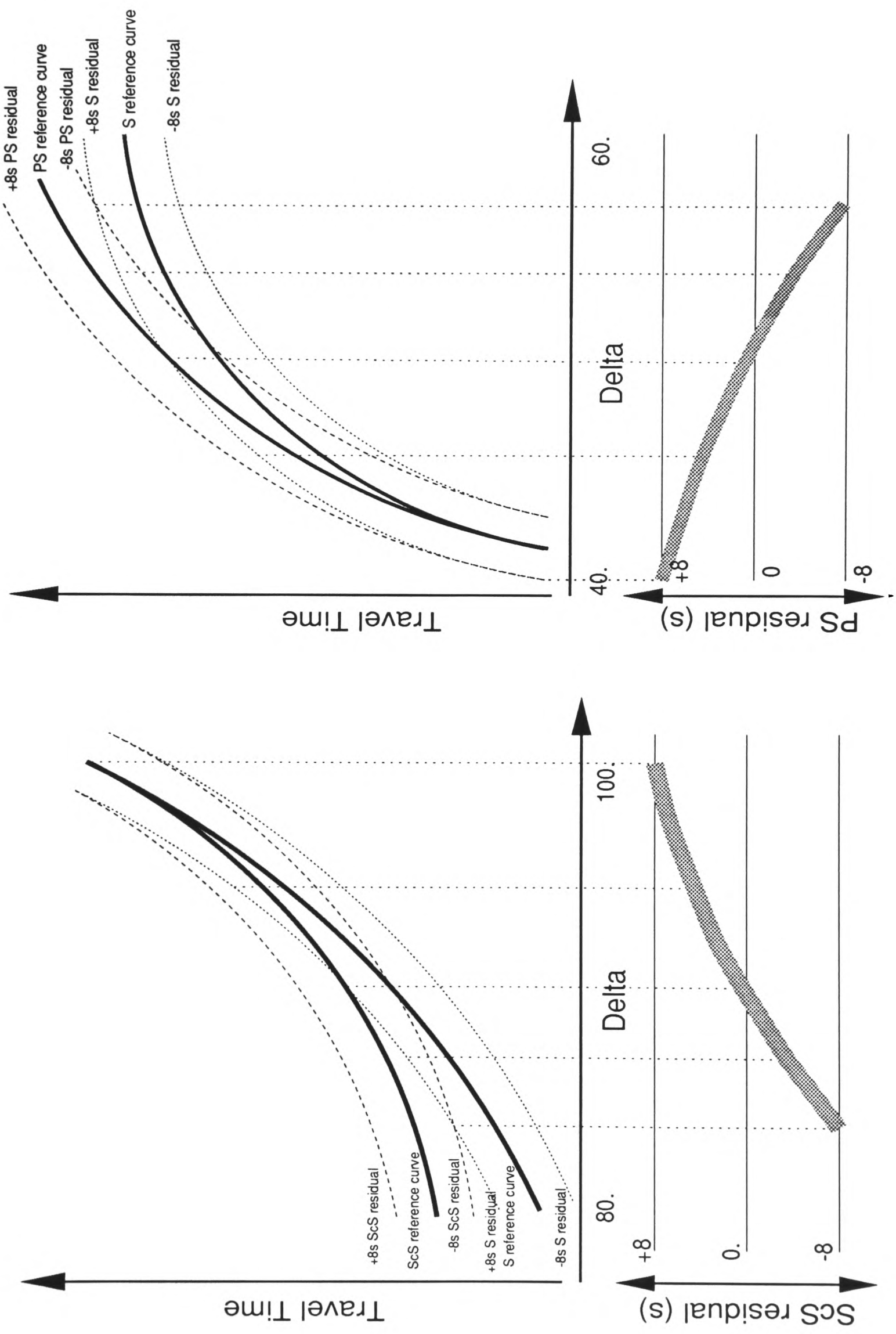


Figure 2.6: Explanation of the shape of misidentified arrivals on raw residual plots. See text for details.

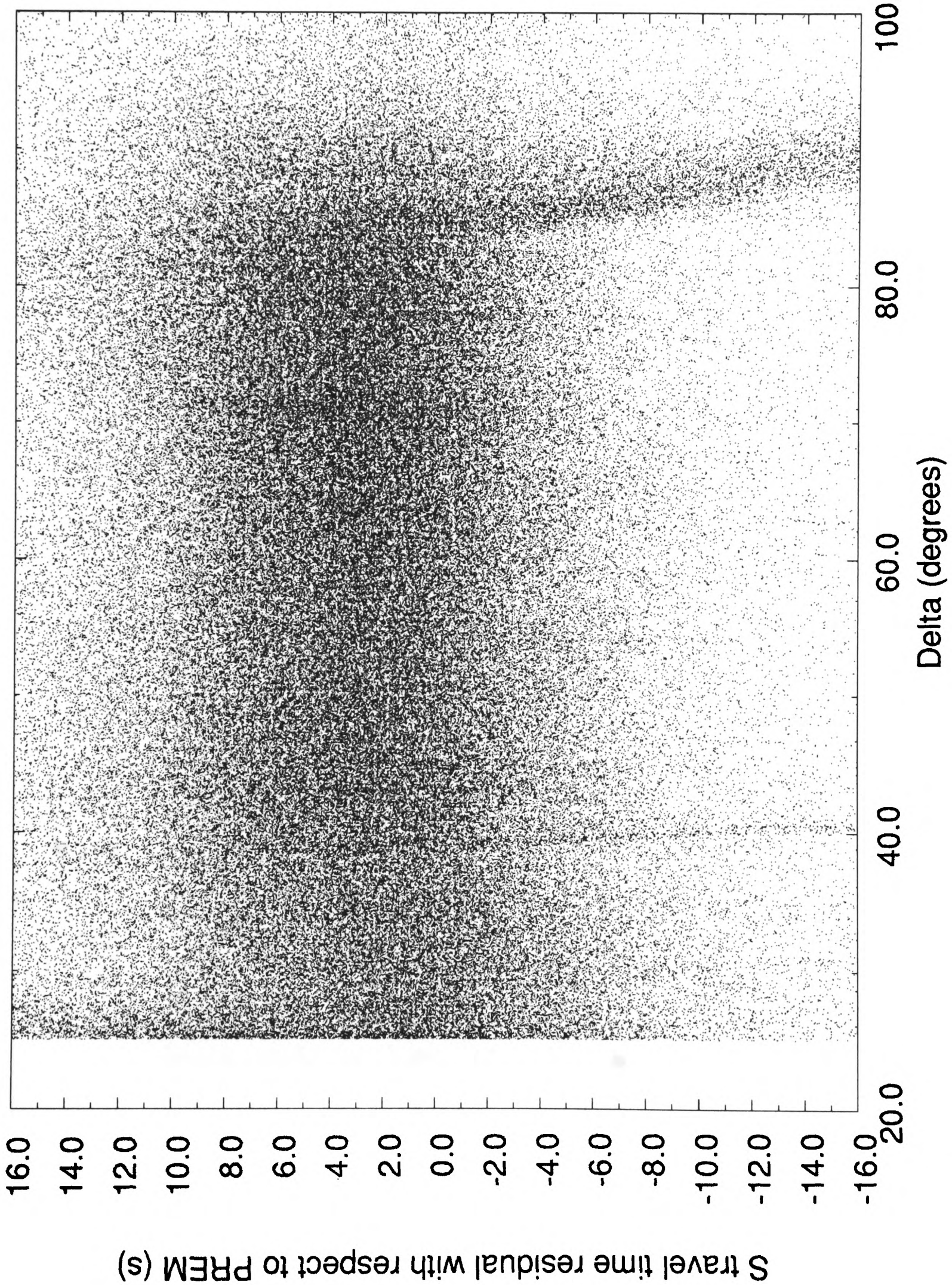


Figure 2.7: S residuals with respect to PREM. This plot is a combination of the S PREM residuals and the 'unidentified' S PREM residuals.

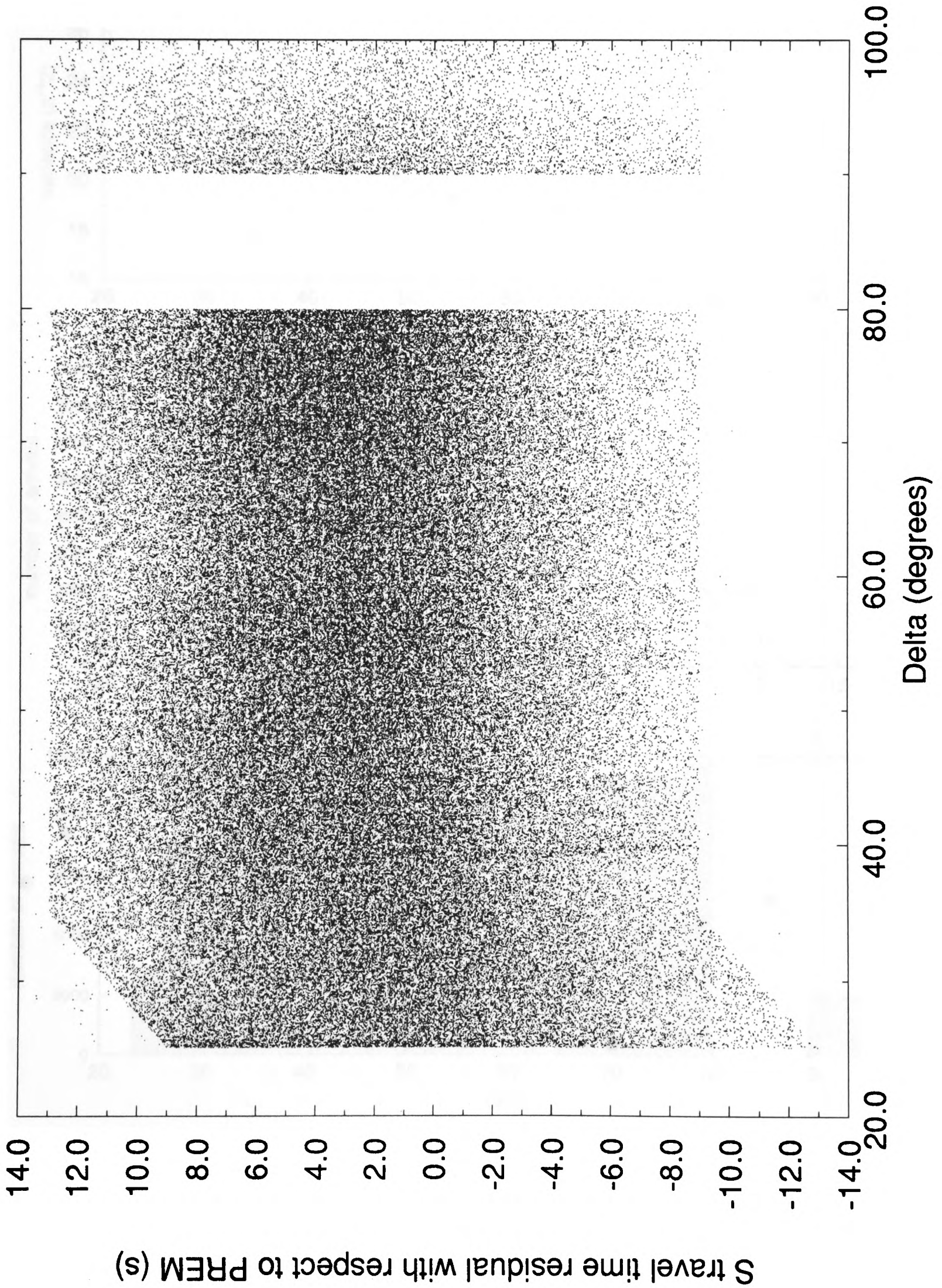


Figure 2.8: S residuals with respect to PREM including cutoffs.

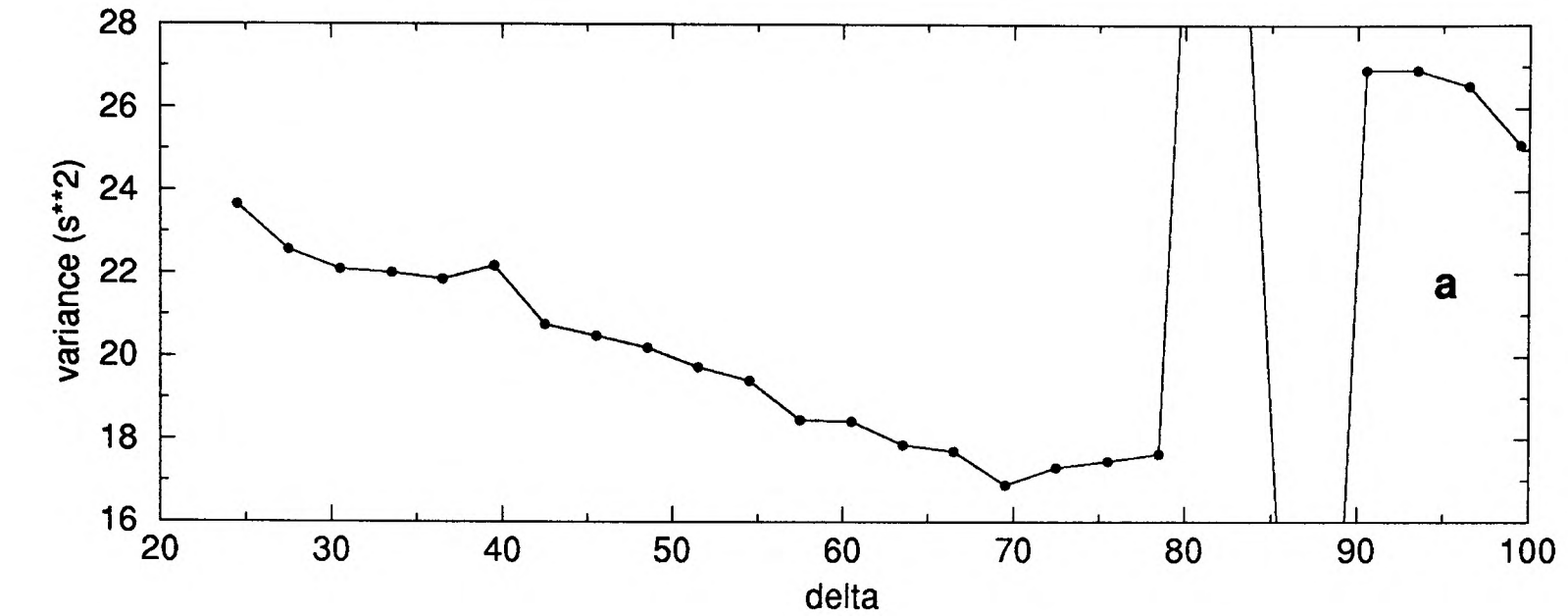


Figure 2.9: Statistical analysis of the final S data.

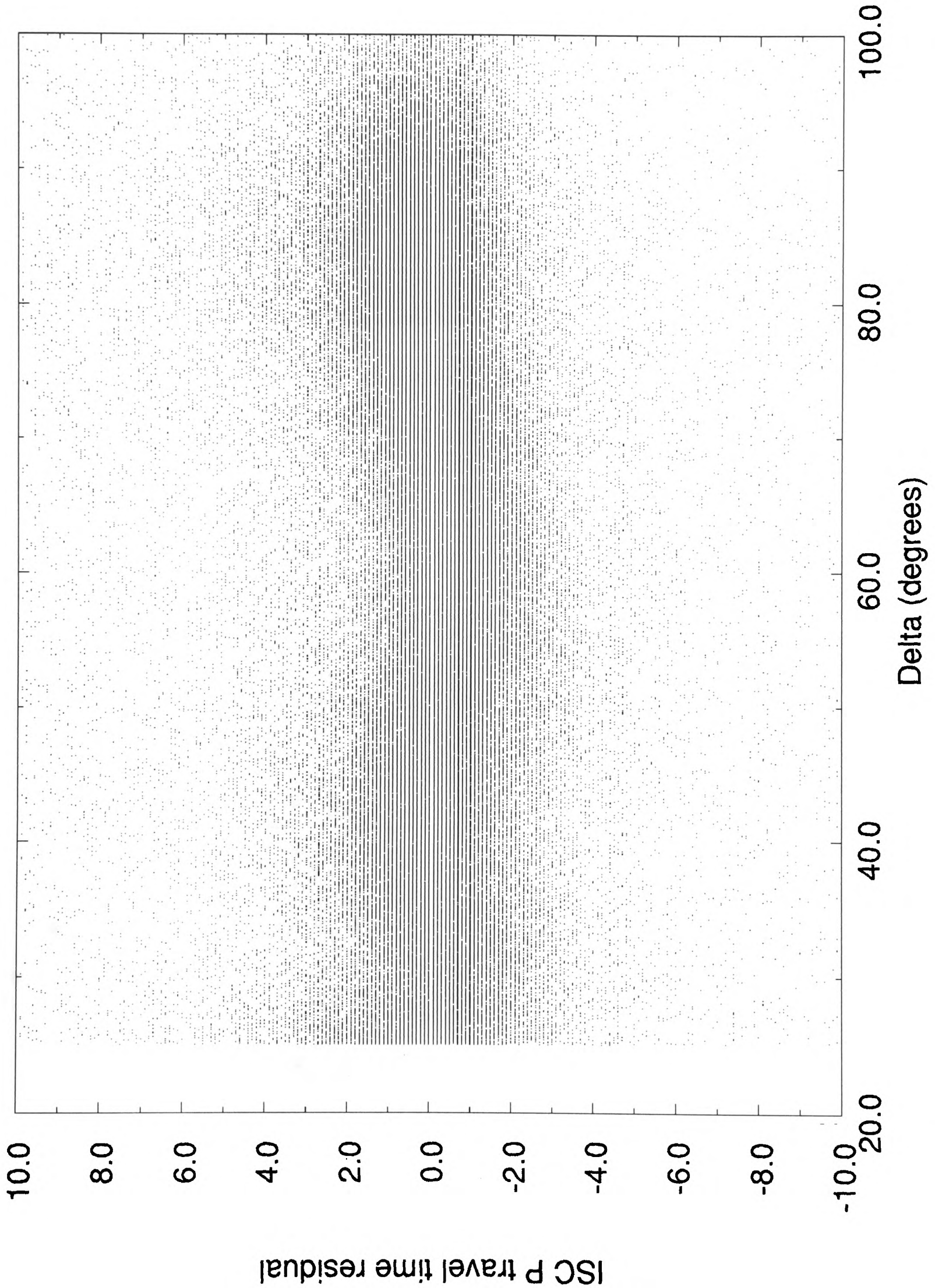


Figure 2.10: ISC 'P' travel time residuals.

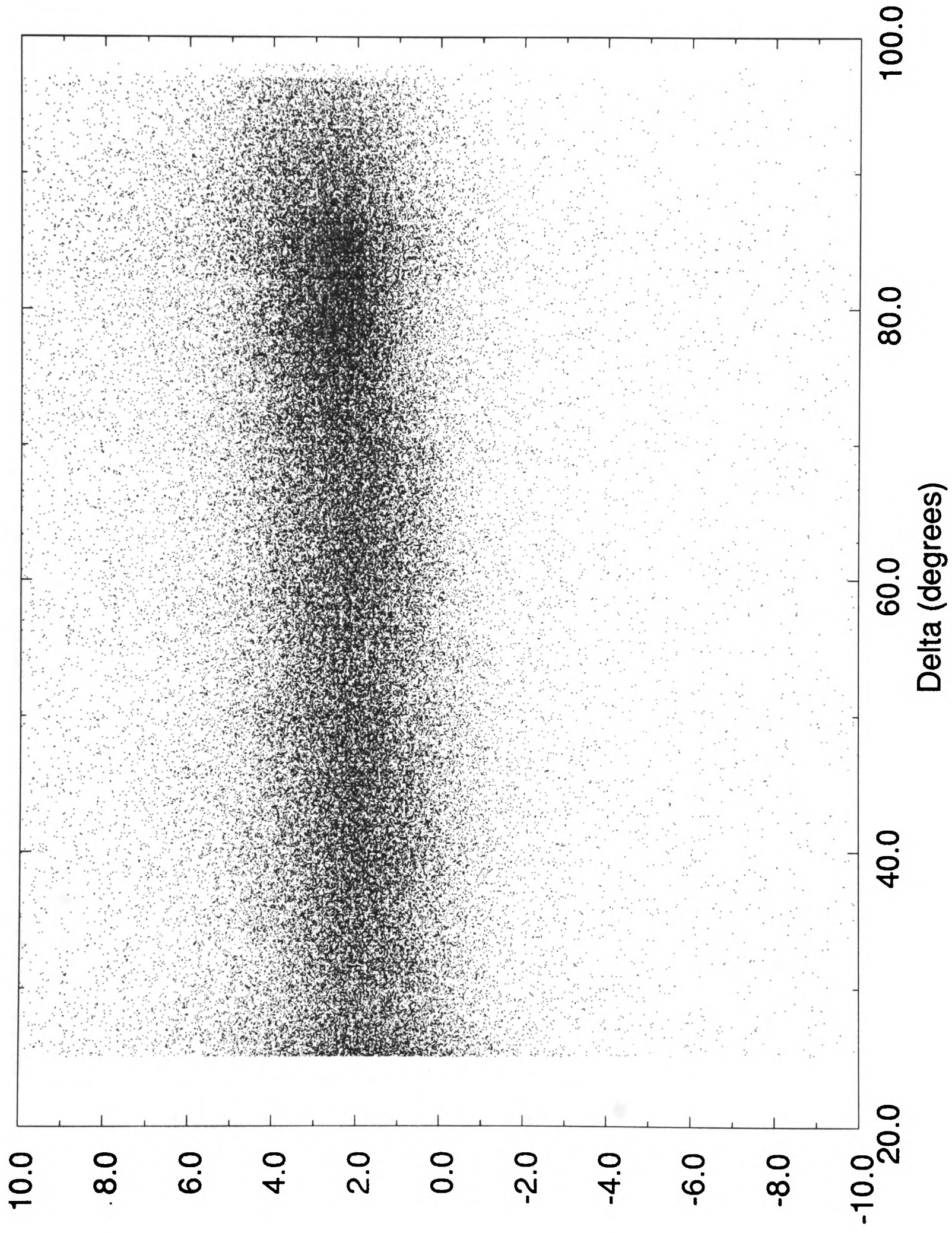


Figure 2.11: P travel time residuals calculated with respect to PREM.

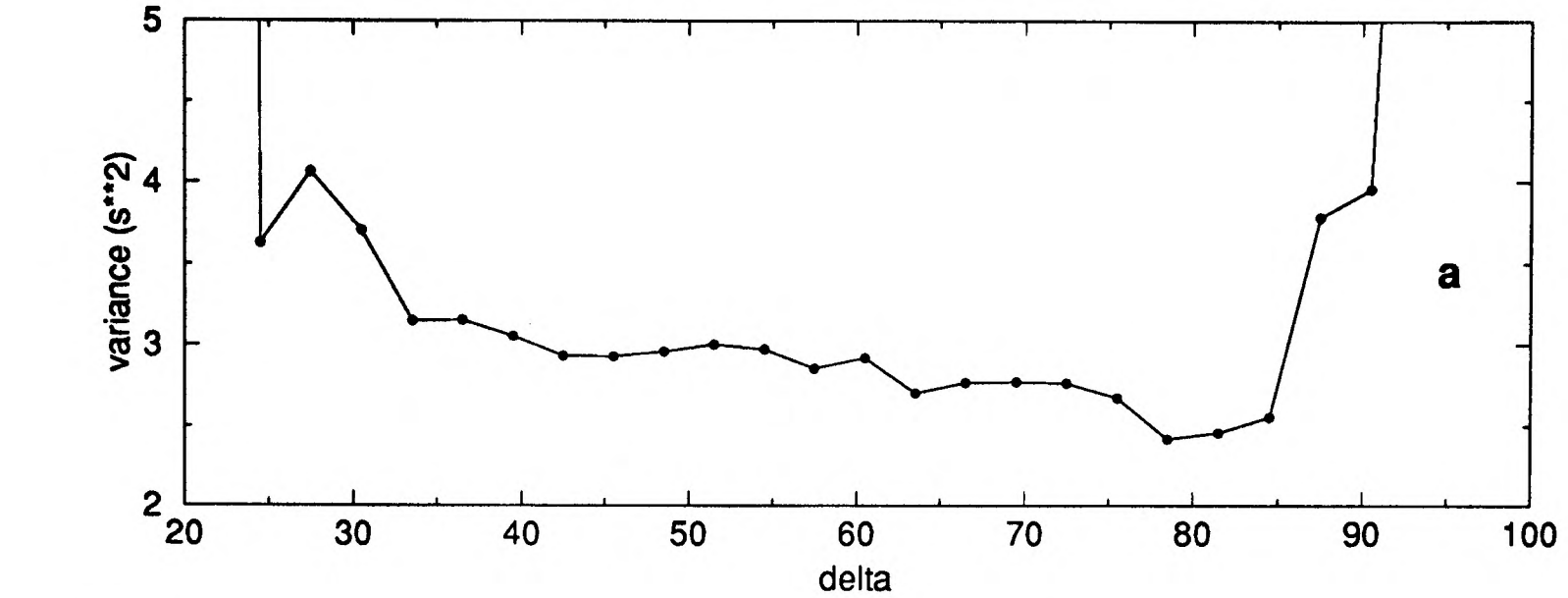


Figure 2.12: Statistical analysis of the P data of the final P data.

Chapter 3

Methodology

The theoretical formalism for the tomographic inverse problem has been described in detail in the literature. The following chapter follows closely the derivations in both Woodhouse & Dziewonski, 1989 and Dziewonski, 1984.

3.1 The tomographic inverse problem

The predicted travel time of a seismic ray from the s^{th} source to the n^{th} receiver can be written as

$$d_n^s = D_n[\mathbf{f}^s, \mathbf{E}] + \epsilon_n^s \tag{3.1}$$

Here ϵ_n^s is the observational error for this arrival and $\mathbf{f}^s$ represents the four source parameters – latitude, longitude, depth, and origin time. $\mathbf{E}$ is a model of the earth which for this study is given simply in terms of velocities at a specific frequency.

$$\mathbf{E} = [v_p(\mathbf{x}), v_s(\mathbf{x})] \tag{3.2}$$

The function D_n gives the travel time between the source and receiver as a function of both the source parameters and the earth model. It is nonlinear because the two are intrinsically linked, that is to say the earthquake location is dependent on the earth model used and vice versa. We are interested in finding the unknowns $\mathbf{f}^s$ and $\mathbf{E}$ which minimize the observational errors ϵ_n^s while at the same time taking into account the statistical properties of ϵ and the *a priori* information on the model.

Tarantola & Valette, 1982 show that if there are no systematic errors in the observations and if the data possess a Gaussian structure, then the inversion can be carried out using the least squares method. However the fundamental problems involved with a global seismic dataset are well known and are discussed in detail in section 2.1. There is no way of quantifying the effects of for example predominantly

subduction related events and mainly continental stations on global models. In addition, as is pointed out by Woodhouse & Dziewonski, 1989, there can also be errors due to parameters which have not been included in the inversion, in this case for example anisotropy. For these reasons the validity of assuming Gaussian errors is unknown, but at this time it is necessary to proceed with whatever assumptions have to be made and then test the results for possible errors.

The derivation of a heterogeneous model of the earth is greatly simplified if the partial derivatives of the travel time computed from an initial model with respect to the heterogeneous model coefficients can be calculated. For this reason equation 3.2 is normally rewritten

$$\mathbf{E}(\mathbf{x}) = \mathbf{E_O}(r) + \delta\mathbf{E}(\mathbf{x}) = \mathbf{E_O}(r) + \sum_{klm} E_{klm} m_{klm}(\mathbf{x}) \tag{3.3}$$

where $\mathbf{E_O}(r)$ is a spherically symmetric reference earth model, E_{klm} are the model coefficients, and m_{klm} are a set of basis functions. At this point the parameterization of the model can be chosen to be either in terms of discrete blocks or a series of continuous functions (see section 1.2). In addition the source parameters can also be written in terms of an initial location plus a perturbation.

$$\mathbf{f}^s = \mathbf{f_O}^s + \delta\mathbf{f}^s \tag{3.4}$$

As a result the function D_n becomes

$$D_n[\mathbf{f}^s, \mathbf{E}] = D_n[\mathbf{f_O}^s + \delta\mathbf{f}^s, \mathbf{E_O}(r) + \delta\mathbf{E}(\mathbf{x})] \tag{3.5}$$

which in vector notation is

$$\mathbf{D}(\mathbf{y}, \mathbf{E}) = \mathbf{D}(\mathbf{y_O} + \delta\mathbf{y}, \mathbf{E_O} + \delta\mathbf{E}) \tag{3.6}$$

where the vector $\mathbf{y}$ has been introduced to represent the source parameters for all events. Using Taylor's theorem this can be expanded to first order as

$$\mathbf{D}(\mathbf{y}, \mathbf{E}) = \mathbf{D}\,(\mathbf{y}, \mathbf{E})|_{(\mathbf{y_O}, \mathbf{E_O})} + \mathbf{A}(\delta\mathbf{y}, \delta\mathbf{E}) + \varepsilon \qquad \text{where } \mathbf{A} = \left.\frac{d\,\mathbf{D}(\mathbf{y}, \mathbf{E})}{d\,(\mathbf{y}, \mathbf{E})}\right|_{(\mathbf{y_O}, \mathbf{E_O})} \tag{3.7}$$

where ε is the error involved in truncating the expansion. The first term in this expansion is simply a vector of travel times from the sources at $\mathbf{y_O}$ through the spherical reference earth model $\mathbf{E_O}$ and is known exactly. If this is called $\mathbf{T_O}$ then equation 3.7 becomes

$$\mathbf{D}(\mathbf{y}, \mathbf{E}) = \mathbf{T_O} + \mathbf{A}(\delta\mathbf{y}, \delta\mathbf{E}) + \varepsilon \tag{3.8}$$

As was indicated earlier in this section the matrix **A** here is a matrix of partial derivatives of the spherically symmetric reference model with respect to the model coordinates and the hypocentre locations. Substituting this into equation 3.1 and introducing vector notation

$$\mathbf{d} = \mathbf{T_O} + \mathbf{A}(\delta\mathbf{y}, \delta\mathbf{E}) + \mathbf{e} \tag{3.9}$$

$$\Rightarrow \delta\mathbf{t} = \mathbf{A}(\delta\mathbf{y}, \delta\mathbf{E}) + \mathbf{e} \tag{3.10}$$

where $\delta\mathbf{t}$ is the difference between the actual travel time of a ray and the theoretical travel time through the reference model $\mathbf{E_O}$. In this equation the error terms ϵ and ε for each individual data element have been added together and then written in the form of the vector **e**. In an analogous fashion to the discussion above, these errors will not necessarily be gaussian in nature, but at this stage it is necessary to use this assumption. Hence, following Woodhouse & Dziewonski, 1989, the maximum likelihood estimate of the unknowns $(\delta\mathbf{y}, E_{klm})$ is the one which minimizes the following

$$L \equiv \sigma^{-2}||\delta\mathbf{t} - \mathbf{A}(\delta\mathbf{y}, \delta\mathbf{E})||^2 \tag{3.11}$$

Here σ^2 is the data variance. In order to be concise the damping term has been omitted from this equation. Differentiating with respect to the unknowns and equating to zero this becomes

$$\mathbf{A^T A}(\delta\mathbf{y}, \delta\mathbf{E}) = \mathbf{A^T}\delta\mathbf{t} \;\Rightarrow\; (\delta\mathbf{y}, \delta\mathbf{E}) = [\mathbf{A^T A}]^{-1}\mathbf{A^T}\delta\mathbf{t} \tag{3.12}$$

which gives the classic least squares solution to the inverse problem.

3.2 Time-term analysis

From a diagram such as figure 1.1 it is clear that contributions to the travel time residual $\delta\mathbf{t}$ in equation 3.12 can occur at any point on the ray path – from the hypocentre to the upper/lower mantle boundary, in the lower mantle, and from the upper mantle near the station. This can be represented crudely as follows:

$$\delta t = \delta t_{SOURCE} + \delta t_{LOWER\,MANTLE} + \delta t_{RECEIVER} \tag{3.13}$$

This method of breaking the residual up into its constituent parts is called 'time-term' analysis and was first used by Cleary & Hales, 1966. In order to derive lower mantle models we need to isolate the second term which means finding some way of calculating the other two.

3.2.1 Source term

The part of the residual that is attributable to the downward leg of the ray to the upper/lower mantle boundary should be absorbed during the relocation process. This is described in detail in chapter 4, but essentially the relocation of events is necessary for three main reasons:

- Minimize the source-receiver residuals with respect to PREM which is recognized to generate a more accurate travel time curve than JB tables.
- The ISC uses only compressional phases, P and pP to locate all the events, so to avoid having a compressional bias in the results it is necessary to include the S phase in the relocation process.
- Average out the effects of small scale heterogeneity. The ISC uses travel times from $\Delta < 25°$ as well as from the teleseismic window to locate their events. This information is dependent on local structure much more than that from larger epicentral angles whose average residuals will be far more representative of the earth as a whole. Hence a strong small scale velocity anomaly near the event could seriously affect the event location which in turn interferes with the large scale information that is being modeled. As a result, by using only the information from the teleseismic window, we obtain a less accurate event location but gain one whose ray travel times are less dependent on small scale heterogeneity.

3.2.2 Receiver term

Station corrections are the standard method of representing near receiver structure. They compensate for the velocity structure below the station and its height above sea level. Both static (Morelli & Dziewonski, 1991) and azimuth dependent (Dziewonski & Anderson, 1983, Dziewonski, 1984) station corrections have been used in the past, and these are calculated by either averaging or fitting an azimuth dependent polynomial to the set of residuals calculated from the arrivals at that station. The inherent danger in using azimuth dependence is in the possibility of including lower mantle model signal. Dziewonski, 1984 compared the corrections generated in studies both with and without allowance for lower mantle heterogeneity. The results were very similar and so he concluded that the azimuth dependent corrections were indeed only accounting for crustal and upper mantle velocity structure. Nevertheless, later studies by this author (Morelli & Dziewonski, 1991) have used only static corrections, and so we have chosen to use this representation. Souriau & Woodhouse, 1987 in fact showed that static corrections correlate well with upper mantle structure.

3.2.3 Ellipticity corrections

A reference model such as PREM represents a global average of the earth's seismic properties. Because it is spherical, a correction has to be added to compensate for the earth's ellipticity, and this has been

done throughout using the method of Dziewonski & Gilbert, 1976 wherever a travel time from PREM has been calculated.

Using the results from this section, the travel time residual due to lower mantle heterogeneity from an event that has been relocated with respect to PREM is:

$$\delta t_{LOWER\,MANTLE} = T_{ACTUAL} - T_{PREM} - \delta t_{ELLIPTICITY} - \delta t_{RECEIVER} \tag{3.14}$$

3.3 Iterative time term inversion

From the previous section, in addition to the hypocentre locations and the model coefficients, the unknown parameters now include station corrections. If in this case there are around 20 000 events contributing to the final inversion and several thousand station corrections to be determined, the total number of parameters involved in the matrix A approaches 85 000. Application of a least squares procedure would lead to a huge inner product matrix $\mathbf{A^T A}$. This is clearly far too large to be solved directly so an alternative method has to be found. Dziewonski & Anderson, 1983 point out that this matrix is highly structured:

$$\mathbf{A^T A} = \begin{bmatrix} C & H & G \\ H^T & D & F \\ G^T & F^T & E \end{bmatrix} \tag{3.15}$$

where C, D, and E, represent the model parameters, the event locations, and the station corrections. F, G, and H are matrices giving the dependencies of these variables on eachother. Dziewonski & Anderson, 1983 argue that the matrix is dominated by its diagonal elements and hence the inverse can be approximated as

$$\left[\mathbf{A^T A}\right]^{-1} = \begin{bmatrix} C^{-1} & 0 & 0 \\ 0 & D^{-1} & 0 \\ 0 & 0 & E^{-1} \end{bmatrix} \tag{3.16}$$

This implies that the three sets of parameters – the model, locations, and station corrections – are not strongly dependent on each other. If we consider that the model is of the large scale structure of the lower mantle then it does seem reasonable to think that a location involving this model will not move from its location by a significant amount. This is assuming that the velocity perturbations are very small, an assumption which will be found in the next section to be essential in tomographic studies on a global scale. Hence it should be possible to solve for each of the three sets of parameters in turn and iterate to a solution. Furthermore the hypocentre locations are only dependent on each other because their combined positions affect the model, so if this dependence is assumed to be very small the events

can be located singly and the station coefficients computed one at a time. The ultimate test of the method is the convergence of the solution.

Morelli & Dziewonski, 1991 used the concept of summary rays and summary earthquakes to reduce the number of parameters in the matrix $\mathbf{A}^T\mathbf{A}$ so that it was small enough to be inverted in one step. In this method the earth is divided up into equal area cells and averages are taken for all rays traveling between two cells in order to obtain a representative ray. Similarly a summary earthquake is defined as an event, initially with zero origin time, located at the centre of a source cell whose travel times are those computed for summary paths. As a result the number of 'events' contributing to the model is governed only by the size of the cell chosen. Dziewonski & Anderson, 1983 discuss the differences between the two methods of inversion – iterative and simultaneous – for the hypocentres and model coefficients, and conclude that the two should give identical results if the sources and receivers are well distributed.

3.4 Fermat's principle and travel time tomography

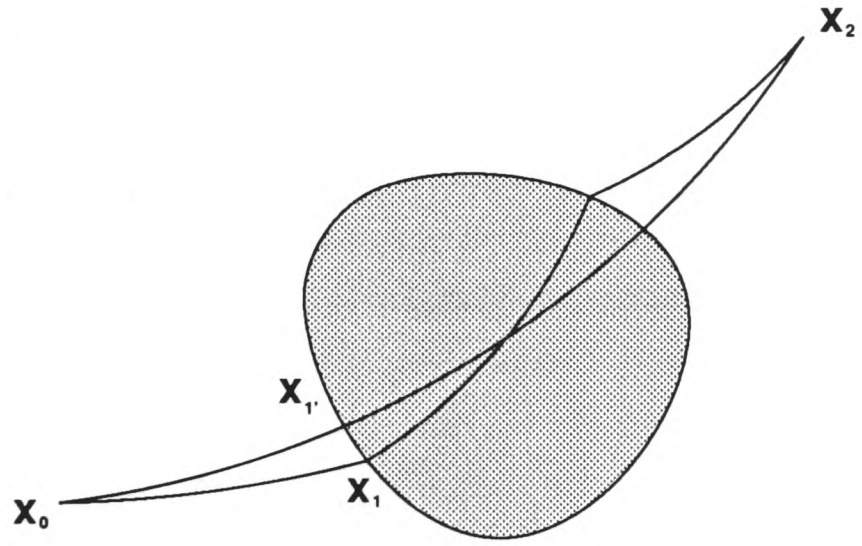


Figure 3.1: The bending of a seismic ray through a velocity anomaly. $\mathbf{x_0} \overset{\mathbf{x_1}}{\rightarrow} \mathbf{x_2}$ is the perturbed ray and $\mathbf{x_0} \overset{\mathbf{x'_1}}{\rightarrow} \mathbf{x_2}$ is the PREM equivalent ray ignoring the anomaly.

The seismic rays shown in figure 1.1 were calculated by ray tracing through PREM. In the real earth the non-spherical velocity structure will perturb the ray geometry. Figure 3.1 illustrates this behaviour. Fermat's principle states that the ray itself, $\mathbf{x_0} \overset{\mathbf{x_1}}{\rightarrow} \mathbf{x_2}$, is the minimum time path between the two points. It can be shown that if the distance between the two rays is of order ε, then the difference in travel time is of order ε^2. This is significant because it means that if the velocity anomaly is small, only a small error in the travel time will be made by integrating the velocity anomaly along the PREM ray path.

The use of Fermat's principle effectively linearizes the inversion problem as it removes the dependency

between the ray path which is used to compute the kernel functions and the heterogeneous velocity structure itself.

3.5 Spherical harmonic expansions

These provide a simple means of expressing the distribution of a given function over a spherical surface (Chapman & Bartels, 1940, 1951). A spherical harmonic consists of a Fourier series for longitudinal dependence and Legendre functions for latitudinal dependence. In addition we use normalized Legendre polynomials to represent the depth variation. The degree of accuracy of the representation is arbitrary, being determined simply from the maximum degree and order of the spherical harmonics and Legendre functions used in the series.

The combination of the spherical harmonics and depth polynomials gives a set of functions which are orthogonal, or orthonormal if they are normalized. In theory this means that each is independent of the other, that is there should be no 'leaking' of signal from one spherical harmonic into the other. However in practice, because the data is not well distributed throughout the earth, aliasing of one harmonic onto the other can occur.

3.6 Lower mantle model inversion theory

Perturbations in seismic velocity can be expanded in three dimensions to an arbitrary degree of accuracy in the following way.

$$\frac{\delta v}{v}(r,\theta,\phi) = \sum_{k=0}^{K}\sum_{l=0}^{L}\sum_{m=-l}^{l} {}_kc_l^m f_k(r) Y_l^m(\theta,\phi) \tag{3.17}$$

where θ and ϕ are colatitude and longitude respectively and ${}_kc_l^m$ are complex model coefficients. $f_k(r)$ are depth polynomials and $Y_l^m(\theta,\phi)$ are spherical harmonics given by:

$$Y_l^m(\theta,\phi) = X_l^m(\theta)e^{im\phi} \tag{3.18}$$

where

$$X_l^m(\theta) = (-1)^m \left[\frac{2l+1}{4\pi}\frac{(l-m)!}{(l+m)!}\right]^{\frac{1}{2}} P_l^m(cos\theta) \tag{3.19}$$

A method needs to be found which relates the observed data, travel time residuals, to the model coefficients above.

The travel time from a source at $\mathbf{x}_s$ to a receiver at $\mathbf{x}_r$ through the earth with velocity heterogeneity δv with respect to the spherically symmetric reference model PREM is

$$T = \int_{\mathbf{x}_s}^{\mathbf{x}_r} \frac{1}{v(r) + \delta v(\mathbf{x})}\, d\mathbf{x} \tag{3.20}$$

Hence the travel time residual is

$$\delta t = -\int_{\mathbf{x}_s}^{\mathbf{x}_r} \frac{\delta v(\mathbf{x})}{v(r)^2 + v(r)\delta v(\mathbf{x})}\, d\mathbf{x} \tag{3.21}$$

If the perturbation is small 3.21 becomes

$$\delta t = -\int_{\mathbf{x}_s}^{\mathbf{x}_r} \frac{\delta v(\mathbf{x})}{v(r)^2}\, d\mathbf{x} \tag{3.22}$$

Incorporating the expansion 3.17 this becomes

$$\delta t = -\sum_{k=0}^{K}\sum_{l=0}^{L}\sum_{m=-l}^{l} {}_k c_l^m \int_{\mathbf{x}_s}^{\mathbf{x}_r} \frac{1}{v(r)} f_k(r) Y_l^m(\theta,\phi)\, d\mathbf{x} \tag{3.23}$$

This equation can be simplified if we rotate the coordinate system so that $\mathbf{x} = \mathbf{x}(\xi)$ and $r = r(\xi)$. In this new system the ray lies in the equatorial plane with the source at $\mathbf{x}_s = (\vartheta, \xi) = (\frac{\pi}{2}, 0)$ and the receiver at $\mathbf{x}_r = (\frac{\pi}{2}, \Delta)$, where Δ is the epicentral angle. The travel time residual can now be written

$$\delta t = -\sum_{klm} {}_k c_l^m \int_0^{\Delta} \frac{1}{v(\xi)} f_k(\xi) Y_l^m(\theta,\phi)\, \frac{d\mathbf{x}}{d\xi}\, d\xi \tag{3.24}$$

The quantity $\frac{d\mathbf{x}}{d\xi}$ can be derived using figure 3.6. From this

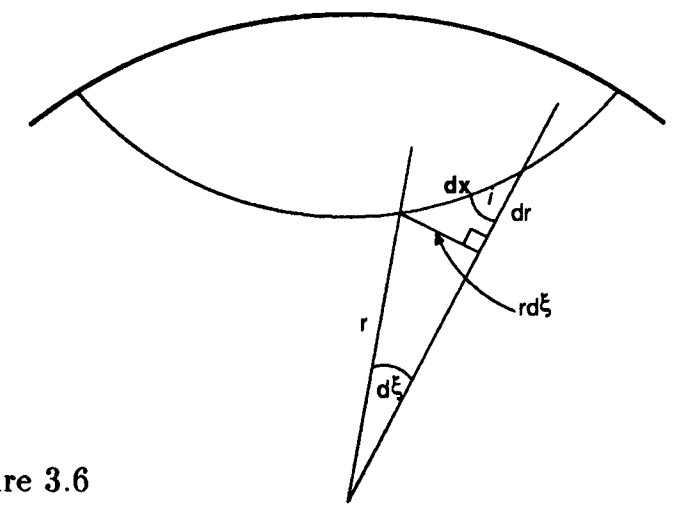


Figure 3.6

$$\sin i = \frac{r\, d\xi}{d\mathbf{x}} \Rightarrow \frac{d\xi}{d\mathbf{x}} = \frac{pv}{r^2} \tag{3.25}$$

where p is the ray parameter. Hence, with the substitution $G(\xi) = -\frac{r(\xi)^2}{pv(\xi)^2}$ equation 3.24 becomes

$$\delta t = \sum_{klm} {}_k c_l^m \int_0^{\Delta} G(\xi) f_k(\xi) Y_l^m(\theta,\phi)\, d\xi \tag{3.26}$$

The spherical harmonics $Y_l^m(\theta,\phi)$ can also be transformed into the new coordinate system using the Euler angles Φ, Θ, and Ψ illustrated in figure 3.2.

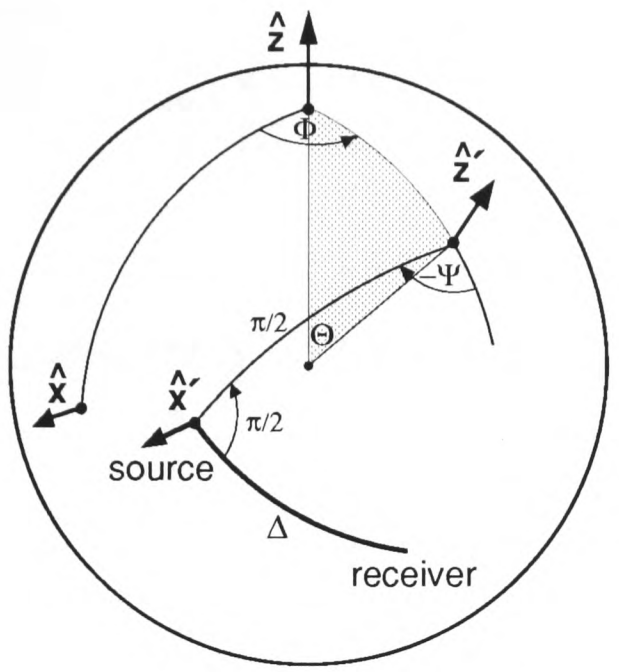


Figure 3.2: The three Euler angles Φ, Θ and Ψ. These are needed to transform the coordinate system so that the source lies at $(\vartheta, \xi) = (0, 0)$ and the receiver $(0, \Delta)$, with the ray traveling through the equatorial plane.

$$Y_l^m(\theta, \phi) = e^{im\Phi} \sum_{n=-l}^{l} e^{in\Psi} Q_l^{mn}(\Theta) Y_l^n(\vartheta, \xi) \tag{3.27}$$

Here $Q_l^{mn}(\Theta)$ is a rotation matrix (see Backus, 1964). In this new coordinate system the spherical harmonics are.

$$Y_l^n(\vartheta, \xi) = X_l^n(\frac{\pi}{2}) e^{in\xi} \tag{3.28}$$

Equation 3.24 for one specific model coefficient ${}_k c_l^m$ now becomes

$$\begin{aligned} {}_k(\delta t)_l^m &= {}_k c_l^m \int_0^{\Delta} G(\xi) f_k(\xi) e^{im\Phi} \sum_{n=-l}^{l} e^{in\Psi} Q_l^{mn}(\Theta) X_l^n(\frac{\pi}{2})\, e^{in\xi}\, d\xi & (3.29) \\ &= {}_k c_l^m e^{im\Phi} \sum_{n=-l}^{l} e^{in\Psi} Q_l^{mn}(\Theta) X_l^n(\frac{\pi}{2}) {}_k I^n(\Delta) & (3.30) \end{aligned}$$

where

$${}_k I^n(\Delta) = \int_0^{\Delta} G(\xi) f_k(\xi) e^{in\xi}\, d\xi \tag{3.31}$$

are *perturbation integrals*, dependent only on the epicentral distance between the source and receiver. From ray tracing through PREM, both $v(\xi)$ and $r(\xi)$ can be found and so the functions ${}_k I^n(\Delta)$ can be numerically integrated. Finally, the equation relating the observed travel time residual to the model coefficients is

$$\delta t = \sum_{k=0}^{K} \sum_{l=0}^{L} \sum_{m=-l}^{l} {}_k c_l^m \, {}_k \alpha_l^m \tag{3.32}$$

where

$${}_k \alpha_l^m = e^{im\Phi} \sum_{n=-l}^{l} e^{in\Psi} Q_l^{mn}(\Theta) X_l^n(\frac{\pi}{2}) {}_k I^n(\Delta) \tag{3.33}$$

which in matrix notation is

$$\delta \mathbf{t} = \mathbf{A}\mathbf{x} \tag{3.34}$$

where $\delta \mathbf{t}$ is the vector of travel time residuals, $\mathbf{x}$ is the model, and $\mathbf{A}$ is the matrix of ${}_k \alpha_l^m$ introduced in section 3.1. Hence the problem consists of solving the linear set of equations 3.32 which from section 3.1 is done by least squares where the ${}_k \alpha_l^m$ calculated for each travel time residual are used to build up the inner product matrix.

3.6.1 Lower mantle representation

PREM velocities vary smoothly throughout the lower mantle and it is expected that the deviations from average will also be smooth, so we have chosen to use normalized Legendre polynomials to represent the variation of velocity perturbation with depth. Again, in accordance with Dziewonski, 1984, we define $u(r)$ so that it spans the interval $[-1, 1]$ throughout the lower mantle:

$$u(r) = [2r - (r_{670} + r_{CMB})]/(r_{670} - r_{CMB}) \tag{3.35}$$

where r_{670} and r_{CMB} are the radii of the 670km discontinuity and core-mantle boundary respectively. Hence, using the same notation as equation 3.19 we have

$$f_k(u) = \left[\frac{2l+1}{2}\right]^{\frac{1}{2}} P_l^0(u) \tag{3.36}$$

3.7 Discussion

Examples of perturbation integrals for the lower mantle are shown in figures 3.3 and 3.4 for both the real and imaginary parts of k=0 and 2. All the curves $n = 0 \rightarrow 6$ are smoothly varying functions of delta and so their values can be tabulated and then interpolated. Examples of their depth variation are illustrated in figure 3.5. Again the differences between adjacent curves vary smoothly so interpolation is also possible in this dimension. Once these functions have been generated and tabulated there are no more numerical integrations to be done, and this results in greatly reduced computing time.

3.7.1 Physical meaning of the perturbation integrals

Equation 3.30 shows the connection between the perturbation in travel time δt, the model coefficients c, and the perturbation integrals I. We can cut out the complicating geometrical factors if we only look at the spherical terms $l = m = 0$, and further simplify by using only the first depth polynomial $k = 0$. This equation then becomes

$$ {}_0\delta t_0^0 = {}_0c_0^0\, {}_0I^0(\Delta)\, X_0^0(\tfrac{\pi}{2}) \tag{3.37} $$

$$ \Rightarrow \sqrt{4\pi}\, {}_0\delta t_0^0 = {}_0c_0^0\, {}_0I^0(\Delta) \tag{3.38} $$

Hence if the model coefficient is $\sqrt{4\pi}$ the perturbation integral ${}_0I^0(\Delta)$ is the change in travel time caused by this model. It is important to examine the size of the velocity perturbation that this size of coefficient represents. Substituting the coordinate transformation for the spherical harmonics and putting $k = l = m = 0$ into equation 3.17 we have

$$ {}_0\left(\frac{\delta v}{v}\right)_0^0 = {}_0c_0^0\, f_0(r)\, X_0^0(\tfrac{\pi}{2}) \tag{3.39} $$

Hence a model coefficient ${}_0c_0^0 = \sqrt{4\pi}$ gives a model perturbation of $\frac{\delta v}{v} = \sqrt{4\pi} \cdot \sqrt{\frac{1}{2}} \cdot \frac{1}{\sqrt{4\pi}} = \frac{1}{\sqrt{2}}$. This is far too large for Fermat's theorem to hold, *ie.* a ray traveling through the lower mantle which is perturbed by $\frac{1}{\sqrt{2}}$ its velocity will follow a dissimilar path than one which is unperturbed. Combining 3.38 and 3.39 and eliminating ${}_0c_0^0$ and $X_0^0(\frac{\pi}{2})$ we have

$$ {}_0I^0(\Delta) = {}_0\delta t_0^0\, f_0(r)\, {}_0\left(\frac{v}{\delta v}\right)_0^0 \tag{3.40} $$

Hence if $\frac{\delta v}{v}$ is small enough so that Fermat's theorem holds, then the perturbation integral is $\frac{1}{\sqrt{2}}\frac{v}{\delta v}$ times the difference in travel time between the unperturbed and the perturbed ray.

Equivalently for a perturbation of $\frac{\delta v}{v} = 1$ while forcing the ray path to be unperturbed, ${}_0I^0(\Delta)$ is exactly the same as the travel time of the ray through the lower mantle itself.

3.8 Transformation of model coefficients

The right hand side of equation 3.17 is a product of complex model coefficients and complex spherical harmonics, so the result is a complex velocity perturbation $\frac{\delta v}{v}$. It is more convenient to work with real perturbations and coefficients, and the transformation required is shown in appendix A. From this, equation 3.17 can be rewritten:

$$ \frac{\delta v}{v}(r,\theta,\phi) = \sum_{k=0}^{K}\sum_{l=0}^{L}\sum_{m=0}^{l}\{{}_ka_l^m\, \Re[Y_l^m(\theta,\phi)] + {}_kb_l^m\, \Im[Y_l^m(\theta,\phi)]\}\, f_k(r) \tag{3.41} $$

where a and b are real model coefficients premultiplying the real and imaginary parts of the spherical harmonics respectively. It should be noted that the index m now starts at 0 and not $-l$.

3.9 Conclusion

This chapter details the theory which links an observed travel time residual to the coefficients of a model of lower mantle heterogeneity expanded in terms of spherical harmonics for its lateral variations, and Legendre polynomials in depth. Several assumptions have had to be made.

- The observational errors ϵ are not subject to systematic errors.
  Section 2.2 shows that this is almost definitely not the case. This problem cannot be avoided. Travel time picks could be done by hand, possibly by waveform cross correlation methods (*e.g.* Woodward & Masters, 1991b), but this would drastically reduce the number of observed S arrivals, possibly to the extent that the study itself might not be feasible.

- The residuals are distributed according to Gaussian statistics.
  Outliers can have a significant effect on an inversion carried out by a least squares procedure (Nolet, 1987). Steps have been taken to avoid contamination of the S dataset by other phases, and figure 2.9 shows that the residuals are evenly distributed about the mean. Hence this assumption would seem to be valid.

- The inversion can be carried out iteratively instead of simultaneously.

- The velocity perturbations are small enough for Fermat's principle to hold.
  The validity of this assumption will only be established when the models are computed.

- The truncation of the Taylor expansion in equation 3.7 does not introduce significant error.
  This assumption is not important because the inversion will be carried out in an iterative procedure in which perturbations become smaller at each stage.

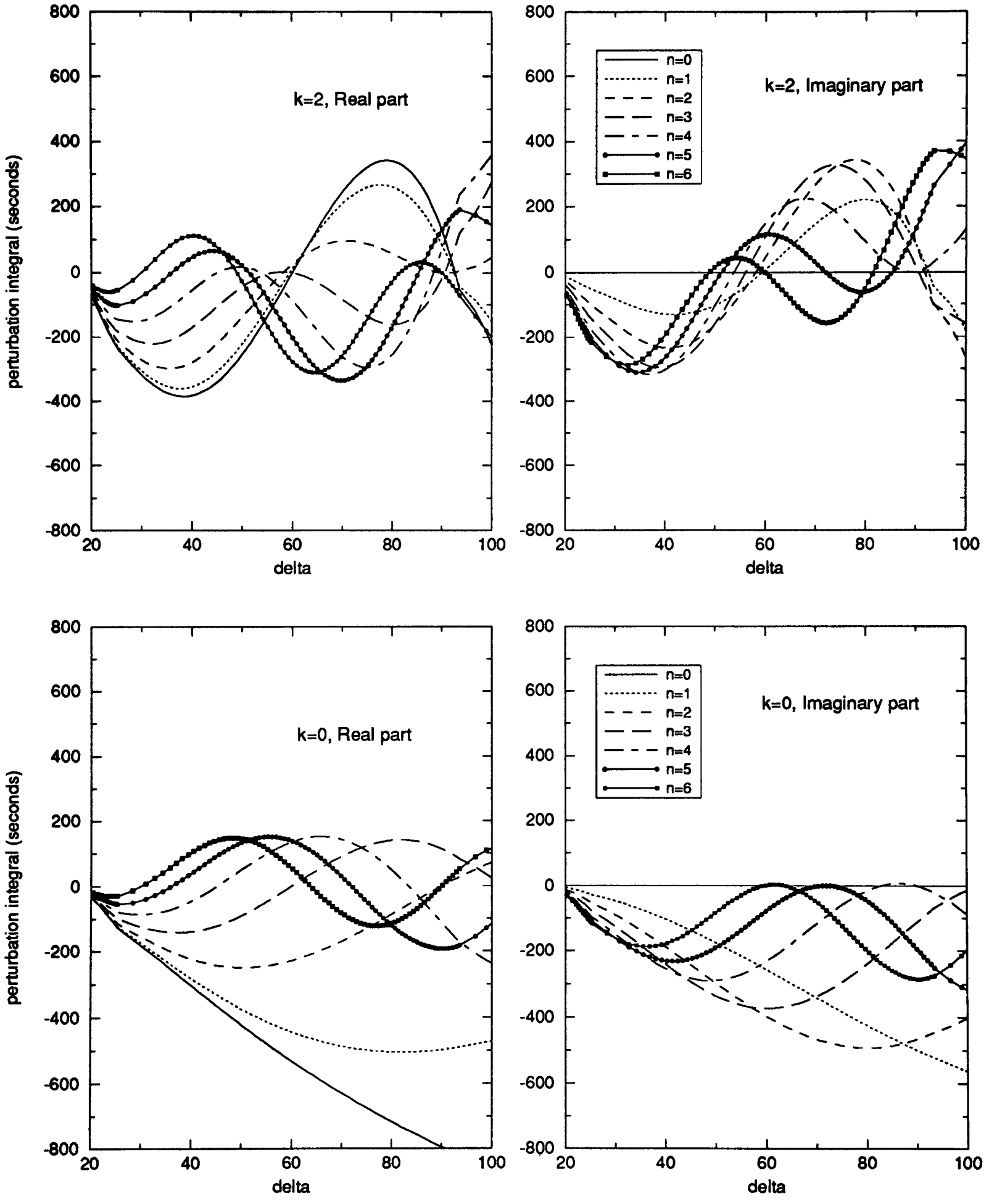


Figure 3.3: Examples of the S perturbation integrals. Both the real (left) and imaginary (right) parts are shown for n=0,6 for k=0 (bottom) and 2 (top).

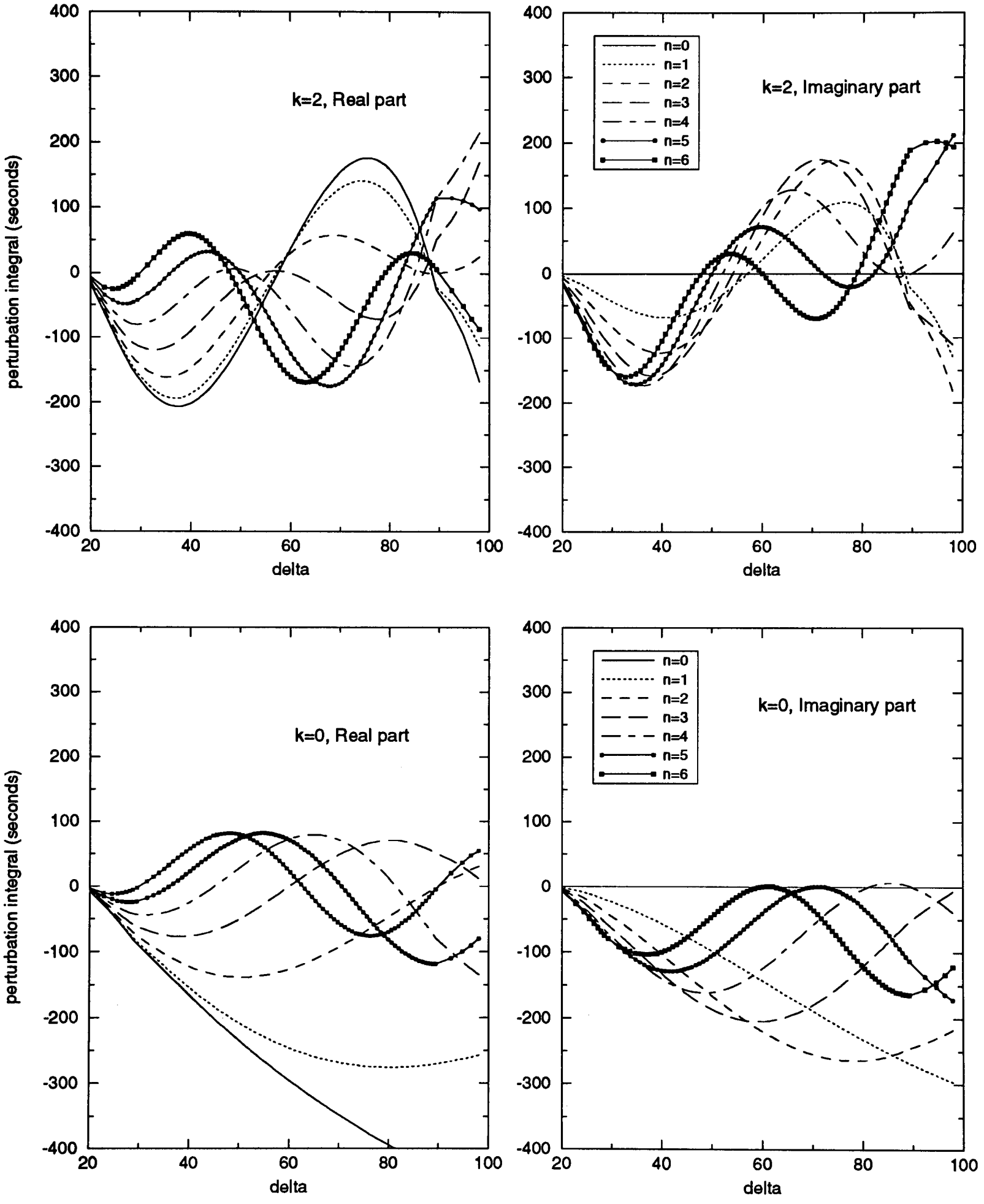


Figure 3.4: Examples of the P perturbation integrals. Both the real (left) and imaginary (right) parts are shown for n=0,6 for k=0 (bottom) and 2 (top).

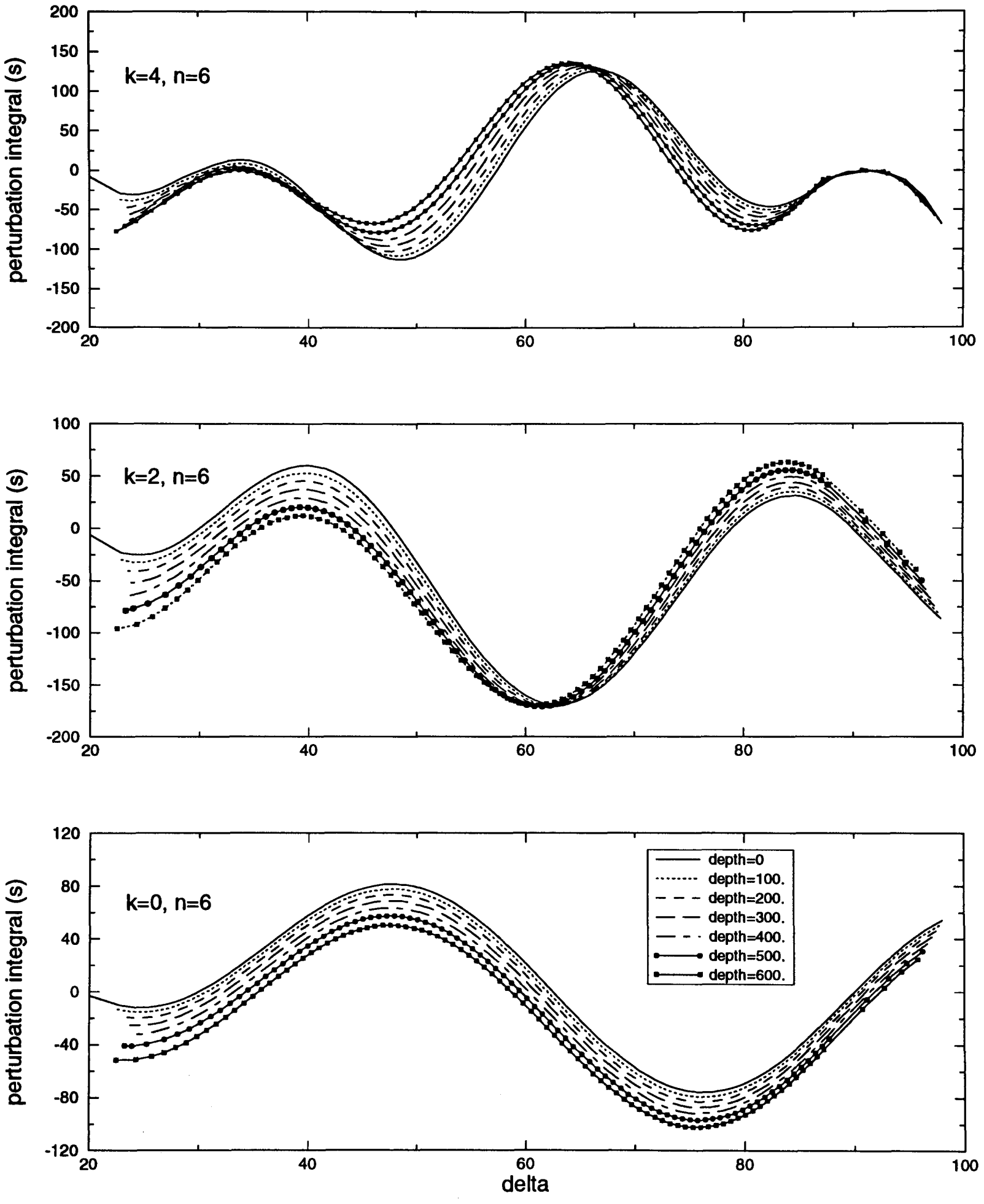


Figure 3.5: Examples of the variation in P perturbation integral with depth. All pictures show curves for event depths 0km to 600km at 100km intervals for n=6 at k=0 (bottom), k=2(middle), and k=4(top).

Chapter 4

Relocation

4.1 Why relocate?

The event locations that are published by the ISC are computed using the travel time tables of Jeffreys & Bullen, 1940 (JB). When these were constructed, it was extremely difficult to calculate the baseline value of the tables at teleseismic distances. This is a consequence of the trade-off problem between the depth and origin time of an event. It occurs because the ray paths of the seismic waves leaving an event are in a predominantly vertically downward direction, and so vertical resolution is low. This is certainly true for shallow events even if they are recorded locally. Deep earthquakes will have some rays traveling to the surface at steep angles, but these events are relatively few in number and are not globally distributed. To the inversion scheme, from which the locations are calculated, a change in depth is almost exactly equivalent to a change in the origin time of the event. For example, for a shallow event which is recorded teleseismically, an increase in the depth of the event by $\approx$4km is almost irresolvable from a change in the origin time by $\approx$0.5s.

It was not until the advent of nuclear testing in the 1950s that the problem with the baseline value could be resolved. For an explosion, all the hypocentre parameters – latitude, longitude, origin time, and depth – are known, and so the travel times of seismic waves at a given delta can be exactly found.

The fact that JB travel time tables are still used today is a testimony to their achievement. Dziewonski & Anderson, 1981, used ISC locations based on these tables to derive PREM, the spherically symmetric model that is used in this study. In addition to 2s of baseline difference, this model gives a travel time curve with a slightly different gradient to the JB tables. As will be seen later in this thesis, however, the mean of all residuals at a given delta increases with delta, *ie.* there is still some spherically symmetric signal left in the data after relocation with respect to PREM. This is attributed to the use of the JB tables in the original locations.

Because of the improvements in global average travel time tables, relocation of the events in the ISC

catalogue is now almost routine.

4.2 Overview

The location of an earthquake is established by determining which four location coordinates – latitude, longitude, origin time, and depth – satisfy the data from the earthquake best. The data here is not the travel time but the difference between the travel time (based on a provisional location) and a predicted travel time given by a reference model or travel time curve. As a result the choice of reference model or curve is very important. Essentially therefore it is a problem of minimizing the travel time residuals. In order to obtain a residual, however, it is necessary to have an initial location which may or may not be accurate, but the speed of convergence to the best fit solution is determined by how accurate this provisional location is. A better constrained set of location coordinates will be obtained by using as much data as possible, especially from a varied selection of phases. One proviso to this, however, is that the data must be coherent and not subject to any contamination or bias.

To date most global body wave tomographic studies have modeled P wave velocity anomalies (Dziewonski, 1984; Morelli & Dziewonski, 1991; Inoue *et al.*, 1990). As a result it is mainly compressional phases that have been used in the relocation process. P waves represent the largest phase dataset available, as they are usually the first arrival and therefore the most easily picked on a seismogram. In addition they are recorded as a short pulse whose error in reading can be quite small. The ISC uses only P and surface reflected pP to give its event locations.

4.3 Choice of seismic phases to be used in the relocations

In this study it is absolutely essential that shear waves are used in the relocation process so that the final locations are not biased towards fitting the compressional phases alone. S waves are far less regularly recorded on a seismogram because they can be contaminated by other phases arriving at the same time (see section 2.2). In addition they have a larger wavelength and a polarity, both of which make S less distinguishable. As a result the variances in the S dataset are larger by almost an order of magnitude. With the inclusion of S in the relocation it is expected that this ratio will decrease. The ultimate justification in using the S phase will be in obtaining smaller hypocentre confidence ellipsoids.

In addition, other than the directly recorded phases P and S, the relocation program used in this study has been set up to use pP, PP, and PcP. These are all reflected phases so it is expected that their variances will be quite large. Given a specific number of arrivals, the best event locations are determined for events whose arrivals are well distributed in terms of azimuth and epicentral distance. pP is a particularly effective phase to use in earthquake relocation because it travels away from the source in an upward direction, an angle not well covered by the other phases. This gives a large change

in travel time for a given change in depth which effectively means that the depth can be constrained much better – so much so in fact that the ISC uses this phase alone to determine the depth of events whose depth error is too large. An element of caution has to be used when pP arrivals are included because there is a great deal of error involved in picking a pP time from a shallow event on a seismogram. For this reason this phase is only used for events with provisional depths greater that 100km.

In a similar manner, PcP has been included because its takeoff angles from an event continue from where the direct P arrivals stop. PcP will inevitably be subject to errors generated due to aspherical topography or high velocity heterogeneity at the bounce point at the core mantle boundary.

The preceding text could apply to the relocation of any dataset for any study. However, as was first mentioned in section 3.2, it is not the most accurate solutions that are of interest in this study. Instead it is necessary that the locations absorb the effects of small scale heterogeneity near to the source so that it does not affect the modeling of large scale structure. Gudmundsson *et al.*, 1990 analyzed the statistics of the ISC dataset to investigate both the size and the scale lengths of mantle heterogeneity and illustrated that there is considerable small scale power in the upper mantle, especially at depths less than 200km.

4.4 Relocation theory

Ignoring the perturbations to the earth model, the travel time to first order from a source at $\mathbf{f}^s$ to a receiver can be written using the same notation as section 3.1 as

$$d_i = T_{Oi} + \mathcal{A}_i(\delta \mathbf{f}^s) + e_i \tag{4.1}$$

where T_{Oi} is the travel time for an event at $\mathbf{f}^s$ through the reference earth model and $\mathcal{A}_i$ is a vector of differentials of the travel time with respect to the hypocentral parameters

$$\mathcal{A}_i(\delta \mathbf{f}^s) = \frac{\partial T_{Oi}}{\partial \theta}\delta\theta + \frac{\partial T_{Oi}}{\partial \phi}\delta\phi + \frac{\partial T_{Oi}}{\partial h}\delta h + \frac{\partial T_{Oi}}{\partial \oplus}\delta\oplus \tag{4.2}$$

where $\theta, \phi, h,$ and $\oplus$ are the latitude, longitude, depth and origin time respectively. The partial differentials can be readily calculated and are

$$\frac{\partial T_{Oi}}{\partial \theta} = p\cos\zeta \tag{4.3}$$

$$\frac{\partial T_{Oi}}{\partial \phi} = -p\sin\zeta\sin\theta \tag{4.4}$$

$$\frac{\partial T_{Oi}}{\partial h} = -\frac{\sqrt{\eta^2 - p^2}}{r} \qquad \text{where } \eta = \frac{r}{v(r)} \tag{4.5}$$

$$\frac{\partial T_{Oi}}{\partial \oplus} = 1. \tag{4.6}$$

(4.7)

Here p is the ray parameter and ζ is the azimuth of the receiver from the source. The best fit location will be the one which minimizes the error e_i, *ie* the one which minimizes

$$L \equiv \sum_i \sigma_i^{-2} ||d_i - T_{Oi} - \mathcal{A}_i(\delta \mathbf{f}^s)||^2 \ = \sigma_i^{-2} ||\delta d_i - \mathcal{A}_i(\delta \mathbf{f}^s)||^2 \tag{4.8}$$

Following section 3.1 this leads to the least squares solution for $\delta \mathbf{f}^s$

$$\delta \mathbf{f}^s = [\mathcal{A}^{\mathbf{T}} \mathbf{W}^{\mathbf{T}} \mathbf{W} \mathcal{A}]^{-1} \mathcal{A}^{\mathbf{T}} \mathbf{W}^{\mathbf{T}} \delta \mathbf{d} \tag{4.9}$$

where $\mathbf{W}$ is a matrix of weights for each source/receiver path based on the variance of the phase.

4.5 Algorithm testing

The algorithm used to relocate the ISC events is a highly modified version of SE89 (Dewey, 1971) adapted for use with teleseismic datasets. In order to obtain a stable solution only events with at least 25 observations distributed with a minimum of 5 arrivals in at least 3 azimuthal quadrants are relocated. To circumvent the problem of bias by strong small scale heterogeneity near the source (see section 4.3), only arrivals from the teleseismic window (25° to 100°) are used.

To test the validity of using the phases described in section 4.3 a dataset consisting of one event per 5° cell, selected using the criterion described in section 5.1, has been relocated. The outcome is shown in tables 4.1 and 4.2.

phases included in relocation	*phase*	*number*	*average after relocation*	*variance after relocation*
P	P	115519	-0.003	1.443
P,PP	P	115523	-0.022	1.445
	PP	9108	1.918	13.004
P,S	P	115449	-0.001	1.474
	S	22169	-0.230	15.561
P,PP,S	P	115469	-0.021	1.477
	PP	9045	1.924	12.895
	S	22173	-0.224	15.549
P,S,PcP	P	115449	-0.006	1.474
	S	22168	-0.240	15.564
	PcP	3402	0.825	10.237
P,PP,S,PcP	P	115468	-0.024	1.476
	PP	9044	1.923	12.904
	S	22172	-0.233	15.544
	PcP	3403	0.805	10.239

Table 4.1: Phase statistics for the test dataset relocation

The mean P residual is always the smallest as a result of their higher weighting caused by their smaller variance and because they are far more numerous than S.

Table 4.2 shows the analysis of the hypocentre locations and their 90% confidence ellipsoids. All the events in this dataset have ISC depths less than 50km, so pP phases have not been used.

The ellipsoid axis length quoted is the average of all three axes. In the case where an event is best located above the earth's surface, it is constrained to the surface and its depth error is necessarily zero. This is why the average ellipse axis length for all events is smaller than that for the subsurface events alone. Clearly this relocation above the surface is unphysical and represents an event which is poorly constrained in depth. This phenomenon is most apparent in the datasets containing compressional phases alone. The addition of S not only greatly increases the number of subsurface events but it also reduces the average ellipsoid axis length by approximately 70%. Inclusion of PP and PcP offer only minor improvements to both P alone and P with S relocations.

phases included in relocation	*number of events*	*average ellipse axis length (km)*	*number of subsurface events*	*average ellipse axis length (km)*	*average depth*
P	589	7.3 ± 3.7	178	31.3 ± 14.5	10.53
P,PP	589	7.2 ± 3.6	177	30.9 ± 14.4	10.71
P,S	589	6.8 ± 3.2	395	11.2 ± 7.4	14.66
P,PP,S	590	6.8 ± 3.2	397	11.1 ± 7.3	14.90
P,S,PcP	589	6.8 ± 3.2	395	11.1 ± 7.3	14.54
P,PP,S,PcP	590	6.8 ± 3.2	399	11.1 ± 7.3	14.78

Table 4.2: Event statistics for the test dataset relocation

This test dataset is a good representation of the type of events which will be relocated in the derivation of the models but it does not illustrate what sort of changes are occurring to the hypocentre coordinates. In order to do this another dataset of the Tonga subduction zone has been used. Events in this region are large and numerous and restricted to the descending slab. Their locations should therefore be tightly constrained.

As has been noted earlier, subduction related events can be biased in specific azimuthal directions because rays can be channelled along the slab structure in which seismic velocities are very different to those in the surrounding mantle. It is hoped, however, that all the events will be subject to the same systematic error so that their relative locations are accurate. Their absolute locations may or may not be quite different. In order to obtain an insight into the overall geometry of the descending slab, the ISC locations have been imaged in three dimensions using AVS of Advanced Visual Systems Inc. With this package it is possible to rotate the data and see the subduction zone from any direction. Figure 4.1 is an example of the sort of image obtained when the dataset is viewed from approximately a north-northwesterly direction.

Using this imaging of the area it is clear that the deep events become shallower towards the south and with the added information from two dimensional maps of the area it was decided to take a cross section

of the slab centred on -23.3° latitude, 182.0° longitude, 350km depth, with an azimuth of 98° and a dip of 80° (measured from the south of the cross sectional plane). The ISC locations for those events that were able to be relocated are plotted in plane view and in cross section in figure 4.2. The cross section width was chosen to be 100km to include only the tightly clustered events at around 550km depth, and it is the intersection of the cross sectional plane with this depth that is plotted as a box on the map. The overall shape of the descending slab is is quite clear, with the predominance of seismicity at the top and bottom of the slab being quite evident. The locations of shallow events on this plot should be treated with caution as the ISC assigns 'NULL' depths of 10km and 33km for those events whose depths are poorly constrained from their locations.

The statistics for the relocations of this dataset using the different phases are shown in tables 4.3 and 4.4. Comparison of the phase analysis tables for both test datasets reveals that the variances of the data from the Tonga region are, as expected, smaller than those of the global dataset.

phases included in relocation	*phase*	*number*	*average after relocation*	*variance after relocation*
P	P	106185	0.000	0.938
P,PP	P	106395	-0.008	0.939
	PP	4543	1.553	12.414
P,pP	P	106487	-0.016	1.072
	pP	6042	0.977	5.765
P,S	P	106615	-0.009	0.972
	S	7714	-1.534	13.179
P,PP,S	P	106894	0.001	0.972
	PP	4553	1.494	12.732
	S	7727	-1.550	13.173
P,S,pP	P	106815	-0.018	1.086
	S	7723	-0.350	14.917
	pP	6055	1.016	5.716
P,S,PcP	P	106684	0.007	0.972
	S	7717	-1.542	13.183
	PcP	2243	0.620	5.808
P,PP,S,pP,PcP	P	107122	-0.028	1.086
	PP	4556	1.355	13.447
	S	7736	-0.374	14.193
	pP	6061	1.033	5.737
	PcP	2262	0.991	5.612

Table 4.3: Phase statistics for Tonga dataset relocation

Figure 4.3 shows the same cross section as figure 4.2 but with the relocated dataset using only the P phase. The ellipse plotted is the intersection of the 90% confidence ellipse in space with the cross sectional plane. Several features are apparent:

- The depth is the worst constrained parameter and is due to the tradeoff with the event origin time.

- The average trend of the largest ellipse axis is also slightly to the west. This is the same direction

phases included in relocation	*number of events*	*average ellipse axis length (km)*	*number of subsurface events*	*average ellipse axis length (km)*
P	1313	12.9 ± 4.7	884	29.1 ± 16.8
P,PP	1318	12.9 ± 4.7	886	29.1 ± 16.7
P,pP	1321	12.2 ± 4.6	899	18.8 ± 17.0
P,S	1325	12.4 ± 4.2	971	23.0 ± 12.0
P,PP,S	1330	12.4 ± 4.2	978	23.0 ± 12.1
P,S,PcP	1326	12.4 ± 4.2	970	22.9 ± 12.7
P,S,pP	1330	11.9 ± 4.2	981	16.5 ± 11.9
P,PP,S,pP,PcP	1337	11.8 ± 4.2	986	16.4 ± 11.6

Table 4.4: Event statistics for Tonga dataset relocation

as the descending slab and can probably be attributed to the large residuals of rays which leave the event and are channelled down the slab itself.

- There are a large number of events that could not be relocated below the surface and have been constrained to the surface

Although obscured slightly by the confidence ellipses, the locations using P alone are far less tightly clustered than the ISC locations in figure 4.2. This is largely attributable to the complete lack of information from local stations with $\Delta < 25°$.

The top plot in figure 4.4 is the same section as before but the locations have been derived using S as well as P. Comparison of the two reveals several differences.

- The confidence ellipsoid major axes are in the same general direction but they are smaller by a factor of about 20%.

- As is indicated by the tighter clustering of events, not just the confidence ellipsoids have shrunk, but the locations themselves are better.

- Far more events have been located below the surface.

Finally, the locations and confidence ellipses derived from relocations using all phases are shown at the bottom of figure 4.4, and without ellipses at the top of figure 4.5. The depth confidence ellipsoids are much smaller, due almost entirely to the use of pP which reduces the average ellipsoid axis length by 35% when it is used with P alone, and by 28% when it is used with both P and S. Comparison of these locations with the ISC locations shows that the use of arrivals from $\Delta < 25°$ outweighs the use of the additional teleseismic phases S, PP, and PcP. The lower section in figure 4.5 illustrates the improvements that can be made when both P and S models of the lower mantle derived in this study are included. The clustering of events at depth has been improved dramatically and is now comparable with the ISC locations.

4.6 Conclusions

PcP and PP introduce only marginal, if any, reductions to the event confidence ellipsoids. However, the additional use of the S phase in event relocations dramatically improves depth resolution in both the test cases of this section.

The use of the S phase is therefore both necessary in order to avoid the compressional bias in the S models, and justifiable because it improves the locations and confidences of the events.

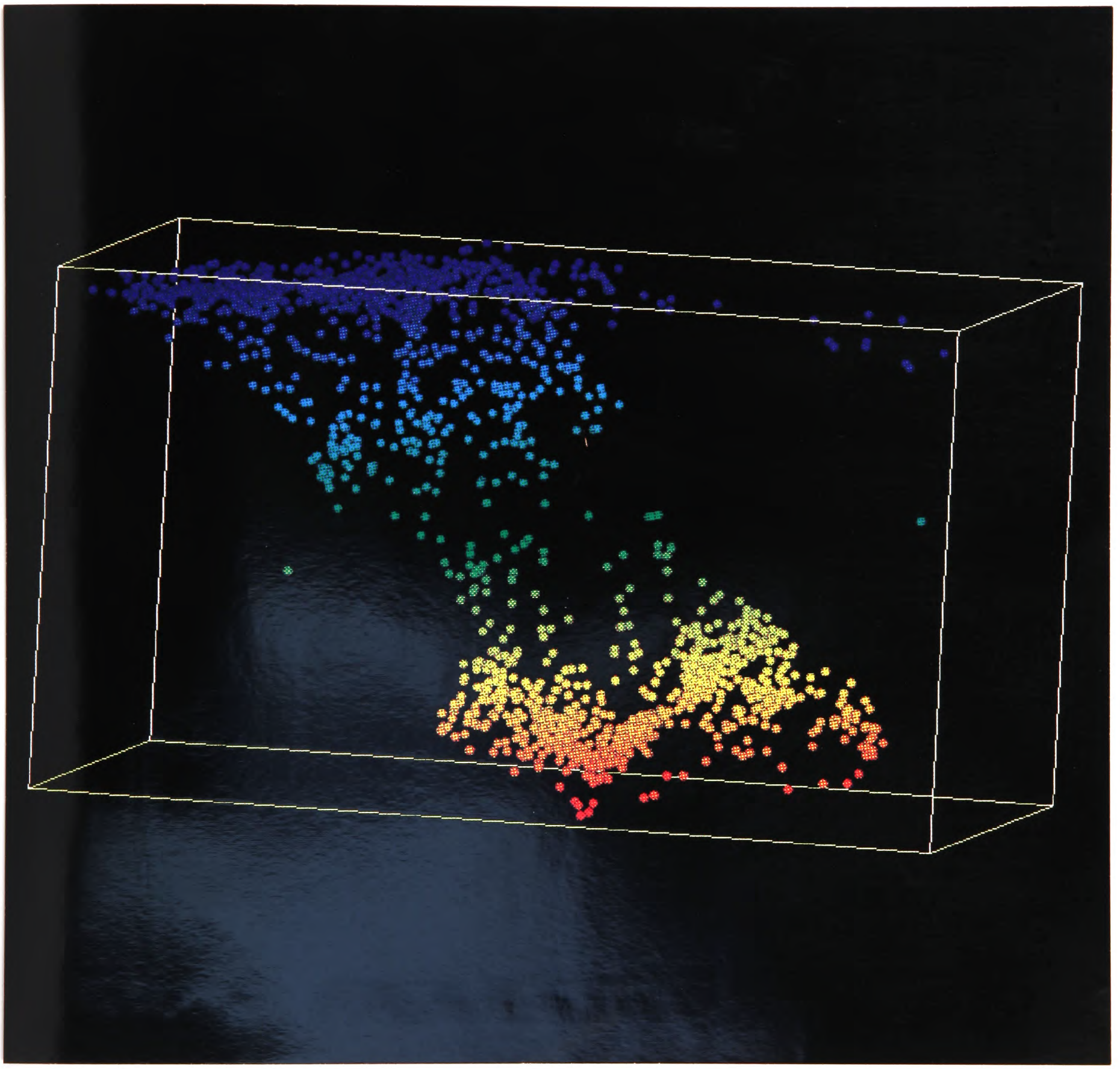


Figure 4.1: AVS image of the events in the Tonga dataset viewed from a north-northwesterly direction. The blue to red dots represent depths ranging from 0 to 700km respectively

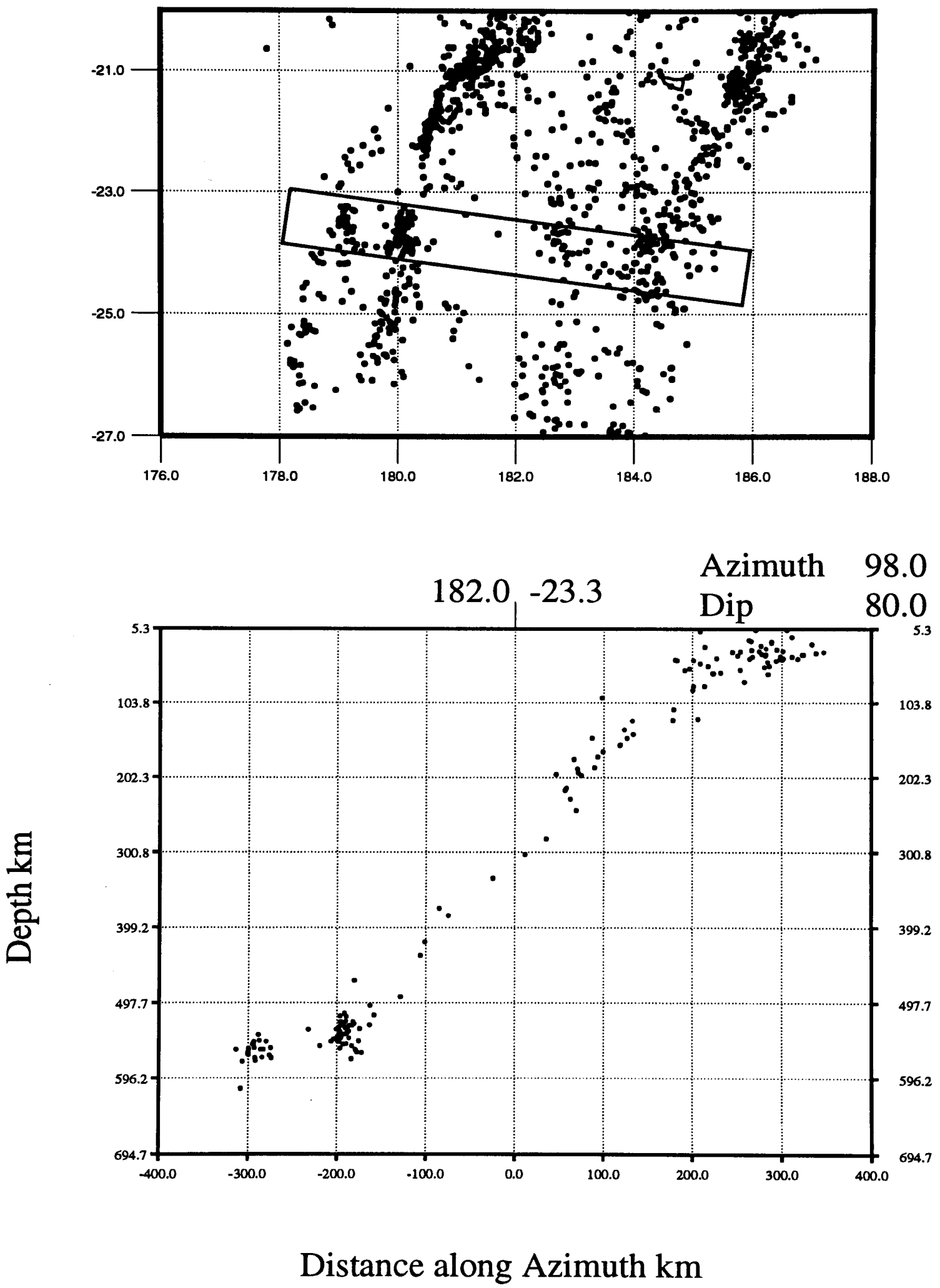
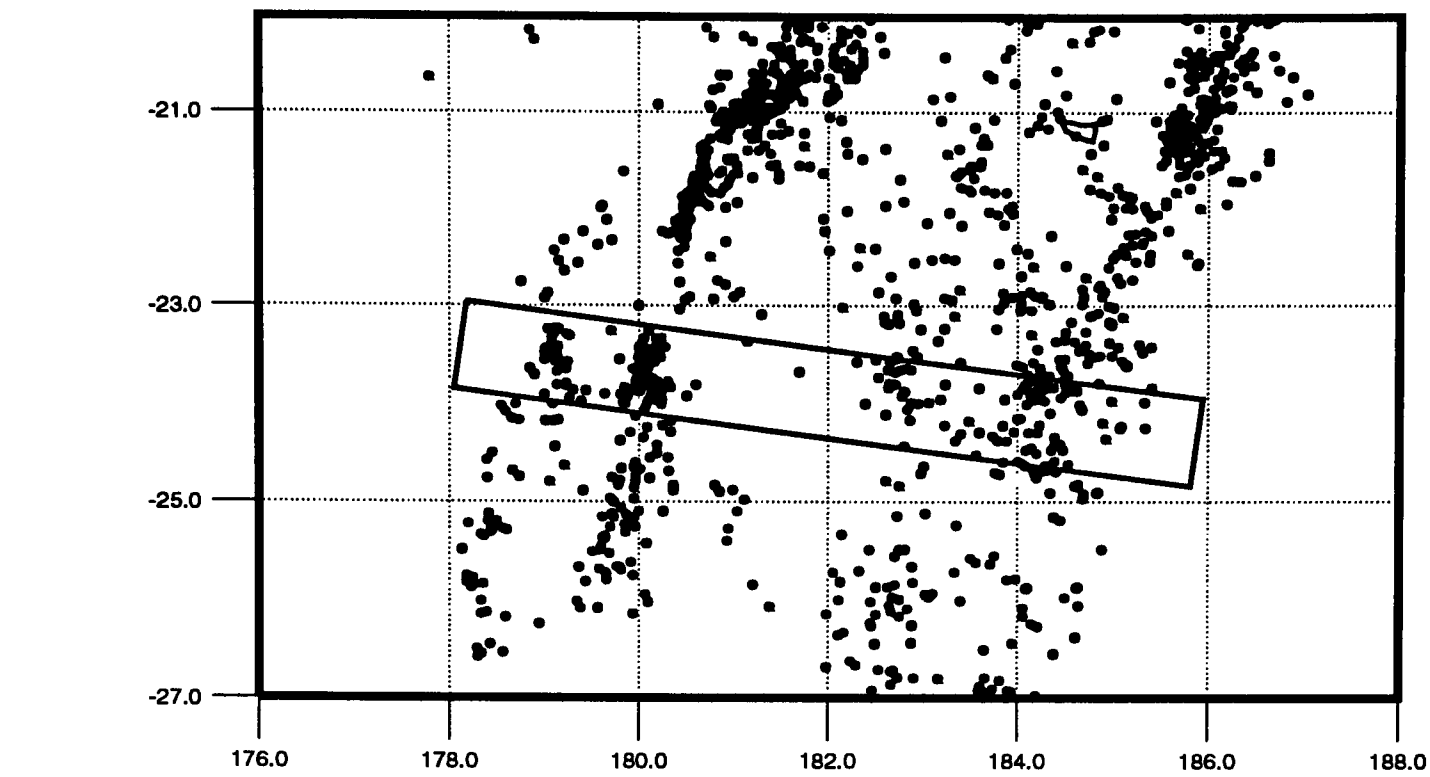


Figure 4.2: Map and cross section of ISC locations in Tonga region. Only those events that could be relocated are plotted. The cross section is centred on -23.3° latitude, 182.0° longitude, 350km depth, with an azimuth of 98°, a dip of 80°, and a width of 100km. The box plotted in the map is a slice through the plane at 550km depth.



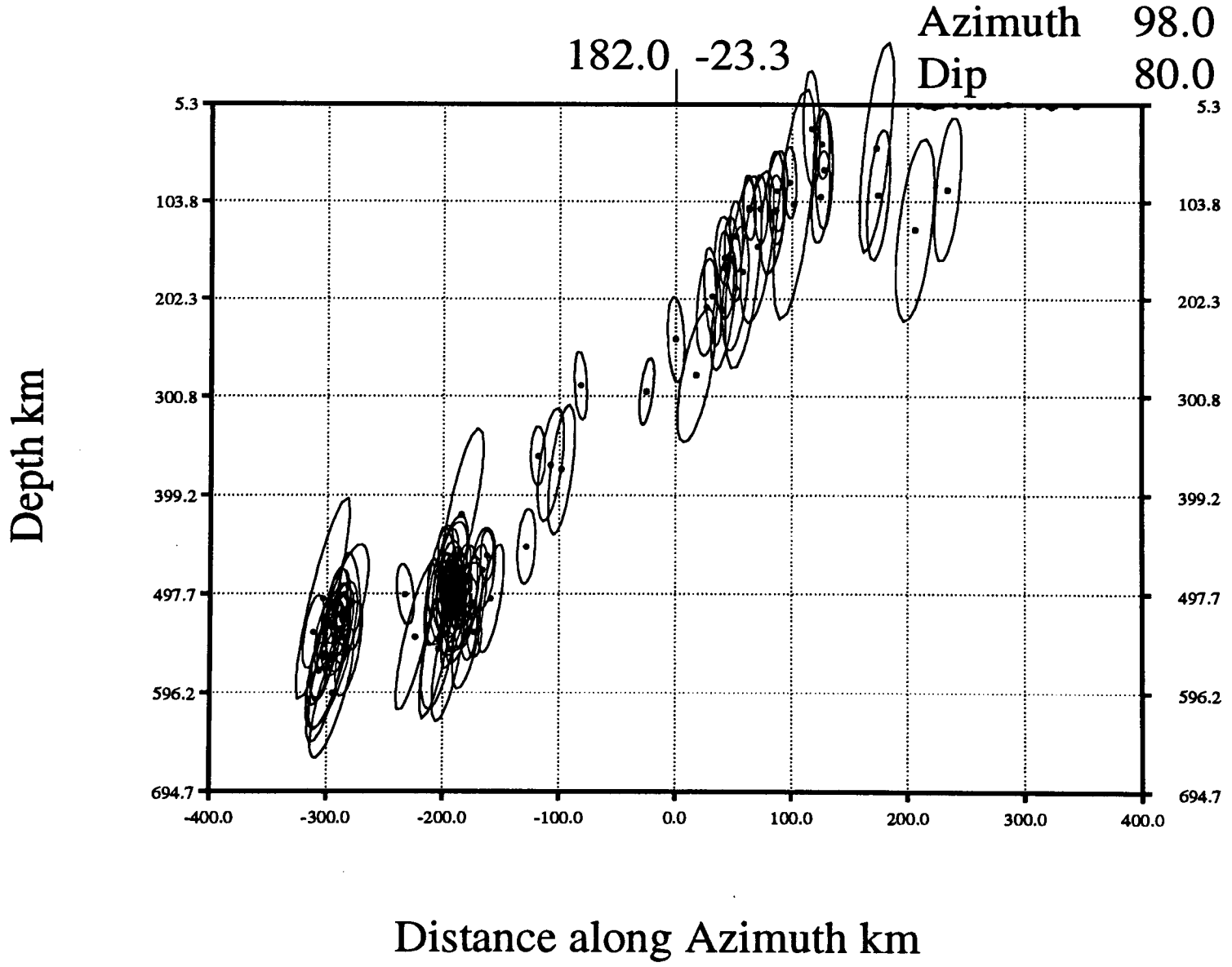


Figure 4.3: Map with ISC locations and cross section relocated with P arrivals only. The ellipse plotted is the intersection of the 90% confidence ellipse in space with the cross sectional plane.

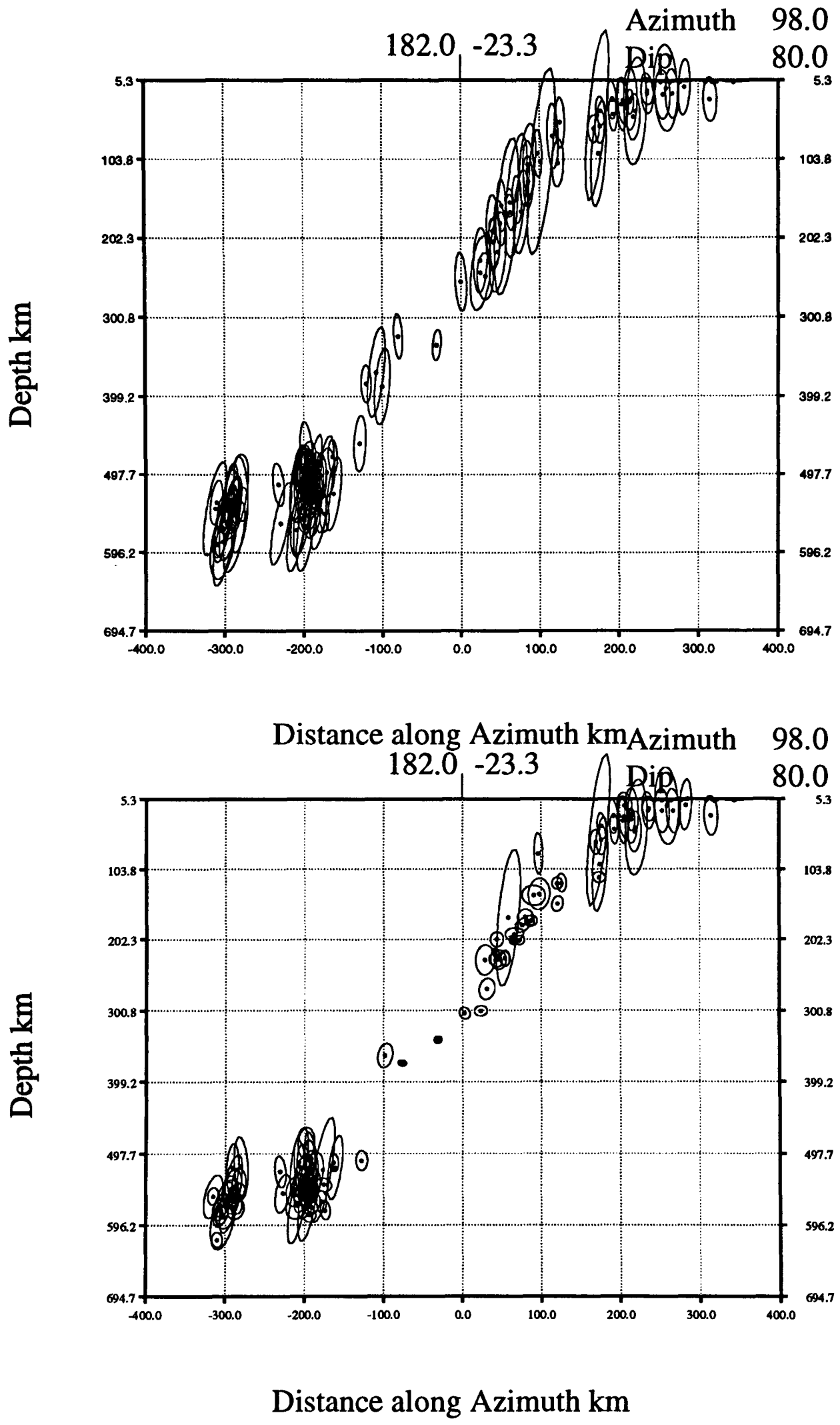
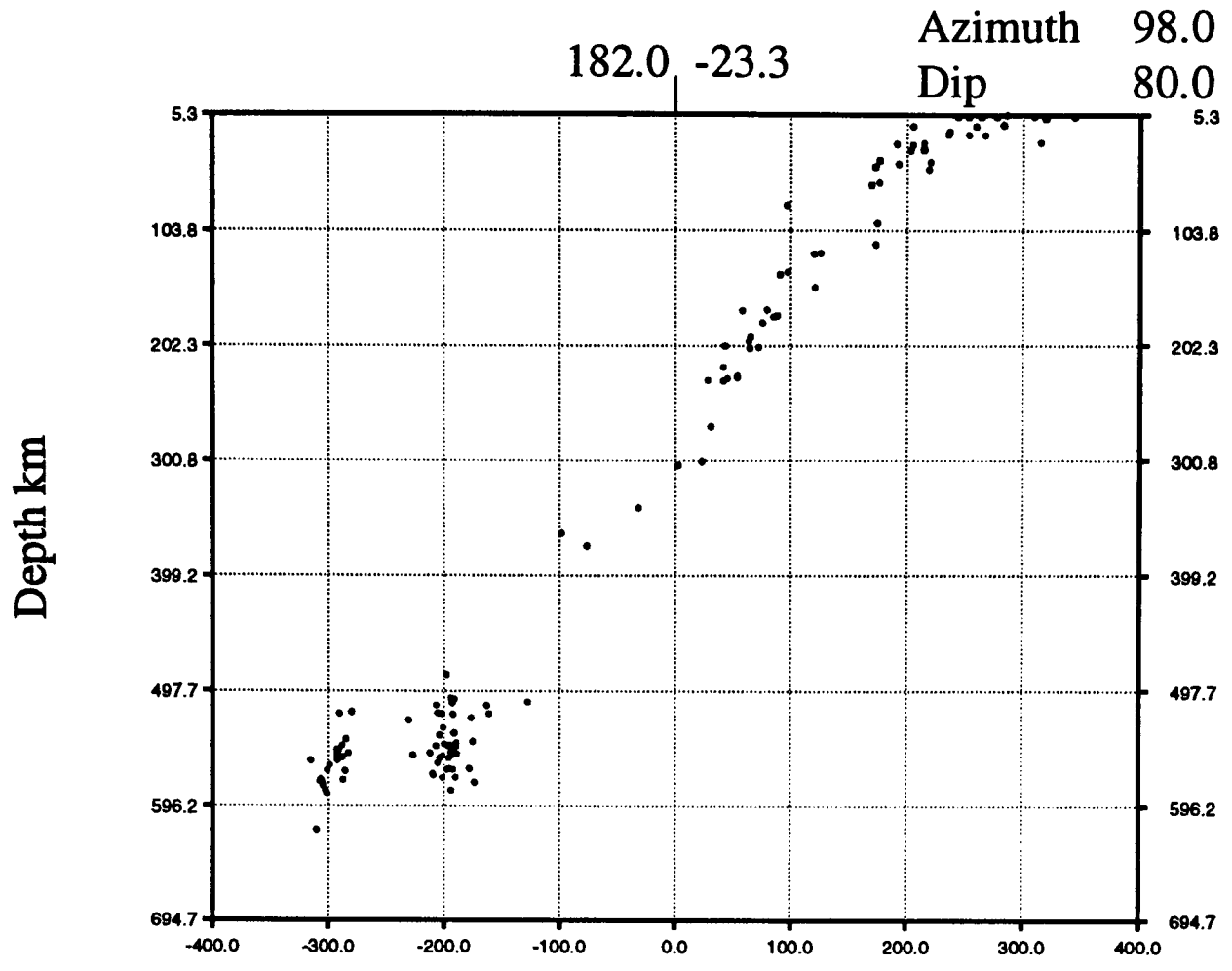


Figure 4.4: Cross sections and confidence ellipses for relocations with P and S, and all phases.



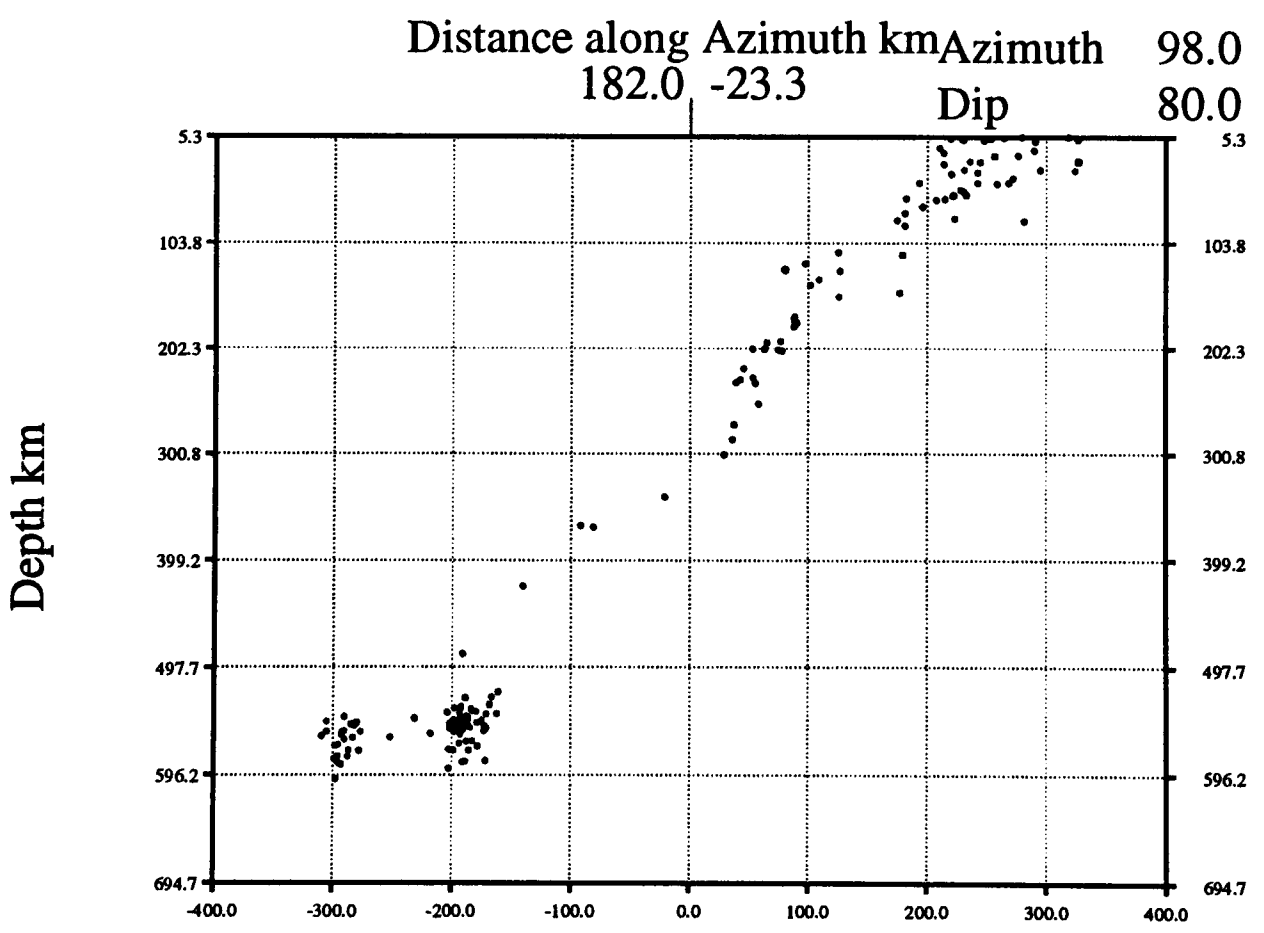


Figure 4.5: Cross sections showing only the hypocentres for events relocated with all phases (top) and including three dimensional models.

Chapter 5

Lower Mantle Models

The iterative approach to the inverse problem was discussed in detail in chapter 3 and it is the purpose of this section to explain the procedure with which the iterative method is implemented.

Ideally an S model should be computed completely independently of the P model so that there can be no compressional bias. This however would involve the relocation of events using S alone, and this is impossible given the substantially reduced amount of S data that is available. For this reason P has to be used, and for consistency a heterogeneous P correction has to be involved in the relocation process. As a check on the method the final P model should be very similar to the identically parameterized L02.56 of Dziewonski, 1984 which was computed using the same selection and iterative procedures.

5.1 Data weighting in the inversions

The importance of data weighting in tomographic work on a global scale cannot be underestimated. The problem has already arisen in the previous chapter where each residual in the relocation is weighted inversely by the variance of that phase type in the entire dataset. Figure 2.1 illustrates the fundamentally uneven distribution of sources and receivers and it is clear that some sort of weighting scheme is essential to avoid the model being biased by areas with the best data coverage. At the relocation stage the worst constrained hypocentres are removed because of the insistence of at least 30 arrivals and no fewer than 5 in 3 azimuthal quadrants. The weighting of the remaining events has been carried out using the method introduced by Dziewonski, 1984. In this technique the surface of the earth is divided up into a grid of equal area cells from which the events are sorted according to the following criteria:

- 1. number of azimuthal quadrants with at least 5 arrivals
- 2. number of cells which have stations recording an arrival
- 3. number of arrivals

From each cell only a certain fixed number of events are selected. In the inversion procedure itself each arrival is given a weight $\frac{1}{j}$ where j is the total number of observations at all stations in one receiver cell from all events in one source cell. This means that each path between a source and a receiver cell is given equal weight.

5.2 Model parameterization

In accordance with L02.56 a maximum of 15 events per 5° cell are chosen to go into the inversion. The maximum degree and order to which the models can be expanded depends ultimately on the distribution of the data throughout the lower mantle. From figure 2.1 it is obvious that the Pacific region is very sparsely covered by sources and receivers. In areas such as this the uppermost part of the lower mantle, where the ray paths are generally almost vertical, is totally devoid of data coverage. As a result the smallest resolvable feature is going to be approximately 30° which corresponds to the half wavelength of a spherical harmonic of degree and order 6. This is the same parameterization that is used by both Dziewonski, 1984 and Morelli & Dziewonski, 1991 simply because the actual distribution of sources and receivers has changed very little. There is nothing that can be done to change the former, so it is not until there is an increase in the number of remote sea floor seismometers that there will be an increase in the resolving power of the dataset.

The extents of the model are chosen to be from the upper/lower mantle boundary at 670km to the core/mantle boundary at 2891km depth. Hence the model actually includes the D″ region as well as the lower mantle. Again this is done in order to be consistent with previous models and hence enable direct comparison with them. For the same reason the maximum degree of the polynomial expansion in depth is chosen to be 4.

5.3 Procedure for the zeroth iteration

At the zeroth iteration there are no known heterogeneous models and so the following steps are carried out in order to determine the station corrections, event locations, and the first models respectively.

- 1. Relocate the entire ISC catalogue of events that satisfy the relocation criterion of section 5.1.
- 2. Calculate the P and S static station corrections by averaging the residuals for each station.
- 3. Relocate the entire dataset again using in addition the station corrections derived from item 2 above.
- 4. Select the 'best' N earthquakes from each cell following the criterion of section 5.1. In order to be consistent with Dziewonski, 1984 the number of earthquakes per cell is chosen to be **15**.

For subsequent iterations the availability of models from the previous iteration means that both relocations can also include changes to the travel times introduced by the heterogeneous velocity structure.

5.4 Model analysis. Question of damping

In sections of the lower mantle that are crossed by few ray paths the model is poorly constrained. In these areas the model often becomes very large as the inversion routine preferentially fits the better constrained parts in order to obtain greater variance reduction. To avoid this 'blowing up' the inversion scheme has to be damped, the degree to which this is carried out being determined by the coverage of the data. The amount of damping required can be estimated from the inverse of the inner product matrix $\mathbf{A^T A}$ in equation 3.12.

Since $\mathbf{A^T A}$ is a real symmetric matrix it has an orthonormal set of eigenvectors with corresponding real distinct eigenvalues. This can be written:

$$\mathbf{A^T A} = \sum_{k=1}^{K} \lambda_k \mathbf{u}_k \mathbf{u}_k^T \tag{5.1}$$

where $\mathbf{u}_{k,k=1,K}$ are normalized eigenvectors and $\lambda_{k,k=1,K}$ are the corresponding eigenvalues. Eigenvectors with large eigenvalues are well determined because the errors associated with an eigenvector scales inversely with the size of its eigenvalue (Press *et al.*, 1986). It is the eigenvectors with small eigenvalues that will ultimately be responsible for the large amplitudes of the model in areas of the lower mantle that are not well covered by ray paths.

There are two ways of dealing with this unreliable information; firstly the eigenvalues can be damped or reduced in size, and secondly the smallest eigenvalues can be set to zero. This second approach was adopted by Wiggins, 1972 and simply involves the introduction of $k^* < K$ as the summation limit in equation 5.1. The inverse of a matrix using a restricted number of eigenvalues and eigenvectors is called the generalized inverse and will be denoted by a $-g$ superscript. For the inner product matrix $\mathbf{A^T A}$ therefore

$$[\mathbf{A^T A}]^{-g} = \sum_{k=1}^{k^*} \frac{1}{\lambda_k} \mathbf{u}_k \mathbf{u}_k^T \tag{5.2}$$

A model $\mathbf{x}_g$ consisting of only k^* eigenvectors can be written:

$$\mathbf{x}_g = [\mathbf{A^T A}]^{-g} \mathbf{A^T d} = [\mathbf{A^T A}]^{-g} [\mathbf{A^T A}] \mathbf{x} = \sum_{k=1}^{k^*} \mathbf{u}_k \langle \mathbf{u}_k^T \mathbf{x} \rangle \tag{5.3}$$

The truncation point at eigenvalue number k^* can be determined by comparing the model norm and variance graphs when both are plotted against the number of eigenvalues and eigenvectors used. If the eigenvectors are ordered by decreasing eigenvalue size there should come a point where the norm of

the model increases rapidly, representing these large amplitude model instabilities, while the variance reduction obtained becomes negligible.

From equation 5.3 above the model norm is given by

$$||\mathbf{x}_g||^2 = \sum_{k=1}^{k^*} \langle \mathbf{u}_k^T \mathbf{x} \rangle^2 \tag{5.4}$$

Similarly the variance is given by

$$\begin{aligned} ||\mathbf{A}\mathbf{x}_\mathbf{g} - \mathbf{d}||^2 &= \mathbf{x}_g^T \mathbf{A}^\mathbf{T} \mathbf{A} \mathbf{x}_g - 2\mathbf{x}^T \mathbf{A}^\mathbf{T} \mathbf{d} + \mathbf{d}^\mathbf{T} \mathbf{d} && (5.5) \\ &= \sum_{k=1}^{k^*} \lambda_k \langle \mathbf{u}_k^T \mathbf{x} \rangle^2 - 2 \sum_{k=1}^{k^*} \langle \mathbf{u}_k^T \mathbf{x} \rangle \mathbf{u}_k^T \mathbf{A}^\mathbf{T} \mathbf{d} + \mathbf{d}^\mathbf{T} \mathbf{d} && (5.6) \\ &= \mathbf{d}^\mathbf{T} \mathbf{d} - \sum_{k=1}^{k^*} \lambda_k \langle \mathbf{u}_k^T \mathbf{x} \rangle^2 && (5.7) \end{aligned}$$

5.5 Results from the zeroth iteration

5.5.1 Hypocentre locations and depths

The average depth per 5° cell for those events contributing to the models for this iteration are shown in figure 5.2

These results are consistent with what might be expected – events on mid ocean ridges (MORs) are predominantly very shallow (< 15km) and those at subduction zones extend to depths of around 30km. Figure 5.3 shows the relocation vectors, based on the same averaging per 5° cell, between the ISC locations and the final locations for this iteration. The main difference between the two locations being compared here is the sensitivity of the ISC locations to local velocity structure because of the use of arrivals with $\Delta < 25°$. It is not surprising therefore that the largest relocation vectors occur in subduction zones, *eg* coast of Chile, Java, Japan, where changes in local velocity structure are quite dramatic. In general the patterns are coherent with the biggest vectors ($\approx$ 20km) trending in roughly the same direction as neighbouring cell average vectors. In continental Asia the change in locations of the events do not have a distinct pattern but they are suitably small ($\approx$ 5km) for this not to be a problem.

5.5.2 Station corrections

The static station corrections of figures 5.4 and 5.5 in general vary smoothly which points to an overall consistency in the data after the first relocations. Stations for which reliable S corrections can be calculated are far less numerous than for P, but the same overall patterns are observed. As has been

shown in previous studies, eg Dziewonski & Anderson, 1983, the station corrections reflect the tectonic setting of the area - major shield areas (Siberia, Canada, western and central Australia, central Africa, and central South America) all have negative corrections corresponding to deep fast continental lithosphere, whereas the tectonically active regions (north east Africa, central America, Japan) all have large positive station corrections caused by the underlying hotter, but seismically slower, mantle. Souriau & Woodhouse, 1987 showed that there is a strong correlation between travel times through the upper mantle model M84 (Woodhouse & Dziewonski, 1984) and station corrections. As an example, the very large P and S corrections near Iceland can be attributed to the large slow velocity anomaly that is indicated by M84 to depths of around 350km in this region.

5.5.3 Models

After the selection of the 'best' 15 events per 5° cell, a total of 4773 out of 14091 events remained. Altogether 126803 paths were used in the final S inversion, and six times this number, 768893, in the P. The models constructed using all eigenvalues of the inner product matrices $\mathbf{A}^{\mathbf{T}}\mathbf{A}$ are shown in figures 5.6 and 5.7.

The plots show four maps at constant depth intervals starting at 680km, 10km from the upper/lower mantle boundary, and finishing at 2700km, corresponding approximately to the boundary of the lower mantle with D''. The light and dark shades correspond to slower and faster than average velocities respectively, and the saturation value of the contours is given in the bottom left hand corner of each sub plot. The zero contour occurs between the second and third lightest shades of grey. For graphical reasons the spherical part is not plotted but its size can be determined from the power spectrum on the right hand side.

A detailed discussion of the physical significance of the plots will be deferred until chapter 8, but general comparisons can be made here. Firstly the degree of heterogeneity in both plots is very small, being at most around 0.5% for P and 1% for S, thus validating the linearity approximations of section 3.4. In addition, in order to avoid saturation, the top sections of the S and P models are both plotted at twice the scale of the other graphs. It is clear from this top map of the S model that the velocity perturbations are very large in the Pacific where, as has been noted, there is very little data coverage. Before any comparisons between the two models can be made it is necessary to apply damping.

The eigenvalue analysis plots described in section 5.4 for both models are illustrated in figure 5.8. It is clear that the size of the S model increases rapidly after about eigenvalue number 230 without a significant reduction in the variance, and so it was decided to truncate the eigenvalues here. On the other hand, the size of the P model increases fairly steadily all the way to eigenvalue number 245, the number of parameters in the inversion, so no truncation is applied.

Effects of damping in the S model

The new S model is shown in figure 5.9. Comparison with the complete eigenvector spectrum model shows significant differences. The largest of these are, as expected, in the shallowest map in the Pacific region. The very large negative anomaly in the southern hemisphere has diminished considerably in both size and geographical distribution, and at the same time a smaller positive anomaly has appeared. The validity of this new feature is reinforced by its presence in the P model.

At shallow depths rays from all epicentral angles constrain the model whereas deeper parts are only covered by rays traveling in excess of 80° epicentral angle. As a result the models in these deeper areas are expected to need some degree of damping, and it is not surprising that there are considerable differences between the damped and undamped models. Whereas the differences between the two at shallow depths are quite localized, all the features here have been damped, and this is reflected in the diminished power spectrum. The two central maps have not changed a great deal either in pattern or power. This is proof that the damping procedure is correct as these are the areas of the model that are expected to have the best data coverage.

Comparison of zeroth iteration models

Without looking at specific features of the S and P models, it is already clear that there are striking similarities between the two. Both sets of spectra are larger at the top and bottom of the lower mantle and both maps at 680km depth need to be plotted with twice the contour interval in order to avoid excess saturation. This implies that there is a coherent pattern of shear wave heterogeneity that is present in the ISC S dataset.

Comparison of the features of the P model and the damped S model reveals close similarities but also non-insignificant differences. Considering first the intermediate depth 1300km where resolution is expected to be best, both maps exhibit positive fast anomalies under India and northern South America. These form the cornerstone of a ring structure around the Pacific which is particularly visible on the P map. Slower than average anomalies also compare well with features being evident in both maps around central Africa and Madagascar, and the south central Pacific region. The principal differences between the two are generally in the southern hemisphere where, as was noted earlier, there are relatively few stations. Here the S model does not share the same ring structure as the P model, although it can be seen that the joining up of the fast features under India and northern central America to Antarctica is almost complete.

At 2000km depth the P model is extremely small with heterogeneity of the order of 0.1%. As a result there are no large individual anomalies, but the ring structure around the Pacific persists in albeit a slightly different form. Instead of a large fast feature over central America that was evident in both models at 1300km, the ring is not closed here – instead it is joined across the Pacific at approximately

220° longitude. The S model also exhibits this feature, although it is much larger. Indeed the S model exhibits distinct fast features at this depth – western central Africa, Chile – and all exist where there are corresponding faster than average areas on the P map. An analogous statement can also be made of the slow features under Tonga and the zone extending east of Madagascar. The larger features of the S model at this depth can be attributed to the lack of model constraints caused by the removal of all S arrivals between 80° and 90° .

At 2700km depth coverage of the lower mantle by ray paths is not expected to be as good as it was at intermediate depths simply because there are fewer rays. In addition these rays will predominantly be bottoming out and hence depth resolution could be restricted. Nevertheless both maps are well correlated. Strong positive anomalies in both P and S heterogeneity down the east coast of Asia into the Indian Ocean, south Australia, east Antarctica, and the Caribbean give rise to another ring structure circumscribing the Pacific. The strong slow anomalies that the models have in common – Tonga, western and South Africa – emphasize this large scale feature. There are however significant differences, most notably in the northern Pacific where the P model exhibits a large positive anomaly from Asia to North America at 30° latitude. Instead the S model has a slow feature to the west of Canada. These differences mean that the ring structure in the S model appears to surround the entire Pacific as opposed to only the southern Pacific in the P model.

Comparisons of the two models at 670km have been reserved until last because little significance can be attributed to any similarities or differences between the two as a result of the poor resolution and large errors associated with this depth region. Nevertheless it can be said that the models are well correlated in all areas except the Pacific. In general there is no correlation with tectonic features. It might be expected that the long wavelength signature of deep subduction zones could be observed at this depth and indeed there are fast anomalies under Japan in both maps. The positive anomaly in the southern Pacific region is probably displaced too far east to be associated with the Tonga subduction zone.

The harmonic spectra show some of the features that have been discussed above. In the intermediate depths both P and S spectra are relatively flat with the ring structure being not particularly apparent at any one degree. At 2700km depth in the S model, however, the existence of high velocities around the entire Pacific region shows up in a strong degree 2 component in the harmonic spectrum. In the P model, with the ring of high velocities only appearing to surround the southern Pacific, most power is concentrated in degrees 2 and 3.

5.6 Subsequent iterations

Corrections to the travel times caused by lower mantle velocity heterogeneity can be calculated from equation 3.32 and then used in the relocation stages for the remaining iterations. This means that in addition to P and S, perturbation integrals for PP and PcP have to be calculated.

5.6.1 One step models

Inversion of the residuals after a relocation which includes heterogeneous models gives rise to a residual model. This is the change in the current model needed to fit the data better because of the new hypocentre locations and station corrections. For a convergent process the size of this residual model should tend to zero with increasing iterations. The new model is then obtained simply by adding together the residual and original models. However the question of damping of these residual models becomes difficult as the size of the residual model becomes smaller and smaller. Instead it is possible to compute a *one step* model based on the new hypocentre locations and origin times. This can be done as follows:

The actual travel time that a ray takes to go from a source to a receiver is not known exactly because it is based on a best fit hypocentre location and origin time. As a result the travel times published by the ISC are based on its own locations. A new set of travel times for a relocated dataset can be obtained by adding the difference between the relocated event origin time and the one published in the ISC bulletins. A set of residuals relative to PREM can be obtained from these by simply removing from them the theoretical travel times, *ie.* the PREM travel time along with station and ellipticity corrections. Symbolically for one source receiver path this is:

$$\delta t(\mathbf{s},\mathbf{r}) = T(\mathbf{s},\mathbf{r})_{ISC} + \delta t_0 - T(h,\Delta)_{PREM} - \delta t_{STATION} - \delta t_{ELLIPTICITY} \qquad (5.8)$$

where **s** and **r** are the source and receiver respectively, and δt_0 is the change in origin time of the relocated event relative to the ISC origin time.

Since the heterogeneous models derived in this study are simply deviations from PREM, inversion of the residuals δt in the above equation should yield a model which is equivalent to the sum of all models derived in previous iterations.

The one step approach to the iteration models has several advantages over the residual model addition method. Firstly, it is the sum of the effects of all iterations that is being damped, not just the damping of a residual model, so the method of damping is consistent throughout. Secondly, and for more practical purposes than theoretical necessity, the one step inversion gives a complete one step eigenvalue analysis of the new model.

5.7 Iteration statistics

Table 5.1 gives the data analysis for those events in the entire dataset, whereas the information in table 5.2 relates specifically to the events which have survived the selection criterion of section 5.1 and hence contribute to the inversion for the model. The second last column gives the percentage variance reduction that is achieved by removing the model contribution from the residuals, *ie.* the

one step residual minus the model travel time obtained using equation 3.32. The last column is the percentage variance reduction in the data that is obtained from the inversion itself using the weighting scheme described in section 5.1. This is the figure that would be obtained from the variance reduction eigenvalue plot such as the ones in figure 5.8.

phase type	*iteration no.*	*no. data*	*mean (s)*	*variance (s^2)*	*av depth (km)*
P	0	1732634	-0.020	1.406	12.8
	1	1732524	-0.018	1.331	17.5
	2	1732454	-0.018	1.323	19.9
	3	1732242	-0.018	1.321	21.3
	4	1732188	-0.018	1.320	22.4
S	0	228982	-0.272	13.635	12.8
	1	228996	-0.182	13.038	17.5
	2	228992	-0.028	12.818	19.9
	3	228968	-0.008	12.789	21.3
	4	228984	-0.002	12.768	22.4

Table 5.1: Statistics of the complete dataset

before inversion					after inversion			
phase type	*it. no.*	*no. data*	*variance*	*one step variance*	*mean*	*variance*	*unw. variance reduction (%)*	*w. variance reduction (%)*
P	0	768893	1.476	1.476	-0.044	1.408	4.66	5.97
	1	769555	1.391	1.504	-0.033	1.384	8.00	9.15
	2	769415	1.379	1.530	-0.029	1.379	9.90	11.06
	3	769165	1.377	1.553	-0.028	1.377	11.33	12.57
	4	768699	1.376	1.575	-0.028	1.377	12.64	13.92
S	0	126803	13.743	13.743	-0.094	13.174	4.29	4.85
	1	126875	13.137	13.911	-0.075	12.940	7.02	7.81
	2	126814	12.912	14.168	-0.069	12.877	9.11	10.16
	3	126838	12.882	14.441	-0.067	12.856	11.00	12.35
	4	126853	12.861	14.704	-0.066	12.844	12.76	14.43

Table 5.2: Statistics of the selected dataset

5.7.1 Discussion

The most important point to note from the data presented in table 5.2 is that there are variance reductions at each iteration in both P and S cases. The variance of both the selected and the whole datasets diminish, and indeed the changes in the variances at each iteration become smaller. This points to a convergent solution.

The variance of the one step data increases with each iteration. This is not as surprising as it seems at first because the zeroth iteration data is based on locations which minimize the hypocentre locations with respect to PREM alone, whereas subsequent iteration locations are based on minimizing the data which includes lower mantle models as well as PREM but whose contribution is not included in this dataset. The one step variance size increases with each iteration because the model becomes larger.

Another factor which indicates a stable convergent solution is the data mean. Firstly it should be restated that the means of the P and S datasets are not zero because of the weightings that have been applied in the relocation procedure. With this in mind the data means do not fluctuate wildly – from table 5.1 the P mean stays constant at -0.018 seconds after the 1^{st} iteration, and it only changes by 0.002 seconds from the $zero^{th}$ iteration. The S mean varies slightly more as a result of its lesser role in the relocation of an event (fewer arrivals, lower weighting), but it still comes very close to convergence changing only by approximately 0.001s.

Despite these positive indicators of a stable convergent iterative procedure the models have not yet converged. The P model is close, changing only very slowly in the 3^{rd} decimal place of the variance, but the S model is still converging with changes in the 2^{nd} decimal place. Slower convergence of the S model is expected for the same reasons given for the convergence of the S mean. The most troublesome factor involves the continued increase in the one step variance. Examination of these figures shows that the changes between iterations decrease only very slowly in the P case. Similarly for S, after an initial rise in the changes to the 3^{rd} iteration there is only a very slow decrease. In other words, the data before the inversion (the one step column) has a variance which is increasing, but converging slower than the decreasing variance after the inversion. As a result the variance reduction at each stage is increasing more than the final variance of the data is reducing. As a specific example to clarify this point, between the 3^{rd} and 4^{th} iterations of the S model, the variance of the dataset before the inversion increases by 14.704 - 14.441 = $0.263s^2$ while the reduction in the final variance is only 12.856 - 12.844 = $0.012s^2$. The reason for this probably lies with a fault in the methodology of the iterative inversion scheme. The models are derived from a set of residuals which are weighted in order to avoid bias in the solution. These weightings are different to those used in the relocation procedure, and so it is quite possible that successive iterations of relocation and inversion will not lead to a convergent solution.

Figure 5.1 seems to validate this hypothesis. Both sets of graphs show the variation of the mean of the P and S data with epicentral angle before and after the inversion for the first three iterations. The left hand graphs are one step residuals resulting from the relocation procedure. The overall shape of these graphs show several interesting features:

- The mean of both P and S residuals before inversion increases with epicentral angle, and this results from the use of PREM as a reference model in this study. This behaviour is a manifestation of the use of ISC locations in the derivation of this model and has been noted in the literature.
- Several peaks exist in the S data means, particularly at large epicentral angles where there is very little data. In addition it is possible that the fluctuations in the mean at epicentral angles of $\approx$ 40° are linked to misidentifications of PcS as S (see the vertical streak in figure 2.8).
- After inversion the mean of the P residuals is far smoother and closer to zero than the mean of the S residuals which results from their controlling influence in the relocations and the decreased chance of misidentifications in the P dataset.

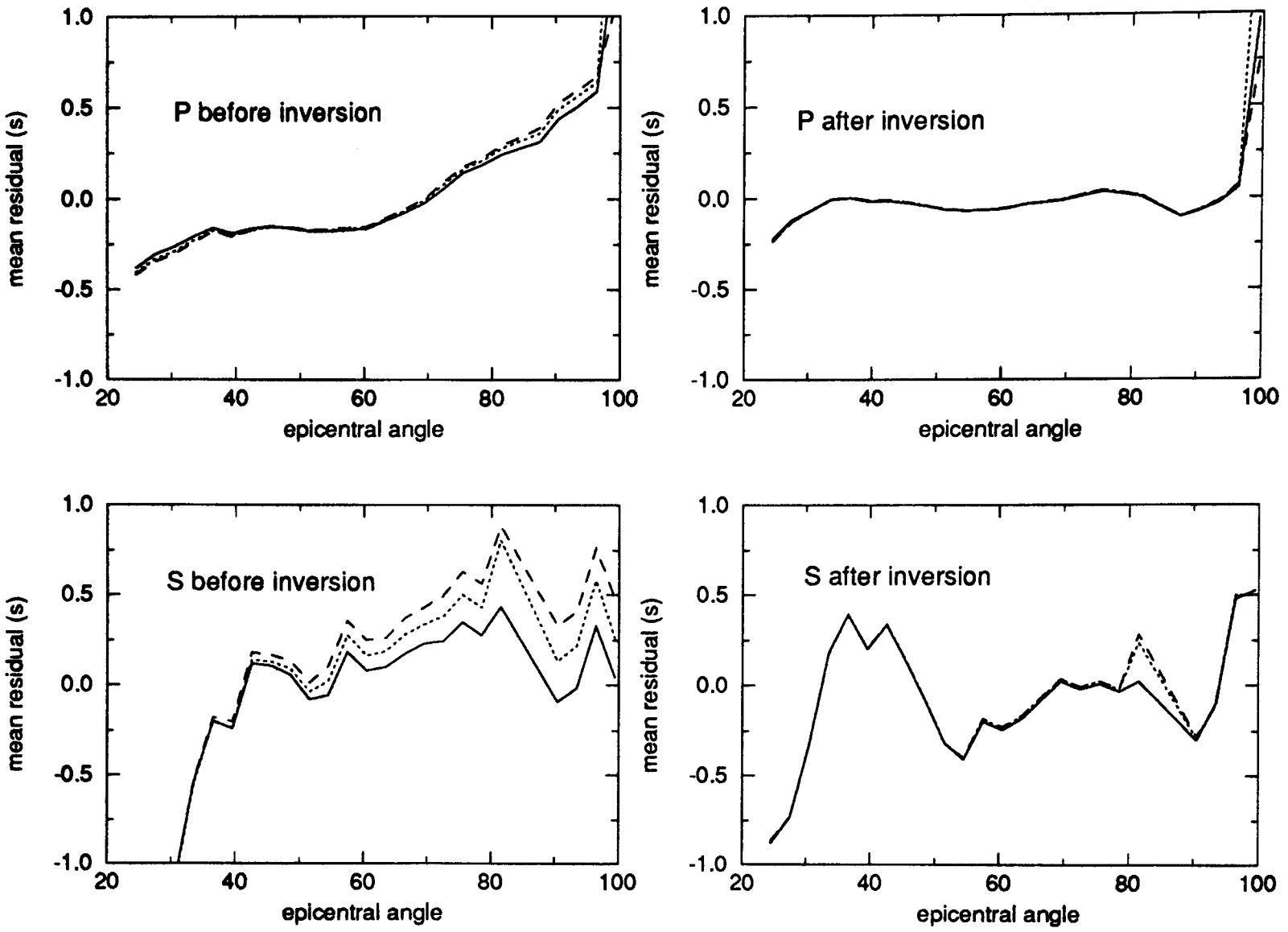


Figure 5.1: Analysis of the mean P and S residual versus epicentral angle before and after inversion. The solid, dotted, and dashed lines represent iterations 1, 2, and 3 respectively.

However, in terms of this argument, the most important point originates from the comparison of the 'before' and 'after' graphs, and this is seen most clearly in the S case. It is evident that the means at a given epicentral angle before inversion increase at an almost constant rate with each iteration, whereas the means after the inversion are almost exactly the same. This observation, which is also evident in the one step variance column of table 5.2, means that the corrections to the travel times generated by the inverted model that enter into the relocations are not the ones which minimize the sum of residuals in the relocation algorithm. In agreement with what was said above, this is probably because of the different weighting schemes used in the inversions and the relocations. This effect is seen to a smaller degree in the means of the P residuals because they have a larger influence on the relocation of an event.

It is also possible that trade–offs with for example station corrections could account for part of the increase in the one step variance. For example in an area with poor data coverage it will be difficult to determine whether the station correction changes or the top of the model changes because a ray path at the top of the lower mantle is almost vertical, and hence constraints on the model are small. The inversion routine will tend to change the model to maximize the variance reduction. In this case, whether the change to the model makes it more negative or more positive, the one step variance will

always increase.

5.7.2 Changes in models

The models obtained at the end of each iteration are shown in figures 5.10 to 5.13 for P and 5.14 to 5.17 for S.

P models

The P models show progressive changes with no new features becoming prominent at any depths. The size of the features in the top map become much larger as a result of poor data coverage. This is illustrated by the harmonic spectrum where there is a doubling in the size of degrees 0, 2, and 3, and increases of around 30% in the other coefficients. The increases after each iteration do not become significantly smaller as the iterations continue. At intermediate depths the features are generally slightly larger. One exception to this is the high velocity feature in the north eastern Pacific at 1300km depth which disappears as the iterations progress. However the corresponding fast growth of the low velocity feature at the same location in the 680km map may be linked to this. The slightly poorer data coverage at depth is probably the cause of the uniform increase in the harmonic power of the 2700km section at all degrees by $\approx$ 20% over all iterations.

S models

As a result of the smaller weighting in the relocation process, larger changes are expected in the S model with each iteration. This intuition is not borne out at the top of the lower mantle where the model does not change throughout the iterations nearly as much as the P model. Instead most of the change occurs at the intermediate depth 1300km where degrees 0 to 3 all double in size. This corresponds to an increase in the positive anomalies under India and the Caribbean, and the development of a slight positive anomaly over New Zealand – all of which are observed in the P model. Apart from a slight accentuation of a few features there is very little change at 2000km depth. In the 2700km map the model becomes quite large as a result of the poor data constraints. Here there is a marked increase in degrees 2, 5, and 6.

5.7.3 Relocation vectors

Relocation vectors between iterations are shown in figures 5.18 to 5.21. Changes between the zeroth and 1st iterations are on average twice as small as those which show the change between the ISC locations and the zeroth iteration location (note the difference in scale between figures 5.3 and 5.19). They also form a much more coherent pattern reflecting the inclusion of large scale three dimensional heterogeneous models rather than a different relocation technique. There is no discernible correlation

with tectonic setting. Changes between the 1^{st} and 2^{nd} iterations decrease in size by 60% over the previous iteration changes, forming a very coherent pattern amongst even the smallest vectors. Relocation vector size from iterations 2 to 3 and 3 to 4 continue to decrease, having average vector sizes of 0.659 and 0.554km respectively. In addition the direction of these vectors have changed from those in figure 5.18. Specifically, those events surrounding the Pacific in figures 5.20 and 5.21 all systematically move towards the centre of the ocean by the same amount. This is probably a direct consequence of the increase in the already large and poorly constrained negative anomaly centred around Hawaii.

5.7.4 Depth changes

Figures 5.22 to 5.25 show the average depth change of the events per 5° cell. It is clear that all cells, except four around southern India, become deeper between the zeroth and 1^{st} iterations. In particular there are increases in the average depths by up to 15km around New Zealand, Easter Island, the Rocky Mountains, and the Indian Ocean triple junction. Progressing through the iterations, the events on land tend to become fixed at a constant depth while others, particularly MORs, continue to become deeper at only a very slightly decreased rate. The reason for this is likely to come from the fact that the depths of MOR events are very poorly constrained as a result of the scarcity of near event receivers. Therefore it is probable that the increase in depth of these events is being caused by a trade–off with the event origin time and possibly the model itself. This will be investigated in section 5.8.1.

In order to investigate the cumulative effects of these depth changes the average depths per 5° cell at the end of the 4^{th} iteration are plotted in figure 5.26. For comparison the equivalent ISC depths are shown in figure 5.27. It is clear that despite the depths of almost all events increasing at all iterations, the depths of the events in this study are still less than those published by the ISC. This results from the shallowness of the original depths from the first set of relocations where the events are not constrained by data at $\Delta < 25°$, although the explanation of why all the events become shallower as a result of this lack of constraint is unknown. At MORs, however, events have very few arrivals at $\Delta < 25°$ and so the ISC depths will also be poorly restrained. In these areas any differences between the depths in figures 5.26 and 5.27 can be attributed to the additional use of PP, PcP, and most importantly S in the relocation procedure used in this study. It can be seen that the ISC locations for the Atlantic MOR are consistently deeper, with the most common depth being between 15 and 25km. Studies of teleseismic events at MORs have been carried out using waveform analysis (Hwang & Solomon, 1988), and these have given depths no greater than $\approx$ 12km.

Figure 5.28 is a scatter plot of the change in origin time of an event versus its change in the depth at the end of the zeroth (top) and 4^{th} (bottom) iterations. The histograms on the right hand side of the page simply show the number of events with a given change in origin time. The peaks in the histogram are probably a consequence of the comparative large number of events that are given ISC NULL depths of 10 and 33km and whose depths have been relocated close to zero. The linearity of the top plot clearly

illustrates the trade–off problem that does exist between origin time and depth. There are no three dimensional models involved in the relocation at the zeroth iteration so this plot is independent of any model trade–off. The lower scatter plot shows the same linearity, illustrating the same fundamental trade–off problem, but there seems to be more points at the right of the plot with a change in origin time greater than +8 seconds. This is also reflected in the wider base of the lower histogram.

As a result, because the only difference between the two diagrams is the introduction of one three dimensional model (the starting datasets are identical), it does seem probable that the model is also involved in the trade–off.

5.7.5 Station corrections

The question of which parameterization of the station corrections should be used is one which is unresolved in the literature (see section 3.2.2). Exactly how much lower mantle model signal is included in azimuth dependent corrections has only been qualitatively stated (Dziewonski & Anderson, 1983), and so it is important in a study like this, where new P and S corrections are generated in each iteration, that the behaviour of these corrections is known.

As a preemptive attempt to examine the problem of model/station correction trade–off, four regions of the earth have been chosen to be studied, and these are listed in table 5.3 below.

These areas have been selected because they represent places where the top map sections change most through the iterations. The reason for this is that the top of the model has poor depth resolution caused by the predominantly vertical nature of the rays at this depth. Consequently it is in these areas that any trade–off problems are going to be most clearly seen.

The results, shown in figure 5.29, have been grouped in terms of underlying velocity perturbation in the 680km map of the 4th iteration P model. Hawaii and the Middle East stations exist on slow anomalies which have increased in magnitude throughout the iterations, whereas southern Africa and Japan overly areas of increasingly faster than average velocities. The plots show the average corrections for all stations within the appropriate zone.

AREA NAME	*lat min*	*lat max*	*lon min*	*lon max*
southern Africa	-40	0	0	40
Middle East	10	40	30	60
Japan	20	40	120	135
Hawaii	20	30	190	210

Table 5.3: Station correction area locations.

In theory, if there is a model/station correction trade–off, then an increase in a positive anomaly in the model at the top of the lower mantle will result in an increase in the station correction in order

to compensate for the shorter travel time of the ray in the model. Similarly an increase in magnitude of the negative anomaly will cause the station corrections to decrease. Examination of the P station corrections of figure 5.29 (the top two graphs) shows this to be the case with the average of the Hawaiian and Middle Eastern corrections both decreasing steadily throughout the iterations. Similarly the stations overlaying the increasingly faster anomalies, represented by southern Africa and Japan, all increase. The corrections for Japan seem to be the only ones that are converging.

The S station corrections in the lower two graphs mimic the P cases in all but southern Africa where there is a decrease in the value instead of an increase. Examination of the relevant S maps at 680km depth (figures 5.14 to 5.17) reveals that there is in fact very little difference in the size of the positive anomaly in southern Africa throughout the iterations so it is possible that there is little trade–off problem in this region. It is slightly surprising that the station correction zone that is expected to trade–off worst with the model, Hawaii, does not change much at all throughout the S iterations – note the difference in scale between the two right hand figures. This could simply be because the large negative anomaly does not directly underly Hawaii on the S maps. However the damping of the S model is expected to have its largest impact on this anomaly, so this fact might also reflect a successful damping procedure.

In conclusion therefore it does seem that there is a trade–off between station corrections and the uppermost parts of the models. Evidence is particularly convincing in the P case where all four zones exhibit the trends expected if a trade–off is occurring. Further experiments need to be performed.

5.8 Trade-off experiments

Since the start of the analysis of the iterations in section 5.6 there have been many suggestions of trade–offs between the model and the different variables involved in the inversion. In fact the explanation of the continued increase of the one step variance in section 5.7 was given partly in terms of trade–offs. The different possibilities are summarized below.

- 1. **Event depths/origin times**. The average depths of the events in the inversions increase at each iteration without convergence. In particular it is the worst constrained depths on the mid ocean ridges that change most in the latter iterations.

- 2. **Station corrections**. The examination of the behaviour of the station corrections was done in such a way as to establish that there is a strong trade–off with at least the P corrections

- 3. **Relocation vectors**. The events around the Pacific all move towards the centre of the Pacific between iterations 2, 3, and 4, with the changes being almost the same size. At the same time the low velocity P anomaly in the north of this region increases steadily in magnitude.

The trade–off effects of the last of these possibilities is expected to be small because the relocation vectors between latter iterations are very small. In order to quantify what effects the interaction of the event depths and station corrections have on the model, two further sets of iterations have been carried out:

- **depth experiment, section 5.8.1** . After the relocation of the events with the zeroth iteration models, *ie.* at the end of the 1st iteration, the depths of the events are fixed.
- **Fixed station correction, section 5.8.2** . The station corrections are fixed to those at the end of the 1st iteration.

5.8.1 Experiment 1: Fixed depth iterations

Statistics

The inability to resolve individually the origin time and depth of an event is one of the greatest problems in the determination of earthquake locations. In other words, the residual minimization technique used to calculate a best fit earthquake location cannot accurately resolve whether, for example, the depth increases by say 8km or the origin time increases by ≈1s. It is the objective of this experiment to investigate whether or not this origin time/depth trade–off is coupled somehow to the model. It will also be important to establish whether the station corrections change significantly as a result of fixing the event depths.

Before describing the results of this experiment it is important to clarify how they might be interpreted. It has already been postulated that there is a three way trade–off between event depth, origin time, and the model. As a result, by fixing the depths, all that could occur is that there might be larger changes in the origin times in compensation. A similar experiment could have been performed by fixing instead the event origin times. This experiment simply tries to eliminate one of the variables in the three way trade–off. The statistics for the iterations keeping the depths of the events fixed after the 1st iteration are shown in tables 5.4 and 5.5.

phase type	*iteration no.*	*no. data*	*mean (s)*	*variance (s^2)*	*av depth (km)*
P	2	1732588	-0.013	1.323	17.5
	3	1732576	-0.013	1.322	17.5
	4	1732572	-0.013	1.321	17.5
S	2	228989	-0.000	12.789	17.5
	3	228984	-0.001	12.774	17.5
	4	228982	-0.003	12.767	17.5

Table 5.4: Statistics of the complete dataset for the fixed depth iterations.

The final variances of the selected datasets are seen to have effectively converged after the 3rd iteration with changes in both P and S variances, albeit very slightly positive, occurring only in the 3rd decimal

before inversion				after inversion			
phase type	*it. no.*	*no. data*	*one step variance*	*mean*	*variance*	*unw. variance reduction (%)*	*w. variance reduction (%)*
P	2	769490	1.526	-0.028	1.380	9.61	10.73
	3	769487	1.545	-0.027	1.379	10.81	11.98
	4	769389	1.564	-0.027	1.379	11.93	13.16
S	2	126814	14.168	-0.057	12.891	8.14	9.13
	3	126838	14.441	-0.051	12.883	8.93	9.94
	4	126853	14.704	-0.049	12.884	9.55	10.62

Table 5.5: Statistics of the selected dataset for the fixed depth iterations.

place. These variances are only slightly higher than those of the reference iterations (1.379 - 1.377 = $0.002s^2$ for P and 12.884 - 12.844 = $0.04s^2$ for S) reflecting the reduced number of degrees of freedom in this experiment. Nevertheless the variances of the complete dataset are almost identical, so it can be concluded that fixing the depths of the events does not significantly change the effectiveness of the models. The one step variance continues to increase between iterations at an almost continuous rate for P and at a reducing rate for S. This is further evidence of the existence of a model/station correction trade–off problem, and in fact it is a clearer example than in the reference iterations because in this case the final variances have converged. Further evidence of complete convergence and the stability of the final solution comes from the means of P and S in both the selected and complete datasets.

Models

The 4^{th} iteration models for this experiment are presented in figures 5.30 and 5.31 for P and S respectively. Comparison of the P model with the reference 4^{th} iteration P model (figure 5.13) shows that the maps are almost identical in all but the top map. Here the degree zero component is decreased by around 30% with small decreases of the order of 10% in the remaining harmonic degrees. As a result it can be concluded that there is only a slight trade–off problem between the P model and the depths of the events, with the main differences occurring in the degree zero part at the top of the model.

Comparison of the new S model with the reference S model at the same iteration number (figure 5.17) reveals many more differences. In fact the differences between the two are almost exactly the same as the differences between the 2^{nd} (figure 5.15) and 4^{th} iteration reference models. Hence figures 5.15 and 5.31 are almost exactly the same. This means that keeping the event depths fixed causes very little change to the starting model and at the same time proves that the reference S model trades off quite strongly with depth.

This observation is not as surprising as it seems simply because of the increased depth sensitivity, $\frac{dT}{dh}$ (where T is the phase travel time and h is the event depth) of the S dataset resulting from its slower velocity. In the location of an event, P arrivals contain very little information to discern the difference between origin time and depth. In other words, for an event which has only P arrivals, if the depth of

the event is fixed then the travel time residuals in the minimization technique are fit almost as well by a change in the origin time of the event. The S phase, however, is much more sensitive to the difference between origin time and depth because it has a larger $\frac{dT}{dh}$ resulting from its slower velocity. As a result, for events with many S arrivals, the trade–off between origin time and depth is much smaller. For the dataset in this study, not only do the P arrivals outnumber the S arrivals by approximately 6:1, but they are weighted by another factor of almost 6 in the relocation because of their smaller variance. Therefore the P dataset probably contributes as much if not more information to the depth determination as the S dataset. It should be noted that this does not mean that the depth is defined any better. In this experiment, where the depths are fixed, the higher weighted and more numerous P arrivals are fit almost as well in the relocation residual minimization procedure by a change in origin time. The S arrivals can resolve the depth and origin times better, but they are poorly weighted, and so the dataset is not fit as well. Consequently, for the iterations in this experiment, it is expected that the S residuals and therefore the S models will change more.

Relocation vectors

The changes between the average hypocentre positions between iteration 4 in this experiment and iteration 4 in the reference inversions are extremely small. In fact they are too small to be plotted on the same scale as the previous relocation vector plots. Therefore fixing the depth of the events does not affect the latitude and longitude changes between iterations.

Station corrections

Throughout the iterations in this experiment the station corrections have been allowed to change. It is clear that in such a complex physical system such as the one being modeled, there will inevitably be more parameter interactions than the ones that are being examined by the two experiments presented here. In other words, the trade–off between event origin time/depth are currently being examined, but it is probable that the station corrections will also be affected. Figure 5.32 shows the differences between the P and S station corrections of the fixed depth and reference experiments at each iteration for the four areas chosen in section 5.7.5. If there are any significant differences between the two sets then they should be seen in these areas. Examination of this figure shows that the areas which appear to have the largest changes – P Japan, P southern Africa, S Middle East – have the smallest scale so the differences at the 4^{th} iteration are at maximum 0.04s. Moreover the changes are not consistent. For example, in the top left hand graph the change in the P station correction is positive for the Japanese area and negative around southern Africa. As a result it can be concluded that the station corrections are not severely affected by fixing the depths of the events.

5.8.2 Experiment 2: Fixed station correction iterations

Statistics

The results of this experiment should be slightly easier to interpret than the last because there is expected to be a direct trade–off between the station corrections and the top of the model. Intuitively, fixing the station corrections should lead to the biggest features in the top map becoming smaller at very little increase to the final variance. The statistics for this experiment are shown below.

phase type	*iteration no.*	*no. data*	*mean (s)*	*variance (s^2)*	*av depth (km)*
P	2	1732461	-0.018	1.322	19.5
	3	1732341	-0.018	1.319	20.9
	4	1732268	-0.018	1.318	22.1
S	2	228995	0.014	12.821	19.5
	3	228989	0.026	12.798	20.9
	4	228988	0.024	12.782	22.1

Table 5.6: Statistics of the complete dataset for the fixed station correction iterations.

		before inversion			after inversion			
phase type	*it. no.*	*no. data*	*variance*	*one step variance*	*mean*	*variance*	*unw. variance reduction (%)*	*w. variance reduction (%)*
P	2	769411	1.377	1.522	-0.031	1.378	9.47	10.71
	3	769564	1.374	1.537	-0.031	1.375	10.57	11.86
	4	769043	1.373	1.553	-0.032	1.375	11.52	12.81
S	2	126816	12.914	14.088	-0.077	12.895	8.47	9.67
	3	126913	12.894	14.258	-0.077	12.879	9.77	11.22
	4	126841	12.879	14.403	-0.075	12.870	10.96	12.59

Table 5.7: Statistics of the selected dataset for the fixed station correction iterations.

Comparison of tables 5.7 and 5.2 for the reference iteration case shows that the final variance of the selected P dataset is lower, although only slightly, than that when the station corrections are allowed to vary. This is not as problematic as it seems because the variance *reduction* involved is greater in the reference iterations, and this is the figure that is attempted to be maximized in the inversion. It follows from this last statement that the variance of the dataset before the inversion must be smaller in this experiment, and from the one step variance this is seen to be the case. The changes in this column are smaller than those in the fixed depth experiment, and much smaller than those in the reference experiment. Nevertheless the one step variance is converging only slowly indicating that there is probably some trade–off with depth/origin time occurring. This is verified by the slightly increasing depths for the iterations. The variance of the entire P dataset also approaches convergence to almost the same value as the previous experiment and the reference experiment. Stability of the solution is confirmed again by the constant value of the data mean.

The variance of the selected S dataset at the end of each inversion also decreases but convergence is

slower, with changes in the 2^{nd} decimal place as opposed to the 3^{rd} for P. Changes in the variance before the inversions, the one step column, are much smaller than those in the reference iterations but much larger than those for the fixed depth experiment. By analogy therefore, since the S model was shown to suffer relatively badly from a depth trade–off, it can be said at this stage that the reference S model suffers relatively less from a trade–off with the station corrections. Both the weighted and unweighted percentage variance reductions are less in this experiment than those in the reference experiment, and the final variances obtained are higher.

Models

The models resulting from the 4^{th} iteration of this fixed station correction experiment are shown in figures 5.33 and 5.34 for P and S respectively. Comparison of the P model with the equivalent model from the reference iterations, figure 5.13, again shows the largest differences at the top of the model, most notably in the Pacific region where the large negative velocity anomaly has reduced in size. In terms of the harmonic spectra, all degrees have decreased by around 15% with the biggest differences being at degrees 2 and 3. Other differences include the reappearance of a fast anomaly in the north eastern Pacific at 1300km depth. This feature is also apparent in the 2^{nd} iteration P map and so it is probable that its subsequent disappearance can be attributed to the trade–off of the model with the station corrections.

Comparison of the 4^{th} iteration S model in this experiment with figure 5.17, the final reference iteration S model, shows that there are relatively few differences, and again these are restricted principally to the top. The degree 2 harmonic falls by $\approx$20% at 680km, and degrees 0 and 1 all fall by $\approx$10% at 1300km depth. This proves that there is very little station correction trade–off problem associated with the reference S model.

Relocation vectors

The changes in the event locations between the 4^{th} iteration in this experiment and the reference 4^{th} iteration are shown in figure 5.35. It is clear that these are very small, especially those vectors circumscribing the Pacific Ocean. Some of these point away from the centre of the ocean, for example at the Alaskan coast, but most others continue to point to the open oceanic areas. As a result the conclusion is that fixing the station corrections does not stop the general trend of the vectors being towards unconstrained data areas.

Event depths

Changes in the depths of the events between this experiment and the reference experiment are minimal and too small to be plotted on the same scale as the previous change of depth plots. This is a positive

result because it means that the model has not simply traded-off with the event depths as a result of being unable to change with the station corrections.

5.9 Conclusions: Choice of lower mantle models

The experiments in the last section have not completely resolved the complex interactions between the parameters that exist in the inversion for lower mantle models, but they have highlighted some of the major trade–offs:

- P model
  - Fixing the depths of the events results in only minor changes to the 4^{th} iteration model, and these are principally in the top map. Therefore the P model does not suffer from a trade–off problem with the event depths. Relative to the 4^{th} reference iteration there is only a very minimal increase in the final variance of the data although the variance reduction is around 0.7% less. Fixing the depths does not result in large changes to the P station corrections.
  - Fixing the station corrections gives rise to larger changes showing that the P model is affected to a greater extent by a trade–off with the station corrections. As before the differences are principally at the top of the model. Final variances are slightly less than those in the 4^{th} reference iteration, and the variance reductions are smaller by around 1.1%. There is very little compensatory change in the depths of the events.

- S model

  The changes that are observed in the S model in the experiments are the opposite to those for the P model.
  - Quite large differences between the final fixed depth model and the 4^{th} iteration reference model indicate that the S model is affected quite significantly by a depth trade–off. Final variances are slightly lower than those in the reference iterations, but the variance reduction is less by $\approx$3.2%.
  - Fixing the station corrections after the 1^{st} iteration does not affect greatly the outcome of the S model. This probably results from the damping procedure which decreases the size of the upper model anomalies, the area most likely to trade–off with the station corrections. Final variances are greater than in the reference experiment for both the selected and complete datasets. Variance reductions are less by $\approx$ 1.8%.

Some of the major points from the above are clearly illustrated in figures 5.36 and 5.37. These show the P and S model norms for each iteration in the three sets of iterations described in this chapter – the lines for iterations 0 and 1 being the same in each case. The bottom plots are the reference model

norms at a given cumulative eigenvalue number. It is obvious from both P and S reference plots that as the iterations increase, the size of the models become larger with no real sign of convergence. In the experiment in which the depths were fixed (centre plot), the changes in the P model norm between latter iterations are smaller but still increasing at an almost constant rate. The equivalent S plot is remarkably different, showing smaller model increases with each iteration. In accordance with the conclusions of the first experiment it is clear that holding the depth fixed eliminates the main trade–off problem in the S model and almost leads to a convergent solution. A similar conclusion can be made when the graphs for the fixed station correction experiments, the top two plots of figures 5.36 and 5.37, are examined. This time changes in the P model are smaller than in either the reference iterations or the fixed depth experiments, which emphasizes the conclusions drawn in section 5.8.2 that the main area of trade–off in the P model is with the station corrections. The S model norms for this case do not show nearly the same decrease in size that was seen in the fixed depth case.

These plots are extremely important as they illustrate the degree of convergence that is obtained. Neither of the two best cases – fixed depth S model or the fixed station correction P model – have actually converged. It is possible that more iterations would result in extremely small changes but this is doubtful. In a complex physical system such as the one being modeled here, there will always be other, possibly less significant, trade–offs whose effects can only be multiplied with increased iterations. For example it might have been informative to carry out an experiment in which the earthquake locations were kept fixed in order to establish the effect on the model of the continued drift of circum Pacific events into the centre of the ocean at each iteration. In addition, when the depths of the events were kept fixed in section 5.8.1, it was shown that there was very little change to the station corrections. Nevertheless there is no way to guarantee that the cumulative effects of these small changes might not be important if the iterations are to be continued indefinitely. The decision of which P and S models should be chosen as the most representative of the velocity heterogeneity in the lower mantle is not an easy one. It should not be made on the variance reduction obtained alone because this is dependent on the variance before the inversion, the one step variance, which in turn includes the effect of any trade–offs and the mismatch in weightings between the inversion routine and the relocations. Instead a decision based on the final variance of the data is justifiable. Both P and S models must come from the same iteration of the same experiment if they are to be used together in any comparisons. If this is not done then the models would be derived from different event locations and station corrections.

Since this is a study of global S heterogeneity, it seems reasonable to base the choice of models on the selection of the best available S model. Using these guidelines, the models from the 3^{rd} iteration of the fixed depth experiment, shown in figures 5.38 and 5.39, have been chosen. The variance of the selected S dataset has converged to $12.883s^2$, only slightly higher than that of the fixed station correction experiment, and only $\approx 0.03s^2$ higher than the reference experiment. The variance of the entire dataset after relocation with this model (the iteration 4 row in table 5.4), and station corrections based on it, is almost exactly the same as the one from the reference iteration ($12.767s^2$ compared to $12.768s^2$). The

most significant factor stems from the model norm, which changes very little between iterations 2, 3, and 4 in the fixed depth experiment.

The corresponding P model is not the optimal choice, but differences in the final variances obtained in both the selected and complete datasets are never more than $0.004s^2$. The choice of the 3^{rd} iteration model of this experiment rather than the 4^{th} cuts down the degree of station correction trade–off that can occur. In any case it should be emphasized that most of the discussion of the last three sections has centred on the changes to the top of the models only. The best determined parts of the model, shown in the middle two map sections in the model diagrams, change insignificantly throughout all three sets of iterations.

5.10 Further work

Future chapters in this thesis will attempt to explore not only the resolution and variance of these models, but also their correlation with each other and with pre-existing lower mantle models. In addition tests will be carried out to establish which differences between the P and S models can be attributed to the different ray paths in the datasets.

Since the choice of model parameterization is a major factor governing whether or not a feature is resolvable it is also important to carry out inversions with different choices of n and l.

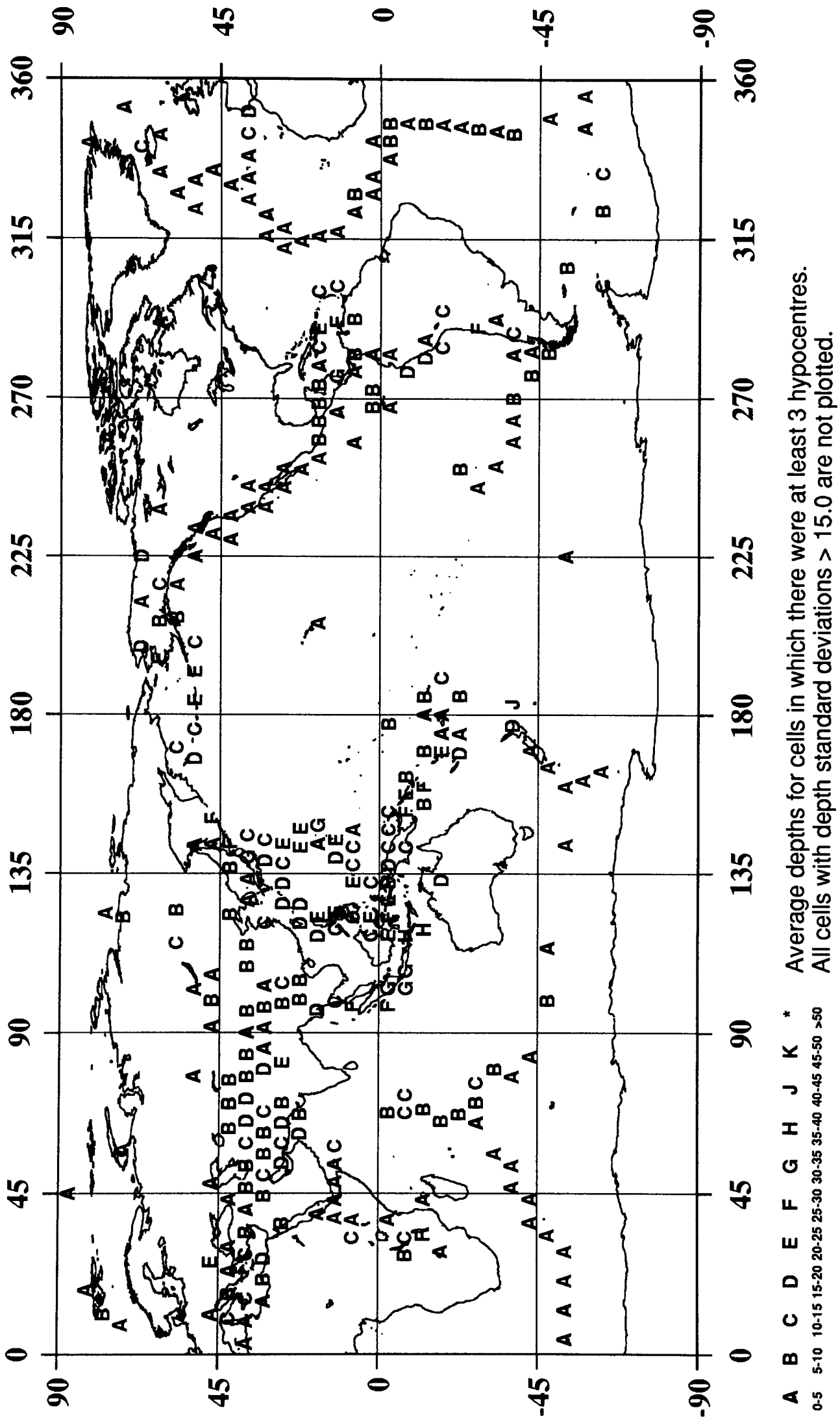


Figure 5.2: Binned depths for the relocated events contributing to the iteration 0 models

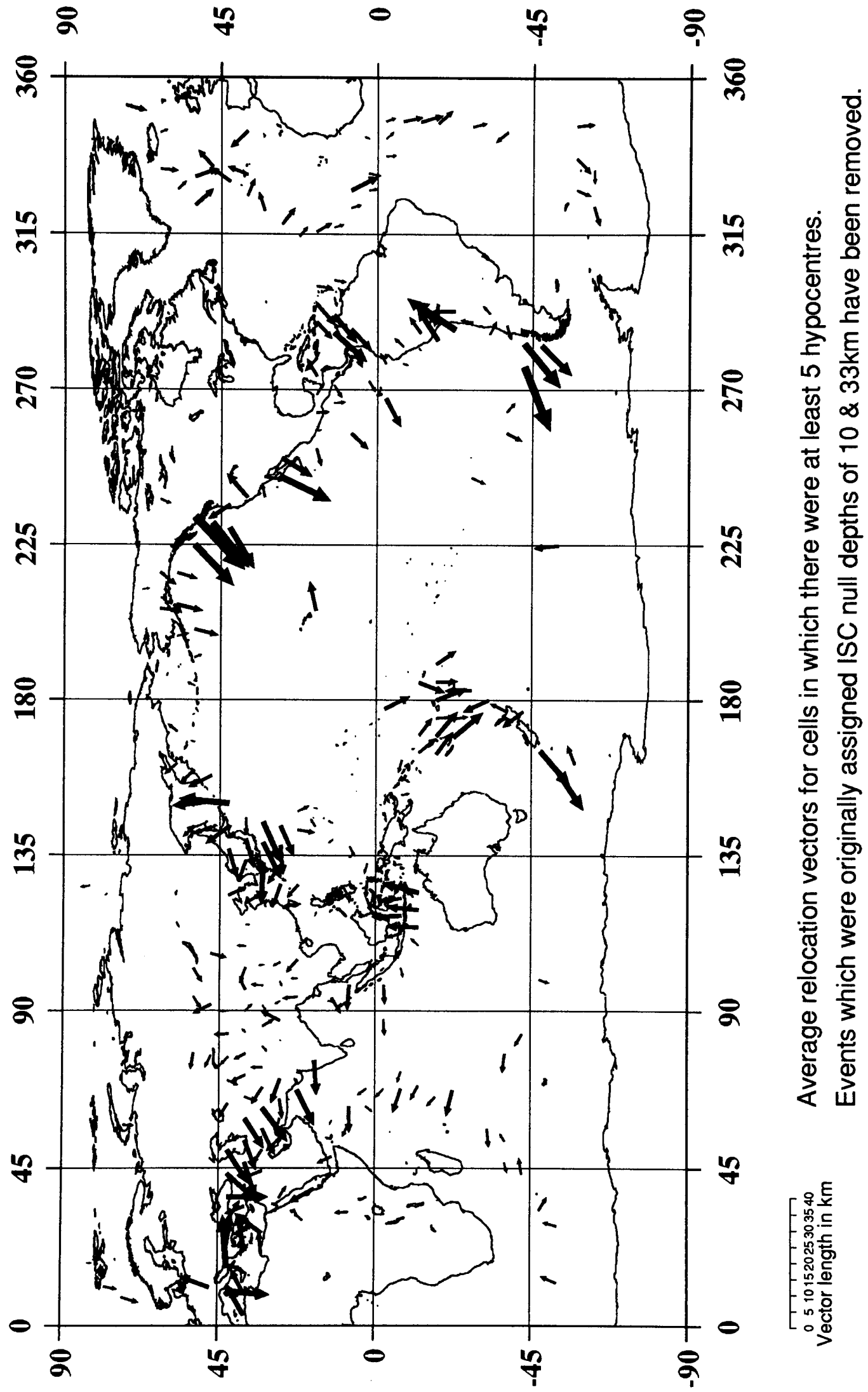


Figure 5.3: Average relocation vectors for events at the end of the zeroth iteration

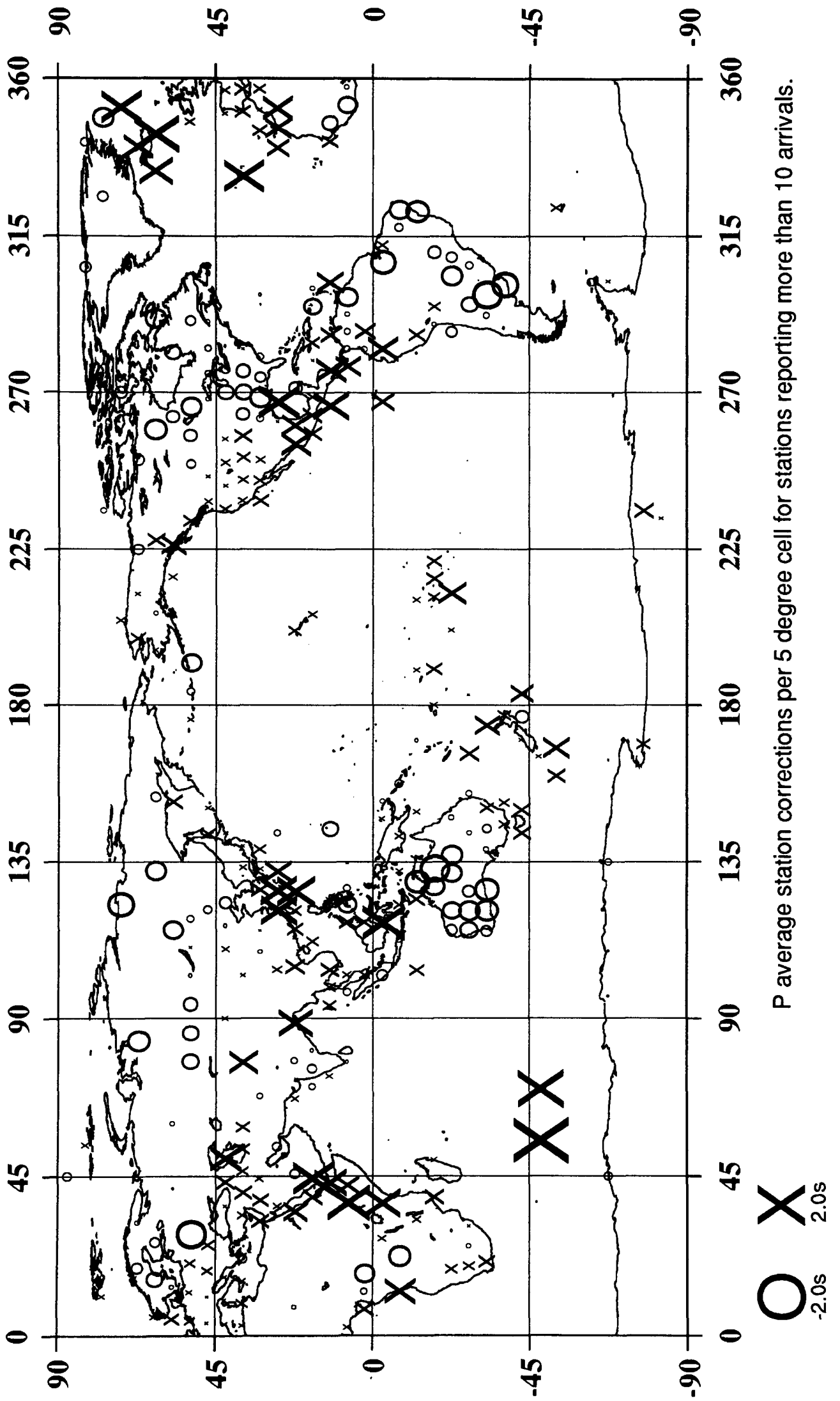


Figure 5.4: Average P station corrections at the end of the zeroth iteration

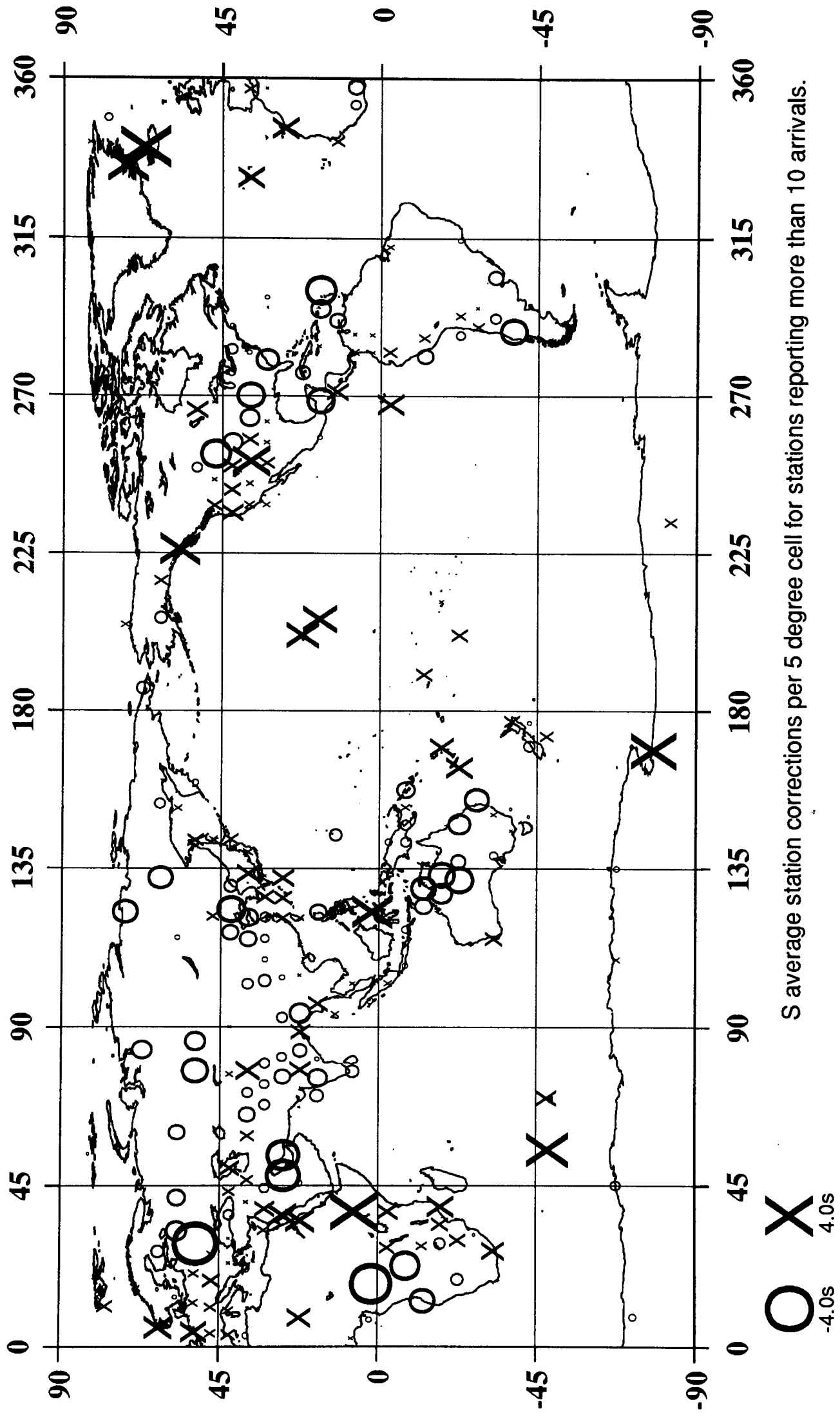


Figure 5.5: Average S station corrections at the end of the zeroth iteration

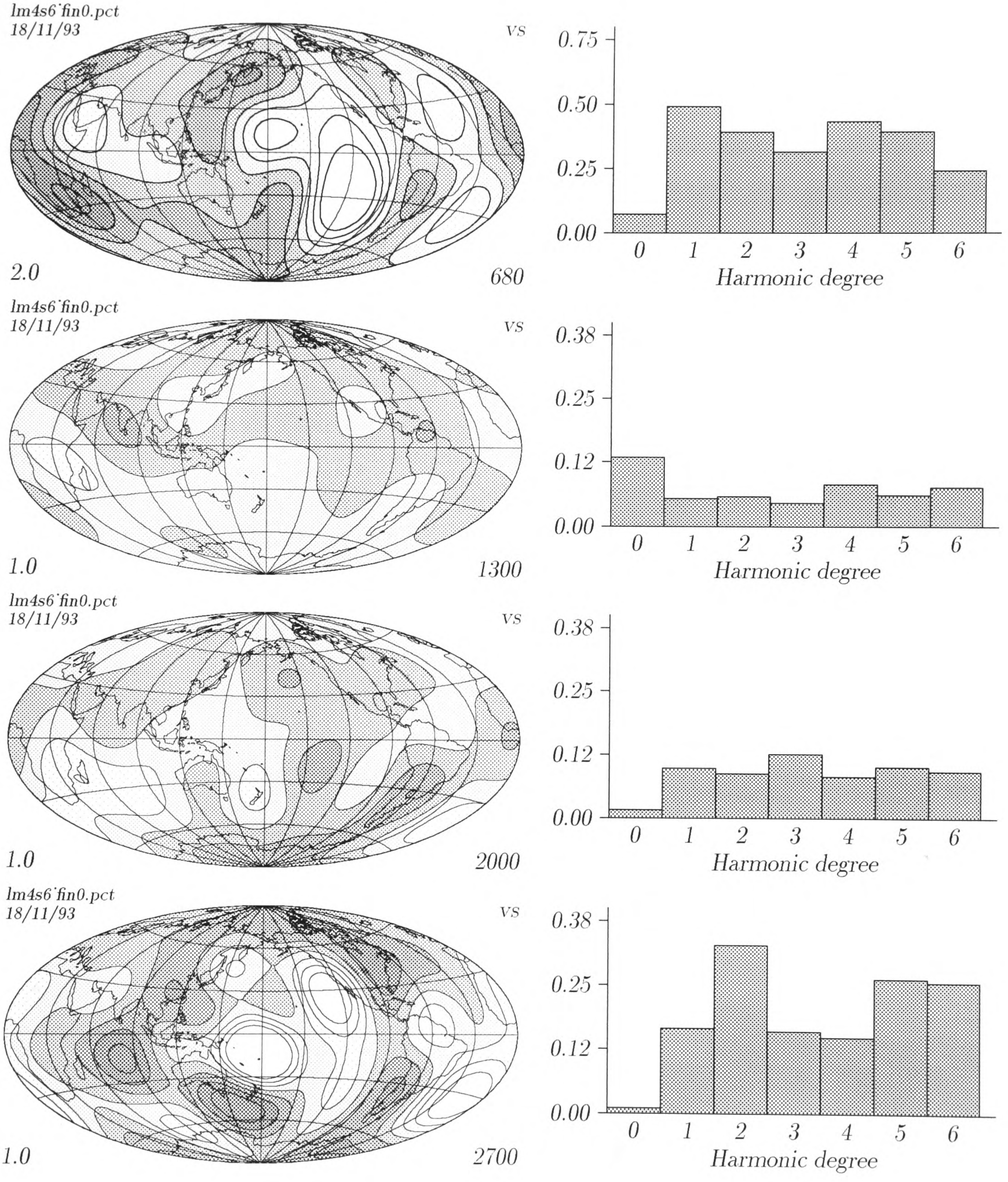


Figure 5.6: Zeroth iteration S model constructed from the complete eigenvalue spectrum. See text for figure description.

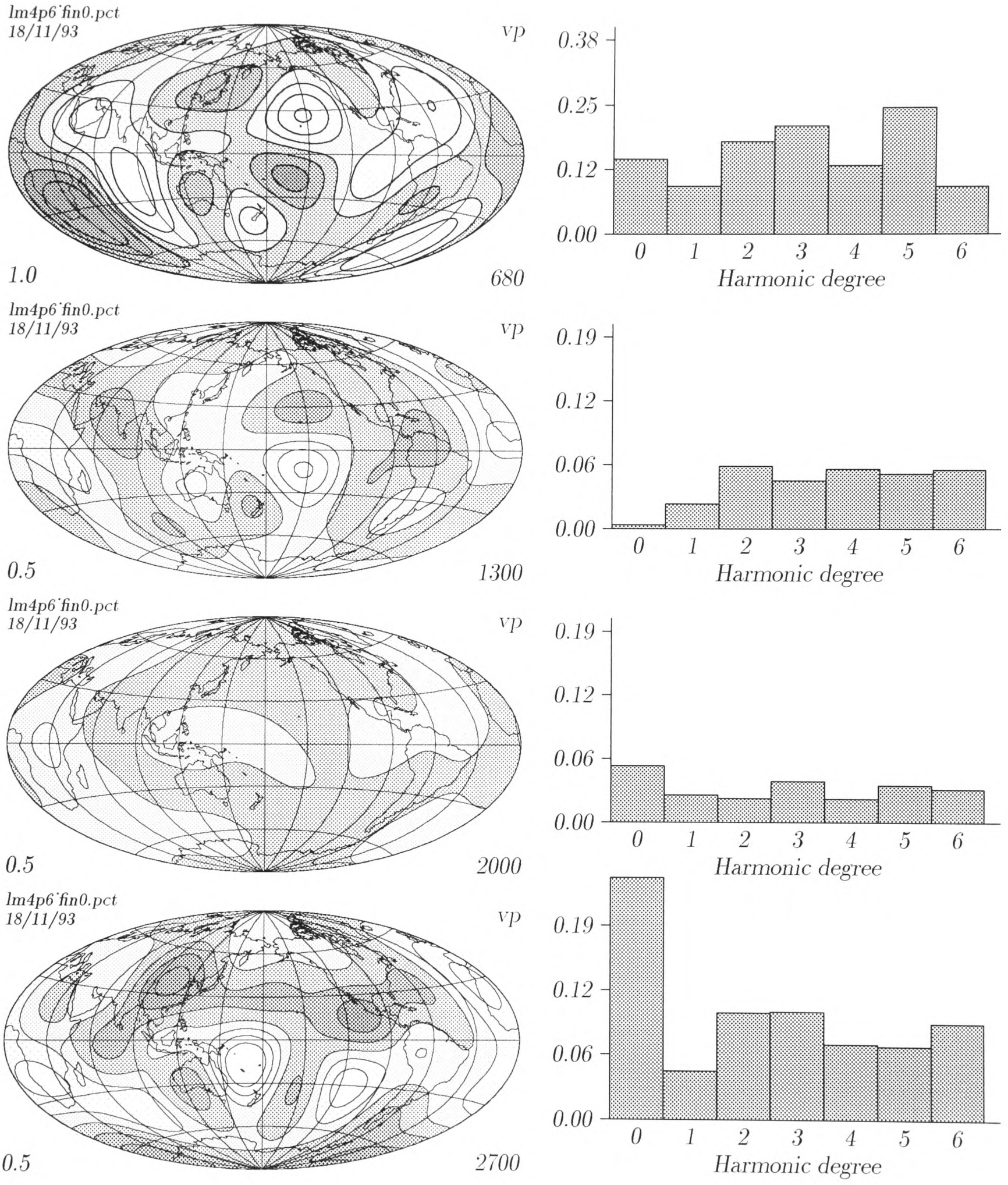


Figure 5.7: Zeroth iteration P model constructed from the complete eigenvalue spectrum. See text for figure description.

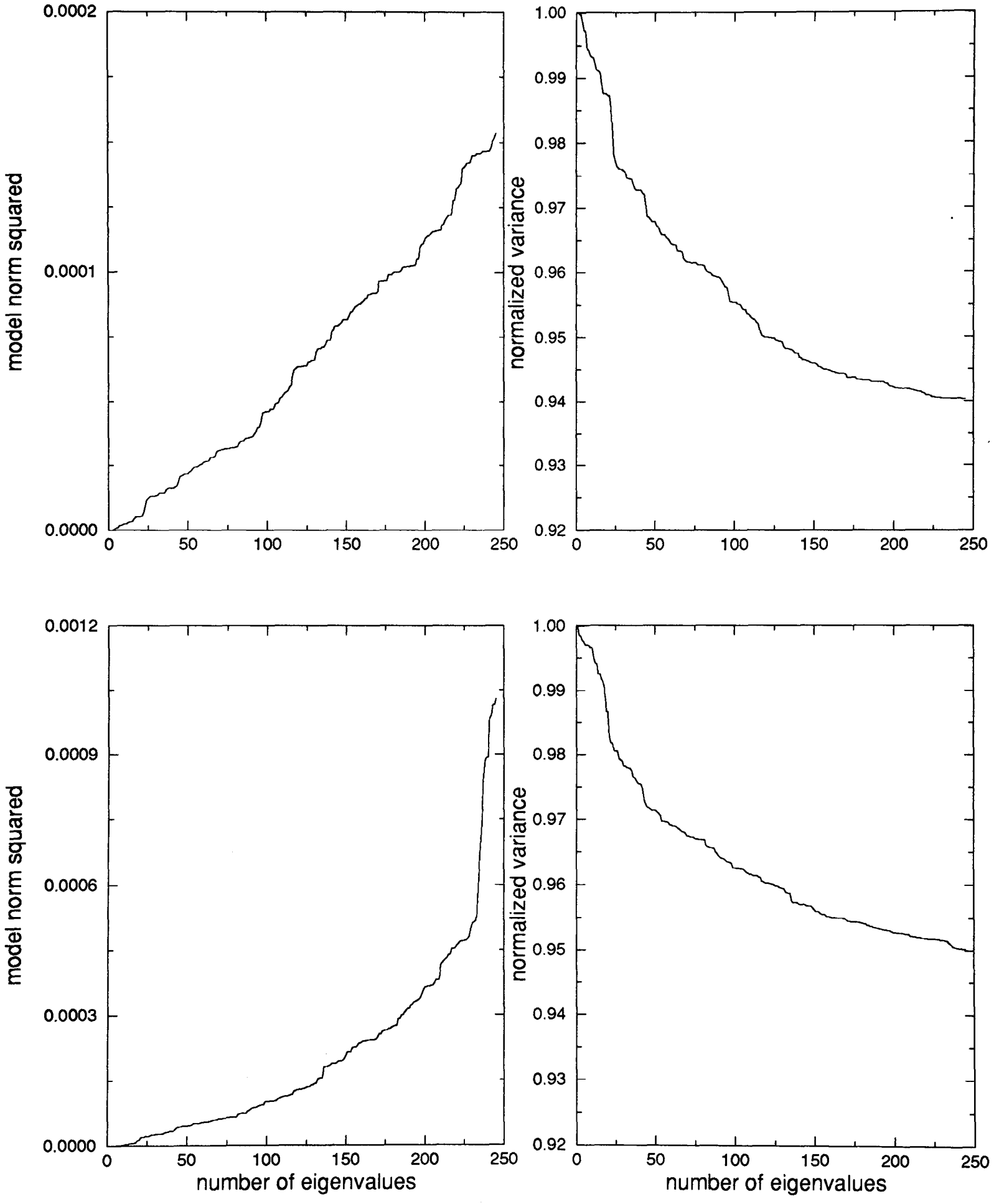


Figure 5.8: Eigenvalue analysis for zeroth iteration models. P top, S bottom.

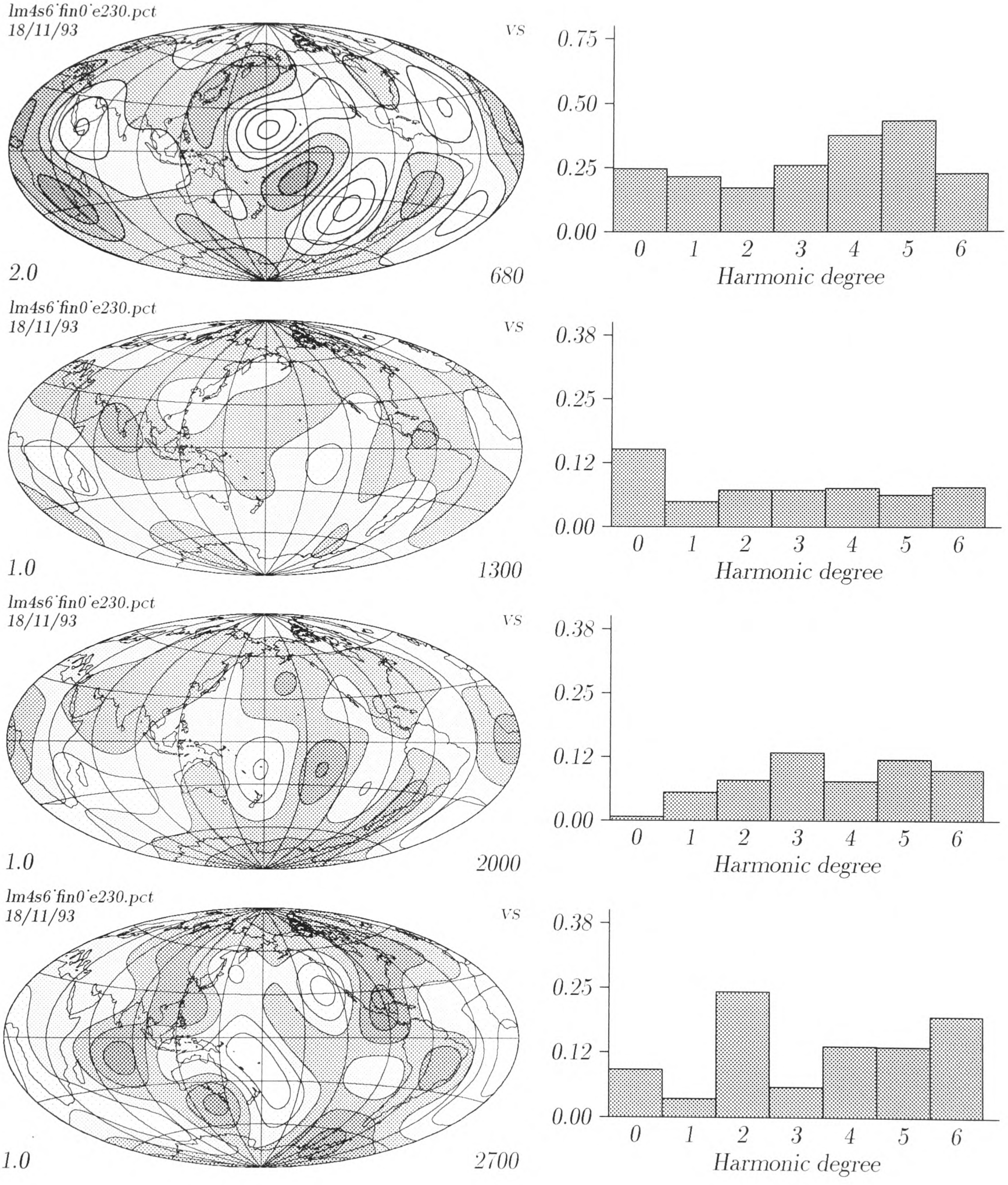


Figure 5.9: Zeroth iteration damped shear wave model constructed using 230 out of 245 eigenvalues and eigenvectors.

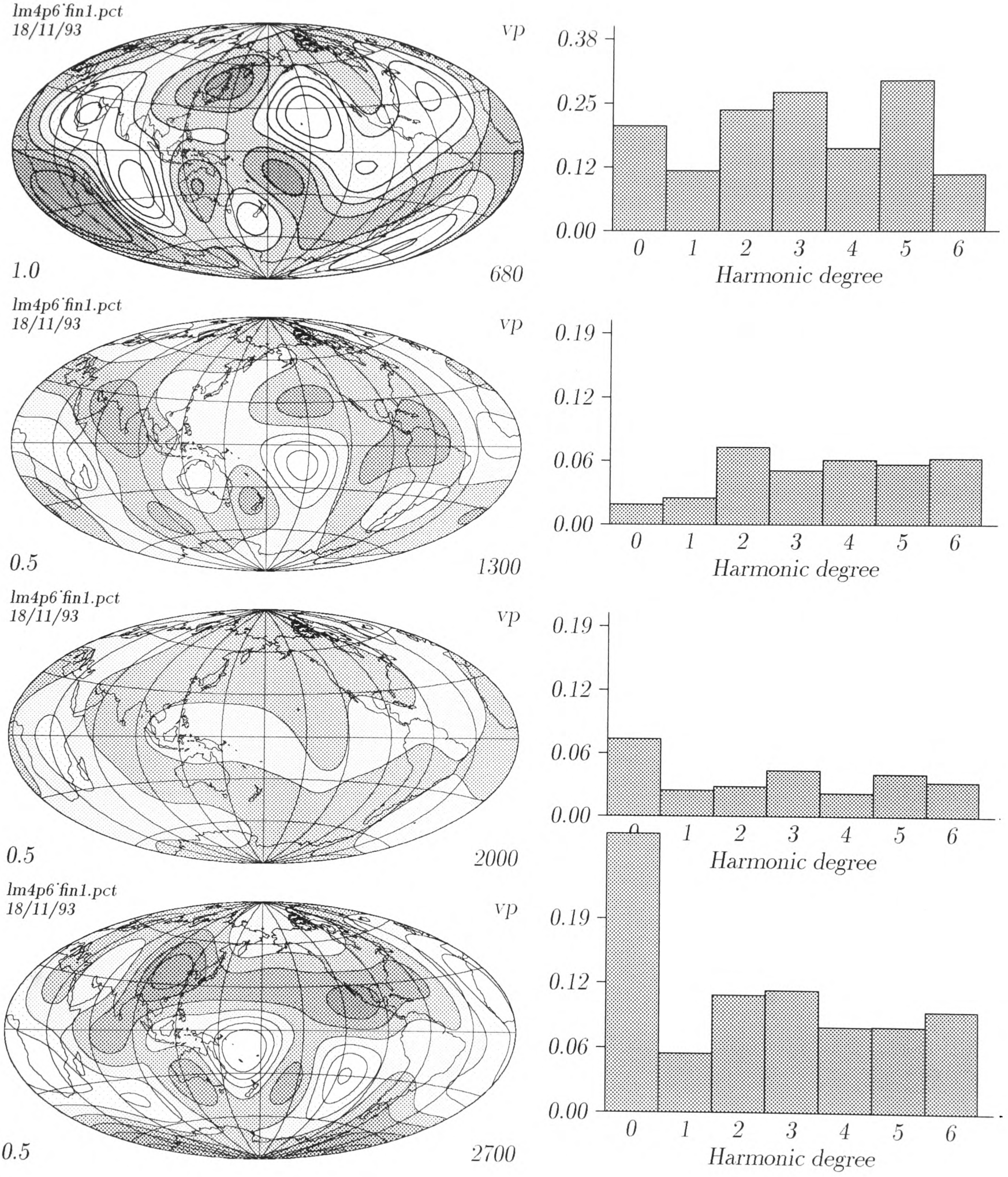


Figure 5.10: First iteration P model.

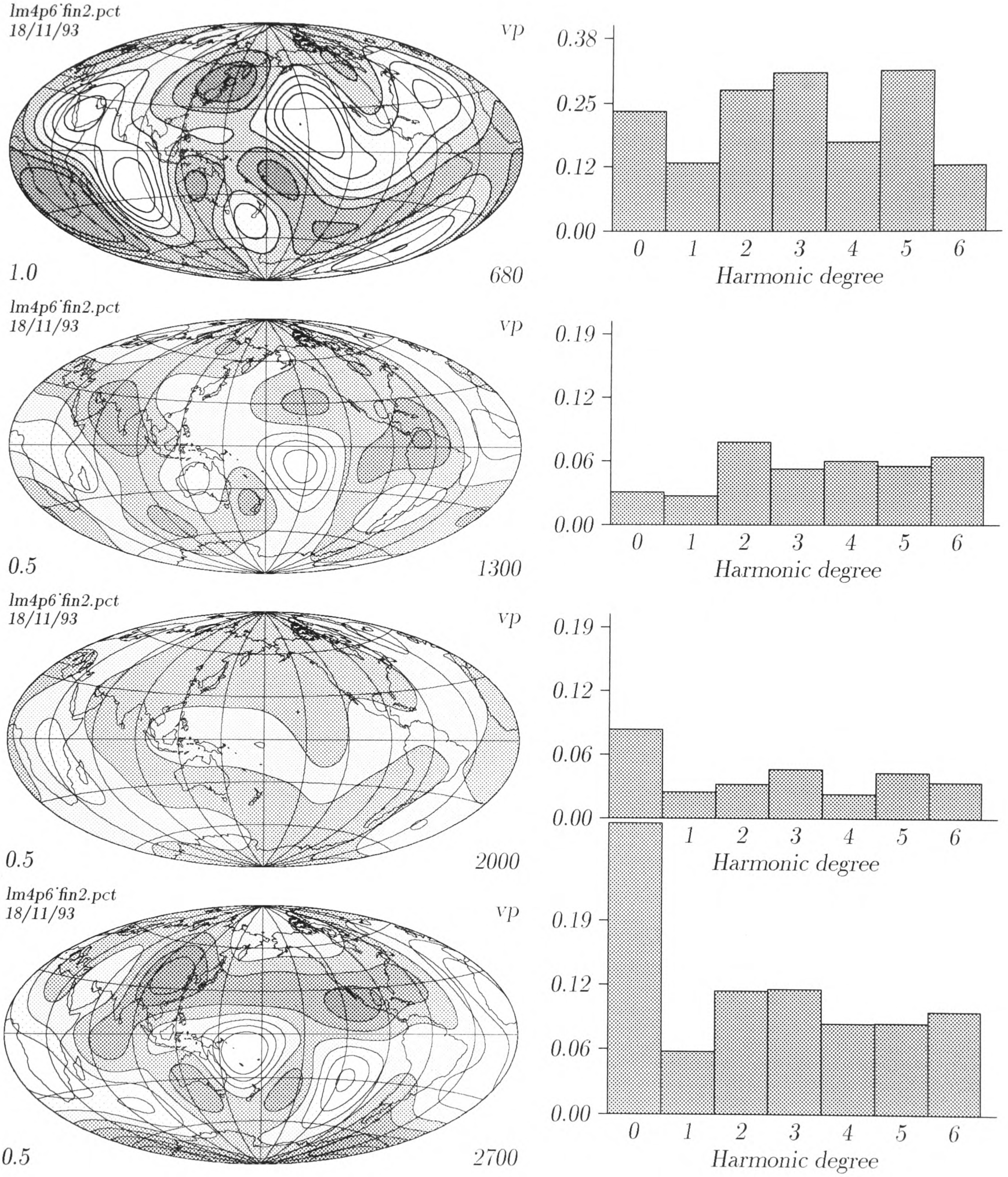


Figure 5.11: Second iteration P model.

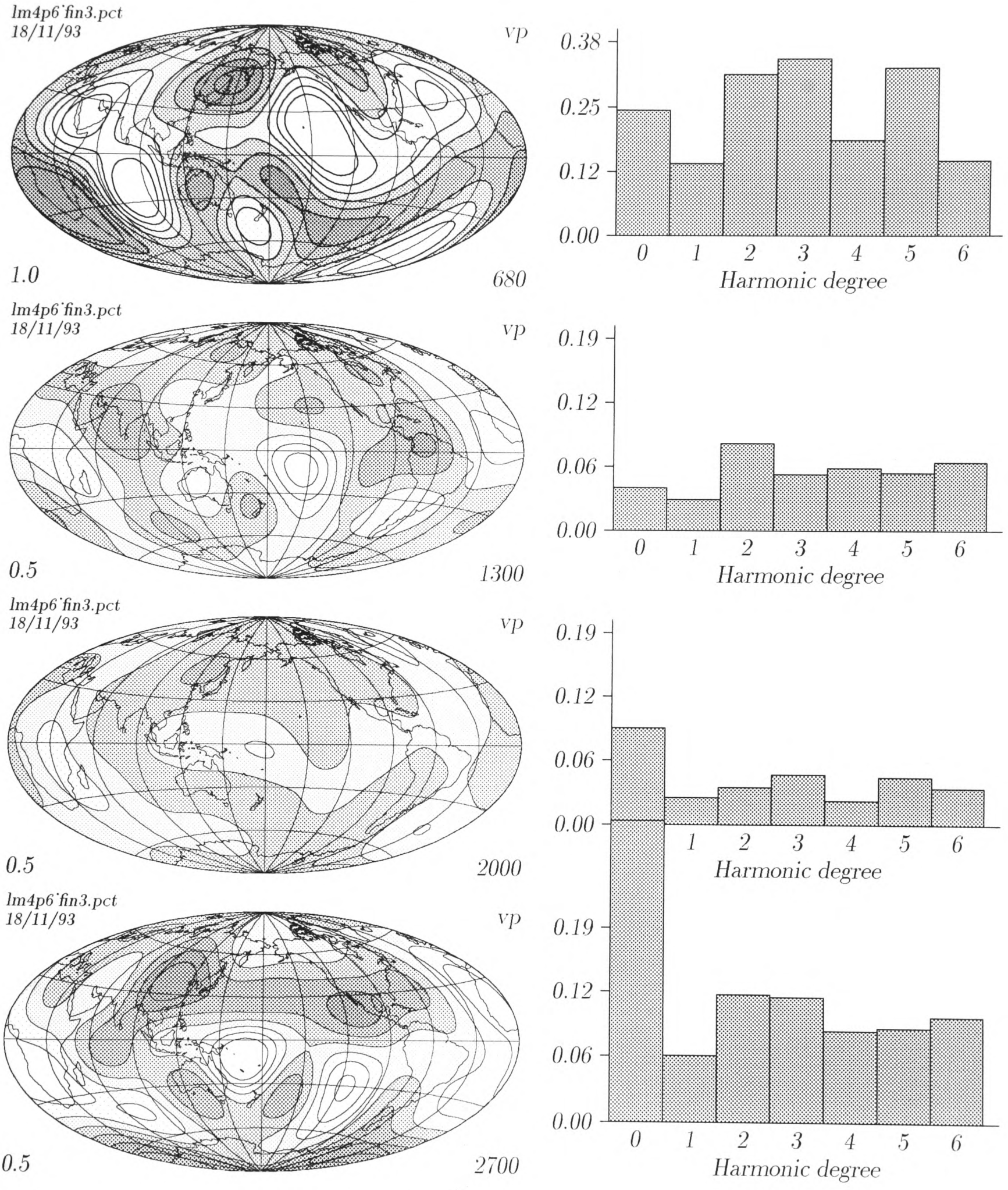


Figure 5.12: Third iteration P model.

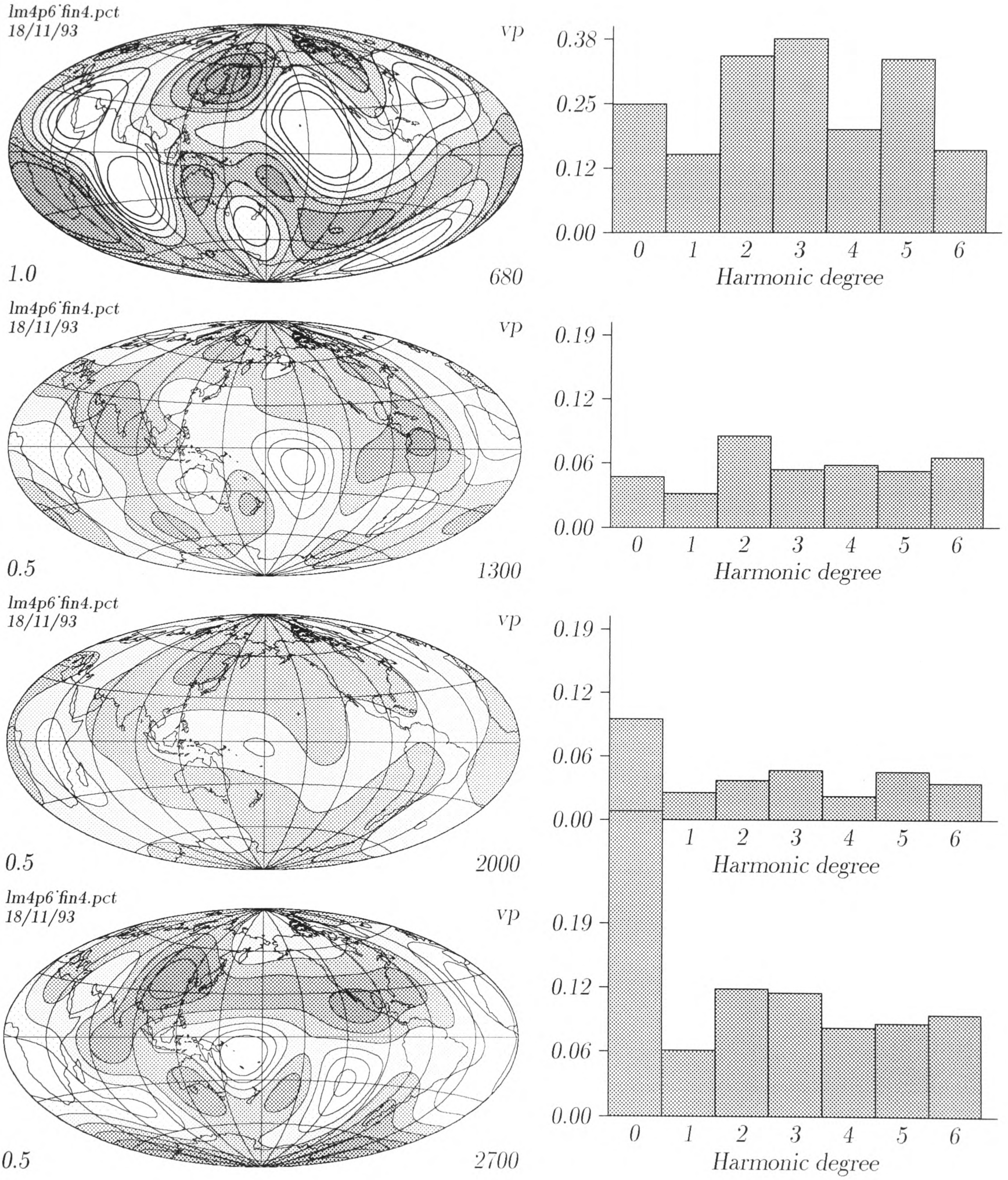


Figure 5.13: Final iteration P model.

Figure 5.14: First iteration S model using only 230 eigenvalues and eigenvectors.

Figure 5.15: Second iteration S model using only 230 eigenvalues and eigenvectors.

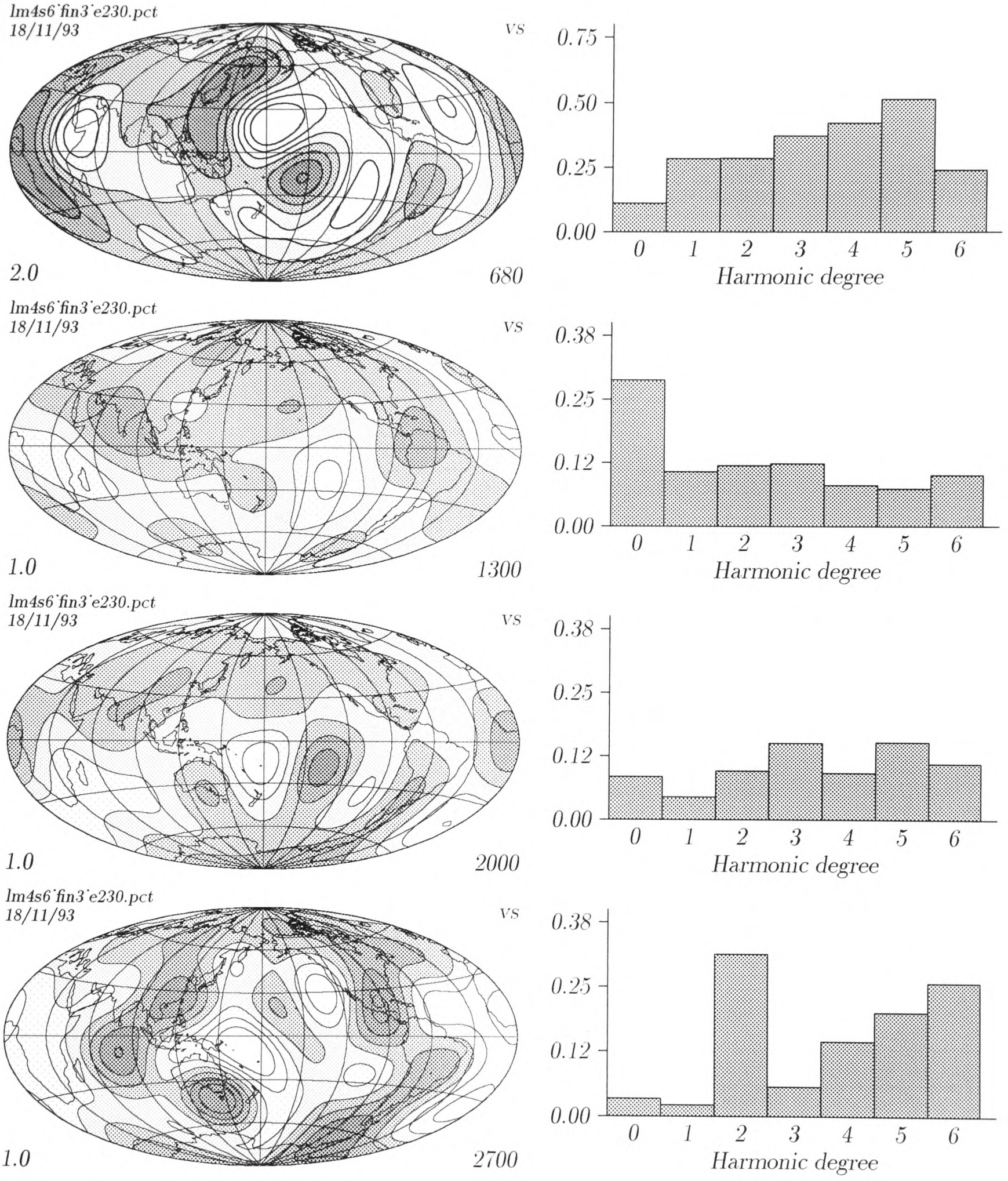


Figure 5.16: Third iteration S model using only 230 eigenvalues and eigenvectors.

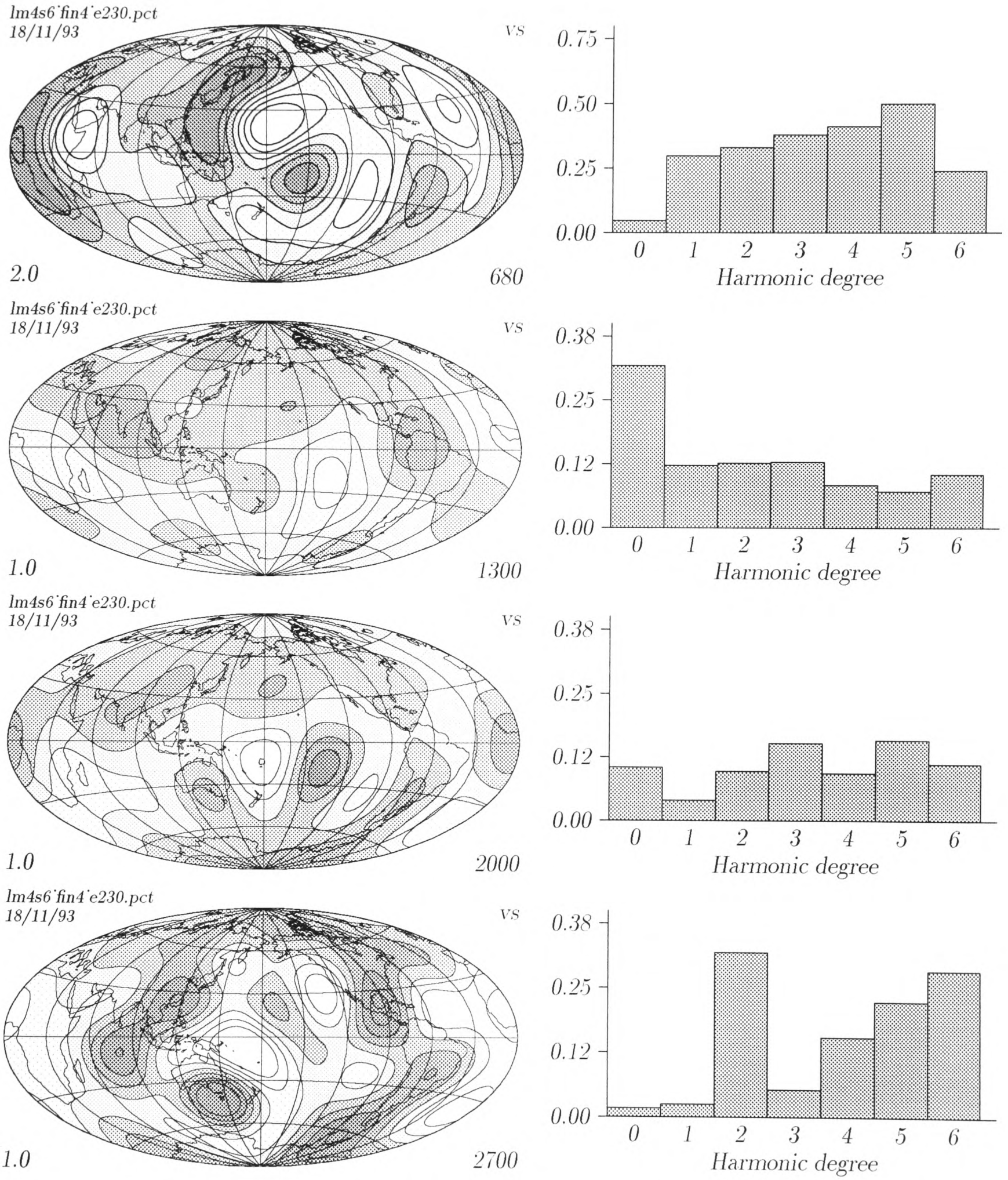


Figure 5.17: Final iteration S model using only 230 eigenvalues and eigenvectors.

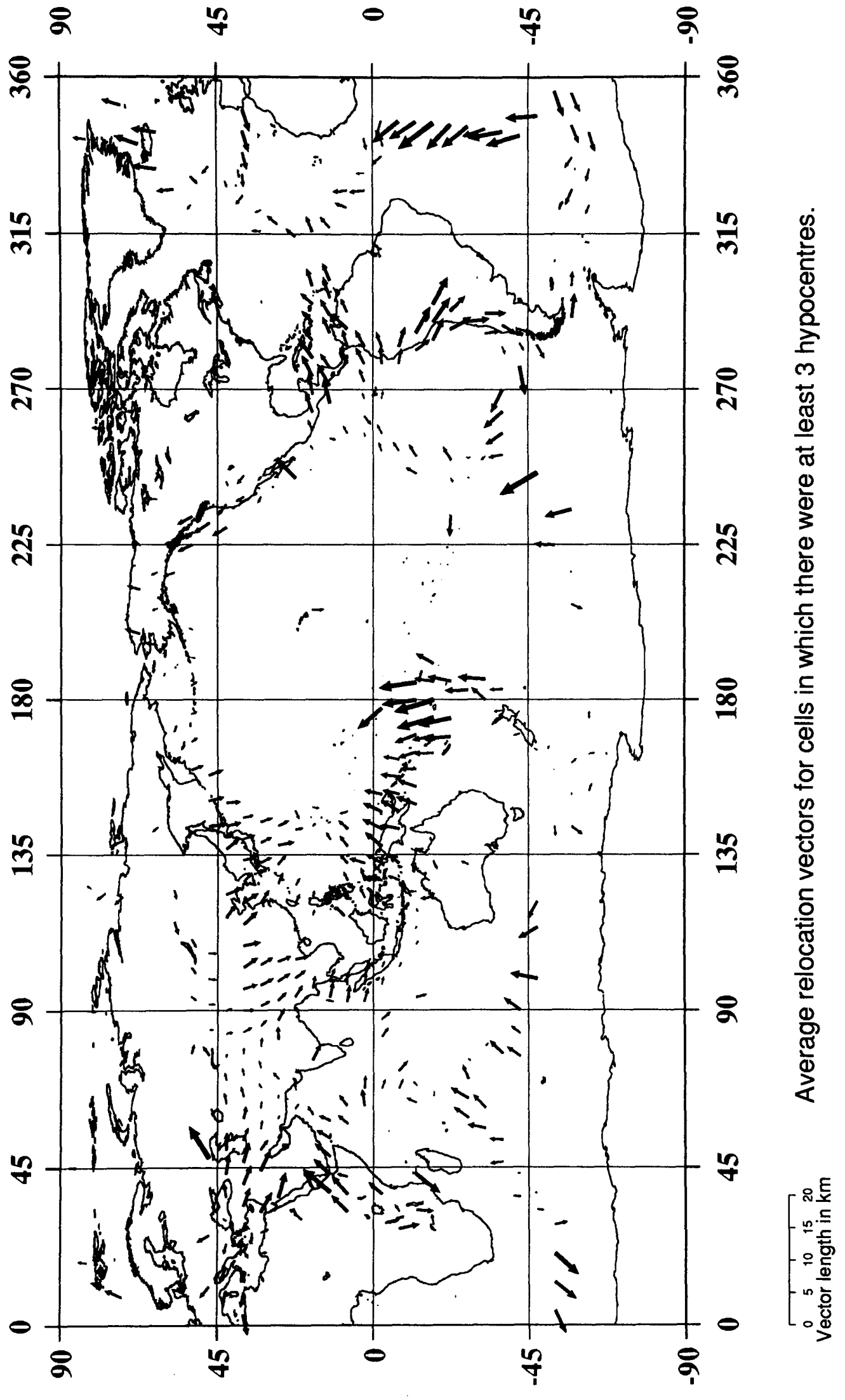


Figure 5.18: Average relocation vectors between the 0^{th} and 1^{st} iterations.

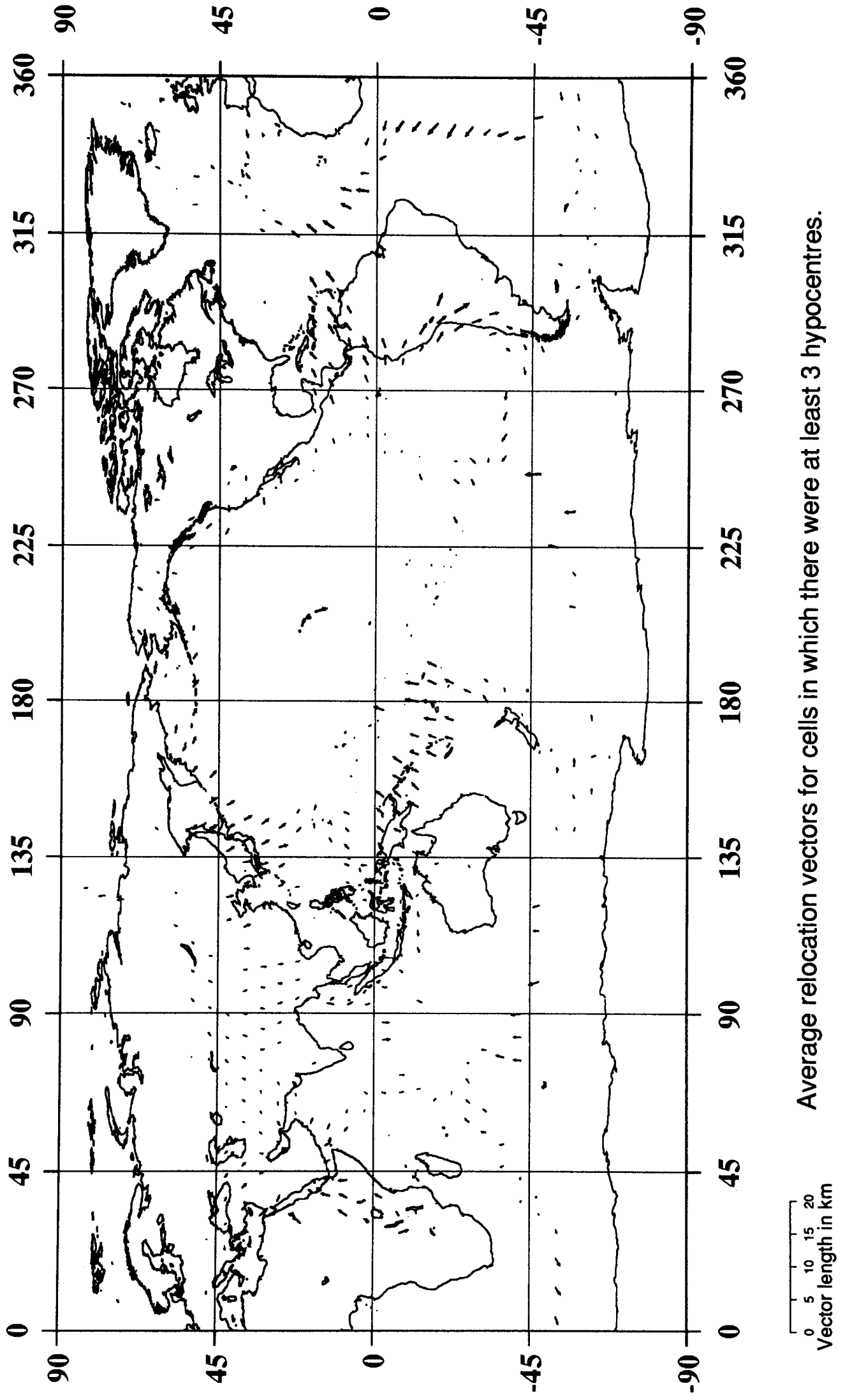


Figure 5.19: Average relocation vectors between the 1^{st} and 2^{nd} iterations.

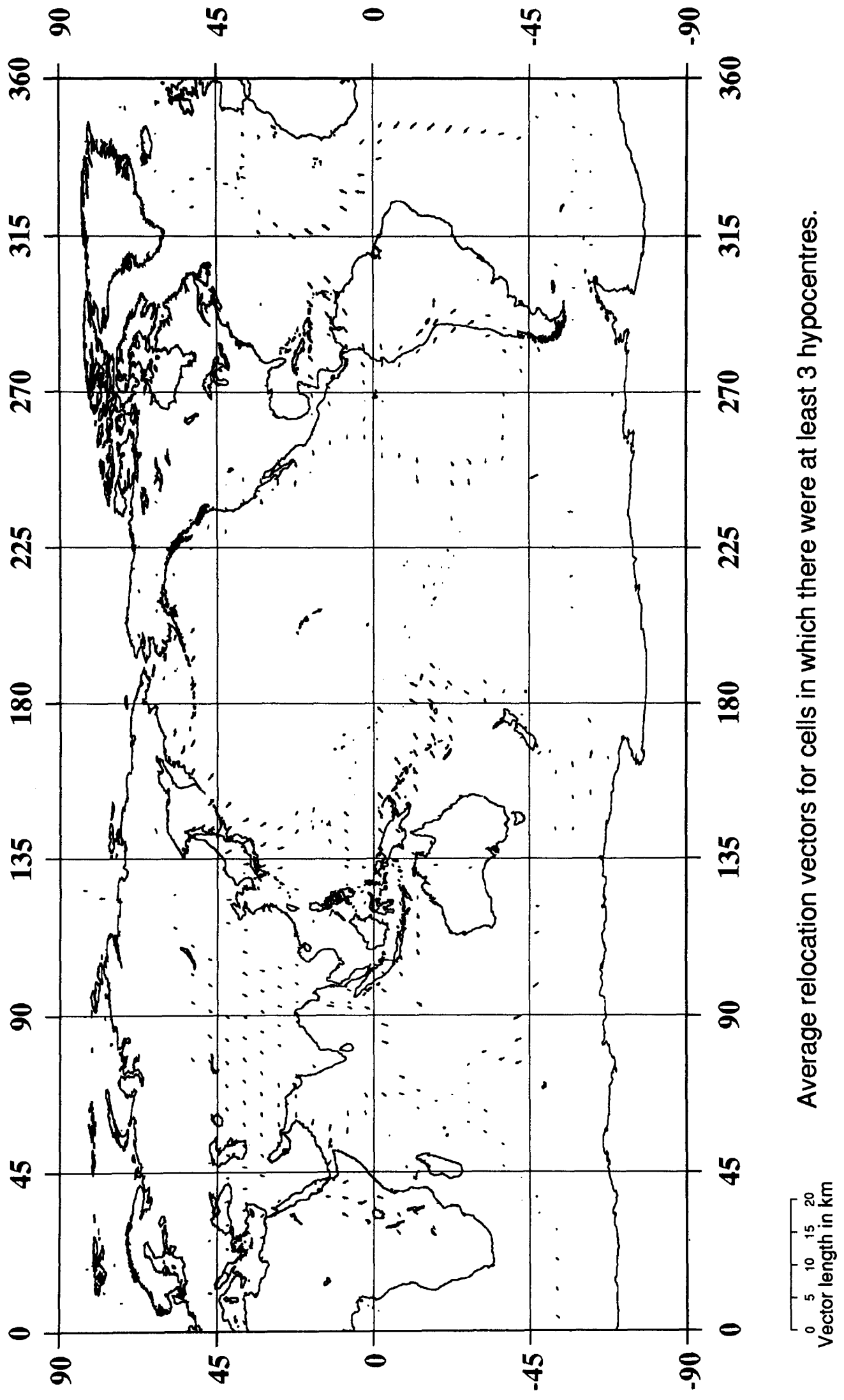


Figure 5.20: Average relocation vectors between the 2^{nd} and 3^{rd} iterations.

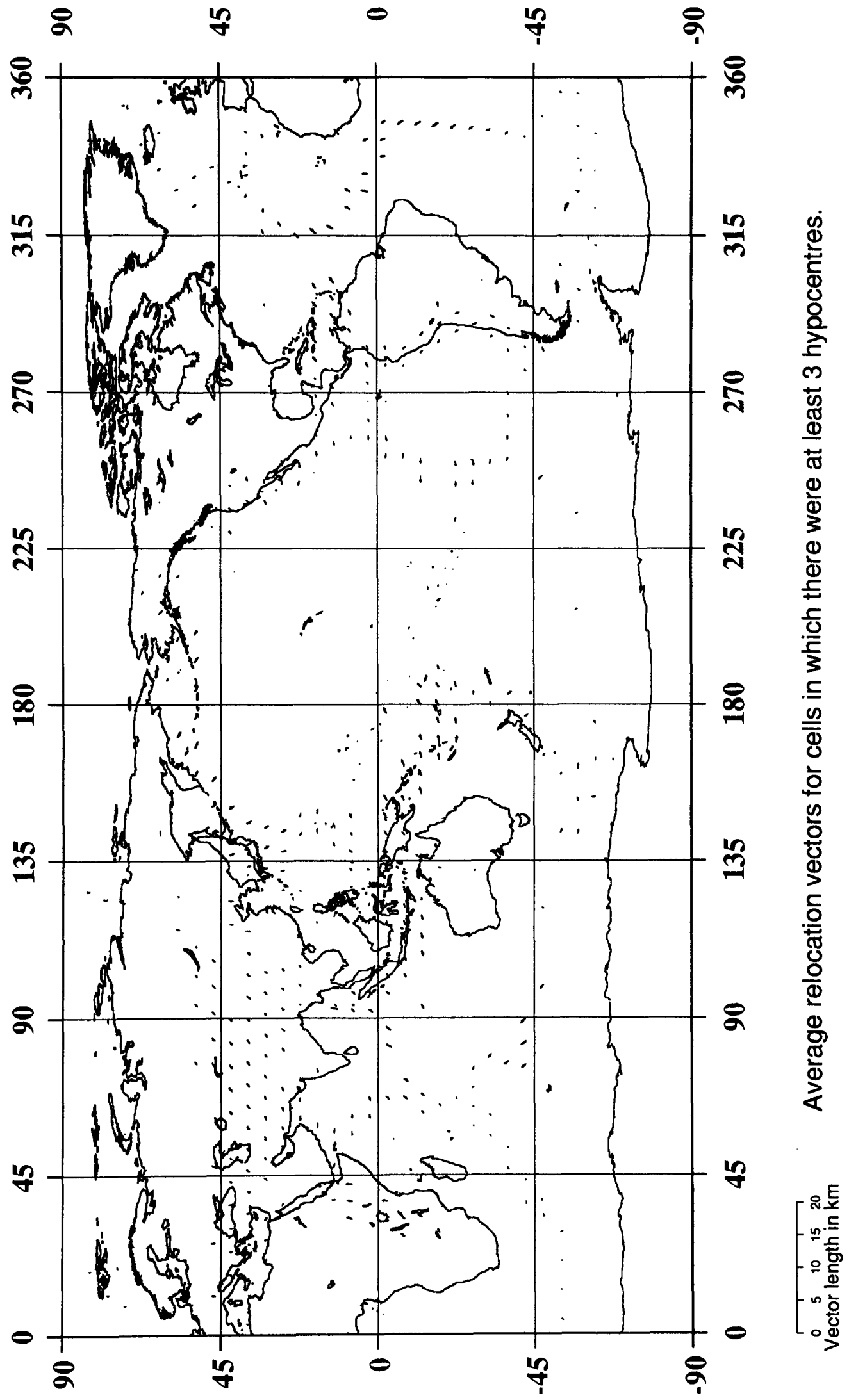


Figure 5.21: Average relocation vectors between the 3^{rd} and 4^{th} iterations.

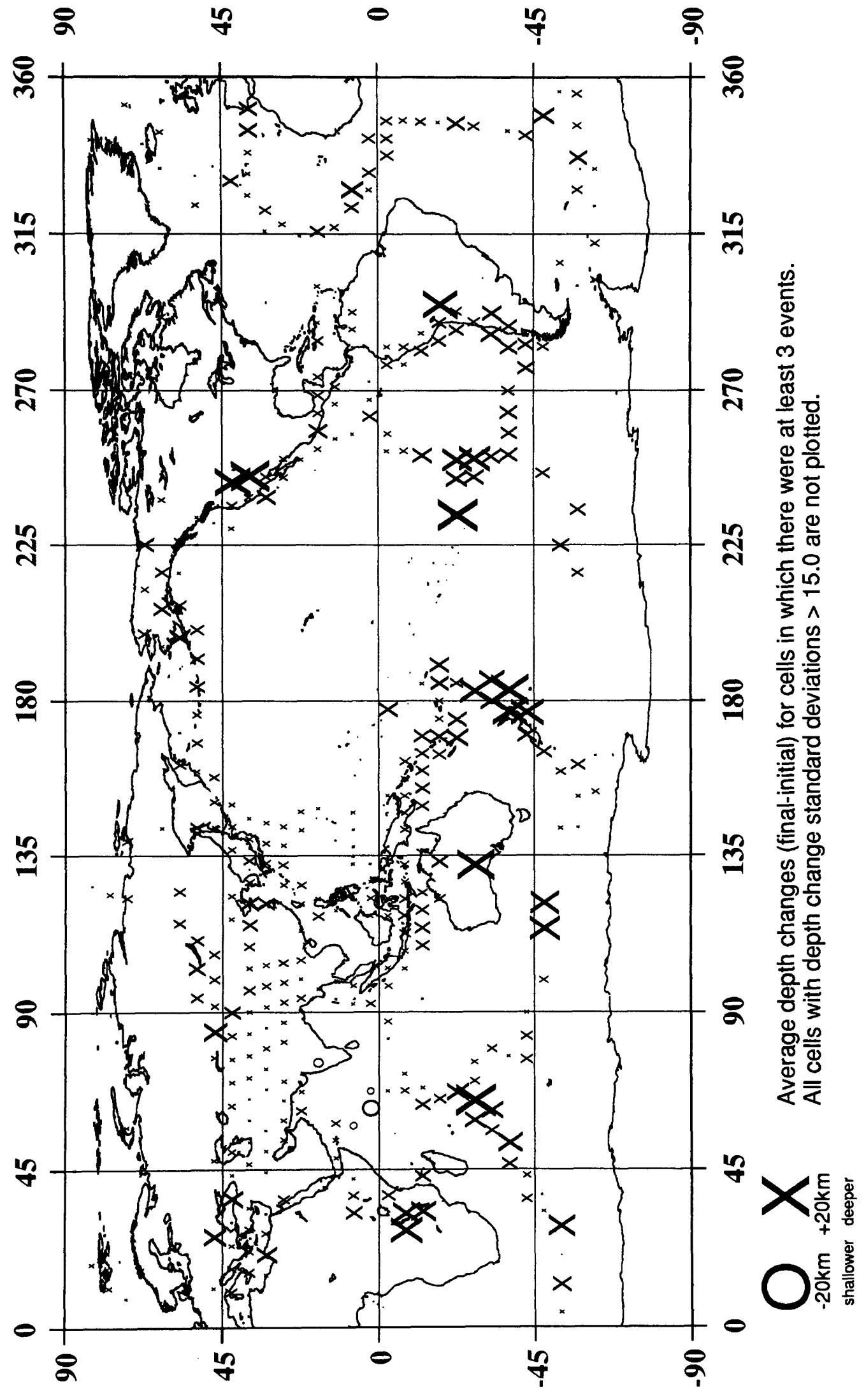


Figure 5.22: Average changes in depths between the 0^{th} and 1^{st} iterations.

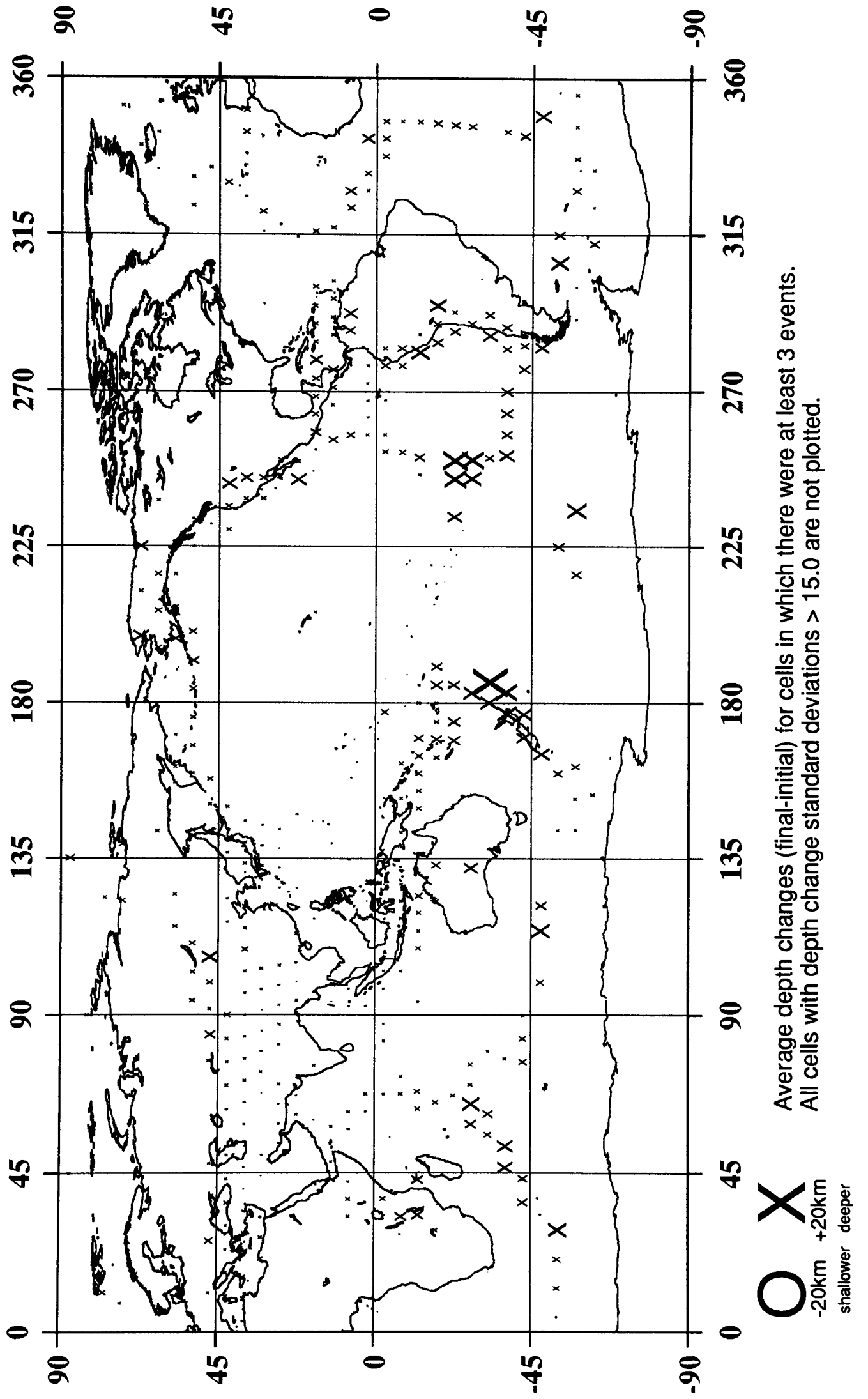


Figure 5.23: Average changes in depths between the 1^{st} and 2^{nd} iterations.

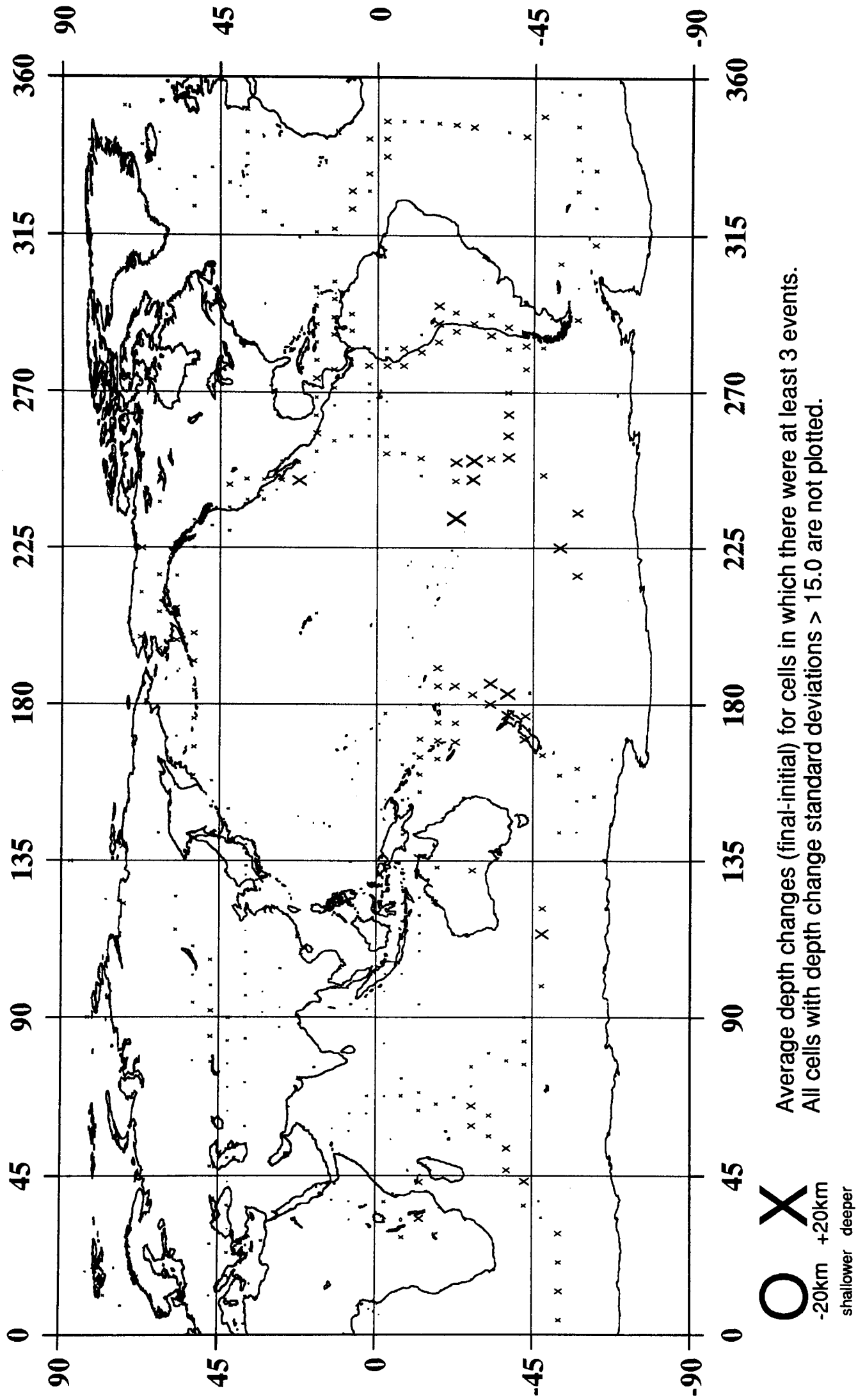


Figure 5.24: Average changes in depths between the 2^{nd} and 3^{rd} iterations.

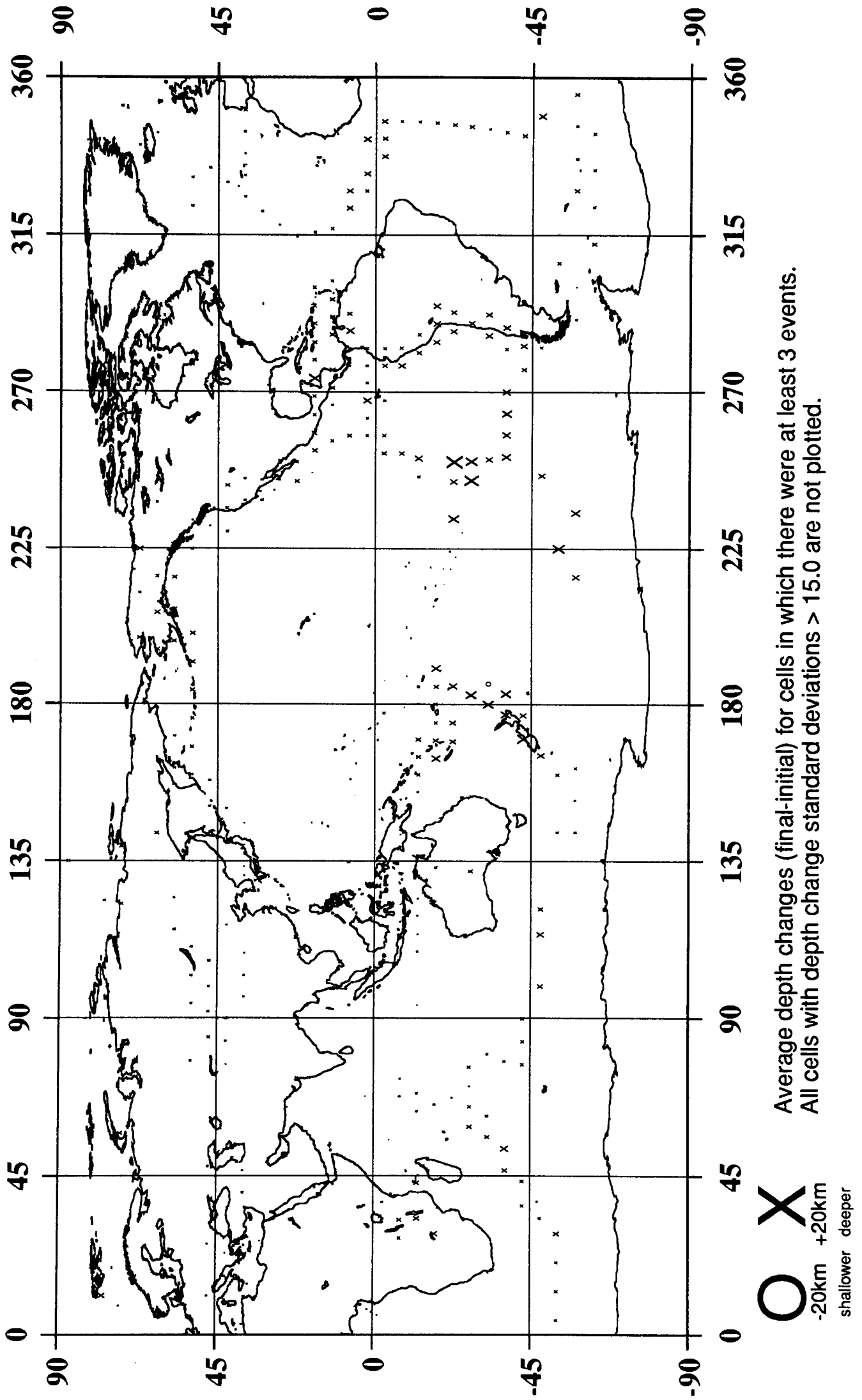


Figure 5.25: Average changes in depths between the 3^{rd} and 4^{th} iterations.

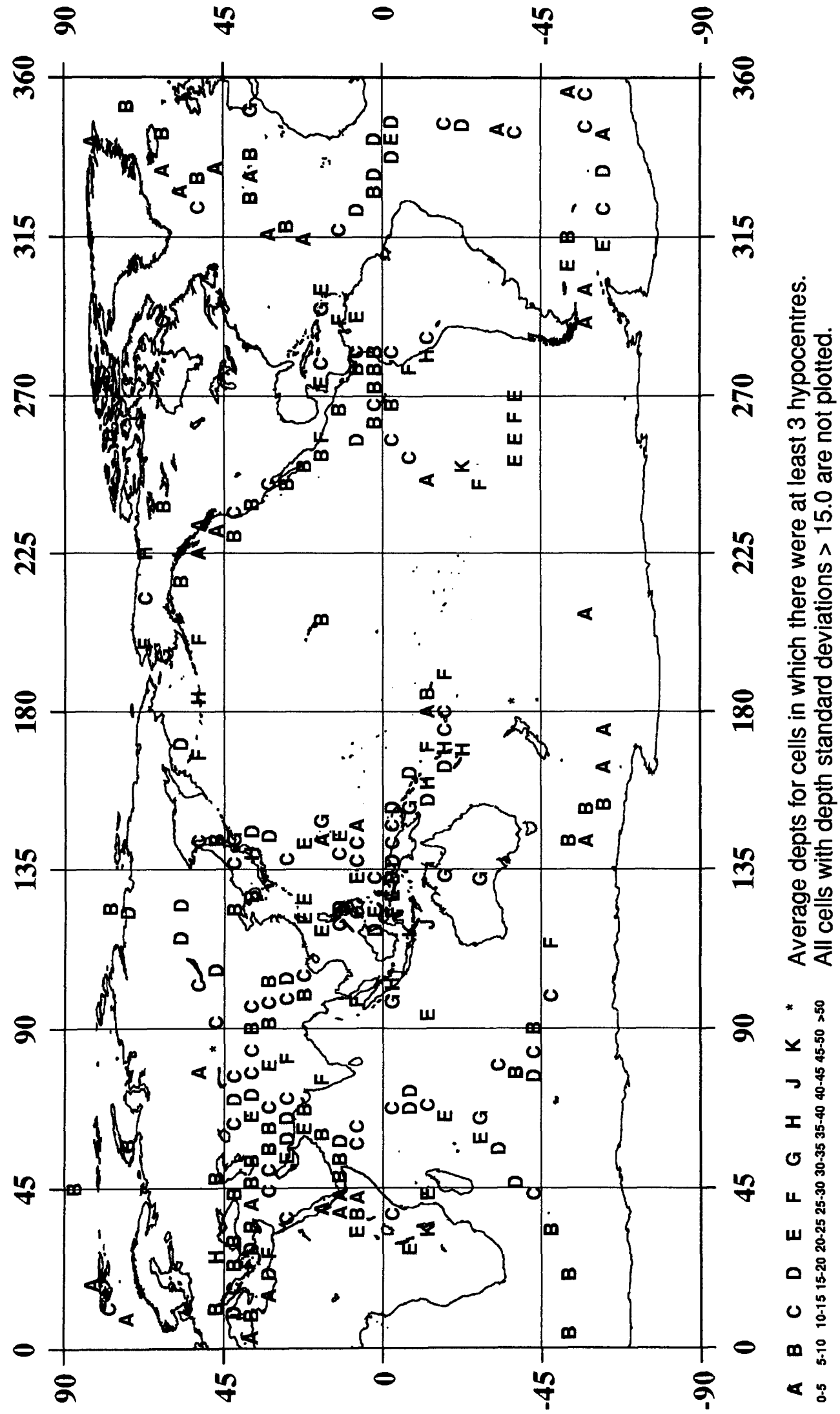


Figure 5.26: Average depths per 5° cell at the end of the 4^{th} iteration.

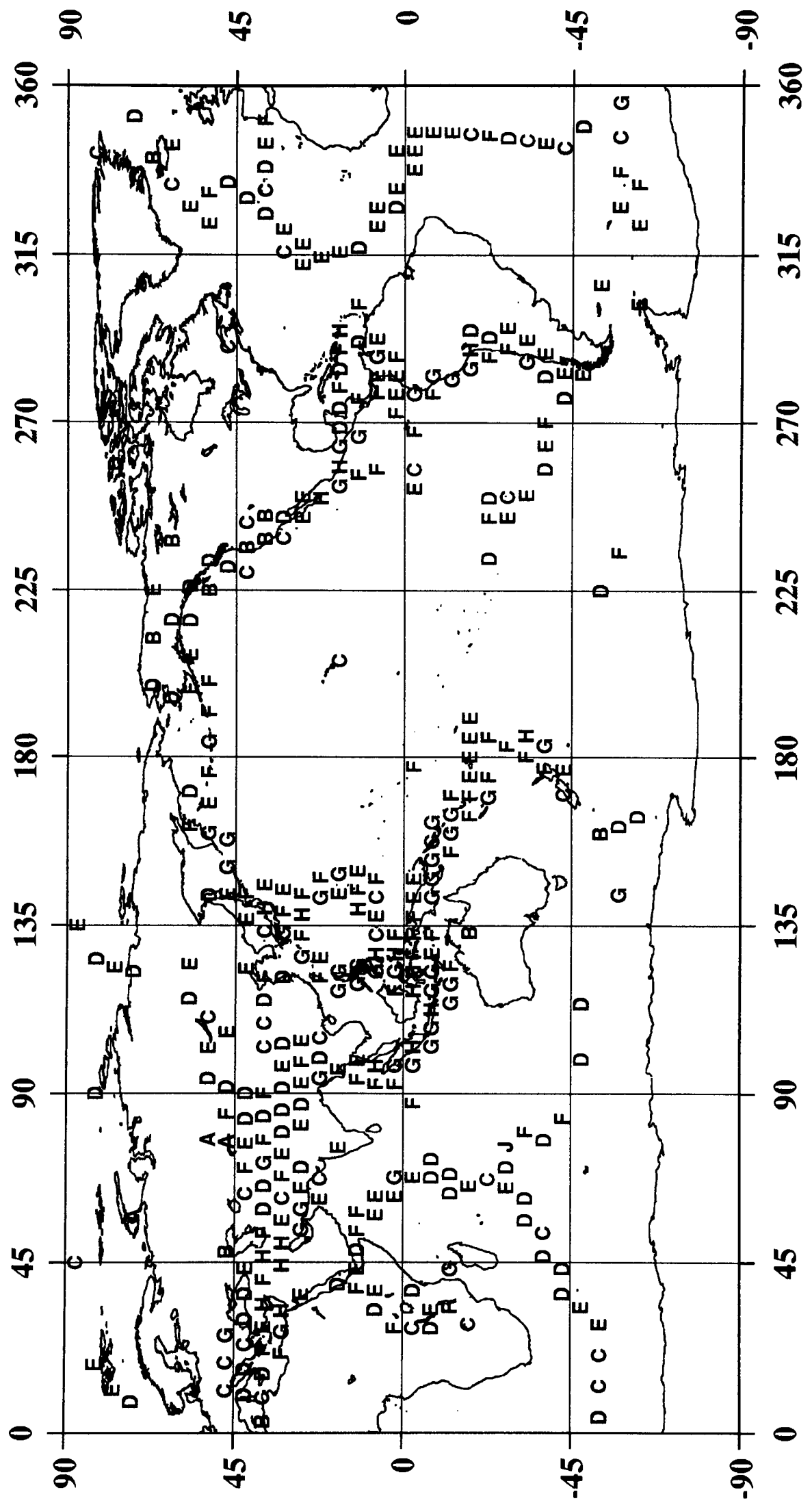
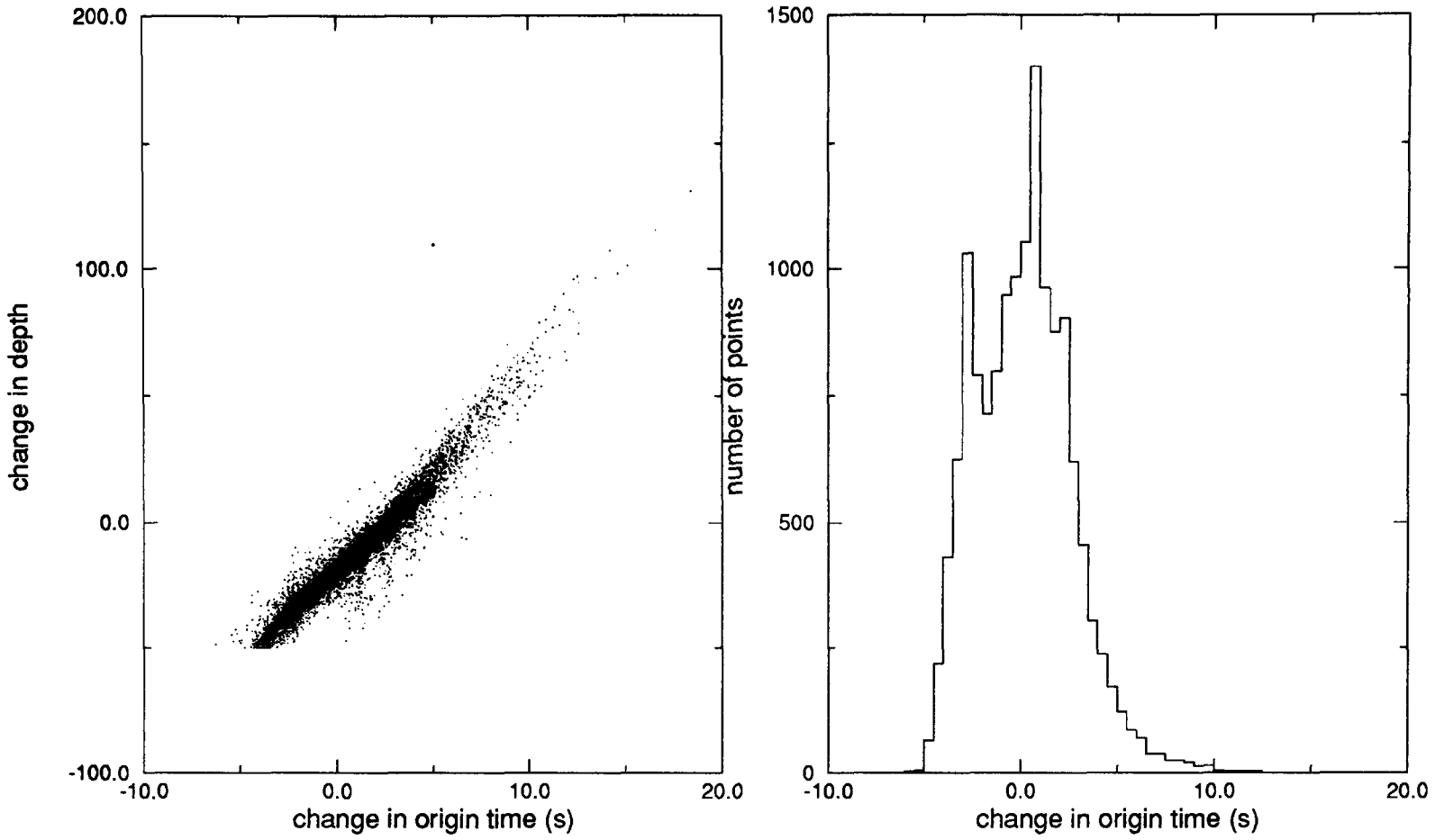


Figure 5.27: ISC average depths per 5° cell.



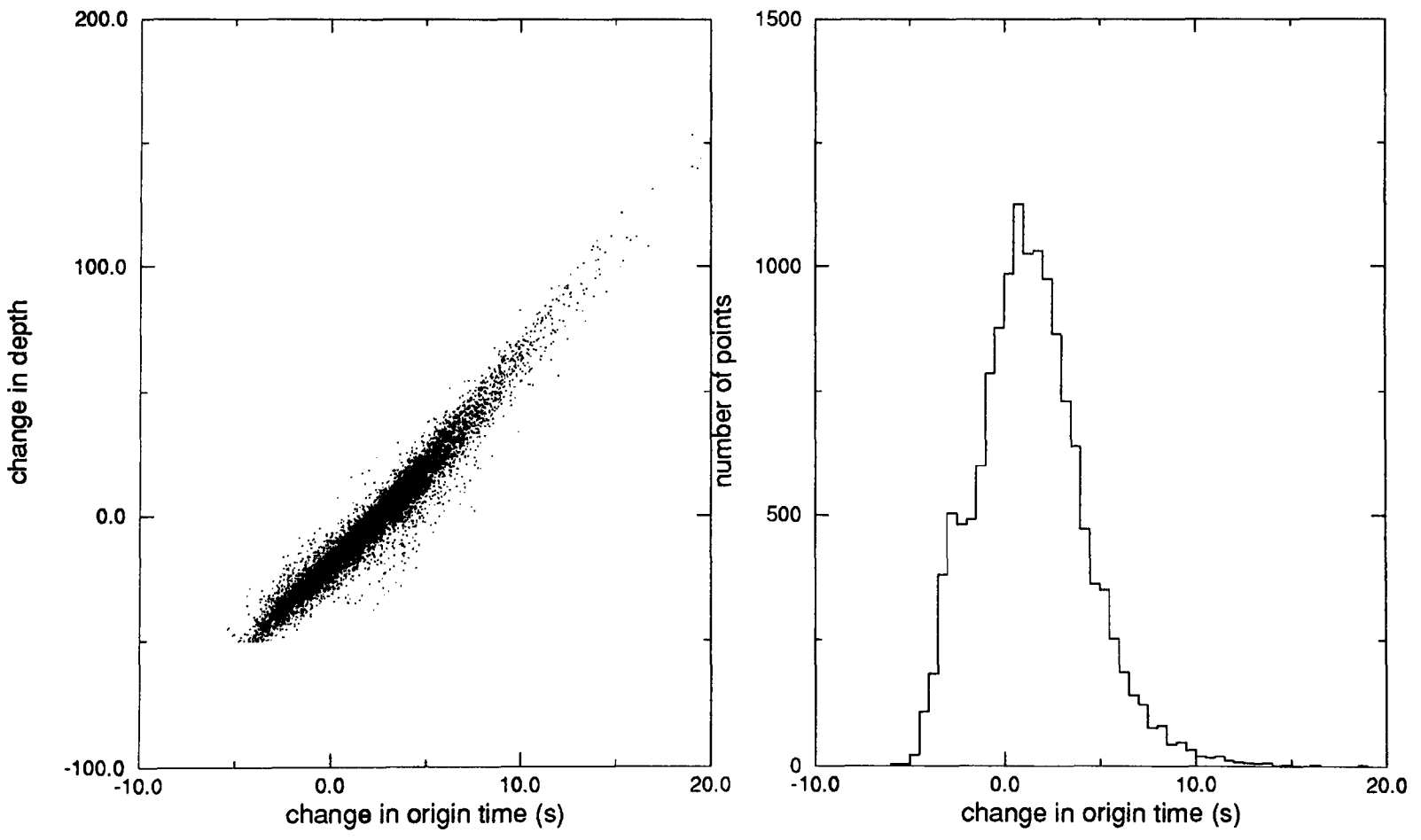


Figure 5.28: Origin time versus change in depth plots for the complete dataset at iterations 0 and 4. The histograms to the right of each plot show the number of events with a given change in origin time.

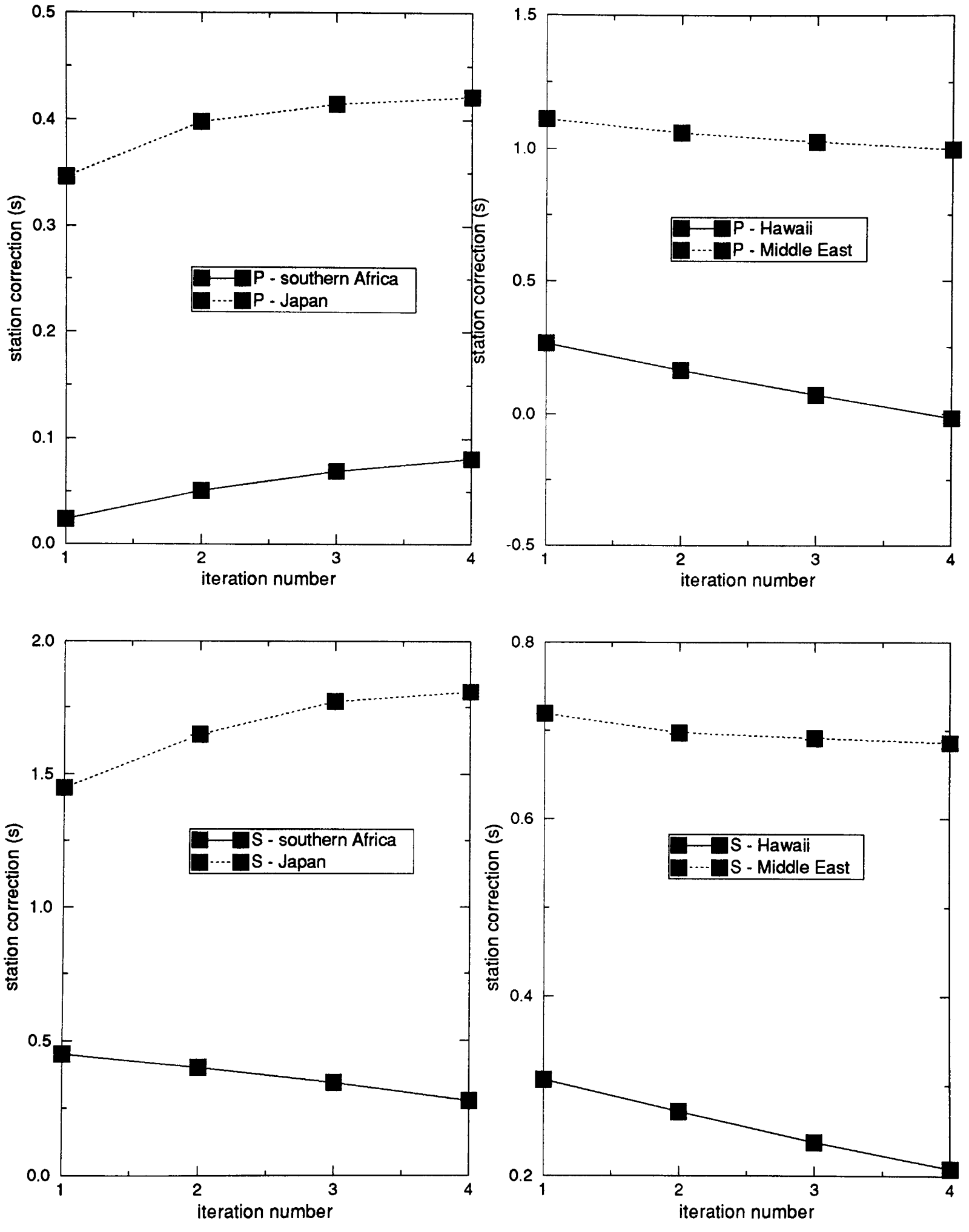


Figure 5.29: Average station corrections for each iteration for the four zones chosen for study.

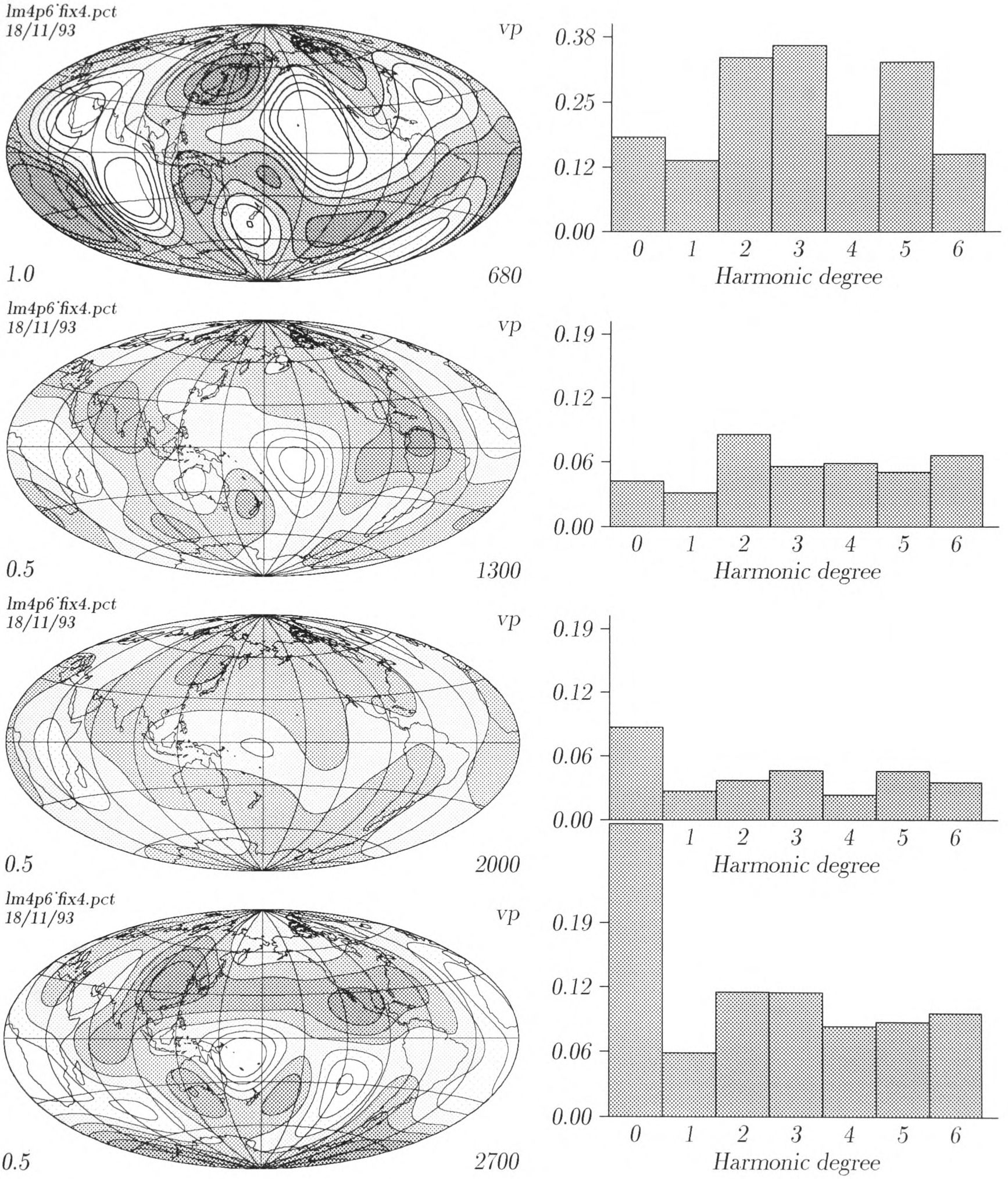


Figure 5.30: Fourth iteration P model from the experiment in which the depths were fixed after the first iteration.

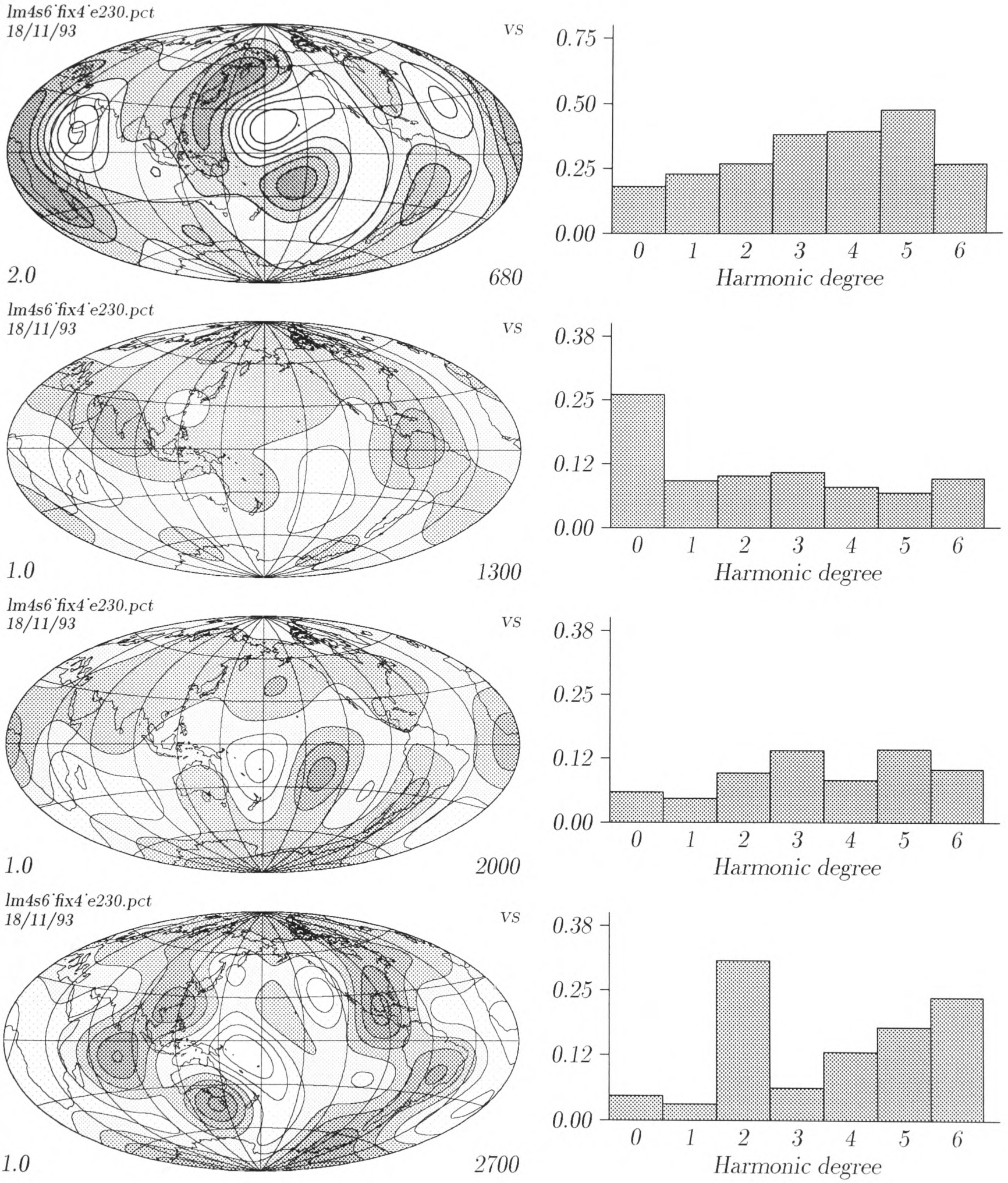


Figure 5.31: Fourth iteration S model using only 230 eigenvectors from the experiment in which the depths were fixed after the first iteration.

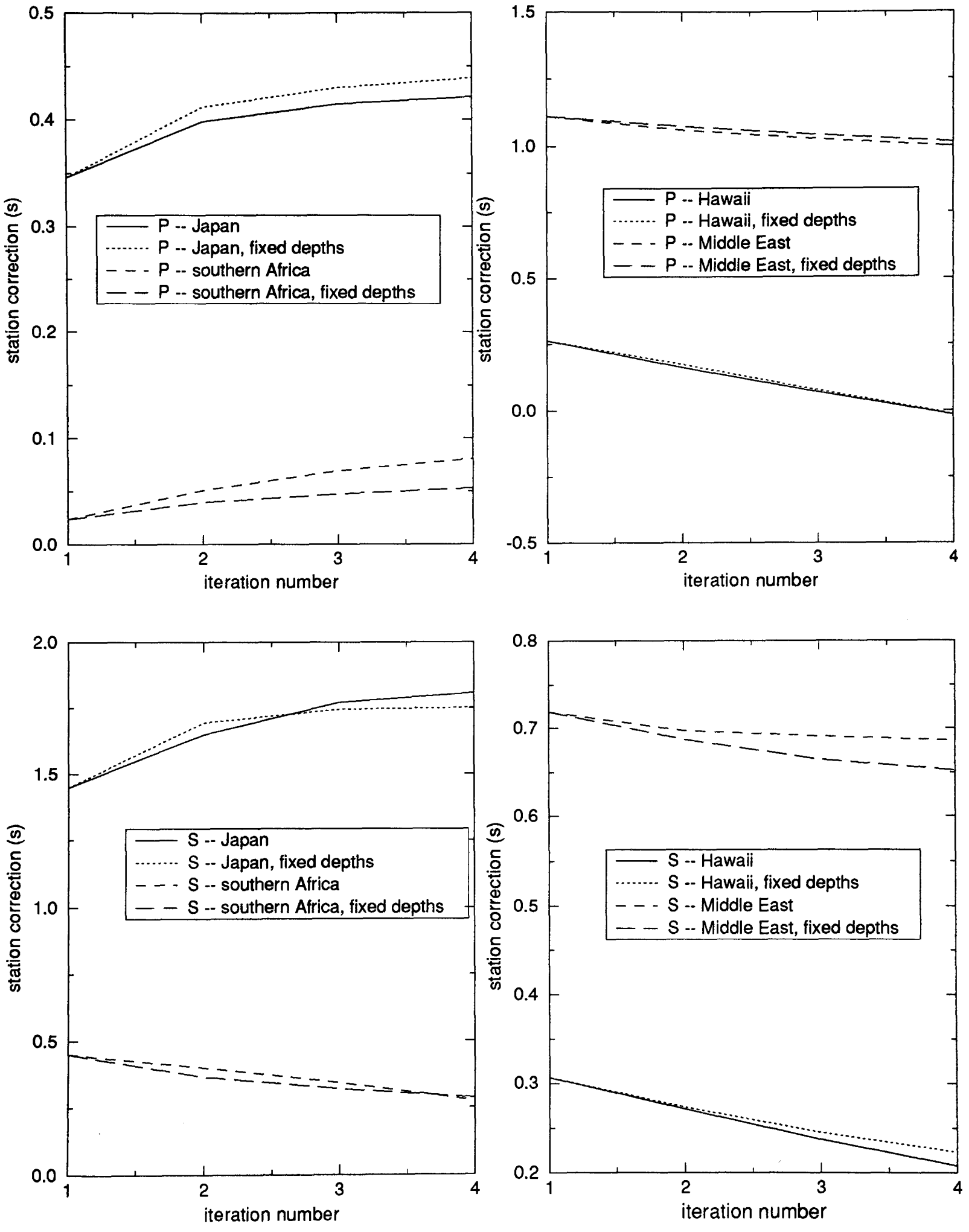


Figure 5.32: Comparison of average station corrections between the reference and fixed depth iterations for the stations around Hawaii and Japan.

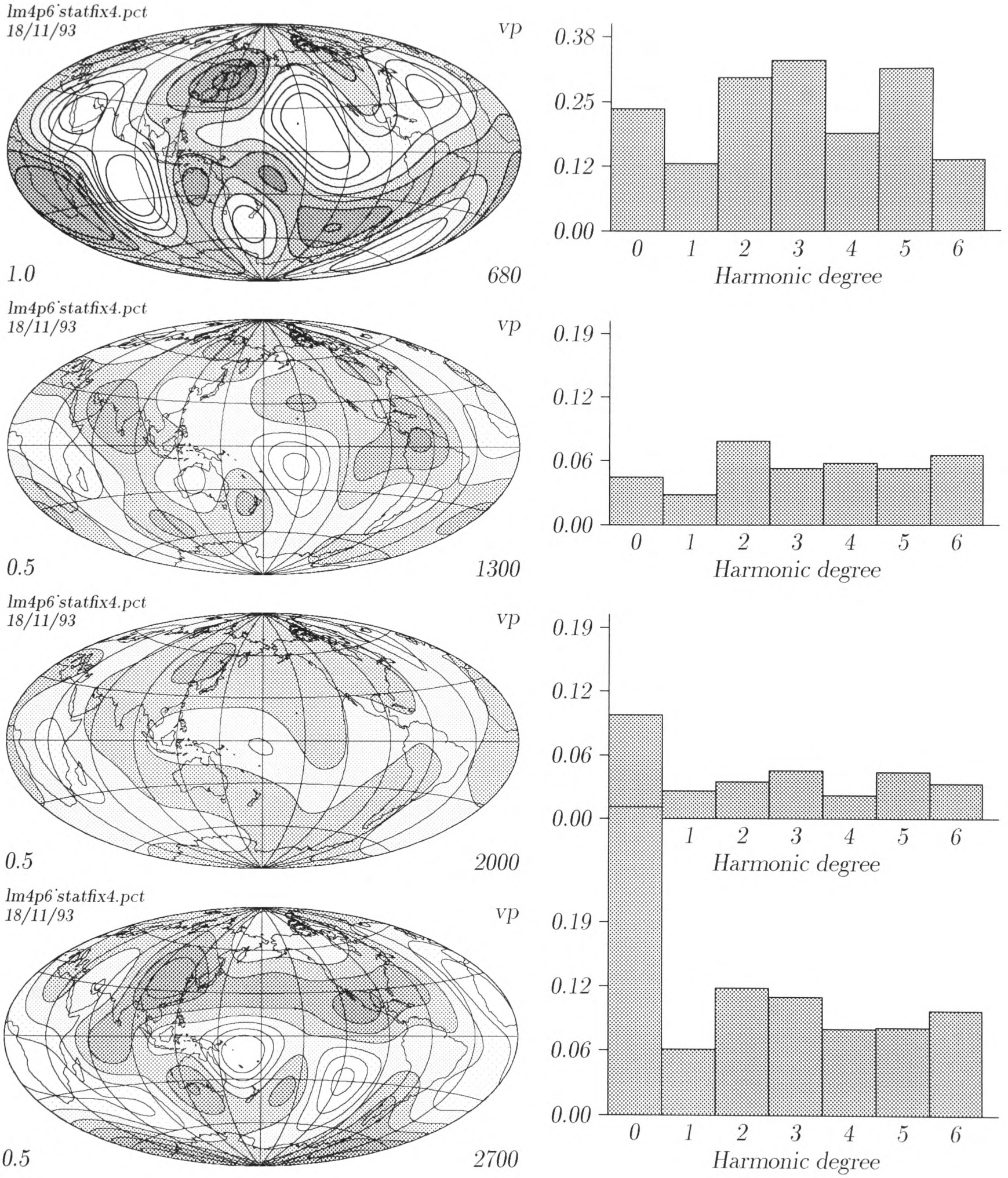


Figure 5.33: Fourth iteration P model from the experiment in which the station corrections were fixed after the first iteration.

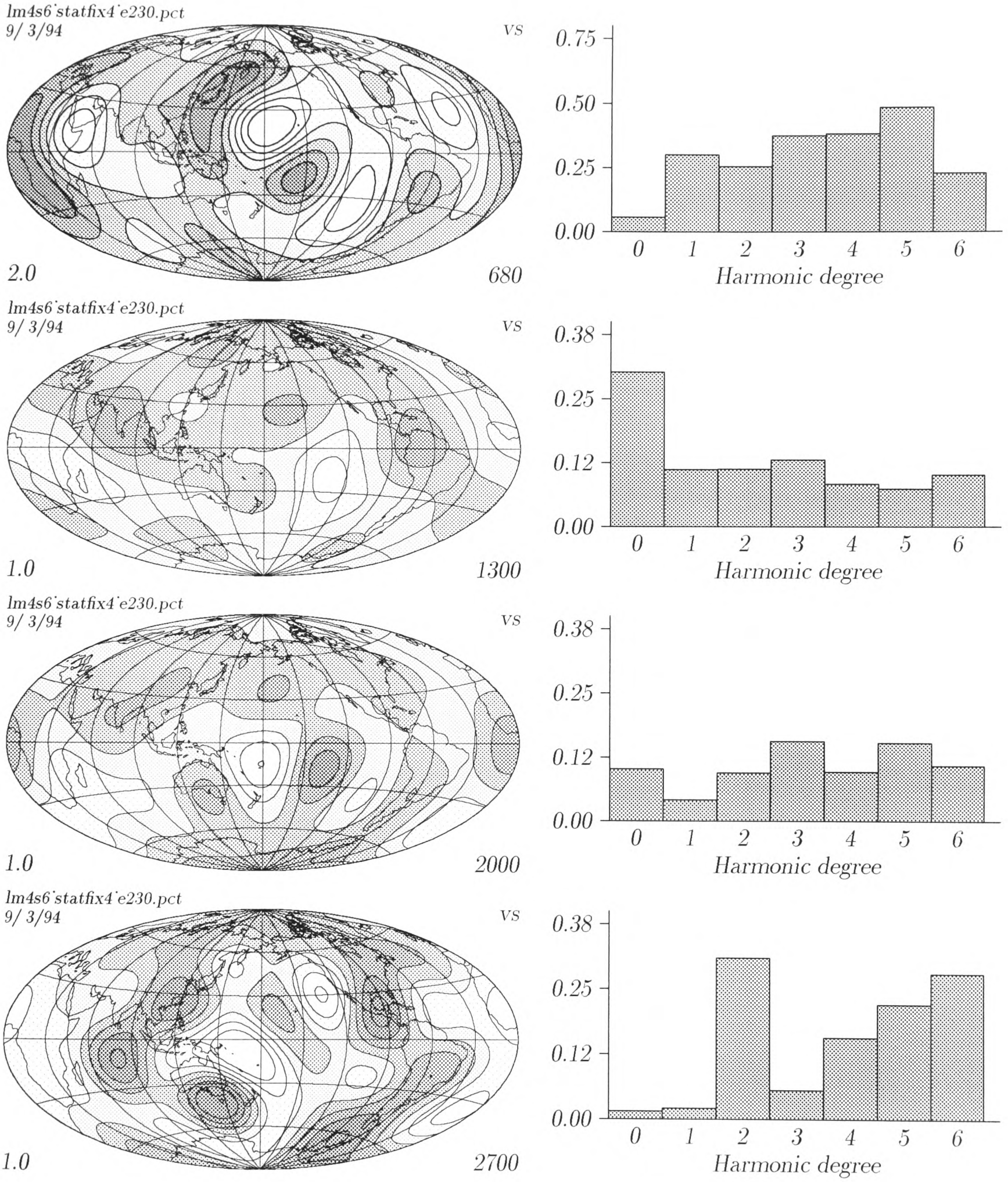


Figure 5.34: Fourth iteration S model using only 230 eigenvectors from the experiment in which the station corrections were fixed after the first iteration.

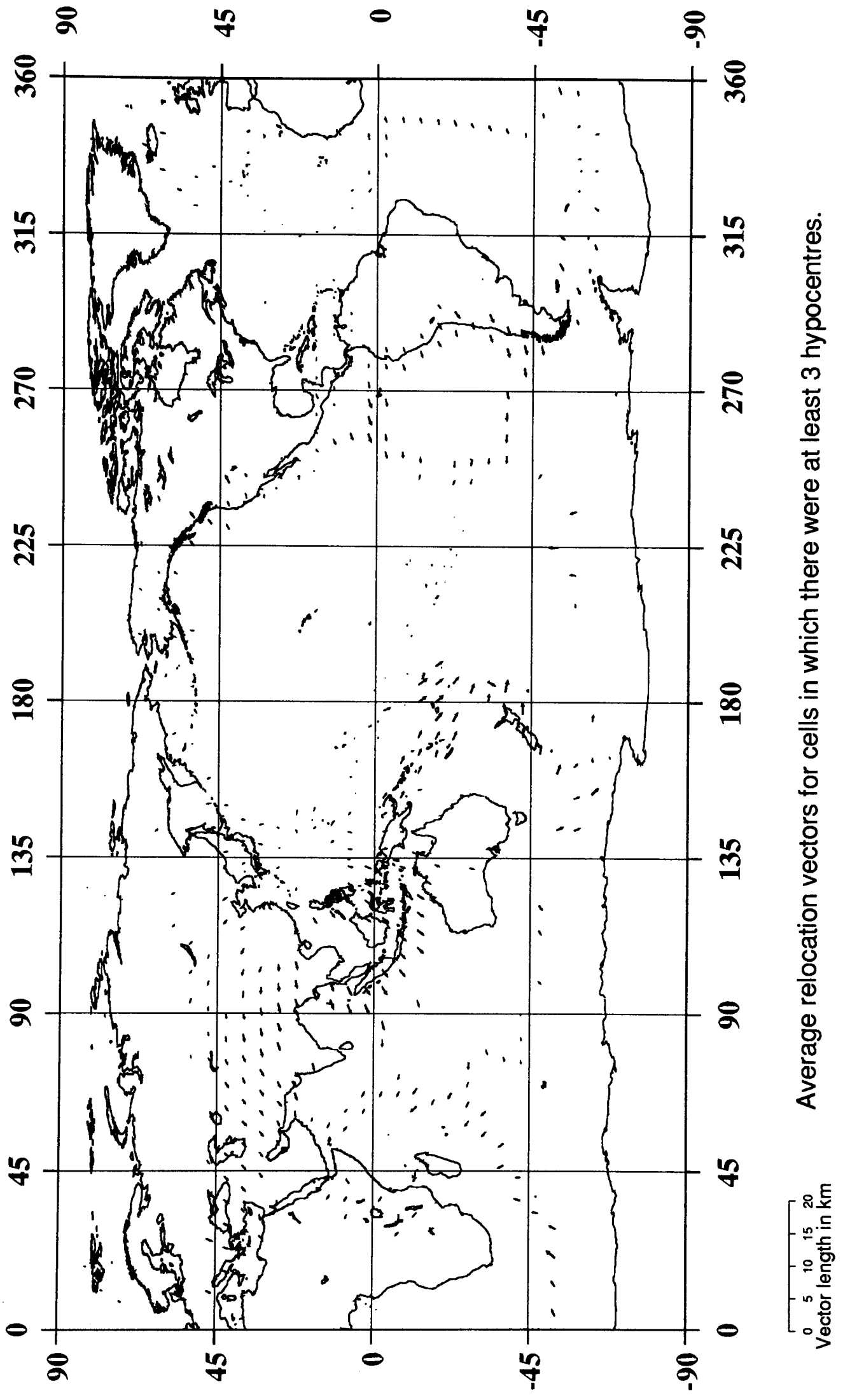
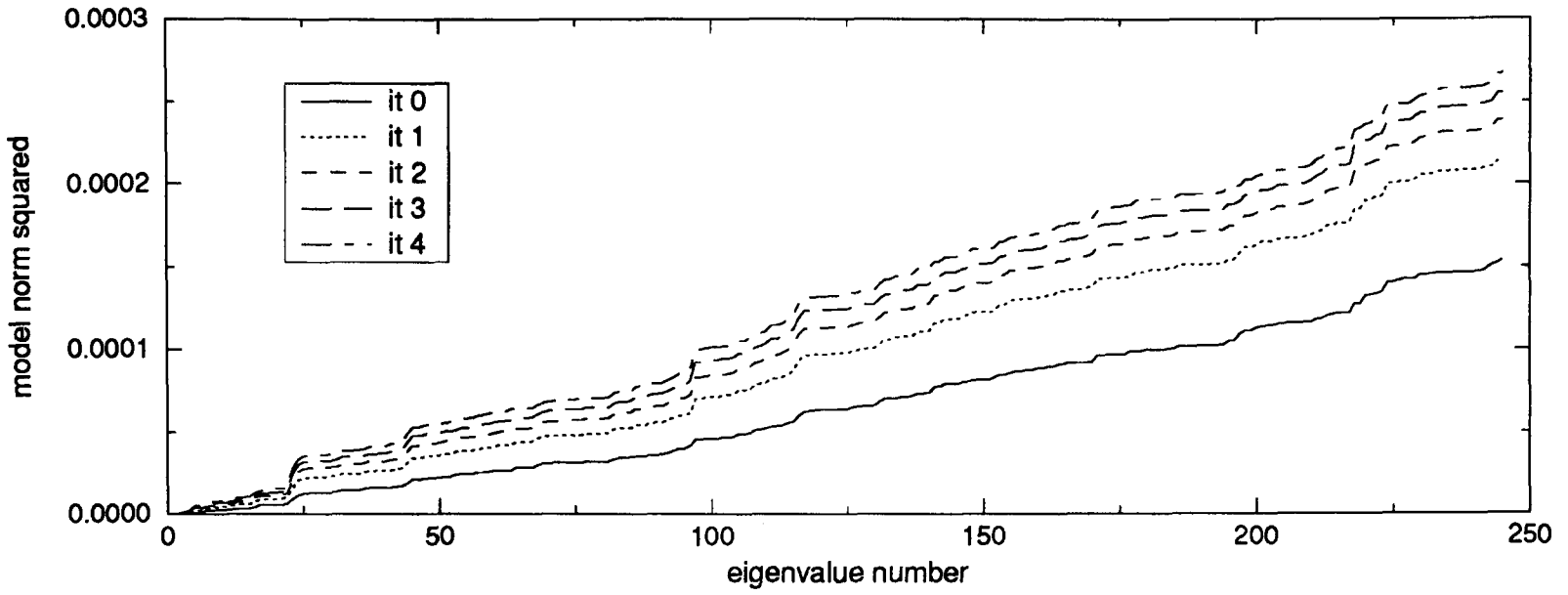
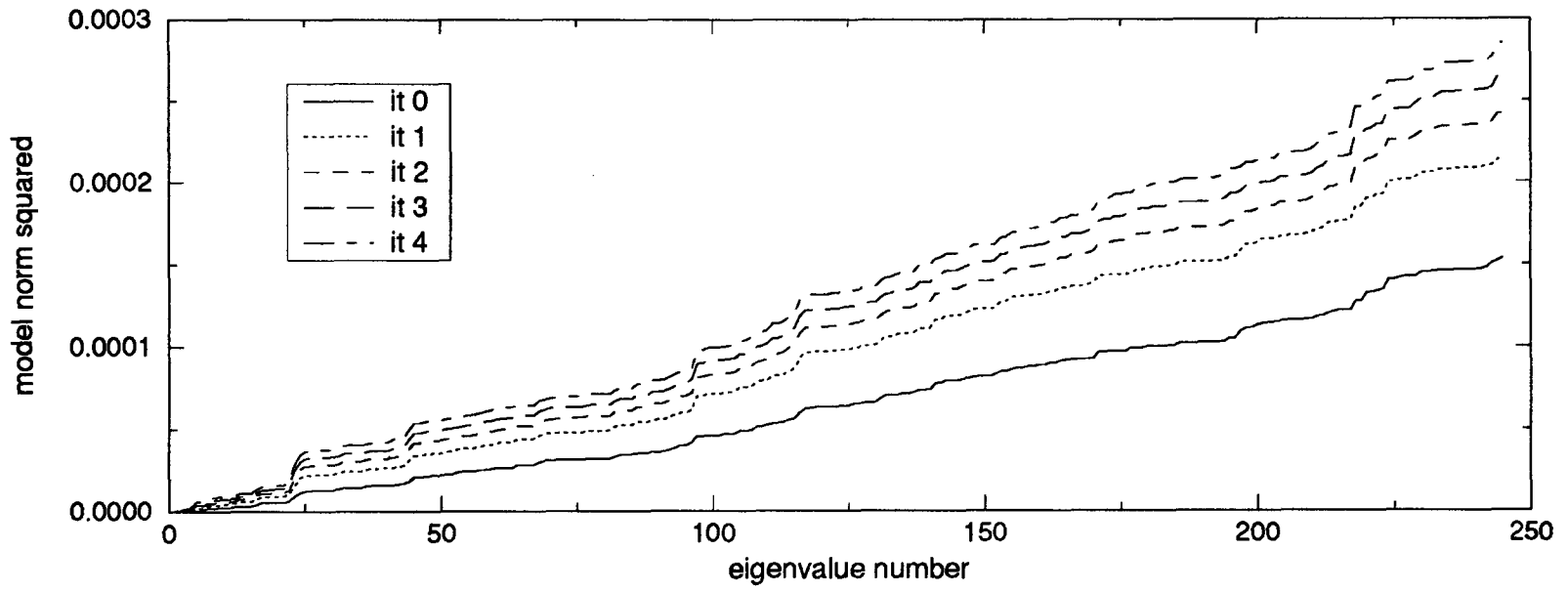


Figure 5.35: Average relocation vectors between the fourth reference iteration and the fourth iteration with station corrections fixed.





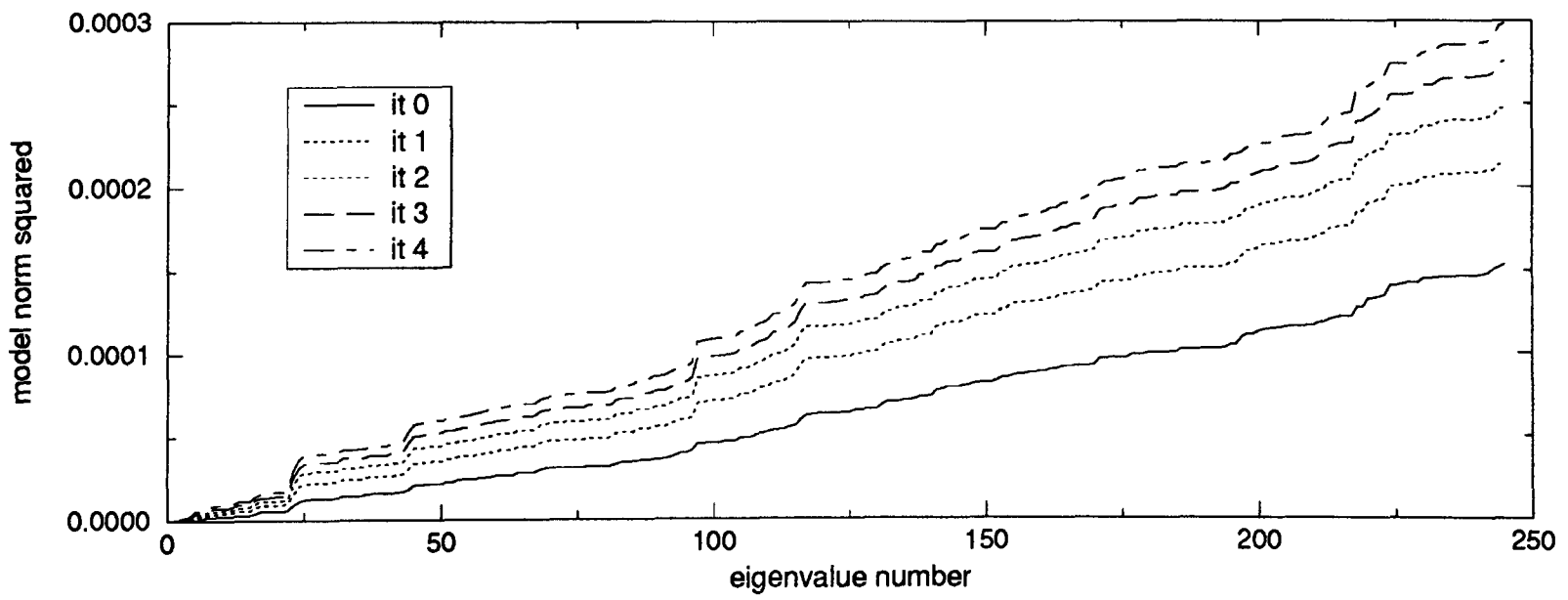
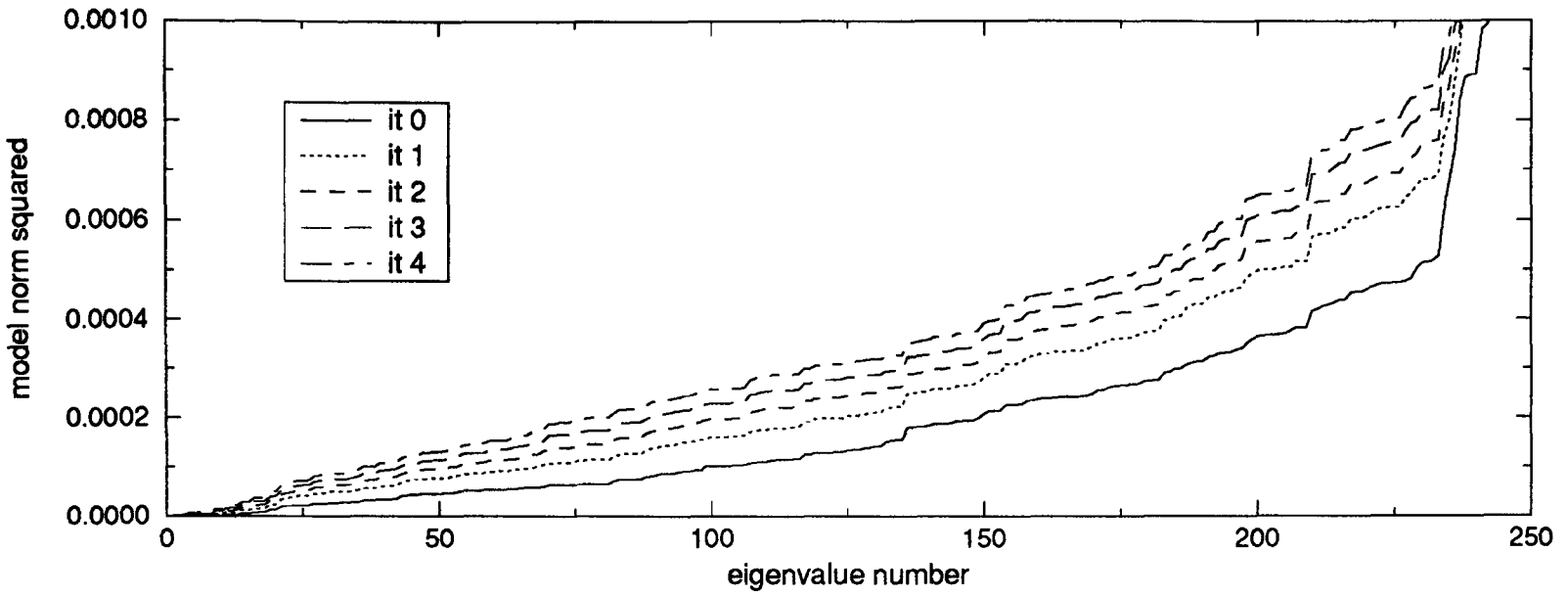
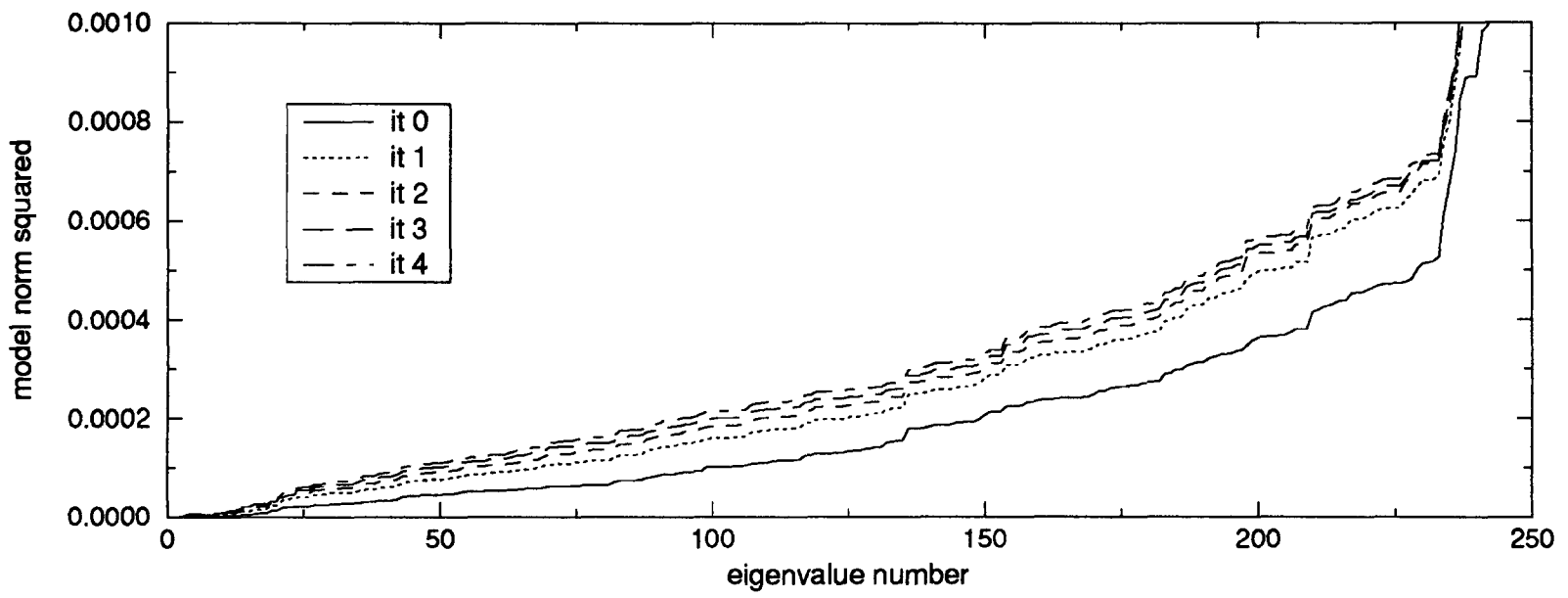


Figure 5.36: P model norm plots versus cumulative eigenvalue number for reference (bottom), fixed depth (middle), and fixed station correction (top) experiments.





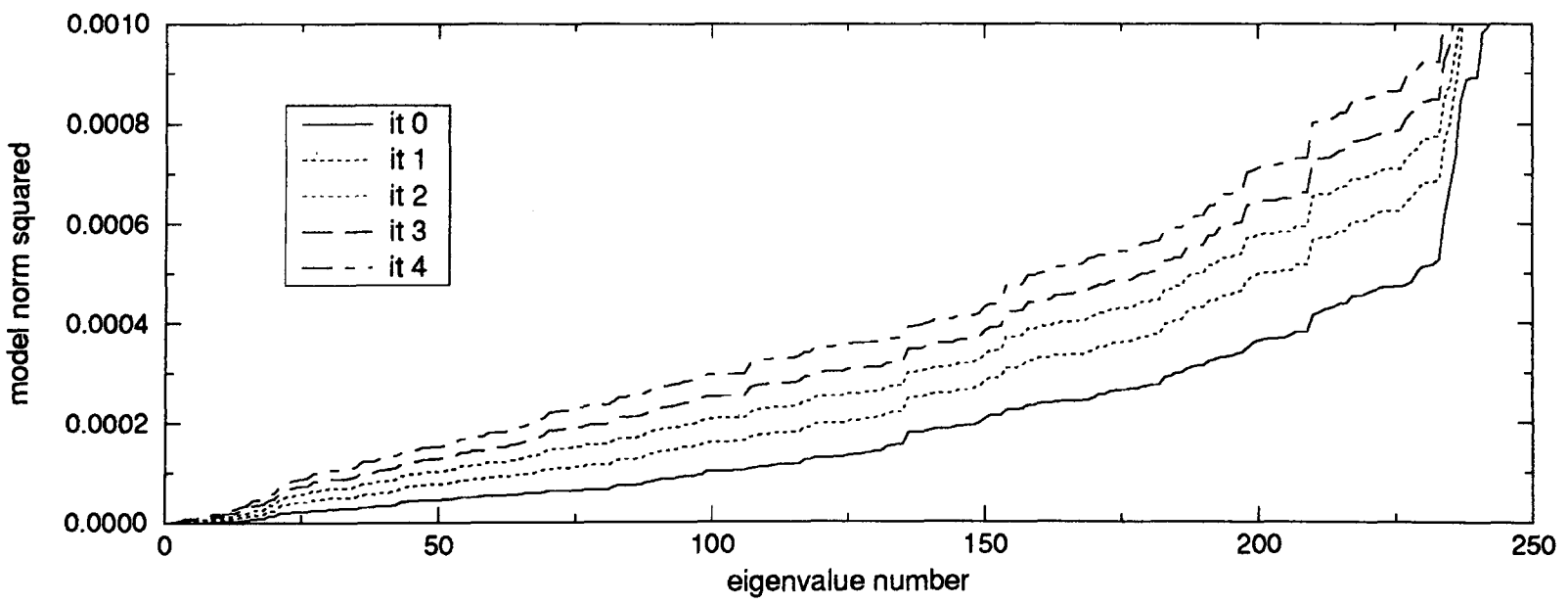


Figure 5.37: S model norm plots versus cumulative eigenvalue number for reference (bottom), fixed depth (middle), and fixed station correction (top) experiments.

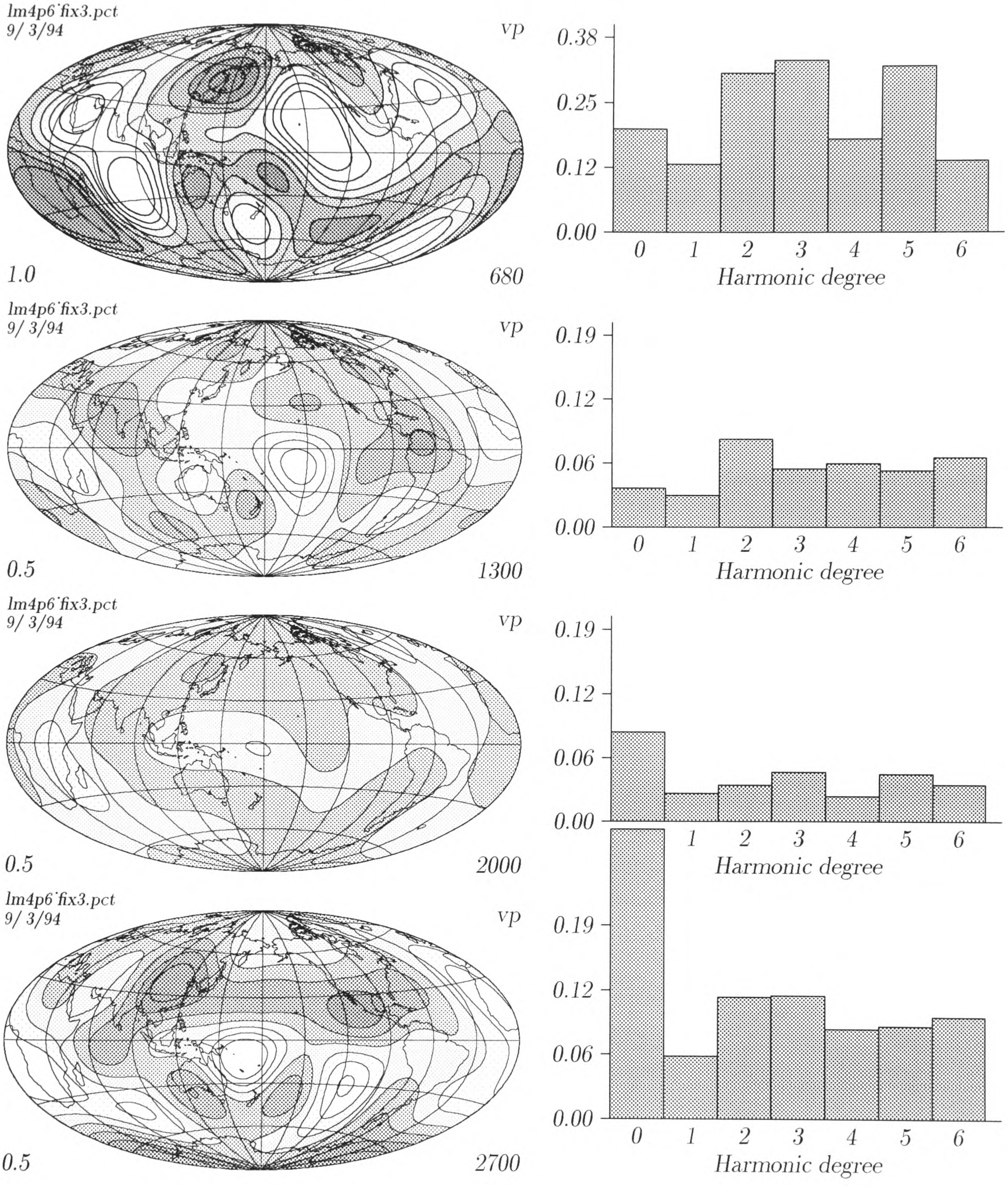


Figure 5.38: Third iteration P model from the experiment in which the depths were fixed after the first iteration. This is the final choice of P model for the lower mantle.

Figure 5.39: Third iteration S model from the experiment in which the depths were fixed after the first iteration. This is the optimum choice of S model for the lower mantle.

Chapter 6

Resolution and variance

Backus & Gilbert, 1970 were the first to point out that in the inversion of any dataset, knowledge of the properties of a model are as important as the model features themselves. For example it is clearly invalid to attach significance to any features of a model where it is known that there is no data.

In the previous chapter several references were made to where the models were expected to be good and bad. These inferences were based on both the density of ray coverage and the azimuthal distribution of the rays within the earth. It is the aim of this chapter to extend these qualitative descriptions into quantitative evaluations of the resolution and errors associated with the models.

With knowledge of both the models and their errors in chapter 8 it will be possible to make legitimate comparisons with pre-existing models by other authors.

At the end of this chapter an experiment will be described which is designed specifically to highlight the differences between the P and S models that are caused by the unequal sampling of the lower mantle by the two datasets.

6.1 Resolution tests

Equations 3.12 and 5.3 give the least squares solutions to the complete and generalized inverse problems

$$\mathbf{x} = [\mathbf{A}^\mathbf{T}\mathbf{A}]^{-1}\mathbf{A}^\mathbf{T}\mathbf{d} \tag{6.1}$$

$$\mathbf{x}_g = [\mathbf{A}^\mathbf{T}\mathbf{A}]^{-g}\mathbf{A}^\mathbf{T}\mathbf{d} \tag{6.2}$$

Combining the two equations to eliminate $\mathbf{A}^\mathbf{T}\mathbf{d}$ leads to

$$\mathbf{x}_g = [\mathbf{A}^\mathbf{T}\mathbf{A}]^{-g}[\mathbf{A}^\mathbf{T}\mathbf{A}]\mathbf{x} = \mathcal{R}\mathbf{x} \tag{6.3}$$

The resolution matrix $\mathcal{R}$ describes the transformation of a model that results from the use of an

approximate inverse. Clearly, as in the case for the P model, if the generalized inverse is in fact equal to the true inverse then the resolution operator is the identity matrix.

Several methods of representation of $\mathcal{R}$ are possible. Some authors (*e.g.* Gudmundsson *et al.*, 1990; Davies *et al.*, 1992) plot the matrix graphically by contouring the matrix elements, but this is only useful if there is an obvious relationship between the elements and physical space. The elements of the resolution matrix in this study correspond to the coefficients of a model described by spherical harmonics and so cannot be plotted directly in physical space. An alternative approach is to investigate the effects of premultiplying a known test model by $\mathcal{R}$ and then plotting the resultant model.

6.1.1 Test model

The test model chosen is the delta function generated from the same basis functions as the model – spherical harmonics laterally and Legendre polynomials in depth. This test model is ideal because the large amplitude peak is localized within the earth and can be used to isolate the effects of the eigenvalue cutoff in specific regions.

The coefficients of a delta function can be generated by using the spherical harmonic normalization relationship. Ignoring the depth dependency, a delta function at $\mathbf{x_0} = (\theta_0, \phi_0)$ can be written as

$$D(\theta\text{–}\theta_0, \phi\text{–}\phi_0) = \sum_{l=0}^{L} \sum_{m=-l}^{l} Y_l^m(\theta, \phi) D_l^m \tag{6.4}$$

where D_l^m are the coefficients of the synthesized delta funtion. Normalization gives

$$\begin{aligned} \int_0^{2\pi}\int_0^{\pi} D(\theta\text{–}\theta_0, \phi\text{–}\phi_0) Y_{l'}^{m'*}(\theta, \phi) \sin\theta d\theta d\phi &= \int_0^{2\pi}\int_0^{\pi} \sum_{l=0}^{L} \sum_{m=-l}^{l} Y_l^m(\theta, \phi) Y_{l'}^{m'*}(\theta, \phi) D_l^m \sin\theta d\theta d\phi \\ \Rightarrow Y_{l'}^{m'*}(\theta_0, \phi_0) &= D_l^m \end{aligned} \tag{6.5}$$

Therefore the coefficients of the test model delta function are simply the complex conjugates of the spherical harmonics themselves. Extension of the delta function to include depth is straightforward and involves the inclusion of a Legendre polynomial in equation 6.4. Figures 6.7 to 6.10 show delta functions at latitude = 45° , longitude = 90° for the four standard plotting depths. The maximum amplitude has been normalized to 2%. It is clear that for a given input depth spike, the largest peaks on each sub plot are not the same. For example, in figure 6.8 for an input delta function at 1300km, the maximum absolute amplitudes at this depth and at 680km are almost exactly the same. For the input spike at 680km however, the maximum amplitude is much larger at 680km than anywhere else. This seemingly erroneous result originates from the fact that there are only five Legendre polynomials being used to generate the delta function. These functions generate better spikes (and larger) at some depths than at others.

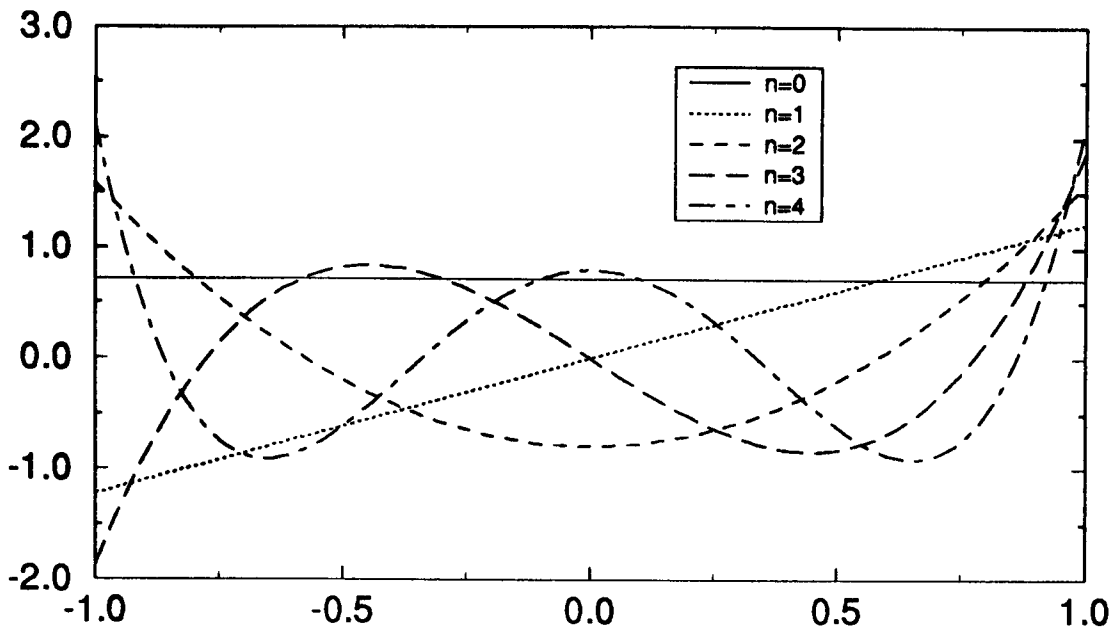


Figure 6.1: Normalized Legendre polynomials to n=4.

Figure 6.2 shows the synthesis of a delta function using Legendre polynomials (figure 6.1) at four depths. In all cases the largest amplitudes occur at the normalized depth, but it is clear that at some depths the 'spike' is far clearer. In particular at intermediate depths (1300km and 2000km) the absolute amplitudes of the functions at shallow depth (normalized depth ≈ 1) are almost as high as those at the peak of the delta function. It should also be noted that due to the nature of the Legendre polynomials, the actual amplitude of the delta function is much higher when it is placed at the top or the base of the lower mantle.

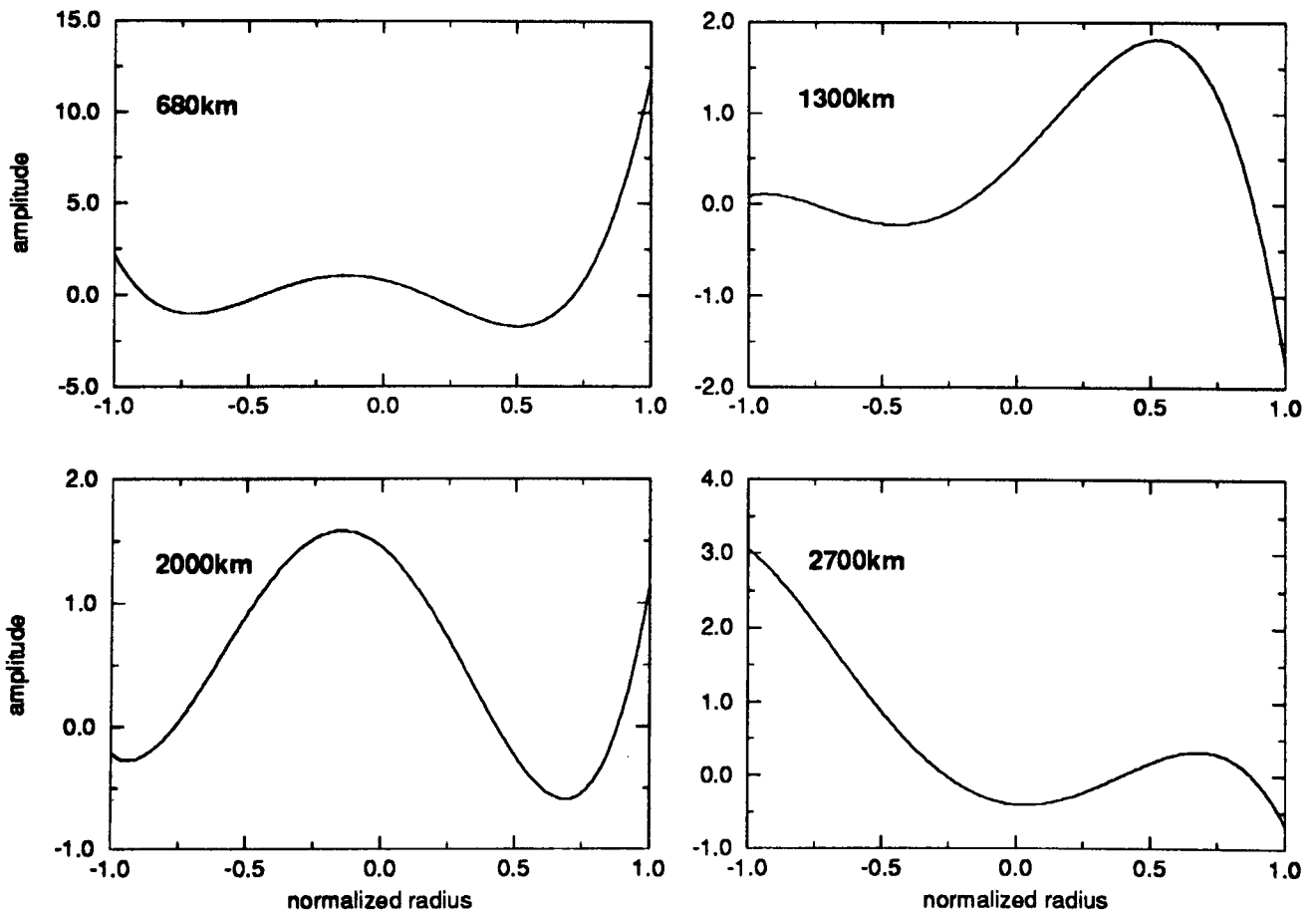


Figure 6.2: Synthesis of a delta function from 5 Legendre polynomial coefficients for the four standard model plotting depths.

Test delta function models are used at all four depths in two different locations. The first position

is in central Asia at latitude = 45° , longitude = 90° (figures 6.7 to 6.10). This is intended to be representative of an area of good ray coverage at least at the top of the lower mantle. The second set of test models are generated in the centre of the Pacific Ocean at $(\theta, \phi) = (0, 210)$ where ray coverage is generally bad. These are shown in figures 6.11 to 6.14, and it is expected that the poor resolution of the models in these places will be highlighted in these cases.

6.1.2 Central Asia input spike

The effects of the resolution operator on the four test models are shown in figures 6.15 to 6.18. Comparison of these models with the equivalent test model shows that, as expected, the resolution is almost perfect for all four depth input delta functions. Even at 2700km depth the effects of eigenvalue cutoff on the resolution is negligible with very little smearing of the delta function pattern at any depth. In the 2000km sub plot of figure 6.16, where the pattern is not clearly reproduced, the harmonic spectrum of the test model is small and so the apparent distortions are not a problem.

6.1.3 Central Pacific input spike

The resolution models for the four input delta function test models are shown in figures 6.19 to 6.22. Again these show results which agree with the qualitative expectations of the previous chapter. For the test spike at 680km (figure 6.19), the pattern in the resolution model at the top is quite similar to the reference model, but the size of the harmonic spectrum is considerably reduced. In particular degrees 0 to 3 are almost half of what they should be. At different depths in the same figure the pattern itself becomes quite diffuse. In figure 6.22 for the input spike at 2700km, both the pattern and the harmonic spectrum are slightly different. The size of all degrees at 2700km decrease marginally while degrees 1 to 5 at 680km double. This leakage is an interesting result which must be caused by the very restricted data coverage at depth.

6.2 Model variance

As well as knowing which parts of the model are resolvable it is important to know the size of the errors associated with the model at a specific position within the lower mantle.

Starting from equation 6.2, the covariance of the model can be written as

$$\begin{aligned} cov\mathbf{x}_g &= [\mathbf{A}^\mathbf{T}\mathbf{A}]^{-g}\mathbf{A}^\mathbf{T}\, cov\mathbf{d}\, \mathbf{A}\, [\mathbf{A}^\mathbf{T}\mathbf{A}]^{-g} \\ &= \sigma_d^2[\mathbf{A}^\mathbf{T}\mathbf{A}]^{-g}\,[\mathbf{A}^\mathbf{T}\mathbf{A}]\,[\mathbf{A}^\mathbf{T}\mathbf{A}]^{-g} \text{where } cov\mathbf{d} = \sigma_d^2\mathbf{I} \end{aligned} \tag{6.6}$$

Here σ_d^2 is the final variance resulting from the inversion, and includes the weighing of the residuals.

Hence, if the model evaluated at (r, θ, ϕ) is represented by the set of coefficients $\mathbf{b}(r, \theta, \phi)$:

$$\frac{\delta v_p}{v_p}(r, \theta, \phi) = \mathbf{b}^{\mathbf{T}}(r, \theta, \phi)\mathbf{x_g} \tag{6.7}$$

$$\text{then} \quad var\left[\frac{\delta v_p}{v_p}(r, \theta, \phi)\right] = \mathbf{b}^{\mathbf{T}}\, cov\mathbf{x}_g\, \mathbf{b} \tag{6.8}$$

These values can be calculated and then contoured within the lower mantle to produce plots similar to the type which have been used to present the models themselves. The variance plots for the P and S models are shown in figures 6.23 and 6.24 respectively. The variations at a specific depth are contoured about a mean value of the variance at that depth, with the mean being given in the top right hand corner of each sub plot. Similarly the contour interval, given in terms of $\frac{\delta v}{v}$, is in the bottom left hand corner.

On initial inspection the most apparent aspect of the two graphs is their similarity. The overall light and dark areas at all depths correlate well. This can be attributed to the similar ray geometries in both datasets. All maps show large variances in the southern hemisphere because of the poor distribution of stations at low latitudes. In addition, in all but the deepest map, the variance in the Pacific region is by far the greatest. The contouring at 680km depth is twice as large as anywhere else in both the P and S sets of plots, and even then it saturates particularly quickly because of the almost vertical nature of the rays at shallow depths.

The contour intervals in the S variance plots are ten times the size of those for P. This is probably explained by the fact that the S dataset is not only one sixth the size of the P dataset, but also because it has almost ten times the variance.

6.3 P_S : P with S paths model

As was indicated at the introduction to this chapter, an experiment has been devised to look specifically at what features of the S model are attributable to the much smaller dataset that has to be used. This experiment involves the calculation of a P model using only ISC P arrivals picked from seismograms which also have contributed an ISC S arrival time. In other words, only the P data from stations which have themselves recorded an S arrival from the same event are used. This model is termed the *P with S paths model* (P_S).

In theory therefore, provided the paths of P and S waves between the same source and receiver are similar, the differences between the S model and the P_S model can be said to be path independent. Alternatively, any differences between the P model and the P_S model can be attributable to the differences in the resolving powers of the datasets.

Before deriving a model it is important to test the assumption that the P and S rays between a source and receiver follow similar paths. Figure 6.3 shows the difference in the bottoming depths of shear and

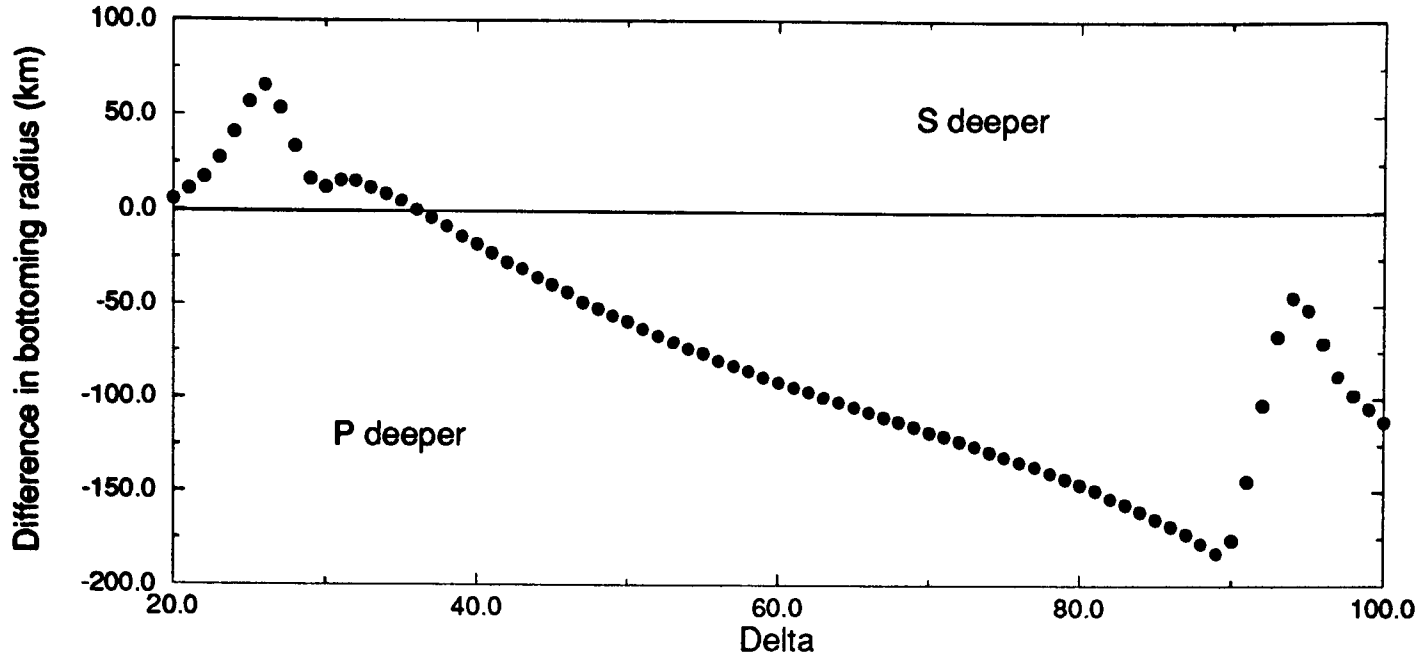


Figure 6.3: Difference in bottoming depths between a P ray and an S ray for the same source and receiver from PREM.

compressional rays for the same source and receiver within the teleseismic window. It is clear that the differences are minimal, being at most $\approx$ 200km at the top of D''.

6.3.1 Calculation of the model

The P.S dataset is selected from the complete P dataset resulting from the third iteration relocations of chapter 5. Therefore the P.S dataset is a subset of the P dataset that is used in the selected P model, figure 5.38.

A total of 120025 paths were used in this model – slightly less than the S model. This difference in numbers can be explained if the S wave ray path emanates from or near the fault or auxiliary plane when the source is assumed to take the form of a double couple. In these regions there is no corresponding P wave.

Computation of the model proceeds in an identical way to the P and S models, and the model norm and variance plots are shown below.

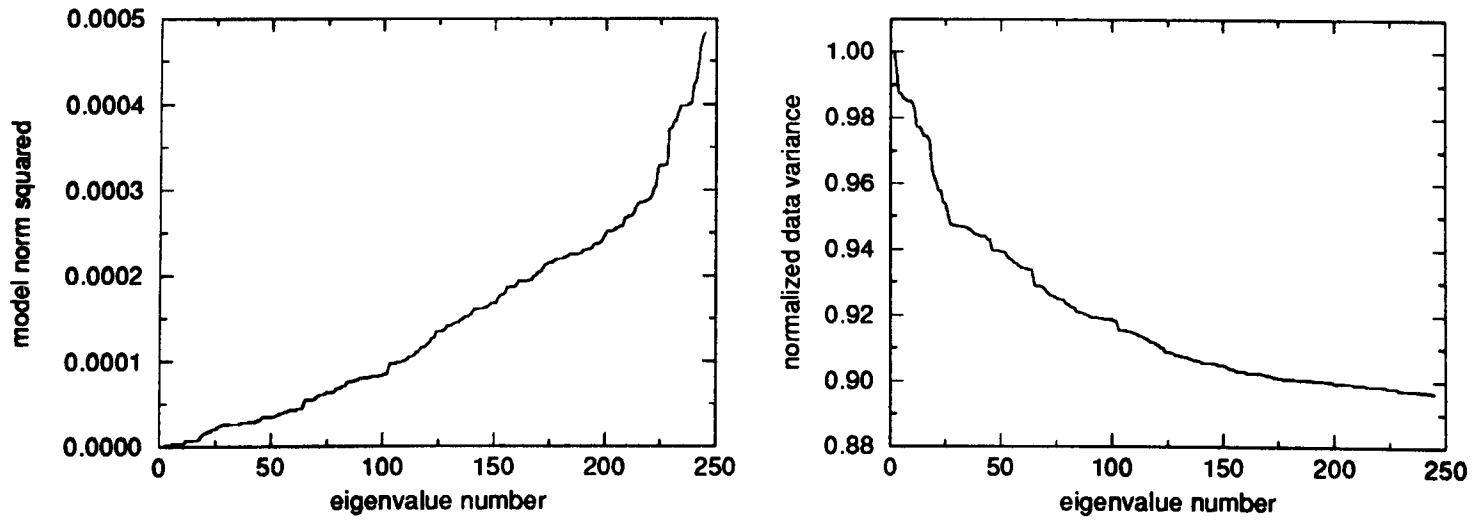


Figure 6.4: Model norm and variance reduction graphs for the P.S model.

In an analogous fashion to the zeroth iteration S model plot (figure 5.8) there is a rapid increase in the size of the model at large eigenvalue numbers with only a very slight decrease in the resulting variance. Consequently the cutoff is chosen to be at 220 eigenvalues and eigenvectors, which is only slightly less than the truncation point in the S model. This P.S model is shown in figure 6.25.

6.3.2 Comparison of the P.S model and P model

Comparison of figure 6.25 with figure 5.38 shows:

- At 680km depth the features are generally well correlated. This is apparent in the harmonic spectra where degrees 3 and 5 are prominent on both maps.
- There is excellent correlation in both amplitude and features at 1300km depth.
- The P.S map at 2000km is bigger than the complete dataset P model at this depth, and is most different in the south central Pacific region where there are additional positive and negative features.
- The deepest maps are not very similar. This can be attributed to the vastly reduced amount of data that contributes to the P.S model at epicentral angles greater than 80° .

6.3.3 Comparison of the P.S model and S model

Comparison of figure 6.25 with figure 5.39 shows:

- Apart from the Pacific regions, where resolution is bad as a result of poor data coverage, the top maps correlate well.
- At 1300km and 2000km depth, the high velocity ring structure circumscribing the Pacific is not as evident in the S model. Nevertheless the individual features, most notably under India and the Caribbean, are apparent in both P.S and S to a greater or lesser extent. In the south central Pacific region at 2000km depth there is a high velocity feature common to the P.S and S model, but not seen in the P model.
- Despite the almost identical ray coverage of the lower mantle at 2700km depth in both models, correlation is not good. Several features are similar but most have moved spatially. It is strange that the correlation of the P model and the S model at this depth should appear to be far higher than the correlation of P.S with S.

6.3.4 Correlation coefficients

These qualitative descriptions can be put on a more quantitative basis by considering how the different models correlate at depth. The correlation coefficient is defined as

$$C = \frac{\sum_i \mathbf{a}_i \mathbf{b}_i}{\| \mathbf{a} \| \| \mathbf{b} \|} \tag{6.9}$$

where **a** and **b** are vectors of model coefficients at a specific depth. We choose to ignore the spherical part because this is dependent on the choice of reference model. For this case the index i starts from 2 and goes to $(L+1)^2$

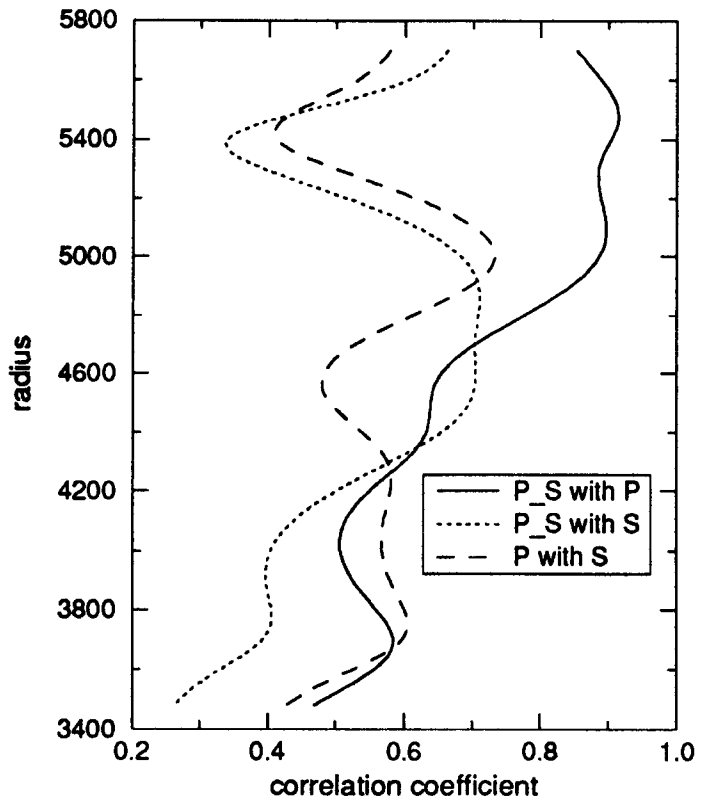


Figure 6.5: Correlation coefficients of the 4_6 models of this study with depth.

Correlation of the P and PS model is excellent in the top 1600km of the lower mantle with a coefficient of approximately 0.9. Below this there is a steady decrease towards the CMB where correlation is poor at 0.5. This can be explained by the relatively poor sampling of the deep mantle by the PS dataset. The correlation of the PS model to the S model is not impressive. It is only near the 670km discontinuity and in the mid mantle regions between 4400 and 5000km radius that it is more similar to the S model than the P model is to the S model. This latter fact has been noticed in the descriptions of the previous two sections. Below 2000km depth the P model is far better correlated to the S model. This possibly results from the fact that there are proportionally fewer PS residuals beyond 90° epicentral angle than S relative to distances less than 80° (see figure 6.6). In fact, beyond 90° there are 26% fewer PS residuals than S residuals compared to only 5% fewer over the entire teleseismic window.

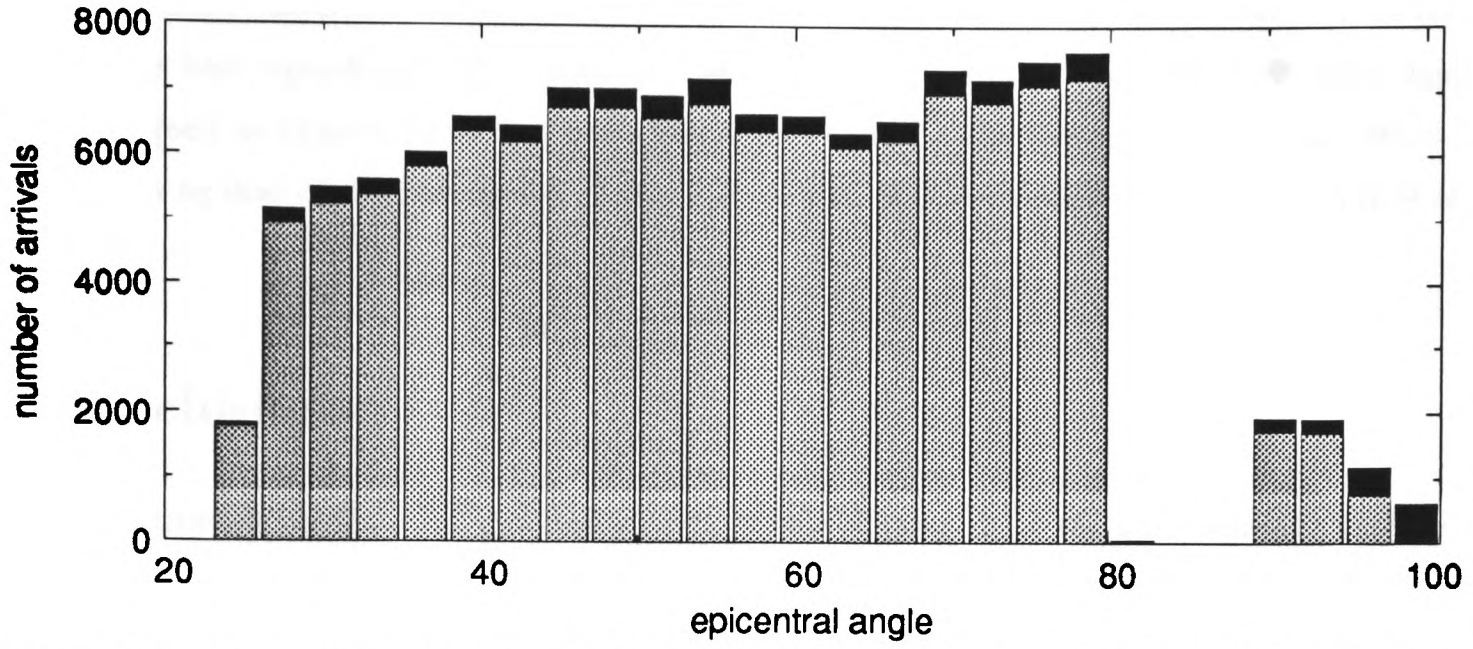


Figure 6.6: Comparison of the number of arrivals at a given epicentral angle for the S dataset (black) and the PS dataset (grey).

6.3.5 PS model variance

The variance in the velocity perturbations for the PS model is shown in figure 6.26. In order to obtain the same saturation levels, the maximum contour value used is 2.5 times that of the P model and one quarter that of the S model. In other words, by using only one sixth of the data, the variance is multiplied by approximately $\sqrt{6}$. As expected, this graph is far more similar to the S model variance plot (figure 6.24) than the P equivalent because of the almost identical sampling of the lower mantle. The one exception to this is in the Pacific region in the top map where the variance is greatly reduced near to and south of the Marquesas Islands. This attribute is also evident in the P model variance plot if 240 instead of 245 eigenvalues are used.

6.3.6 PS model resolution

Central Asia input spike

Despite using fewer eigenvalues in the construction of the model, the resolution patterns for the PS model at all depths are almost identical to the corresponding S model graphs, and as a result they are not shown here.

Central Pacific input spike

The effect of using 10 fewer eigenvalues in this model is much more clearly seen in diagrams 6.27 to 6.30 compared to those for the S models. At 680km the effect is worst with over 50% of the test model signal being lost in degrees 0 to 5 in the top map. In addition the patterns at greater depth are more diffuse than those in the equivalent S plot (figure 6.19).

With the input delta function at 1300km depth the problem improves slightly. At 2000km, figure 6.29, the test model is best reproduced. The resolution pattern for the input delta function at 2700km depth is not quite as good as figure 6.22 for S. Unlike this figure, however, the harmonic spectra at 680km in this plot is close to that of the test model, so the leakage that was mentioned in section 6.1.3 is of less concern.

6.4 Conclusions

- The quantitative variance and resolution plots of this chapter show the same features that have been qualitatively discussed in the previous chapters.
- Apart from the very top of the lower mantle and mid mantle regions, in general the PS model does not correlate as well to the S model as the P model does. At least for the deepest mantle the reason for this may be that there are substantially fewer data in the PS dataset than in the S dataset beyond 80° . Nevertheless, the result of the PS model experiment is that the differences between the P and the S models are not caused by the different sampling of the lower mantle by the two datasets.

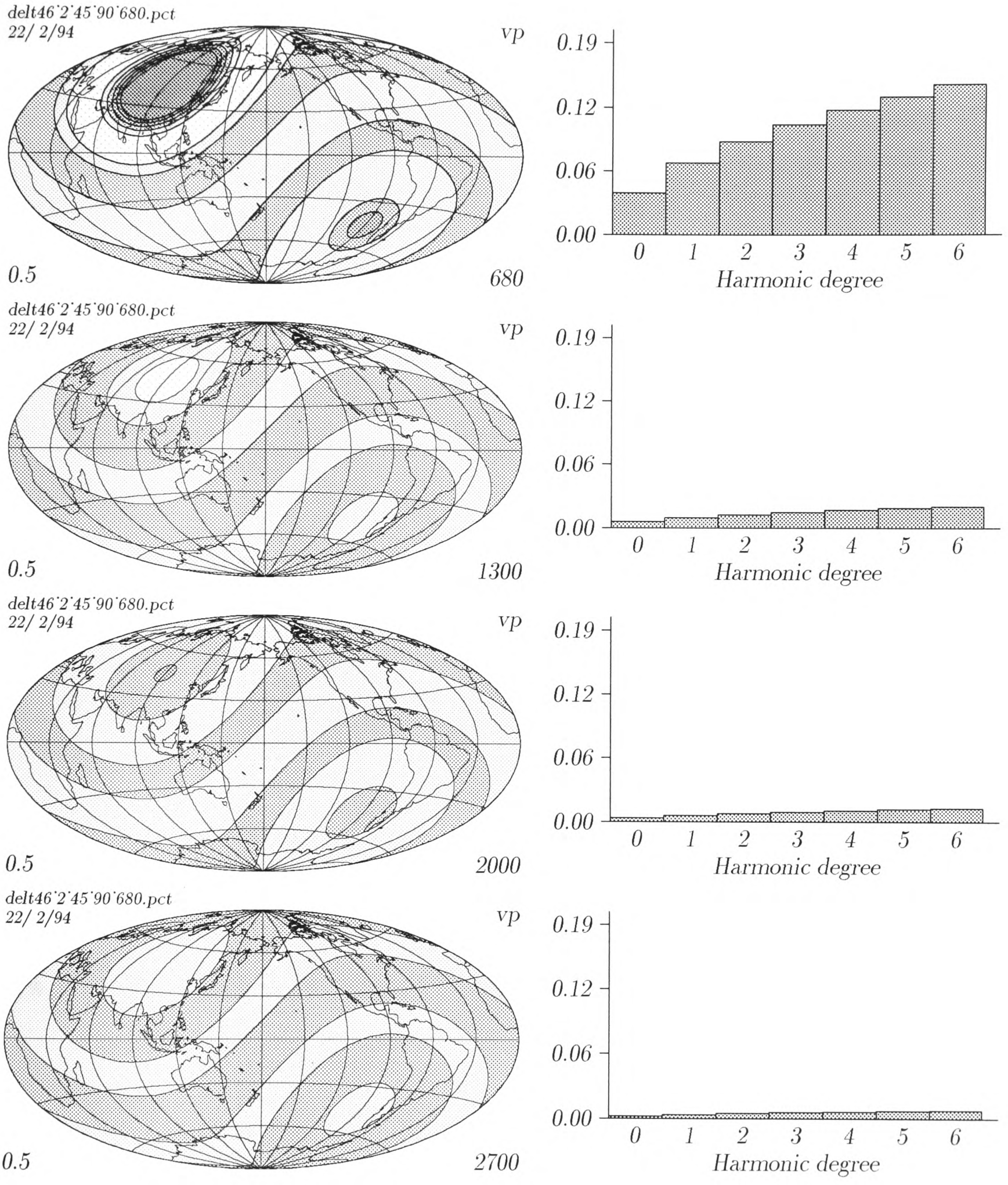


Figure 6.7: Test model with delta function placed in central Asia at 680km depth.

Figure 6.8: Test model with delta function placed in central Asia at 1300km depth.

Figure 6.9: Test model with delta function placed in central Asia at 2000km depth.

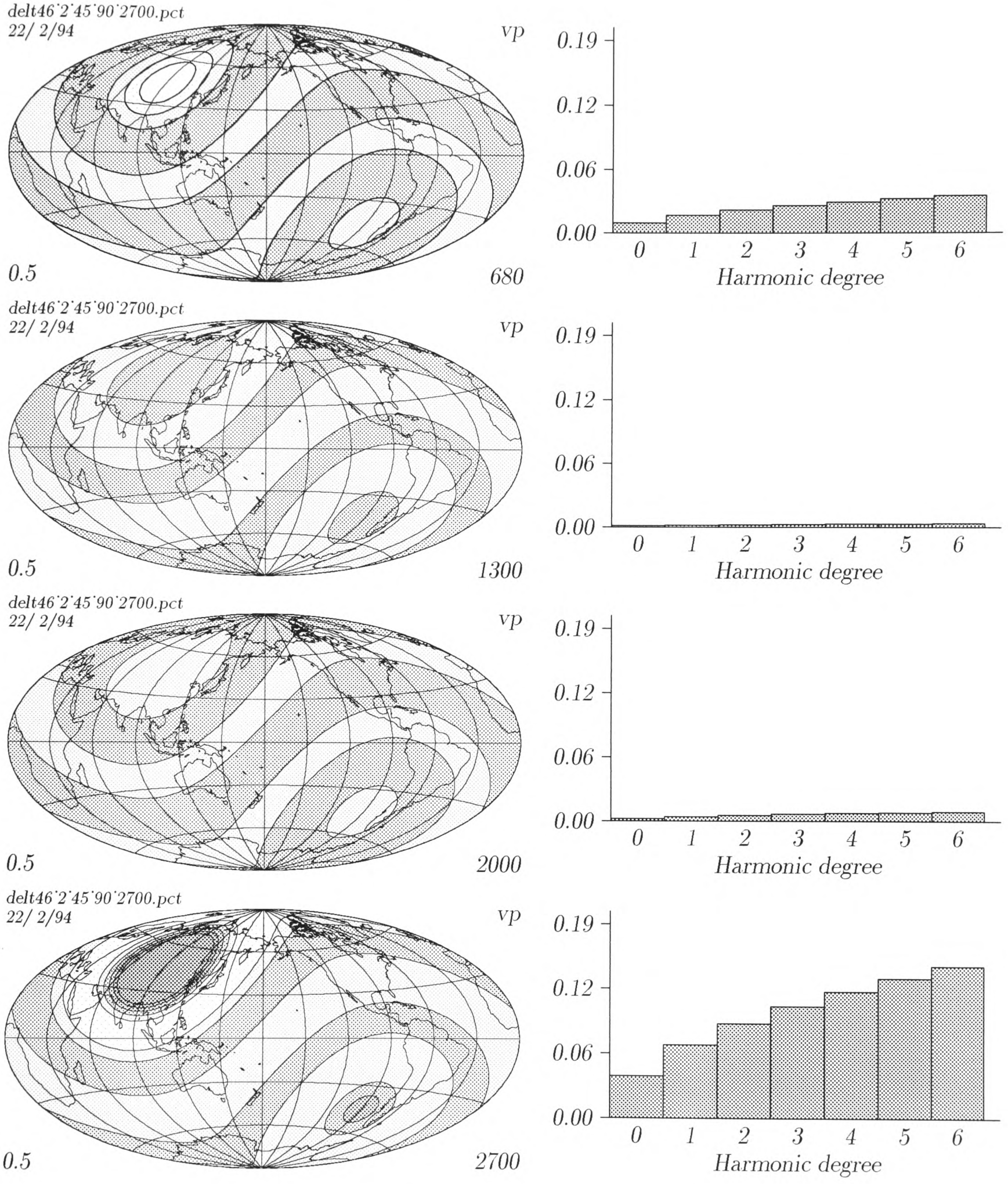


Figure 6.10: Test model with delta function placed in central Asia at 2700km depth.

Figure 6.11: Test model with delta function placed in central Pacific at 680km depth.

Figure 6.12: Test model with delta function placed in central Pacific at 1300km depth.

Figure 6.13: Test model with delta function placed in central Pacific at 2000km depth.

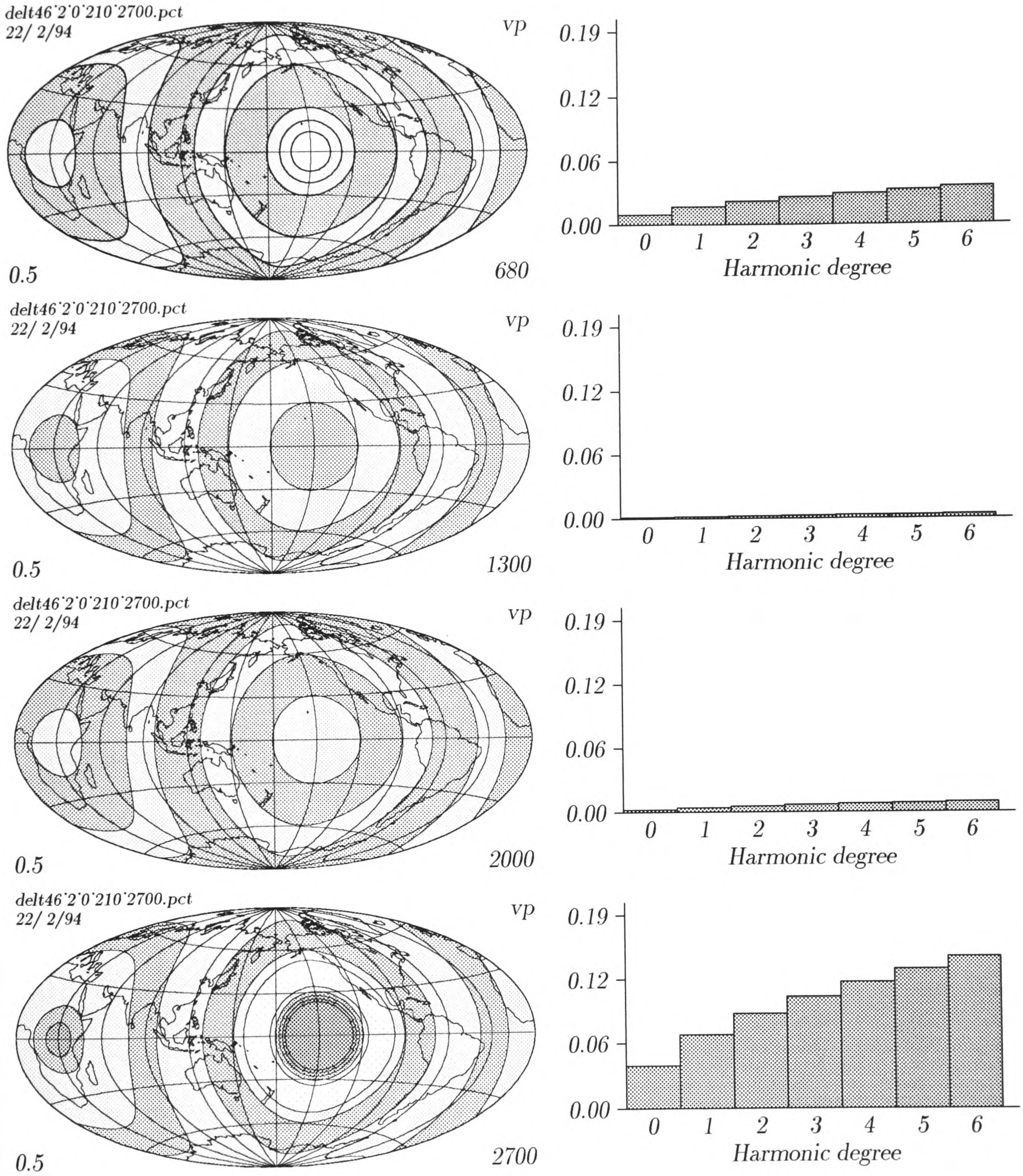


Figure 6.14: Test model with delta function placed in central Pacific at 2700km depth.

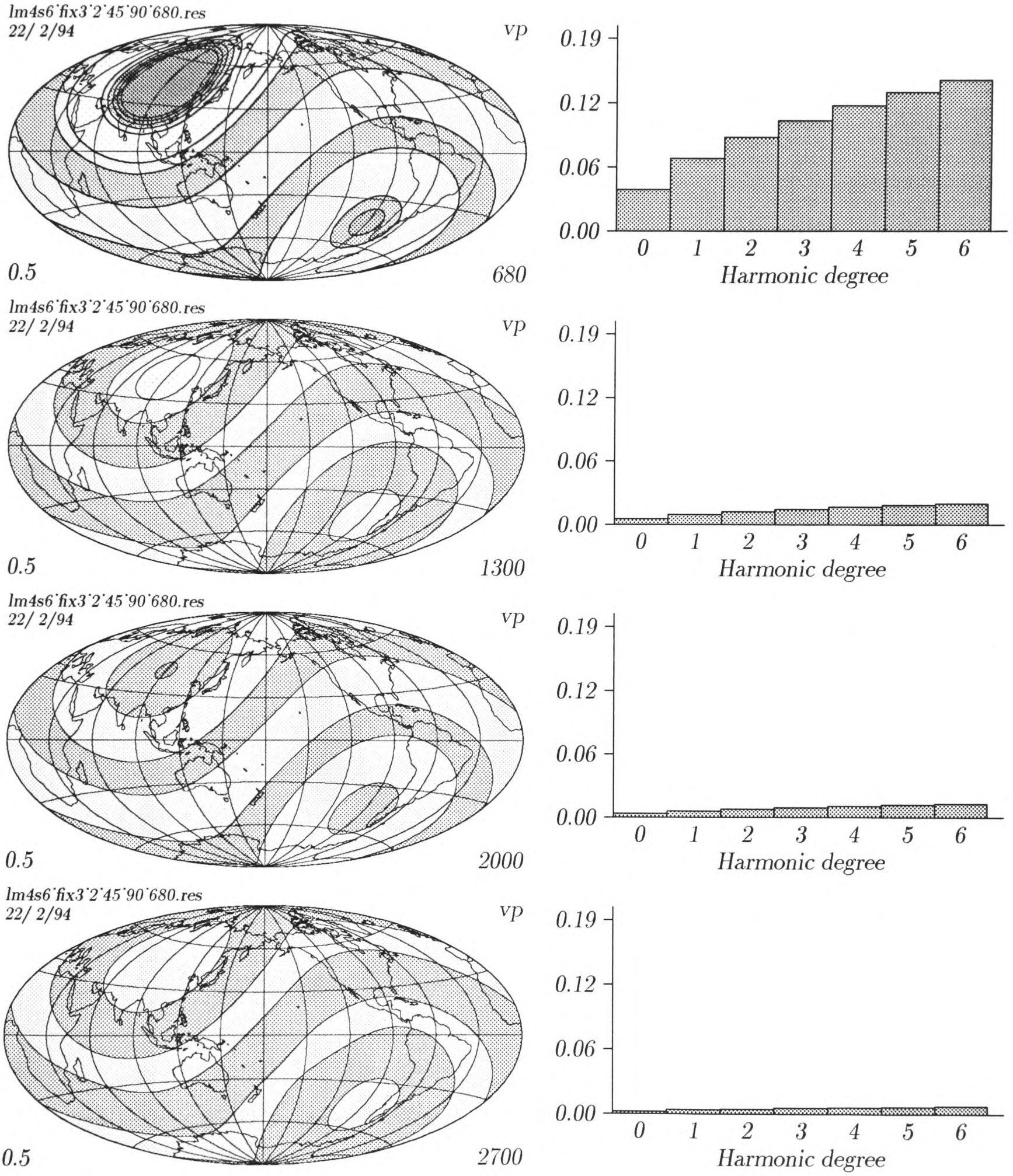


Figure 6.15: Resolution model to be compared with delta function placed in central Asia at 680km depth.

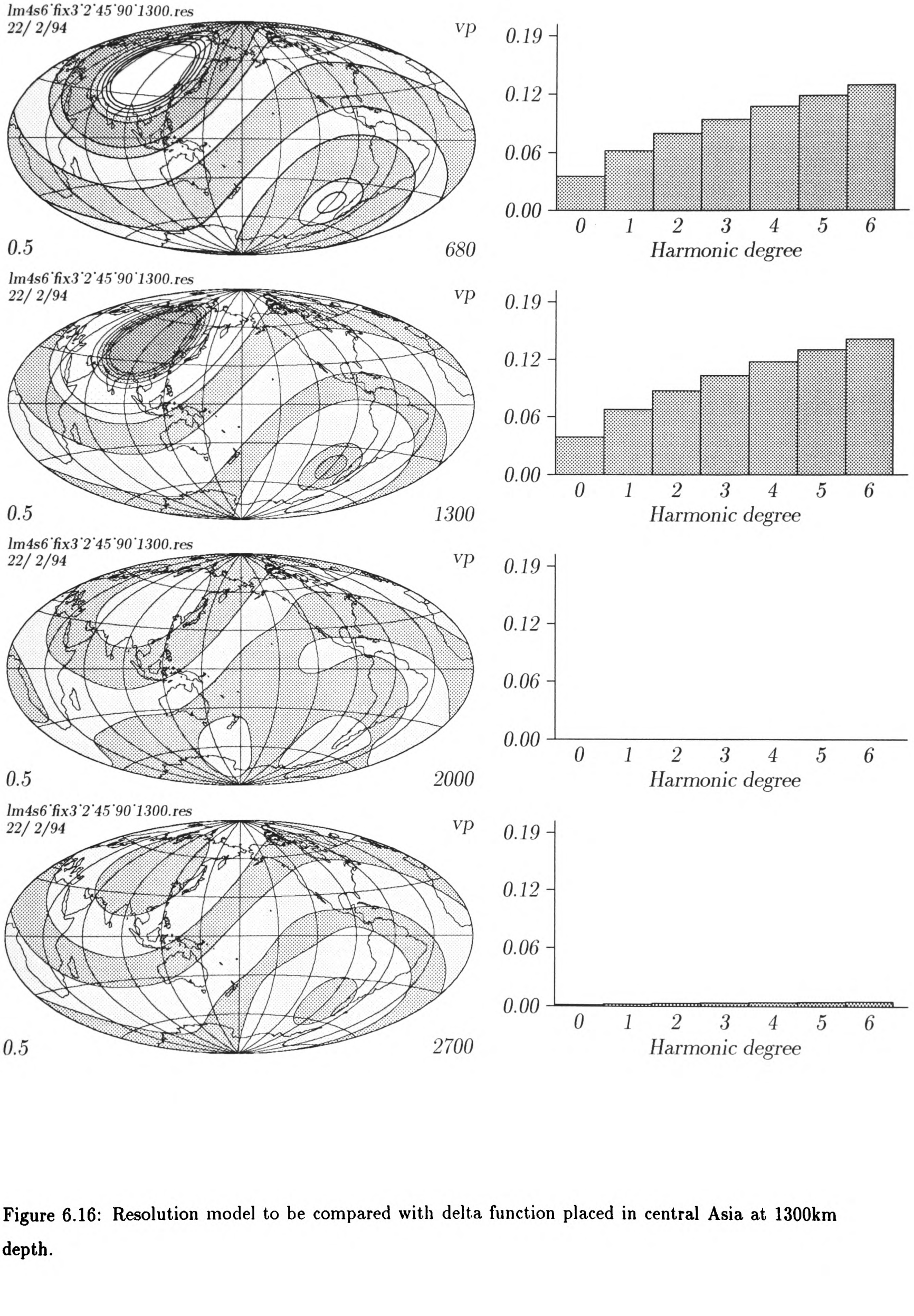


Figure 6.16: Resolution model to be compared with delta function placed in central Asia at 1300km depth.

Figure 6.17: Resolution model to be compared with delta function placed in central Asia at 2000km depth.

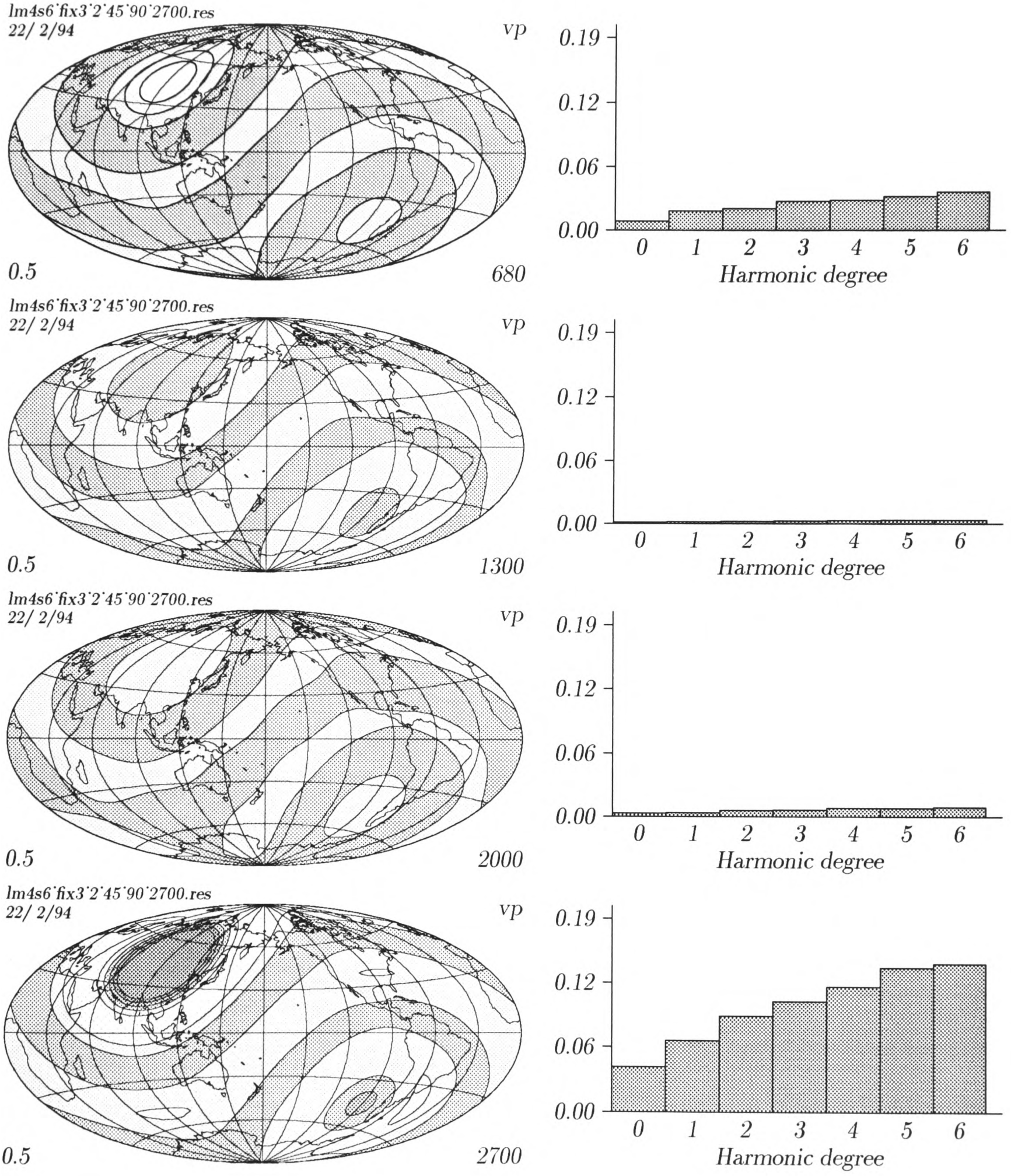


Figure 6.18: Resolution model to be compared with delta function placed in central Asia at 2700km depth.

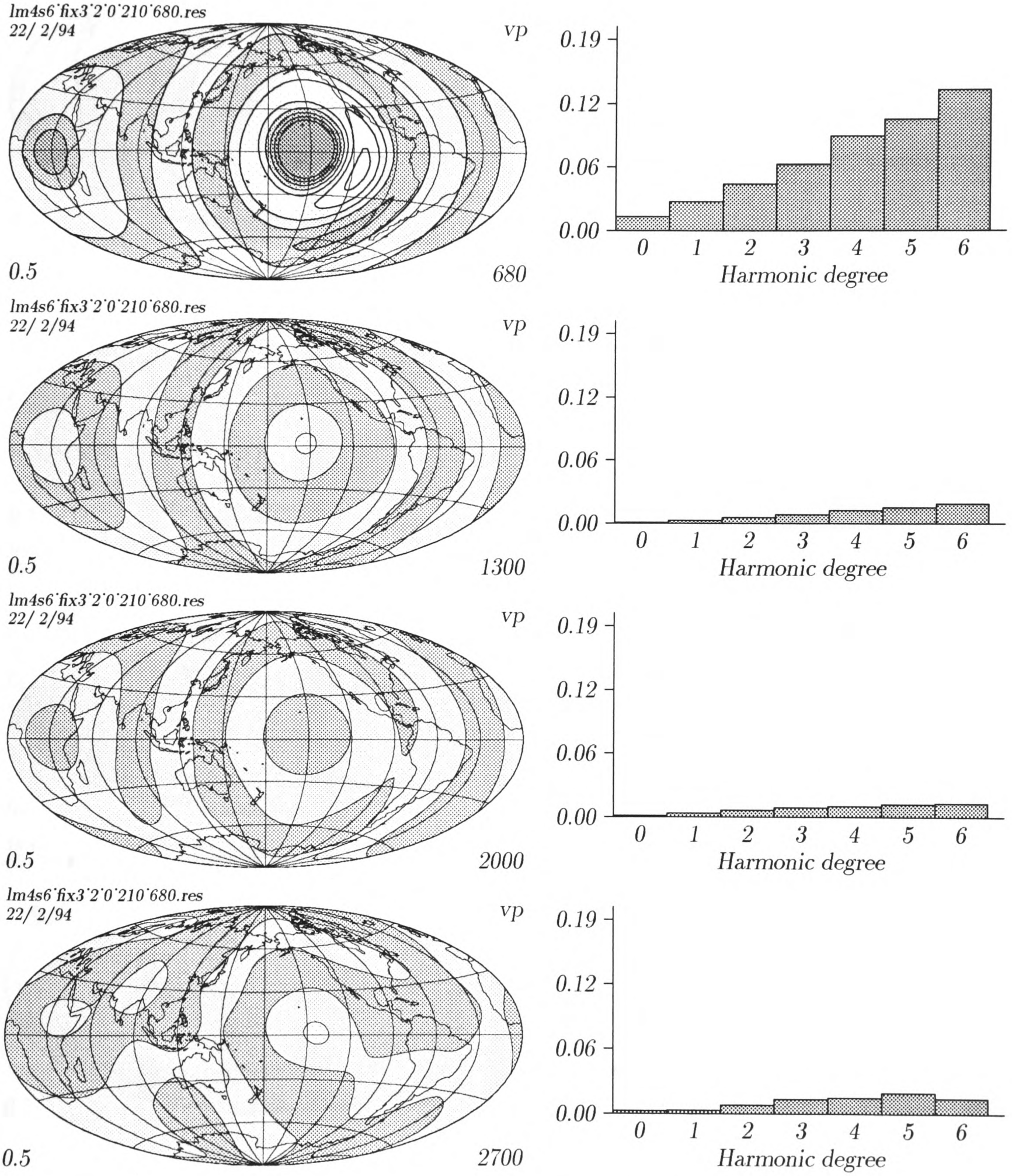


Figure 6.19: Resolution model to be compared with delta function placed in central Pacific at 680km depth.

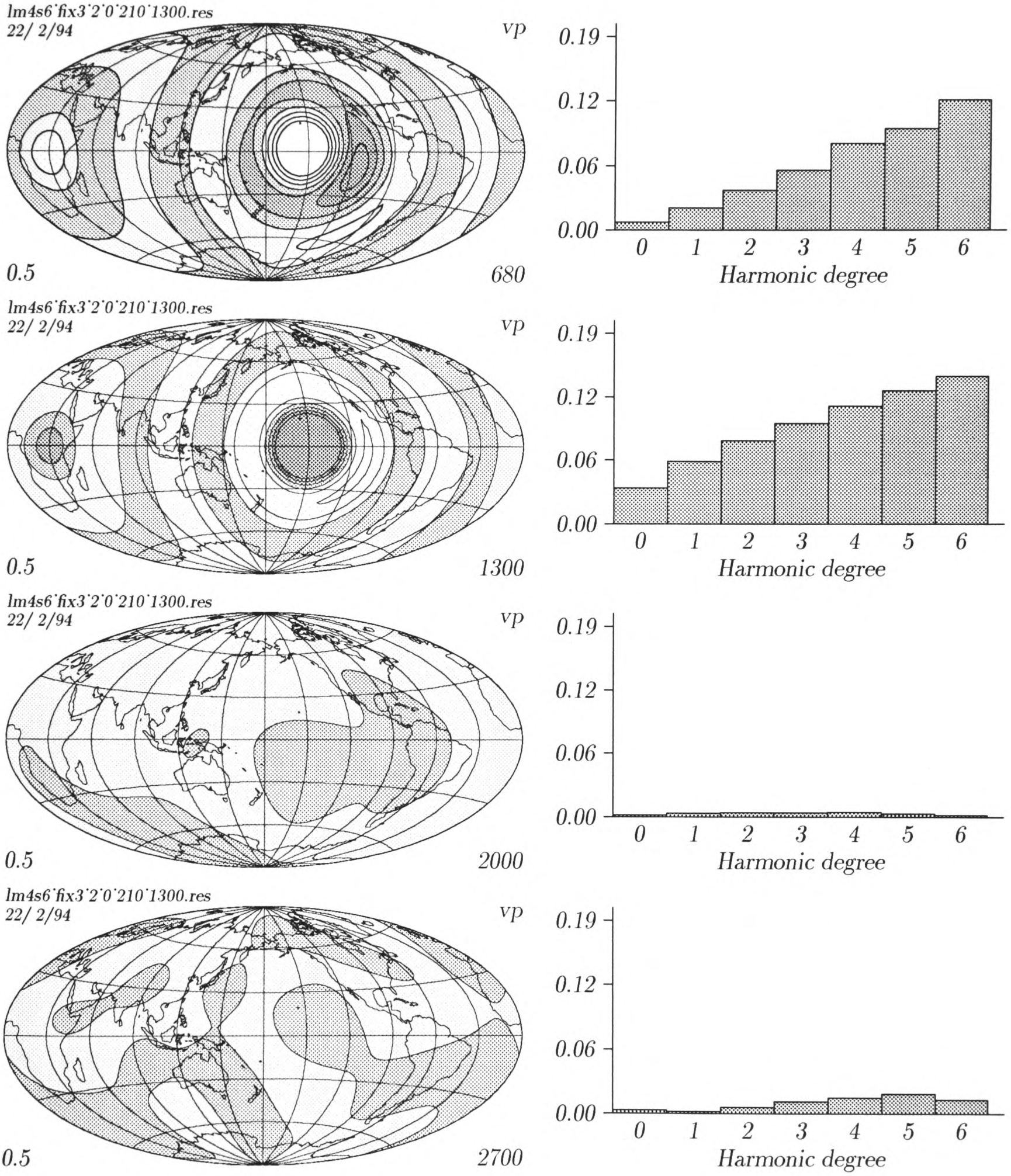


Figure 6.20: Resolution model to be compared with delta function placed in central Pacific at 1300km depth.

Figure 6.21: Resolution model to be compared with delta function placed in central Pacific at 2000km depth.

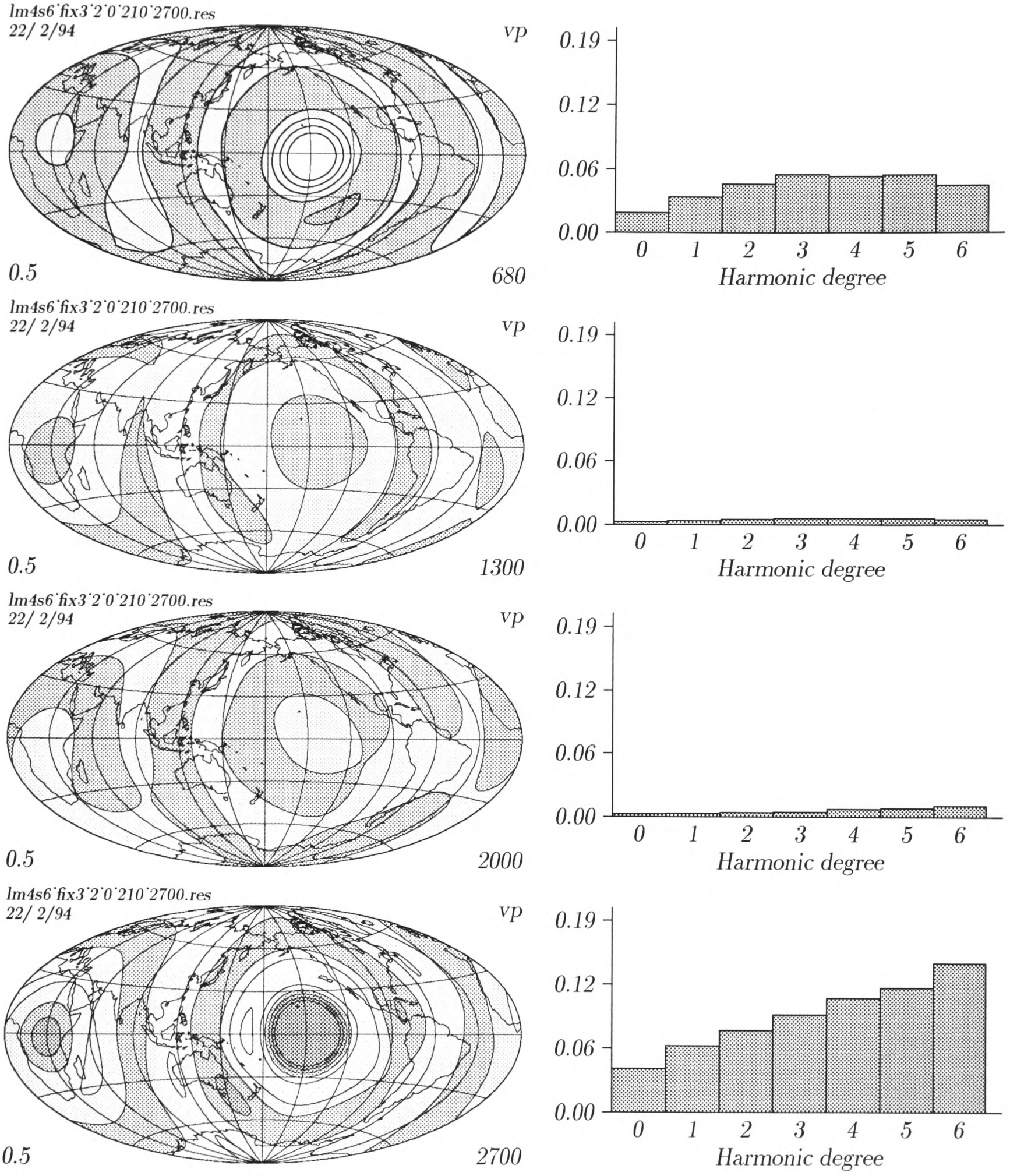


Figure 6.22: Resolution model to be compared with delta function placed in central Pacific at 2700km depth.

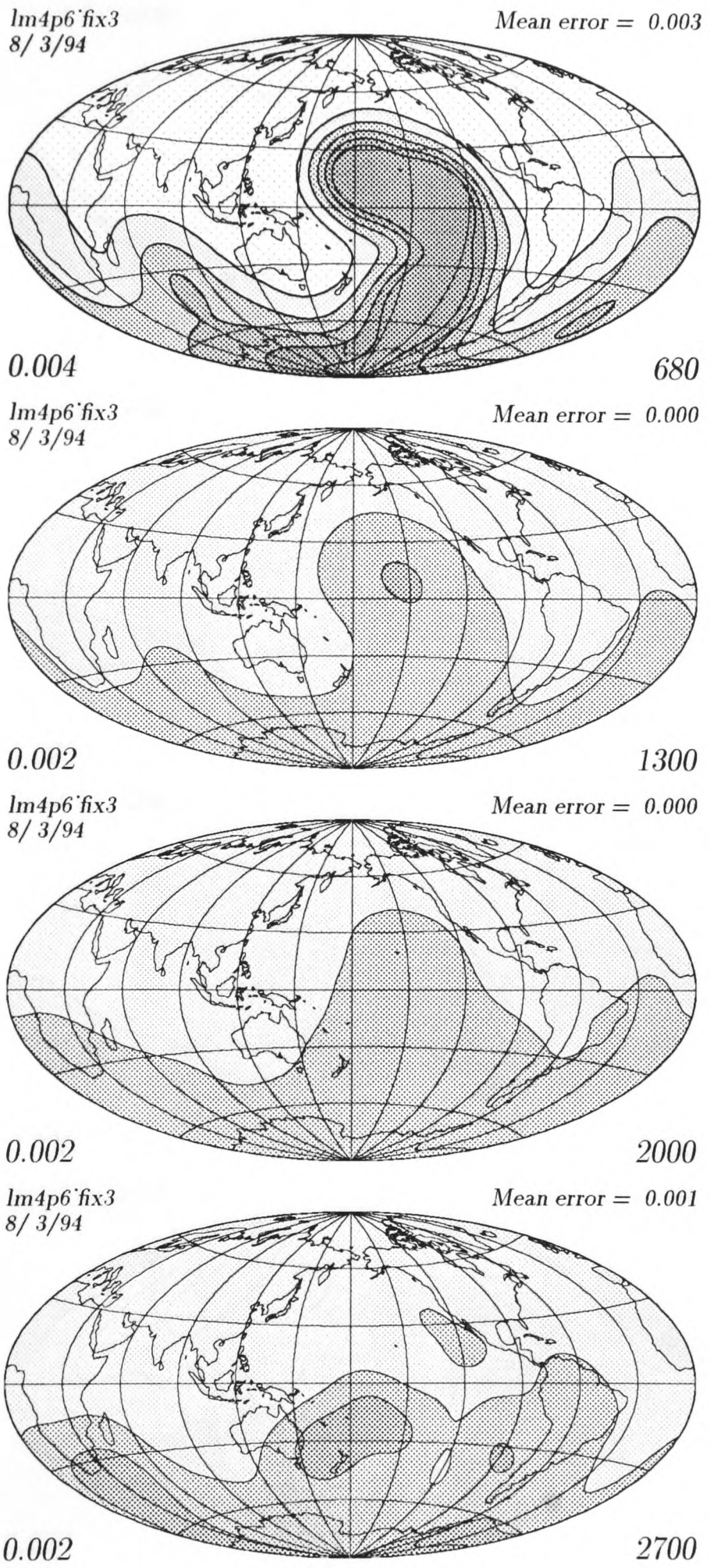


Figure 6.23: Velocity perturbation variance of the P model. The contouring is done about a mean value given in the top right hand corner of each sub plot. The contour saturation level is given in the bottom left hand corner.

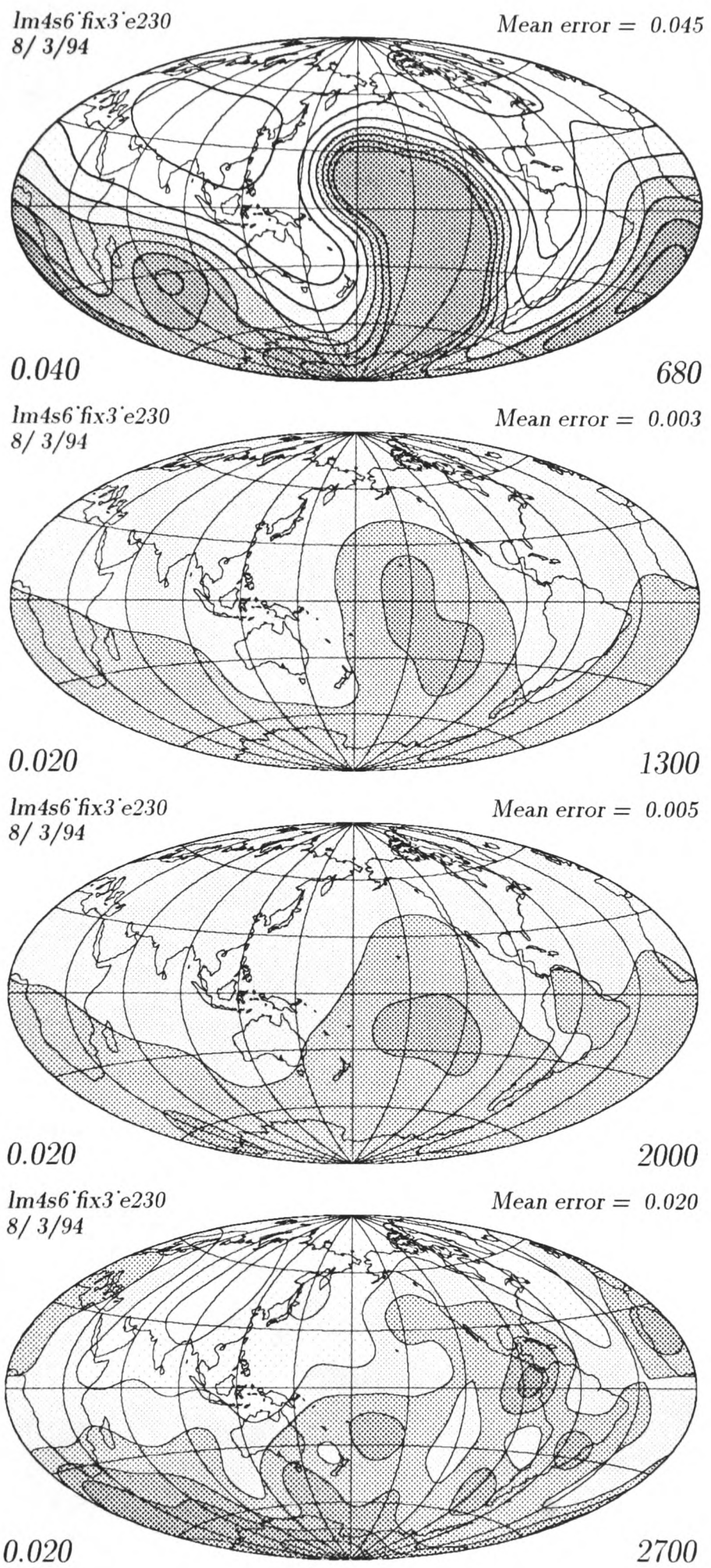


Figure 6.24: Velocity perturbation variance of the S model. The contouring is done about a mean value given in the top right hand corner of each sub plot. The contour saturation level is given in the bottom left hand corner.

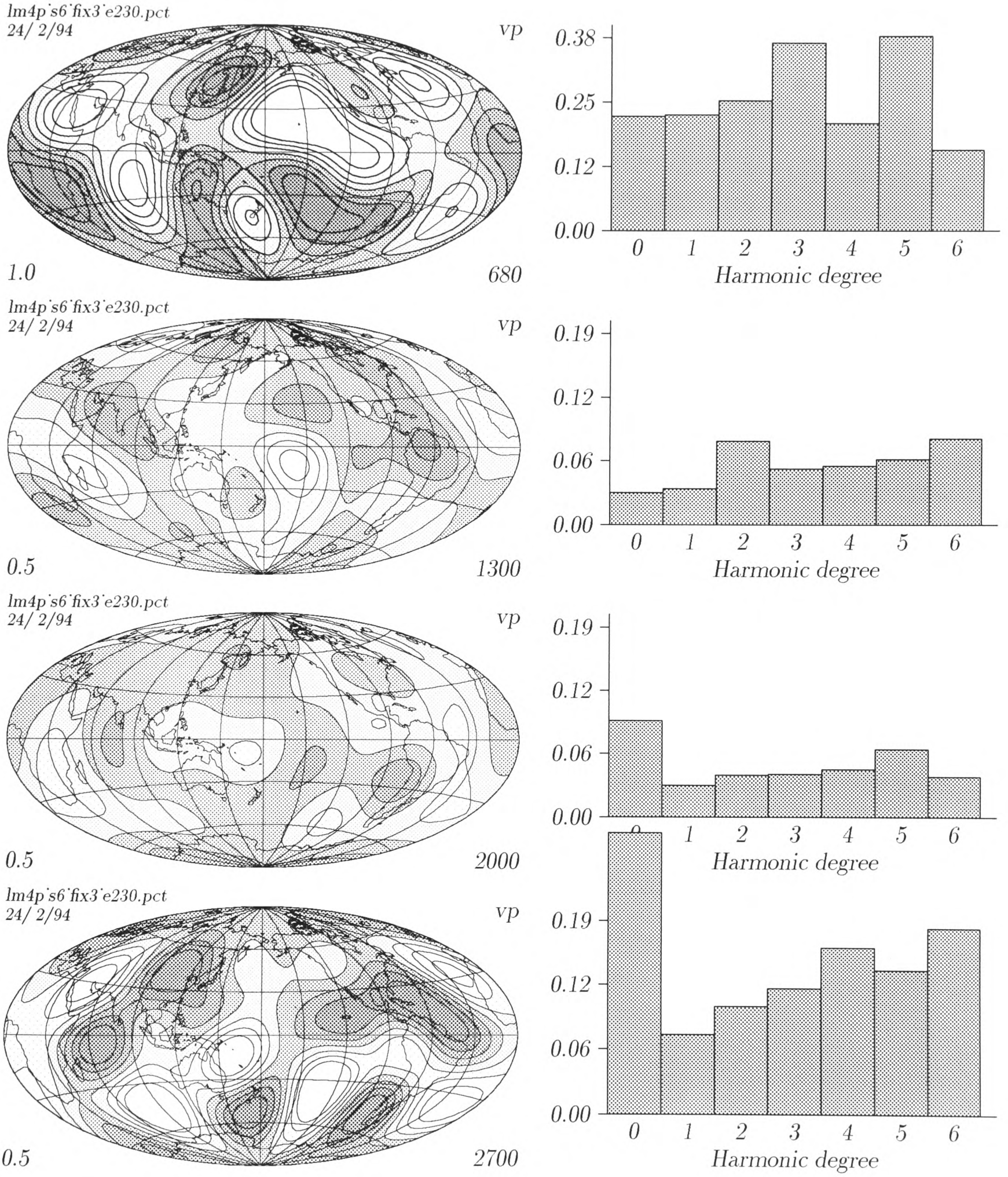


Figure 6.25: PS model using 220 out of the possible 245 eigenvalues.

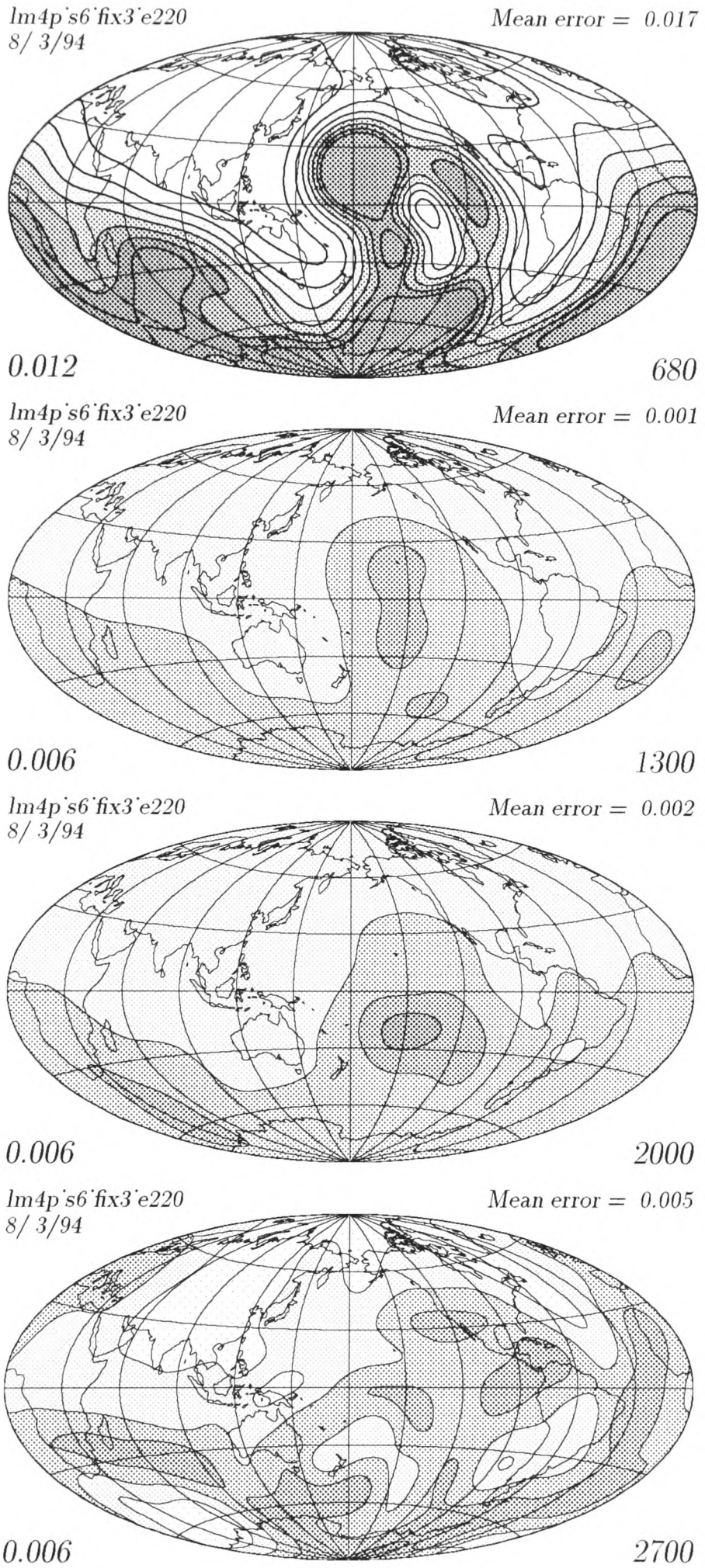


Figure 6.26: Velocity perturbation variance of the PS model constructed from 220 eigenvalues. The contouring is done about a mean value given in the top right hand corner of each sub plot. The contour saturation level is given in the bottom left hand corner.

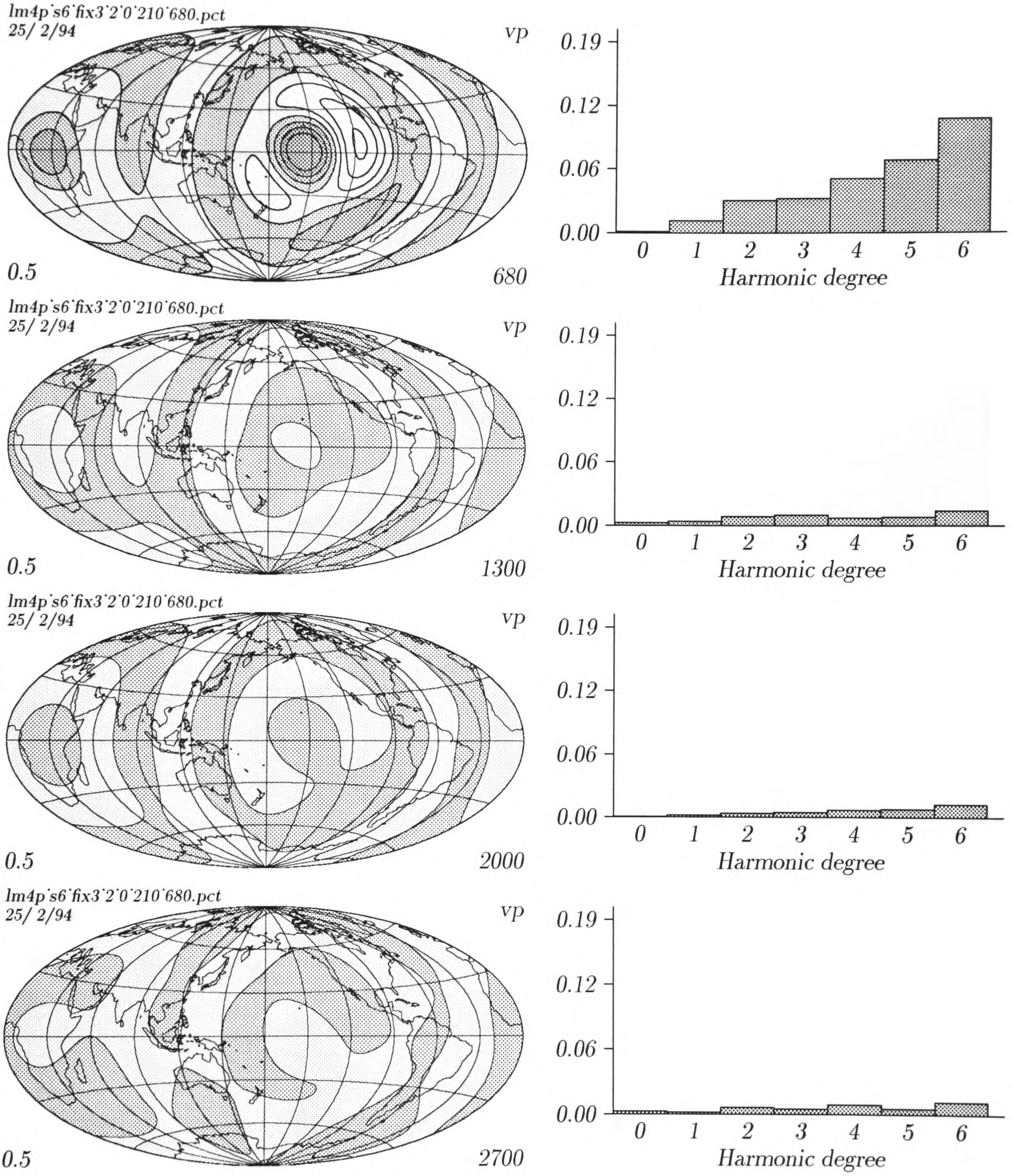


Figure 6.27: P.S resolution model to be compared with delta function placed in central Pacific at 680km depth.

Figure 6.28: P.S resolution model to be compared with delta function placed in central Pacific at 1300km depth.

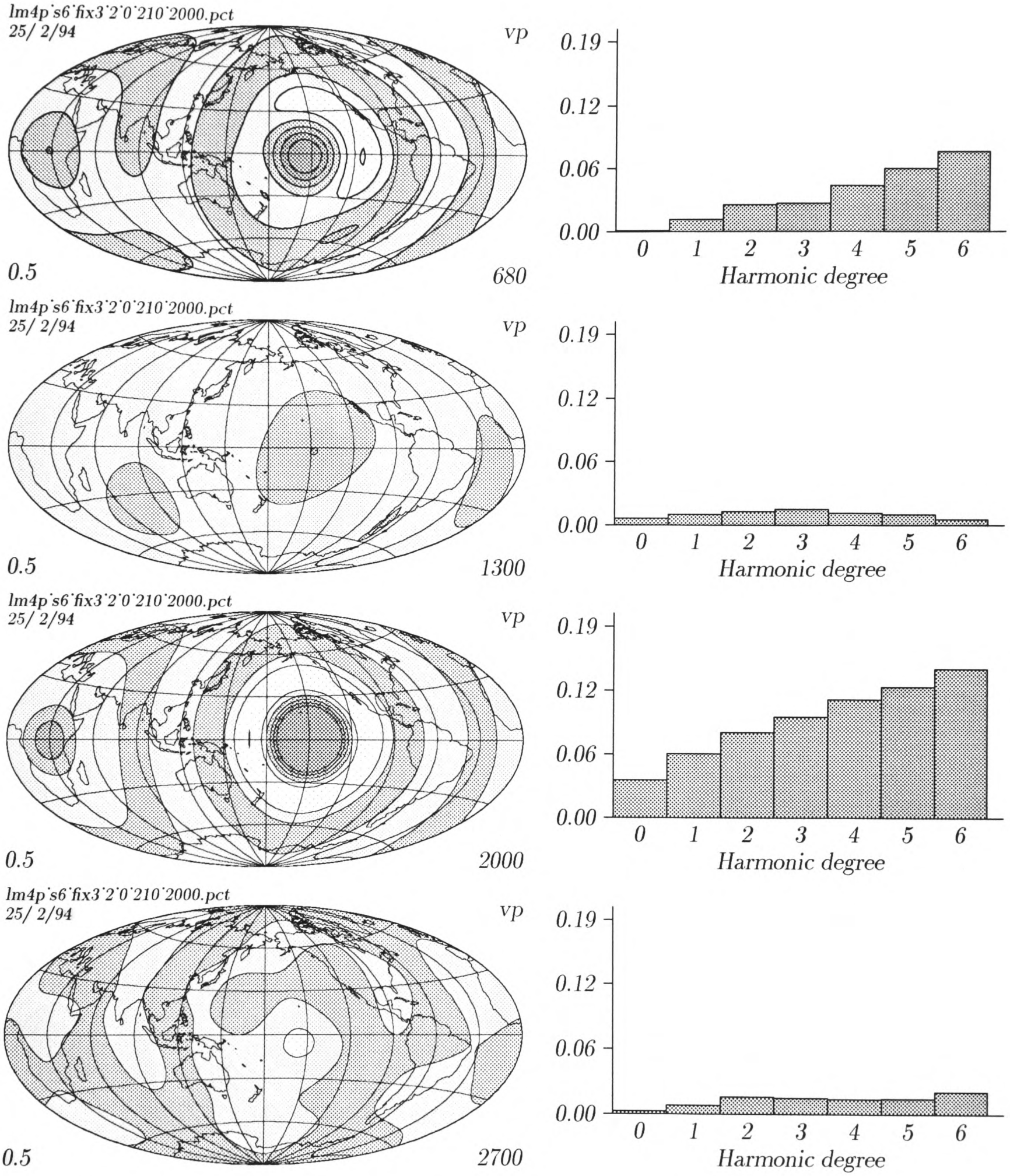


Figure 6.29: PS resolution model to be compared with delta function placed in central Pacific at 2000km depth.

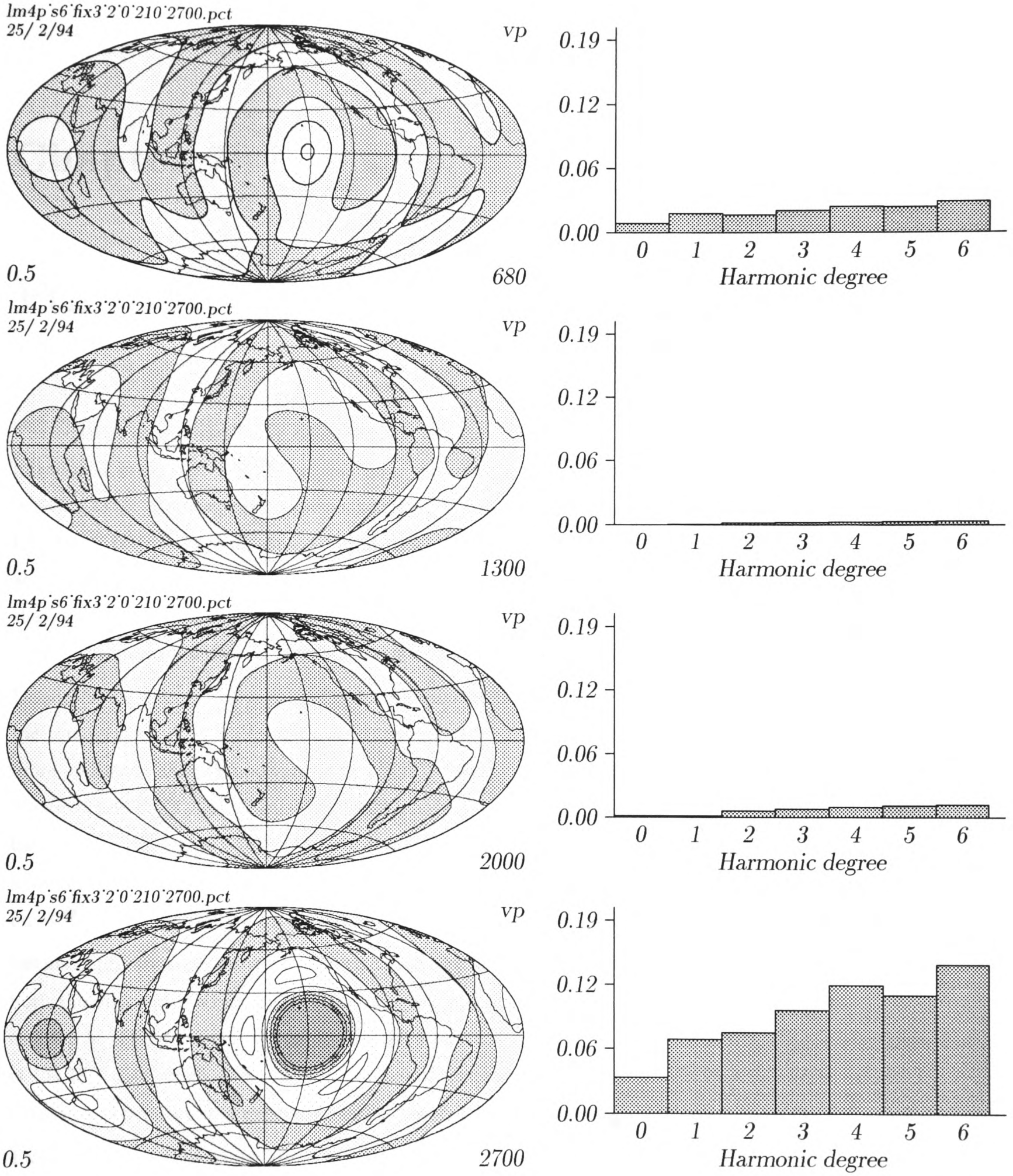


Figure 6.30: P.S resolution model to be compared with delta function placed in central Pacific at 2700km depth.

Chapter 7

Further parameterizations

The concept of a model being dependent on the parameterization as well as the data themselves was introduced in section 1.2. There has been considerable debate in the literature over the validity of deriving three dimensional low order harmonic expansions of velocity perturbations within the earth because of the effects of aliasing – does the higher degree heterogeneity map onto the lower ones if they are not included in the inversion? The use of orthonormal functions as the basis for the models means that, in theory at least, all harmonics should be independent of eachother. In reality however, because of the non uniform nature of the ISC dataset, aliasing is possible.

Despite using datasets of vastly different frequencies, resolving powers, and various parameterizations, the tomographic models of mantle structure that have been derived since the late 1970s are becoming more and more alike (Woodward *et al.*, 1992). Several authors (*e.g.* Inoue *et al.*, 1990; Woodward & Masters, 1991b; Zhang & Tanimoto, 1991) have argued that heterogeneity is concentrated in the lowest harmonics with degree 6 being the cutoff point. There can still be areas of large amplitude small scale heterogeneity if the high degree harmonic coefficients, albeit with small coefficients, are in phase at one point. This fact does however suggest that the effects of aliasing will be small.

In this study aliasing is investigated by computing lower mantle models with higher parameterizations both radially and laterally. These are then truncated to the same parameterization as the models of chapter 5. The damping by eigenvalue cutoff point is vital in these models because the distribution of the ISC data alone does not warrant parameterizations beyond $n = 4$ and $l = 6$ – those chosen in chapter 5. Therefore it is expected that the models will need extensive damping.

Two new parameterizations have been chosen, $n = 6, l = 10$ and $n = 8, l = 12$. These are denoted 6A and 8C models respectively. The 8C models involve the calculation of 1521 coefficients, and this was found to be about the limiting size for the computer power available. Ideally the entire iterative process should be carried out with these parameterizations, but the time involved has proved prohibitive, so we use the same dataset and station corrections that were used to derive the final S model.

7.1 Calculation of models

The inversion for these models proceeds in exactly the same way as before, the only difference being in the use of more perturbation integrals (see equation 3.31). The model norm and variance versus eigenvalue number plots for the 6A and 8C cases are shown in figure 7.3. Choice of cutoff proves to be very difficult because of the large number of eigenvalues which makes both the model norm and variance curves smooth giving no obvious truncation point. The P model variance plots for the two parameterizations become almost horizontal quite quickly. However the equivalent S plots, particularly for the 8C model, continue to decrease steadily with increasing eigenvalue number. The apparent cutoff point seems to vary depending on the size of the Y axis of the model norm plots, so care has to be taken to ensure that the gradients of the initial linear parts of the model norm curves are equal on all graphs. As in any underdetermined inverse problem the choice of cutoff is somewhat subjective, and represents a choice of a particular point on the 'tradeoff curve' between resolution and error.

After experimentation with various plots the cutoffs are chosen to be 600 and 770 eigenvalues and eigenvectors for the S and P 6A models respectively, and 1030 and 1280 for the equivalent 8C models. For the standard depths these are plotted in figures 7.4 to 7.7.

One of the most noticeable features of these maps is the very low amplitude of the anomalies in the Pacific region at 680 km depth compared to those of the equivalent smaller parameterized models in figures 5.38 and 5.39. This is undoubtedly a result of the damping that has been applied to these models. These maps should be analyzed only in conjunction with their resolution and variance plots.

7.2 Resolution

Figures 7.8 to 7.15 show the resolution plots for the new higher parameterized models. They are presented in a slightly different way to those of chapter 6 in order to make the direct comparison of the resolution patterns of the P and S models easier. Each figure shows three sub plots:

1. Top: The input test model delta function plotted at the depth at which the spike is synthesized.
2. Middle: The S model resolution pattern plotted at the same depth.
3. Bottom: The P model resolution pattern for the same depth.

Not all depths and spike locations are used for all models because the number of plots involved would become very large. The examples chosen are representative of the properties of the resolution operator and are shown in the table 7.1.

These resolution patterns are consistent with those of the lower parameterized models in chapter 6 – the resolution is good where the ray coverage is good. Both the 6A and 8C resolution maps display the

	6A models		*8C models*	
depth	*central Asia*	*central Pacific*	*central Asia*	*central Pacific*
680	...	...	fig 7.12	fig 7.14
1300	fig 7.8	fig 7.10	...	...
2000	...	...	fig 7.13	fig 7.15
2700	fig 7.9	fig 7.11	...	...

Table 7.1: Key to plotted resolution maps.

same characteristics to a greater or lesser extent, and the following descriptions can be applied to both parameterizations.

The delta function is reproduced almost perfectly in both pattern and amplitude for all depths when the input spike is placed under central Asia. The S map is always very slightly worse than the P equivalent, with the differences increasing with depth. However, when the delta function is placed under the central Pacific region, the resolution is severely restricted. At the top of the lower mantle the resolution of both P and S models are shown to be extremely bad. Almost all of the input signal is lost and the size of the peak is hardly larger than the remaining pattern. This means that a strong localized anomaly in the central Pacific region at this depth cannot be resolved. Figure 7.10 shows that at 1300km depth the resolution improves greatly and a strong peak in the central Pacific is again resolvable. Nevertheless the harmonic spectra shows that at least 70% of the overall amplitude is lost, with the majority missing from the lower harmonic degrees. Resolution steadily improves with depth down to 2700km (figure 7.11) where the replication of the test delta function by the P model resolution matrix is much better, with good amplitude and pattern recovery. The lack of shear wave data at this depth severely affects the resolution of the S model – only $\approx$ 50% of the input signal is recovered, and this only slightly resembles the delta function signal.

In conclusion, therefore, the features of the 6A and 8C models under central Asia can be treated as reliable, whereas those under the Pacific need to be treated with caution, with their amplitudes at least being severely underestimated.

7.3 Variance

The variance plots for the 6A parameterizations are shown in figures 7.16 and 7.17 for the S and P models respectively. The contour intervals of these plots are five times greater than those for the $n = 4, l = 6$ (denoted 4_6) models of chapter 5 (figures 6.23 and 6.24). Similarly the mean values of the variances at each depth are at least three times as large. The one exception to this is in the 2700km map of the 6A S model variance plot, which is greater by only around 60%, and could be an indicator that this model is proportionately more damped in this region compared to the 4_6 model. The smaller contour values of this plot compared to figure 6.24 at this depth are also consistent with this hypothesis.

In terms of the features in the variance plots, the overall patterns are approximately the same as those

for the lower parameterized models – relatively small variances in the northern hemisphere compared to the southern hemisphere and the Pacific. However in the top map (680km) there are significant differences. In addition to the continents which show small variances at this depth, the central Pacific region variances are also very small. This apparent contradiction between having simultaneously no data and very small model variances is explained when figure 7.14 is taken into account. Here the resolution is very bad, and since the resolution is a function of only the eigenvalue cutoff number, the effects of damping are most significant here. Hence there are very small errors because the model is highly damped. There exists a fundamental trade–off between model resolution and model variance. If the model is undamped the resolution is perfect, but the errors are large as a consequence. If the model is highly damped, the errors associated with the model are small, but the resolution suffers.

The 8C models variance plots of figures 7.18 and 7.19 have the same characteristics as the 6A plots described above. The mean errors are greater by a factor of approximately two which makes them greater than the 4_6 models of chapter 5 by at least six.

7.4 Comparison of the models

7.4.1 6A

At 680km depth, restricting comparison of the models to where resolution is good and model variance is low effectively means looking at continental regions. However these land masses are where most of the seismic stations are located, and, as was described in detail in chapter 5, this is where the model is going to be most severely affected by the trade–off with the station corrections in the iterative procedure. As a result, comparison of the models at this depth will not give physically meaningful results.

Examination of the P and S models at intermediate depths is legitimate everywhere except in the central Pacific region where, as figure 7.10 shows, there is considerable loss of resolution as a result of the eigenvalue cutoff damping. The 1300km maps of figures 7.4 and 7.5 show several similarities:

- fast under northern South America, New Zealand, south of Tasmania, India, and eastern Siberia. This forms the ring of high velocities that is observed in the 4_6 models in section 5.5.3
- slow under southern South America and Australia.

Correlation at 2000km depth is not as pronounced but there are distinct similarities. Again these are predominantly where resolution is good.

- The maps under the entire Asian continental land mass show several features in agreement – fast under India, eastern China, and the Middle East.
- There are slow anomalies under northern Europe, Indonesia and Greenland.
- North America is predominantly fast, although there are discrepancies in some of the anomalies.

It should be noted that these similarities are all in the northern hemisphere where there is good data coverage.

At 2700km depth the dominant degree 2 pattern is more pronounced in the S model plot. However, contributing to the ring of high velocities around the Pacific, both the P and S models show fast anomalies in Eastern Asia, in the Indian Ocean, south eastern Pacific, under Kamchatka, and the west coast of Africa extending both north into western Europe and south into the Atlantic Ocean. There are however several features present in one but not the other. The most obvious case is in western North America where the P model shows a large fast anomaly in disagreement with the large slow anomaly of the S model.

In conclusion, therefore, the models do correlate well where the data coverage is good, *ie.* predominantly under the continents in the northern hemisphere.

7.4.2 8C

Examination of the two 8C models of figures 7.6 and 7.7 reveals many of the similarities described above for the 6A models. Again it is clear that correlation is best in the upper mid mantle regions especially under the Americas and Asia. Furthermore, comparison of the two sets of further parameterized models, 6A and 8C, shows striking similarities and provides further evidence that these are real features within the lower mantle and not artifacts of the model parameterization.

7.4.3 Correlation coefficients

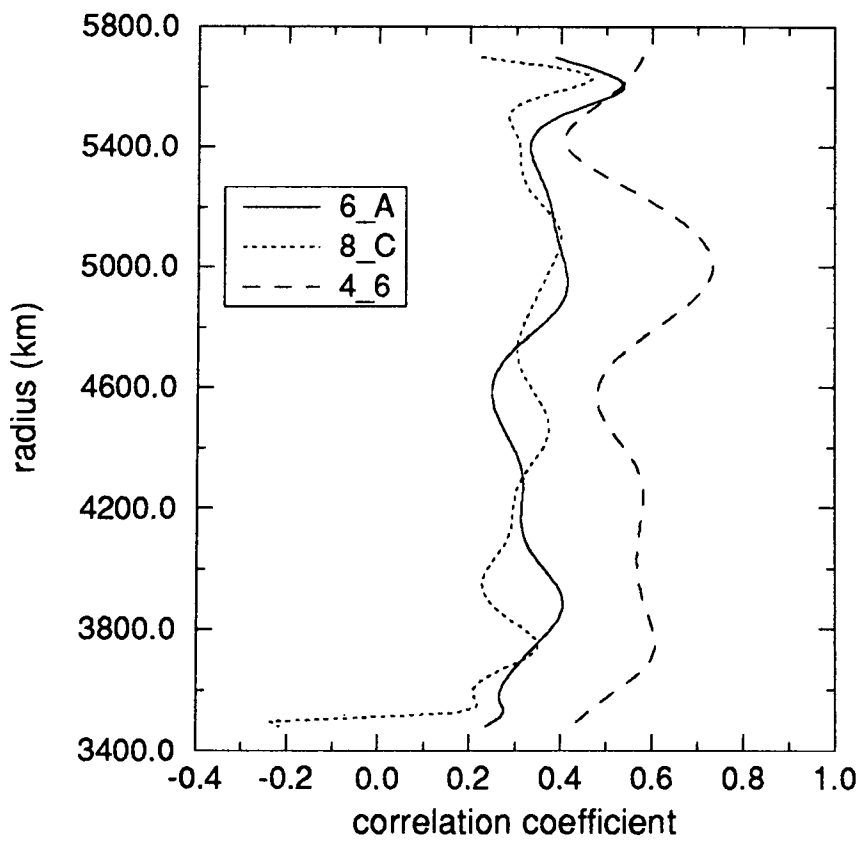


Figure 7.1: Correlation coefficients of the P and S models with all parameterizations

The correlation coefficients between the P and S models with all three model parameterizations to date are shown in figure 7.1.

In general the 6A models correlate better than the 8C models, and both range from 0.2 to 0.5 close to the 670km discontinuity. Considering the number of model parameters involved, these values are encouraging. In the next chapter it will be shown that the models of this study generally correlate well with other models at 1300km and 2700km depth, and this feature is reproduced here albeit to a lesser degree.

7.5 Aliasing

The effects of aliasing can be investigated by truncating the further parameterized models of this chapter to the standard parameterizations $n = 4, l = 6$ of chapter 5.

7.5.1 S

The results are shown in figures 7.20 and 7.21 for the 6A and 8C models respectively. It is clear that the two are almost identical in terms of both harmonic spectra and features. Comparison of these maps with the final lower parameterized S model in figure 5.39 shows that the models are very similar in the mid mantle regions, but there are significant differences elsewhere. For example, at 680km depth the main problem lies in the regions with poor data coverage, most notably in the Pacific where the anomalies are of the same sign but vastly different amplitudes. This description can be extended to the whole model pattern near the CMB where the features of the 4_6 models are exactly the same, but different in terms of amplitude.

At 680km depth the localized differences cause the power spectra to be uncorrelated, while at 2700km depth, because the features are the same, there is a factor of two difference in each harmonic coefficient. As a result, and because the models are so similar in the well constrained mid mantle regions, the differences in the top and bottom maps are probably not attributable to aliasing but to the different degrees of damping. Results from section 8.2 will show that the 4_6 S model of this study is far larger in the deepest mantle than all other S models examined. It is highly unlikely that these models systematically underpredict the S heterogeneity at these depths because they are derived using a variety of datasets. At the same time it is likely that the 4_6 model of this study is underdamped in this region as there is very little data to constrain the pattern of heterogeneity. 4_6 S models computed with fewer eigenvalues do indeed correlate better with the truncated higher parameterized models, but this choice of eigenvalue cutoff would not have been the primary one.

The correlation coefficients for the three models discussed here are shown in the left plot of figure 7.2. These agree with what has been said qualitatively above – correlation of the two truncated 6A and 8C models is excellent, averaging 0.9 throughout the lower mantle. When these are compared to the 4_6

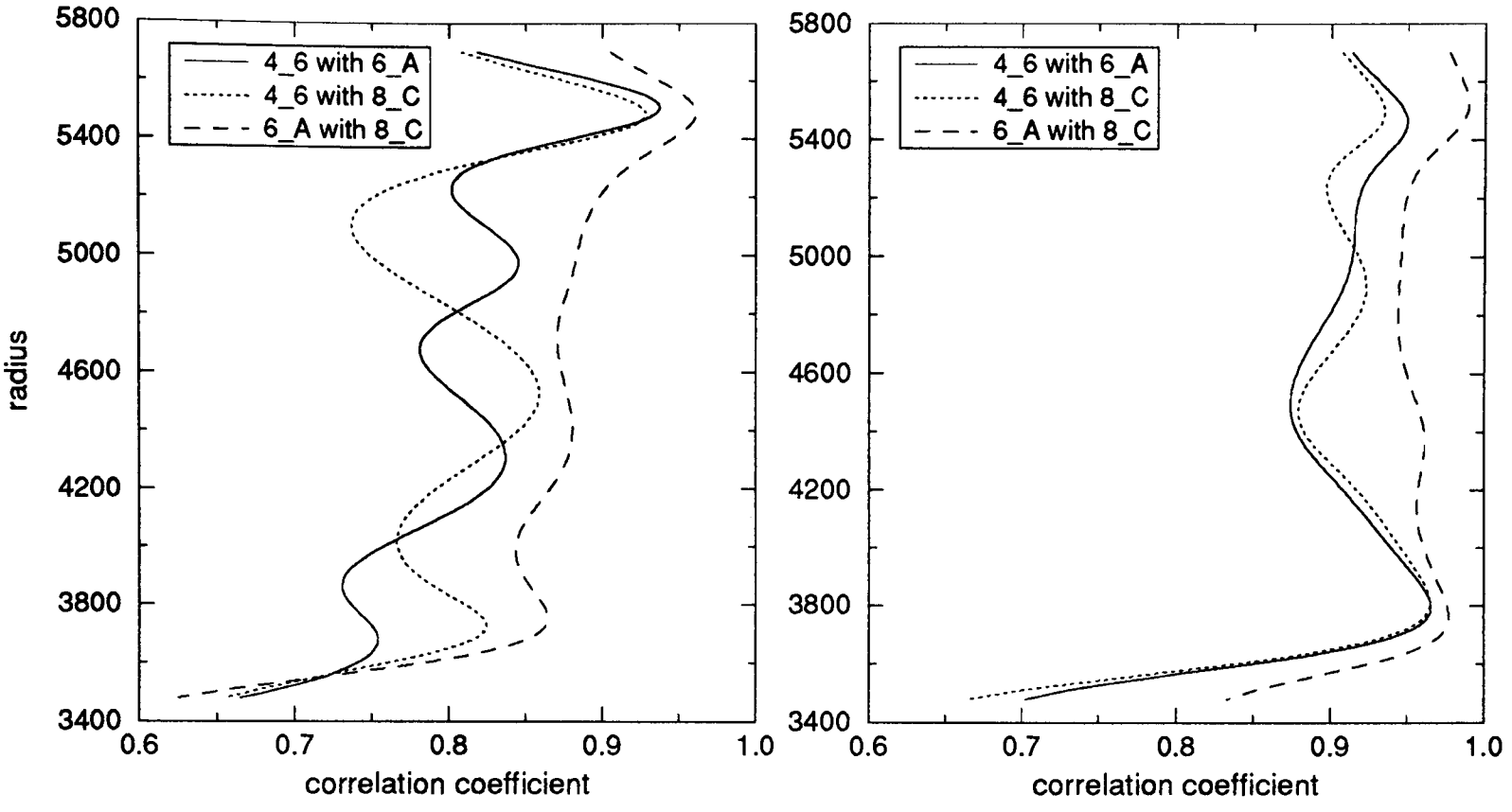


Figure 7.2: Correlation coefficients of the truncated models of this chapter and the 4_6 models of chapter 5. S left, P right.

model the similarities are not quite as good, ranging from about 0.9 at 800km depth to 0.7 near the CMB. It is slightly strange that the correlation coefficients for the depths at which the two middle maps are plotted are approximately the same as the correlation coefficients at 680km depth, representing the top map, where it was believed the features and harmonic spectra were not that similar. This may be caused by the models being almost identical in areas where resolution is good, *e.g.* Asia, India, and Africa.

7.5.2 P

The similarities between the truncated 6A and 8C P models in figures 7.22 and 7.23 are even more pronounced than those of the S models. This is evident from the correlation coefficients between the two which average at over 0.95. They also compare far more favorably with the final 4_6 P model of chapter 5 (figure 5.38). Again correlation is excellent in mid mantle regions, but this time the sub plots at 2700km depth also agree well in terms of features and harmonic spectra. In the same way as the S model, at the top of the lower mantle differences exist in the poorly constrained regions, particularly under the Pacific and Indian Oceans. However these differences are less pronounced and only affect degrees 2 and 5. The correlation coefficients between these models and the 4_6 model are higher than the equivalent S plots. This agrees with the hypothesis of the previous subsection that the differences between the truncated larger expansion S models and the 4_6 S model are attributable to differences in damping rather than aliasing.

7.5.3 Variance reductions

The variance reductions obtained for the 6A and 8C truncated S models are 7.35% and 6.93% respectively, which is to be compared with 8.93% for the standard 4_6 model. The equivalent P variance reductions are 10.02% and 9.95%, and 10.81% for the standard model. The differences in the truncated higher parameterized S models variance reductions are lower probably because of the differences in damping.

7.6 Conclusions

In this chapter it has been shown that it is possible to derive models of lower mantle heterogeneity with large parameterizations provided that careful attention is paid to damping. Analysis of these models can only be done in conjunction with plots of model resolution and variance.

Considering the number of degrees of freedom involved in the calculation of these models, average correlation coefficients of 0.3 to 0.4 are quite high. In areas where resolution is high and model variance is low, the agreement of features between the different parameterizations of the shear or compressional models is excellent, proving that they are not artifacts of the model parameterizations used, and verifying their existence. In the same areas, the good correlation of features between the P and S models at each parameterization suggests that the heterogeneities may well be proportional.

The objectives of this chapter have been principally to investigate the effects of aliasing. Correlations of all P model parameterizations are very high and show that aliasing, at least from the additional degrees considered, is not a problem in the 4_6 models. Correlations of the S models are not as good, but these differences are probably attributable to different damping and not aliasing.

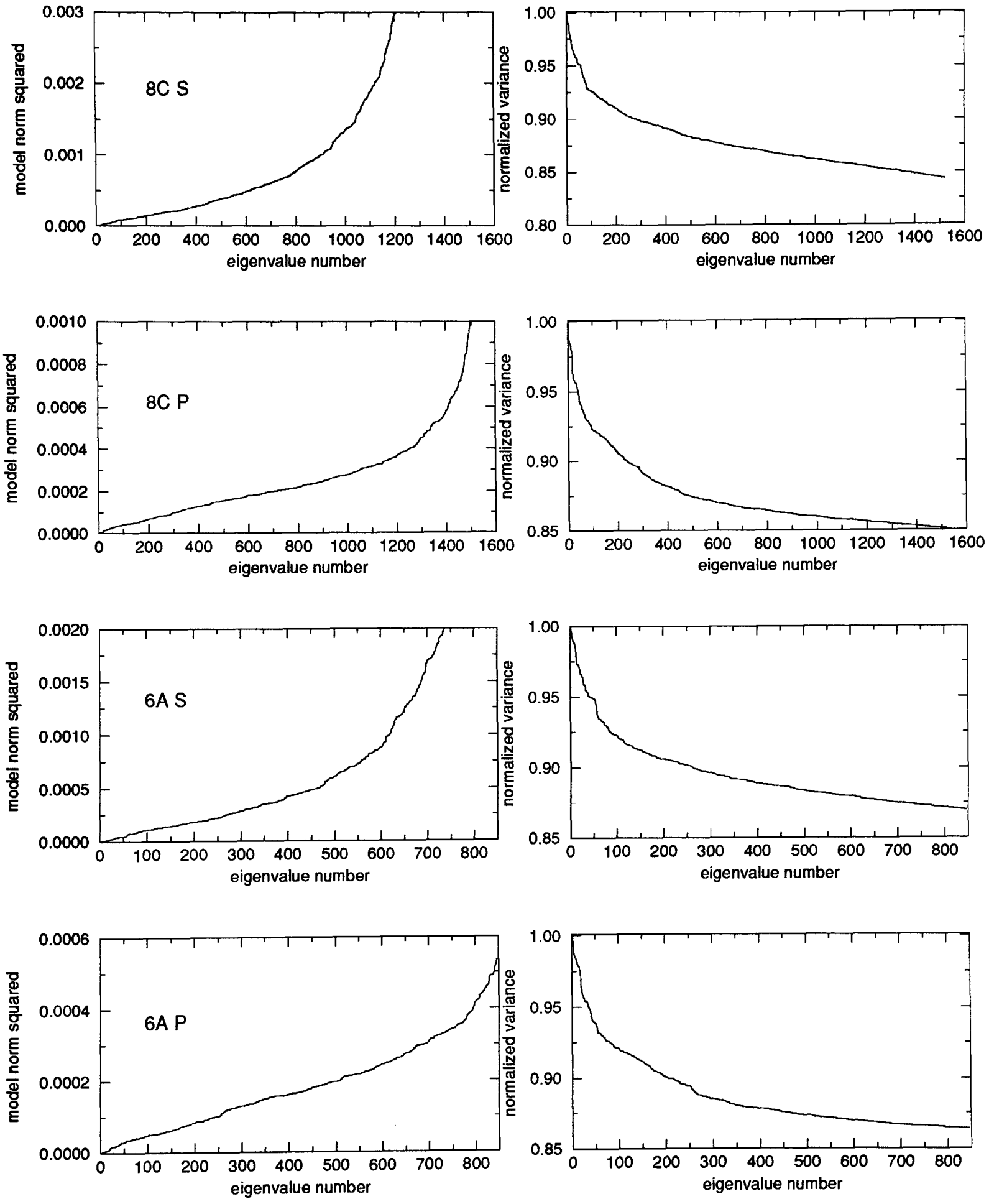


Figure 7.3: Model norm and variance plots for the larger parameterized P and S models. The eigenvalues are ordered largest to smallest.

Figure 7.4: $n, l = 6, 10$ S model constructed using the best known 600 eigenvalues and eigenvectors of the inner product matrix.

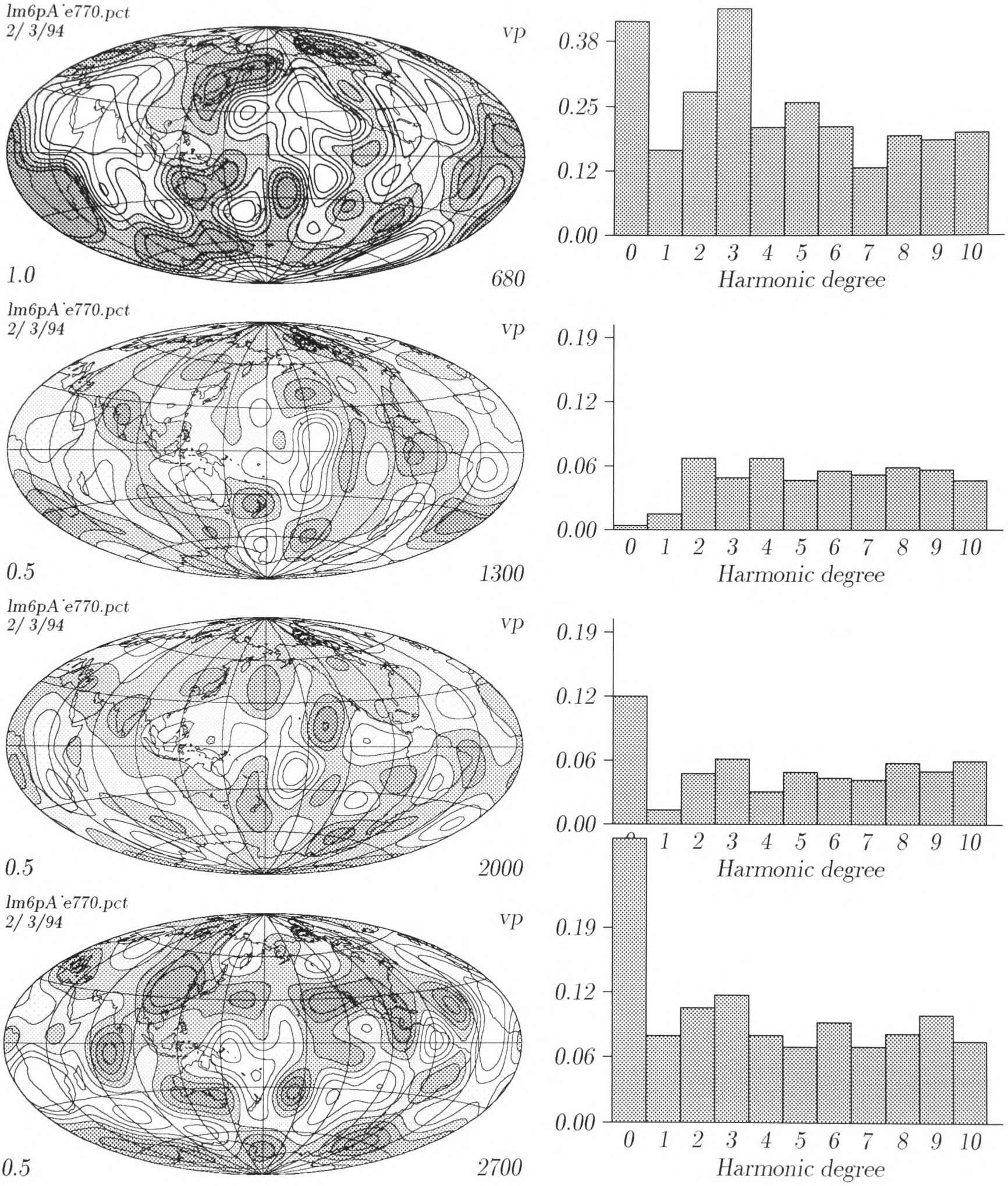


Figure 7.5: $n, l = 6, 10$ P model constructed using the best known 770 eigenvalues and eigenvectors of the inner product matrix.

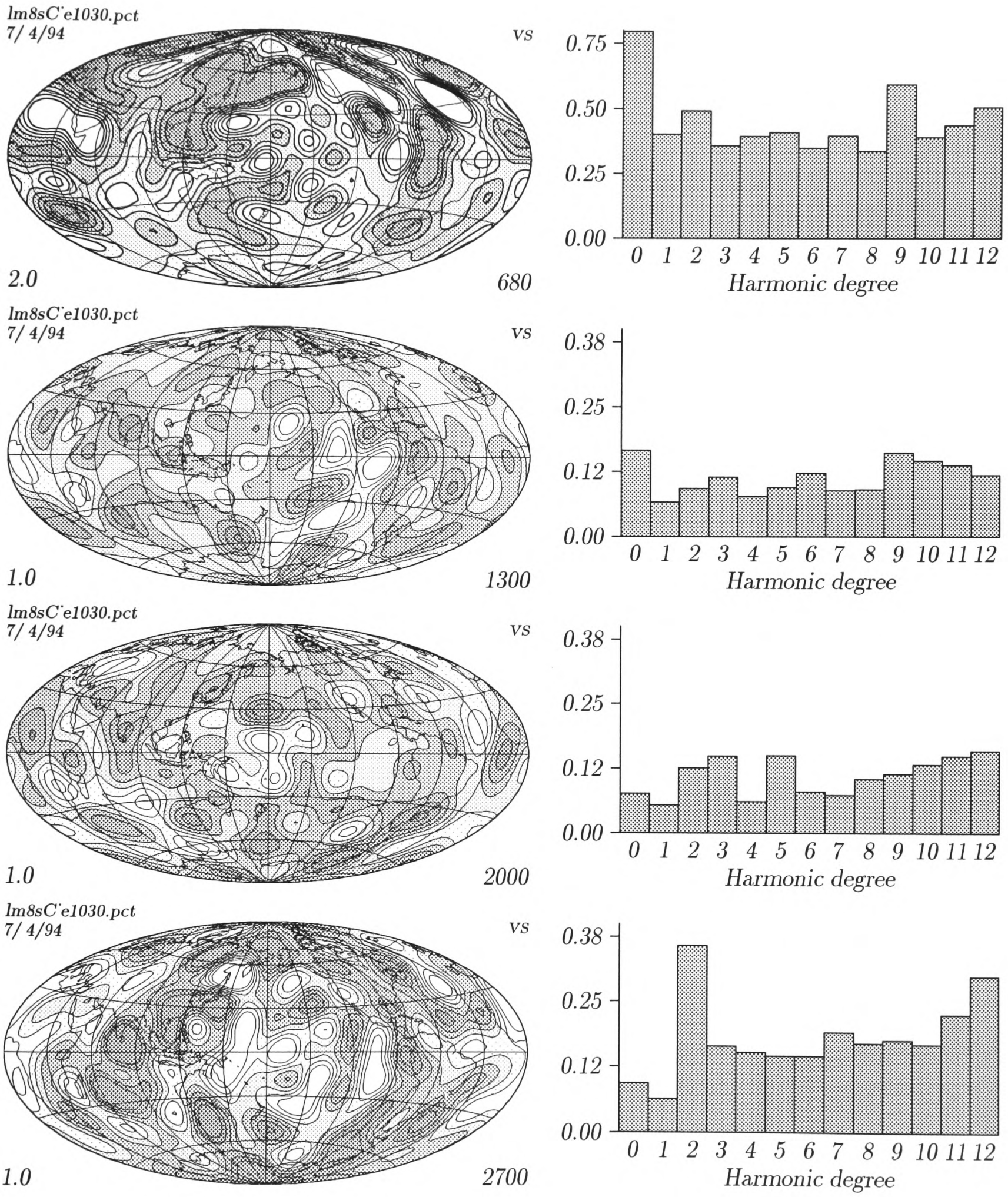


Figure 7.6: $n, l = 8, 12$ S model constructed using the best known 1030 eigenvalues and eigenvectors of the inner product matrix.

Figure 7.7: $n, l = 8, 12$ P model constructed using the best known 1280 eigenvalues and eigenvectors of the inner product matrix.

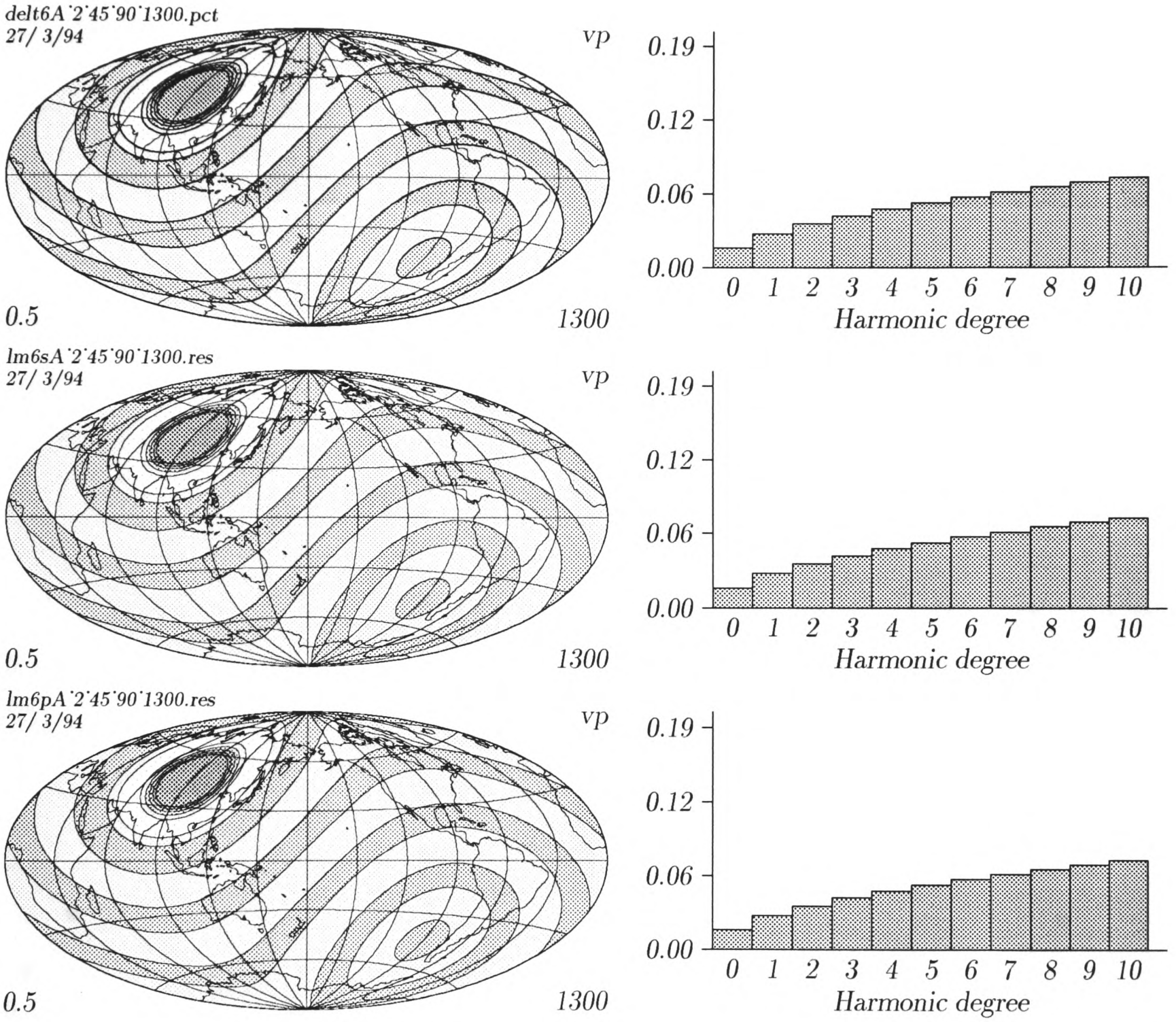


Figure 7.8: Resolution maps for the 2% amplitude input delta function (top) in central Asia at 1300km depth. Middle and lower maps correspond to the resolution patterns of the S and P 6A models at the same depth.

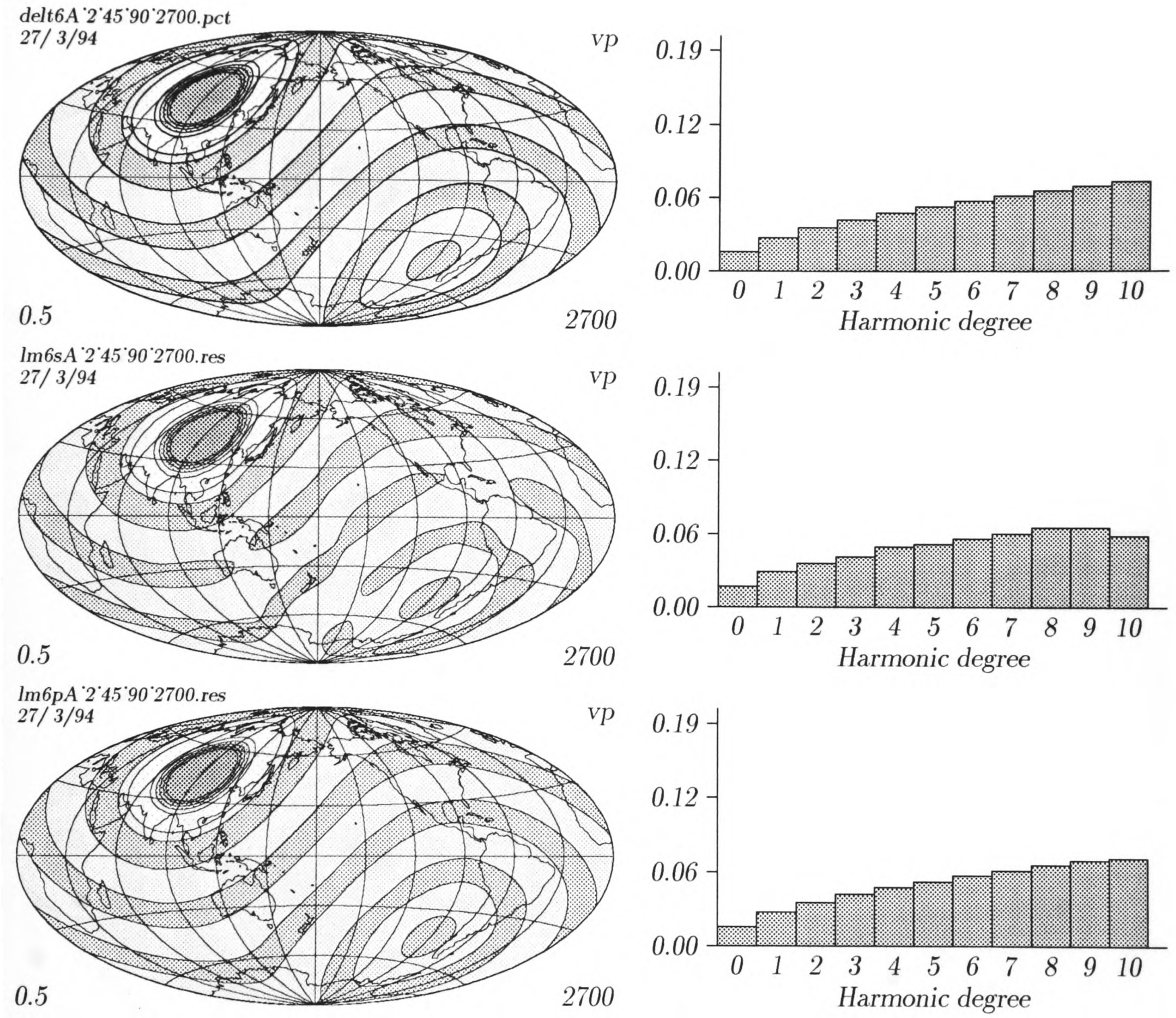


Figure 7.9: Resolution maps for the 2% amplitude input delta function (top) in central Asia at 2700km depth. Middle and lower maps correspond to the resolution patterns of the S and P 6A models at the same depth.

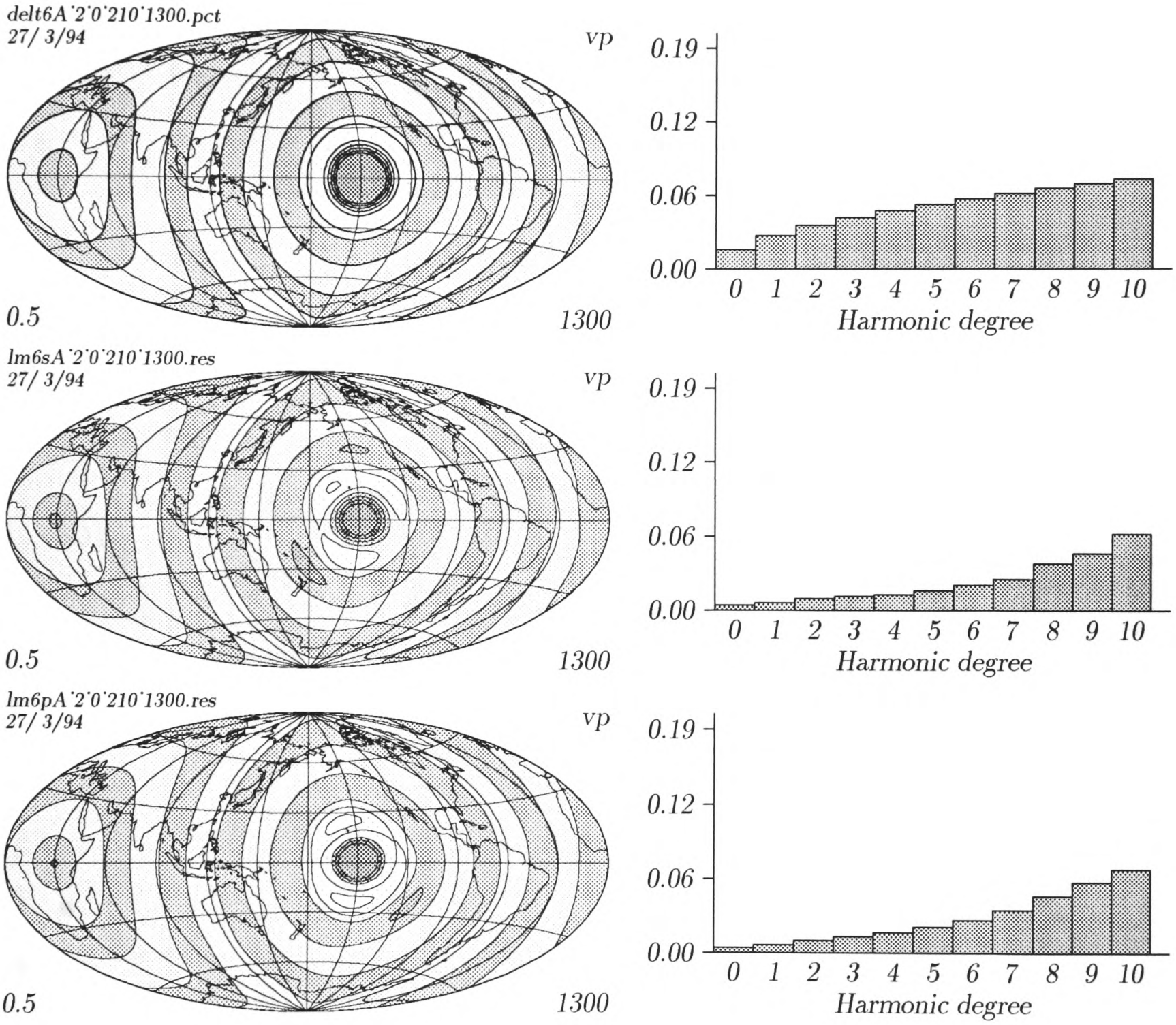


Figure 7.10: Resolution maps for the 2% amplitude input delta function (top) in central Pacific at 1300km depth. Middle and lower maps correspond to the resolution patterns of the S and P 6A models at the same depth.

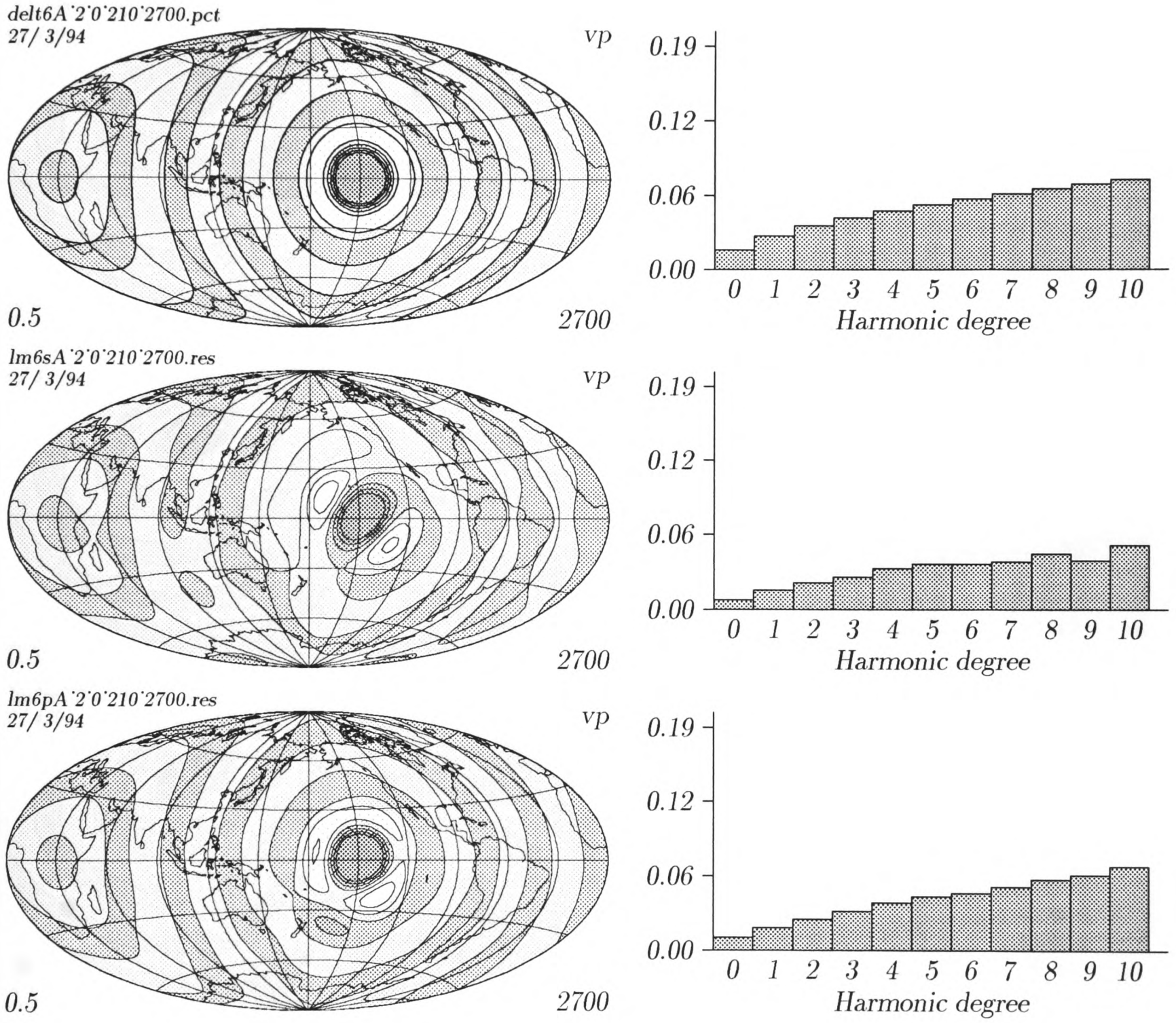


Figure 7.11: Resolution maps for the 2% amplitude input delta function (top) in central Pacific at 2700km depth. Middle and lower maps correspond to the resolution patterns of the S and P 6A models at the same depth.

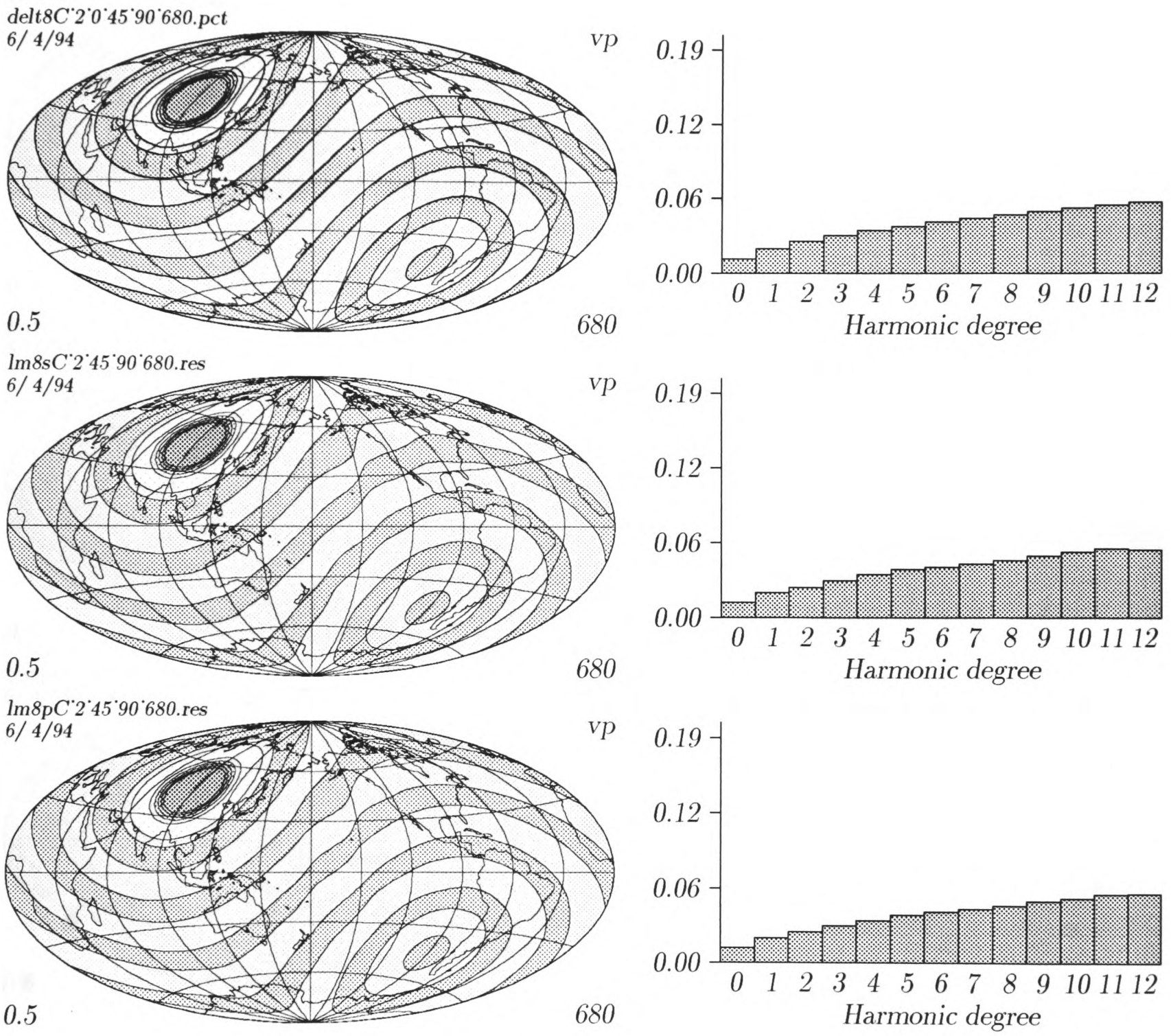


Figure 7.12: Resolution maps for the 2% amplitude input delta function (top) in central Asia at 680km depth. Middle and lower maps correspond to the resolution patterns of the S and P 8C models at the same depth.

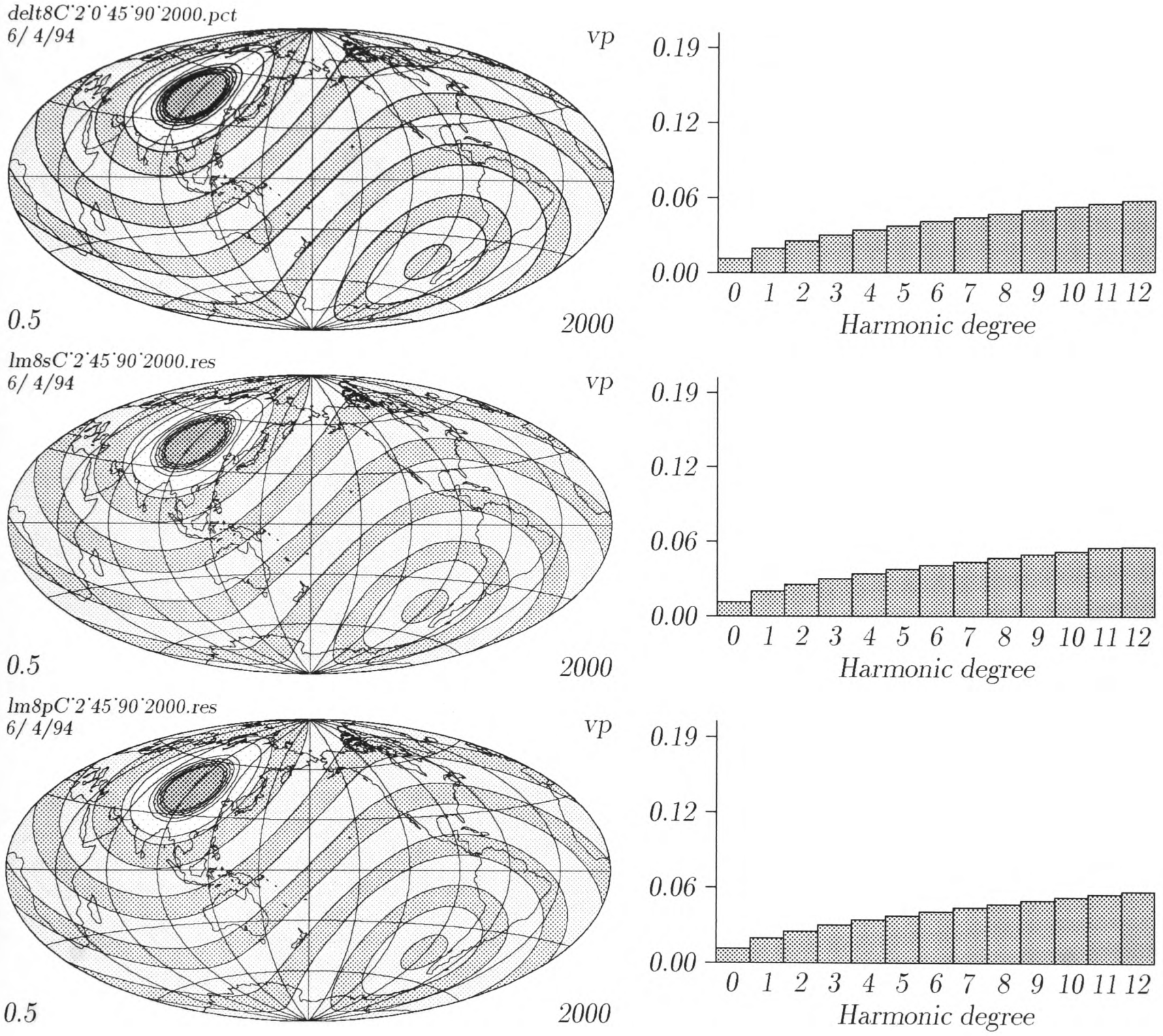


Figure 7.13: Resolution maps for the 2% amplitude input delta function (top) in central Asia at 2000km depth. Middle and lower maps correspond to the resolution patterns of the S and P 8C models at the same depth.

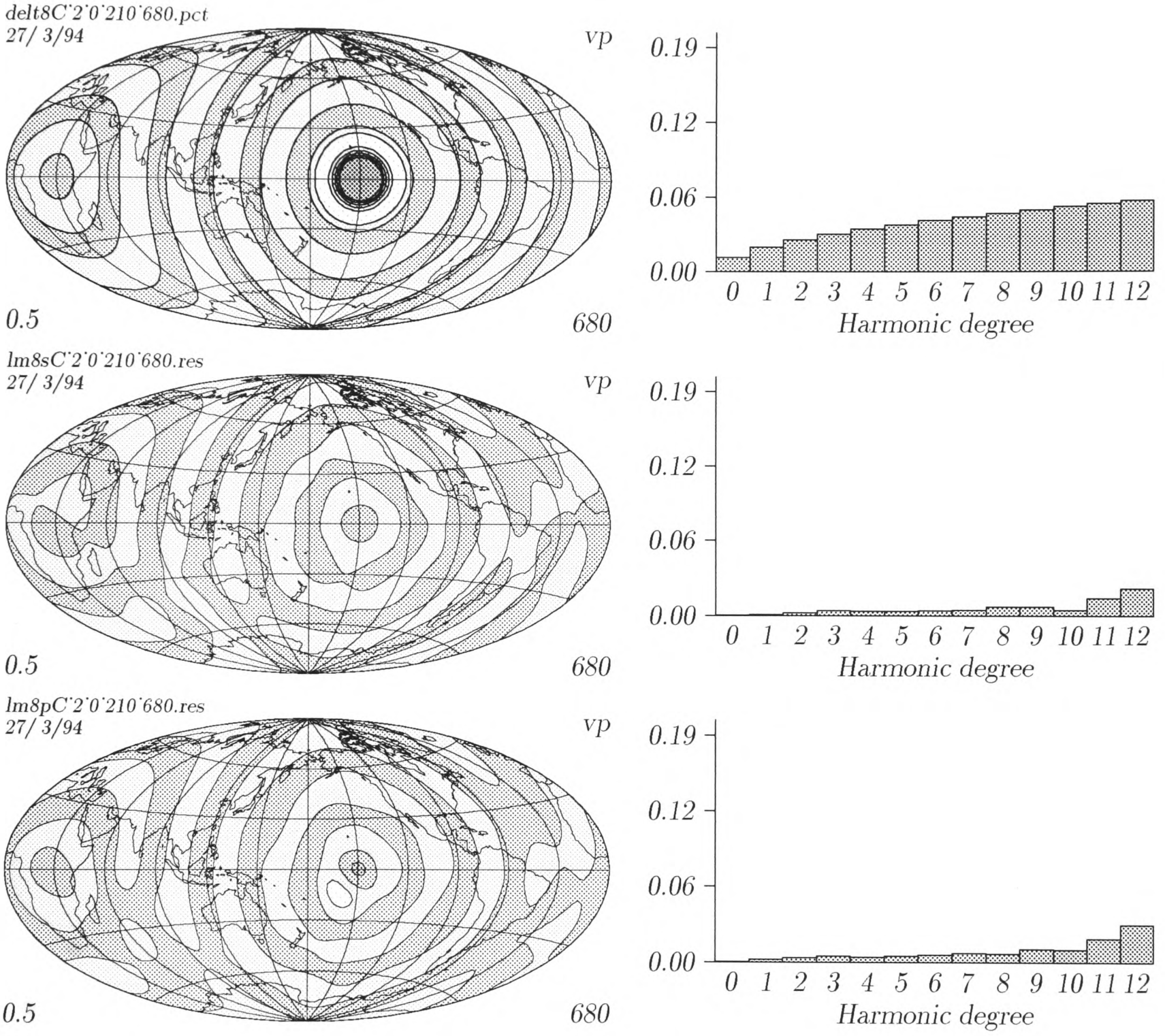


Figure 7.14: Resolution maps for the 2% amplitude input delta function (top) in central Pacific at 680km depth. Middle and lower maps correspond to the resolution patterns of the S and P 8C models at the same depth.

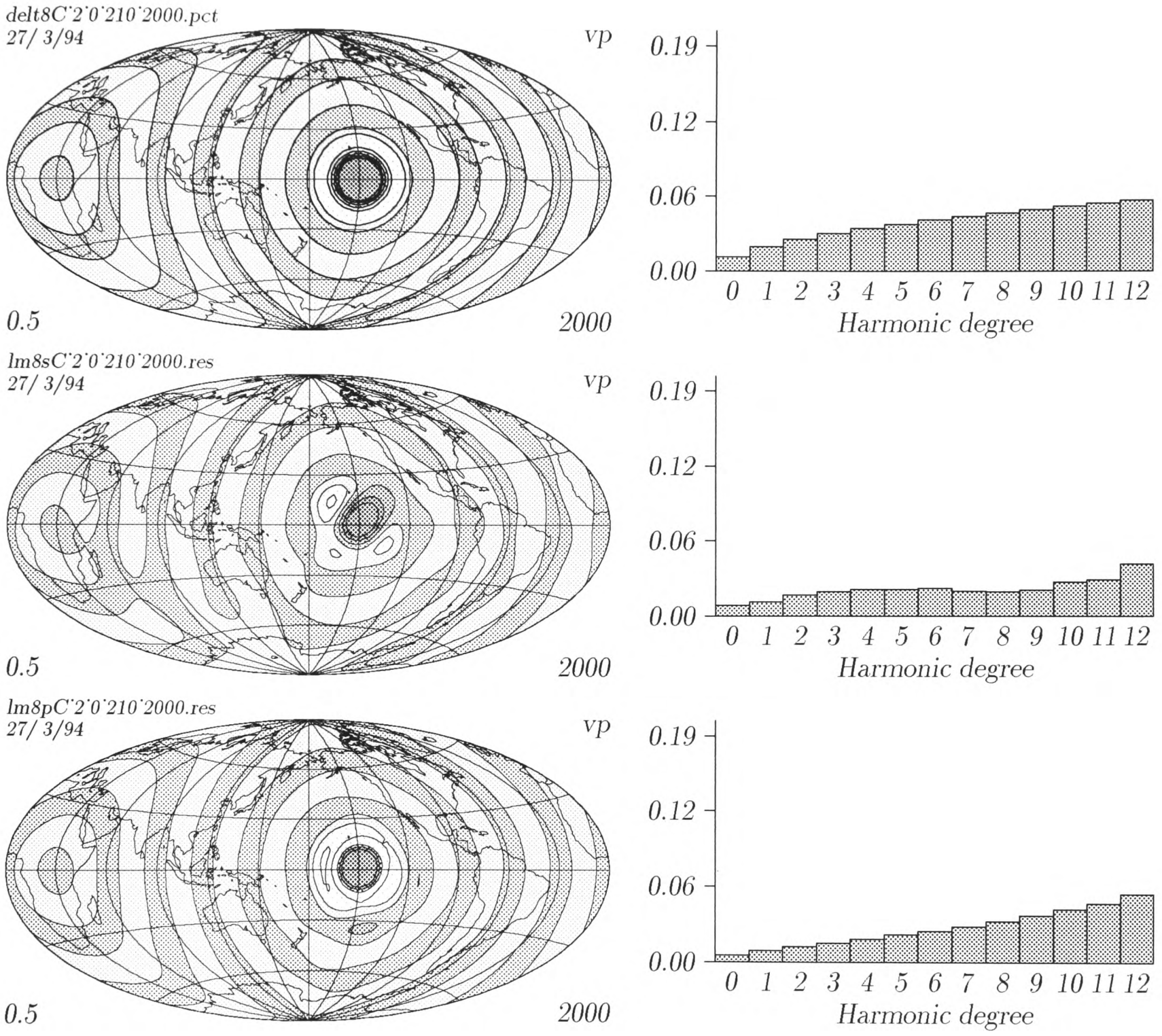


Figure 7.15: Resolution maps for the 2% amplitude input delta function (top) in central Pacific at 2000km depth. Middle and lower maps correspond to the resolution patterns of the S and P 8C models at the same depth.

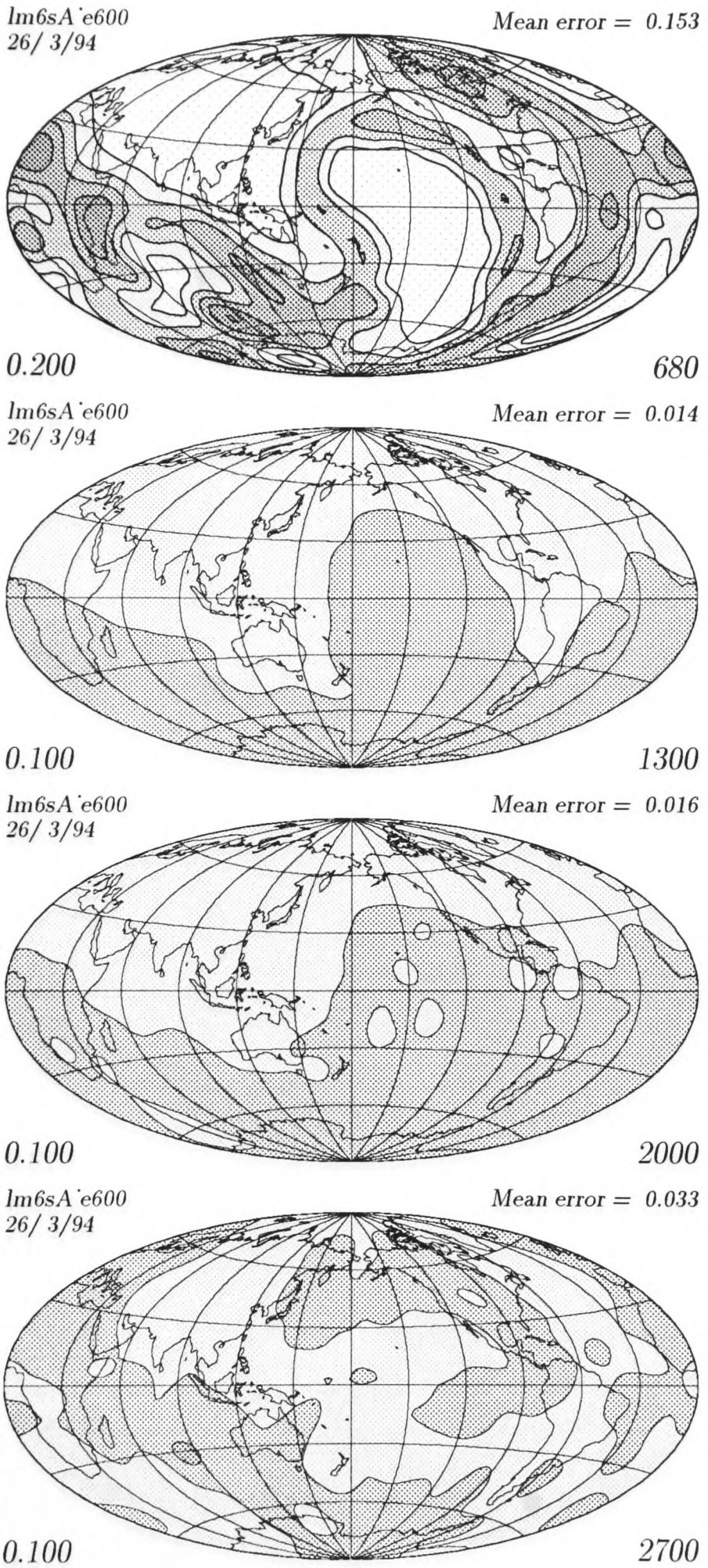


Figure 7.16: Variance of the 6A S model. These are contoured about the mean value in the top right hand corner with a contour interval given in the bottom left hand corner.

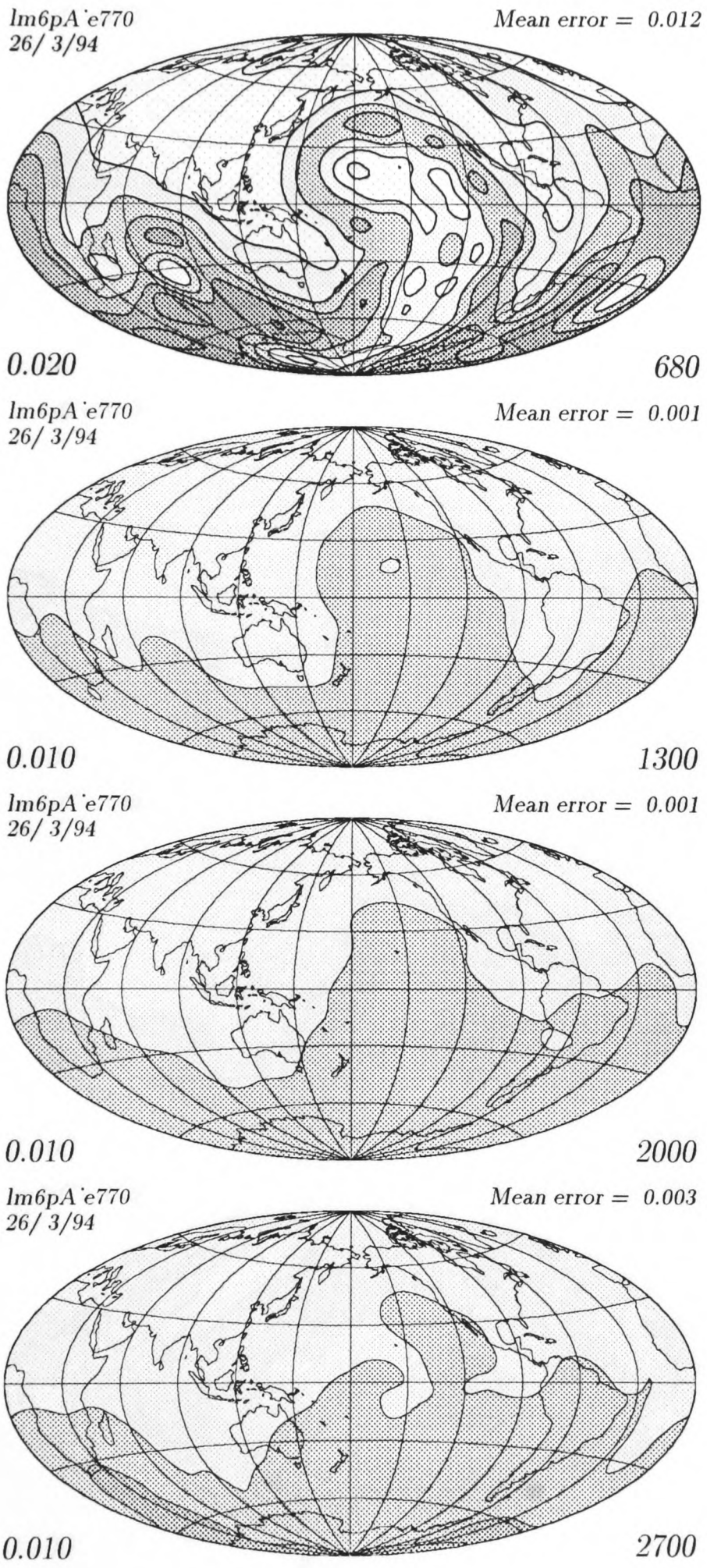


Figure 7.17: Variance of the 6A P model. These are contoured about the mean value in the top right hand corner with a contour interval given in the bottom left hand corner.

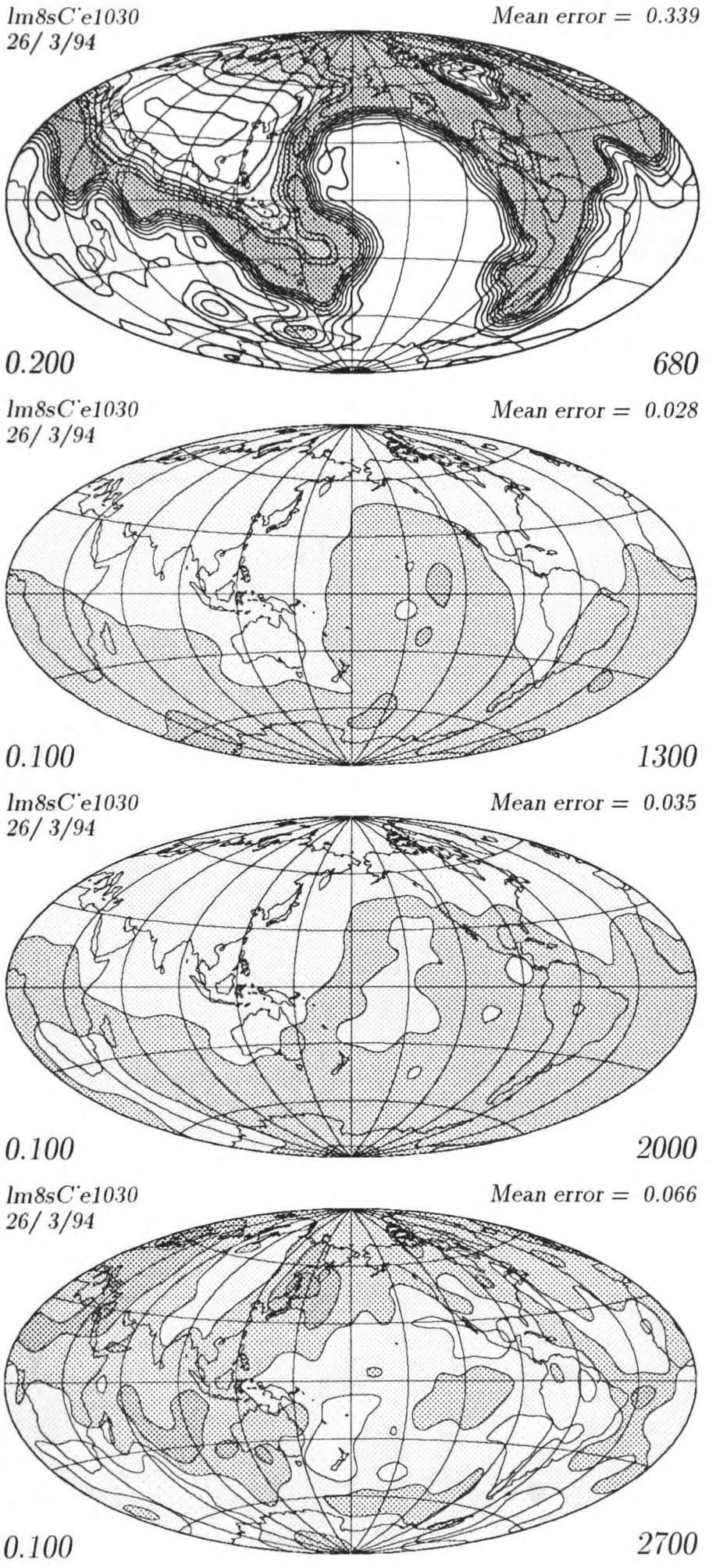


Figure 7.18: Variance of the 8C S model. These are contoured about the mean value in the top right hand corner with a contour interval given in the bottom left hand corner.

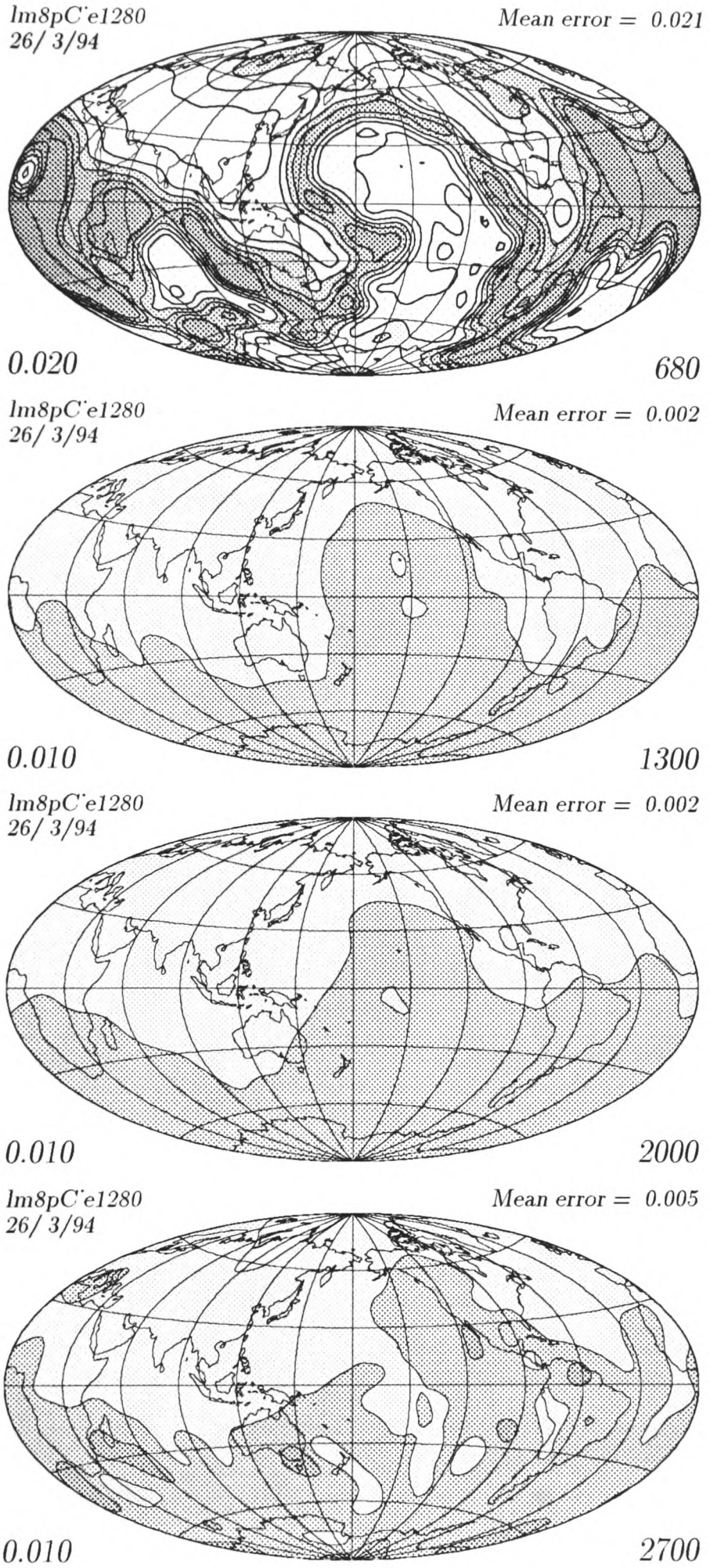


Figure 7.19: Variance of the 8C P model. These are contoured about the mean value in the top right hand corner with a contour interval given in the bottom left hand corner.

Figure 7.20: 6A S model truncated to $n = 4, l = 6$.

Figure 7.21: 8C S model truncated to $n = 4, l = 6$.

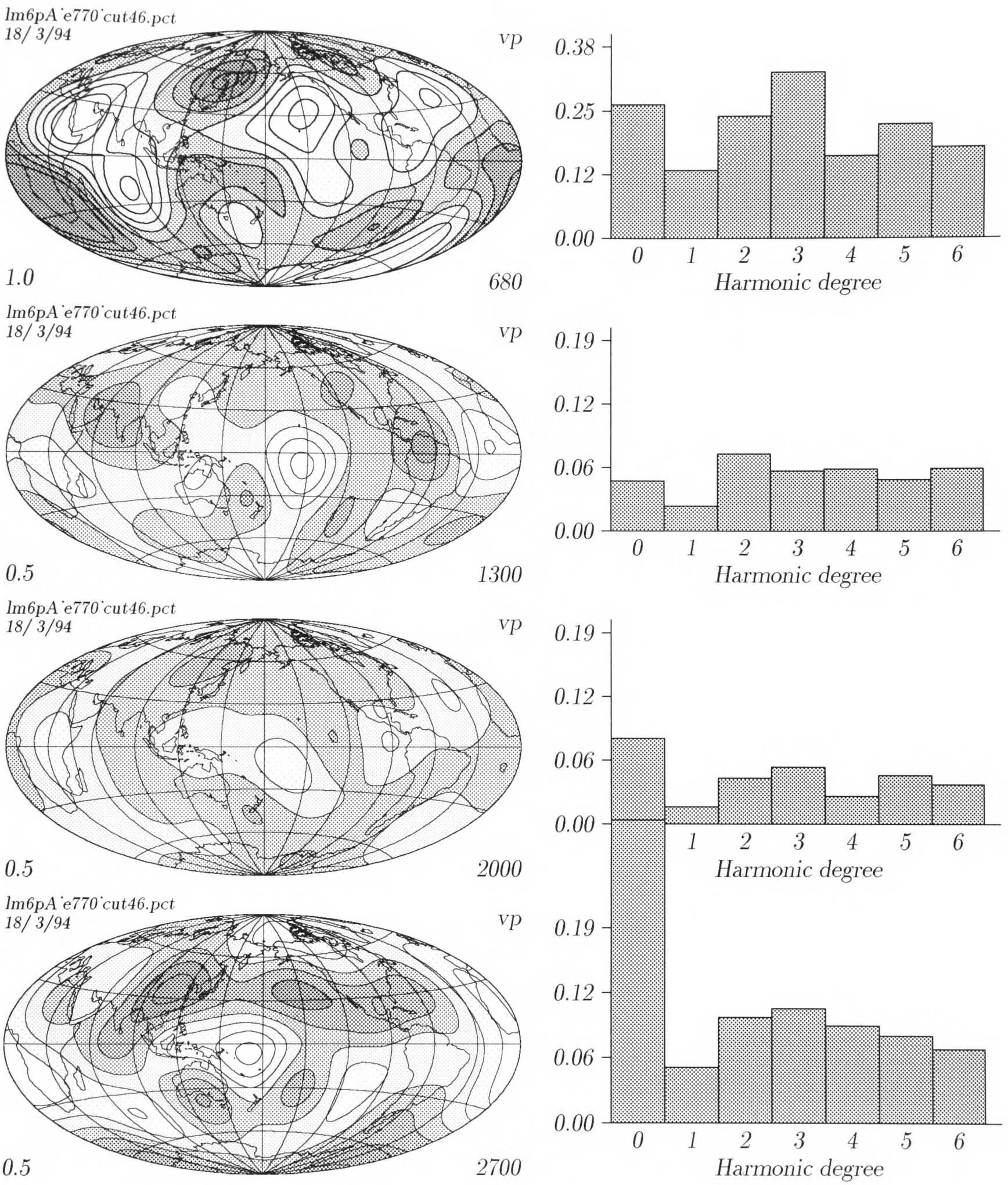
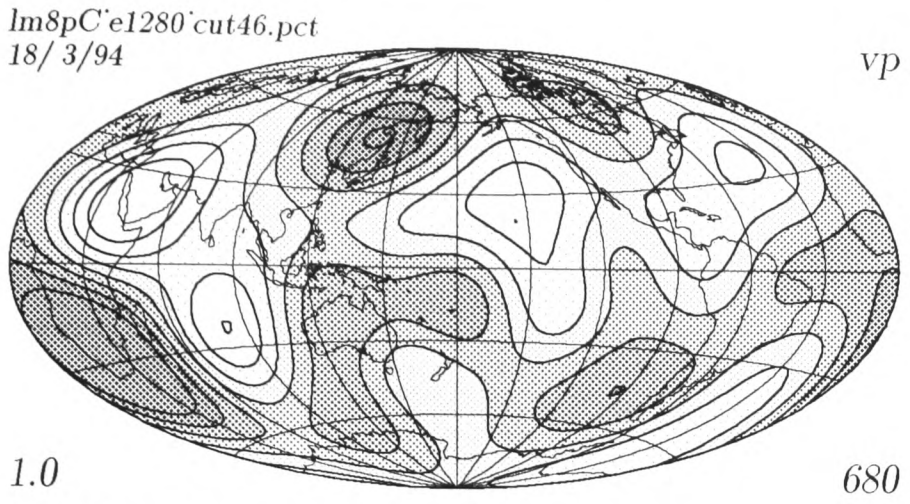
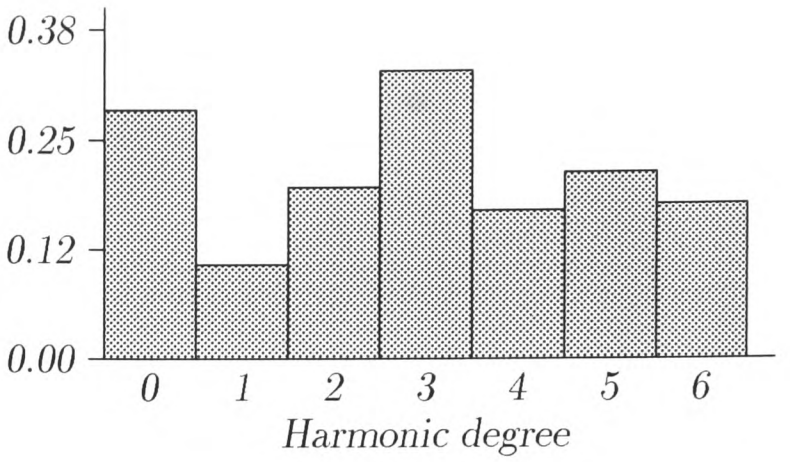
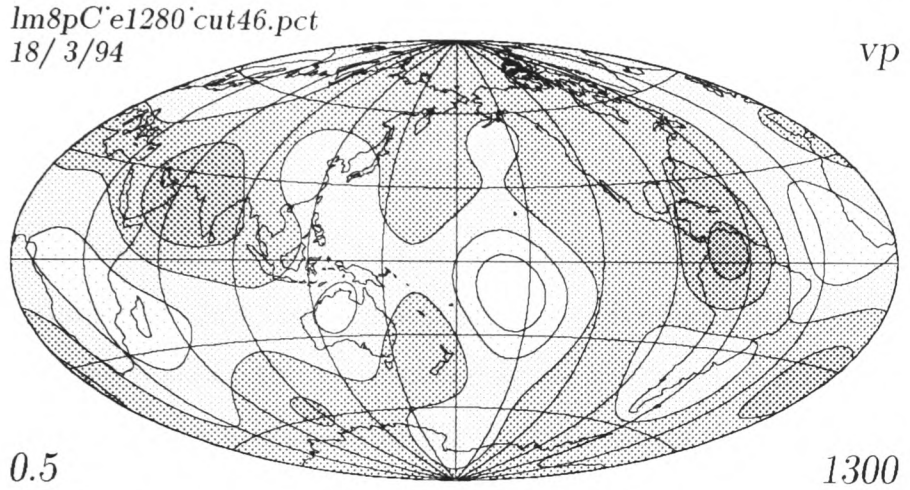
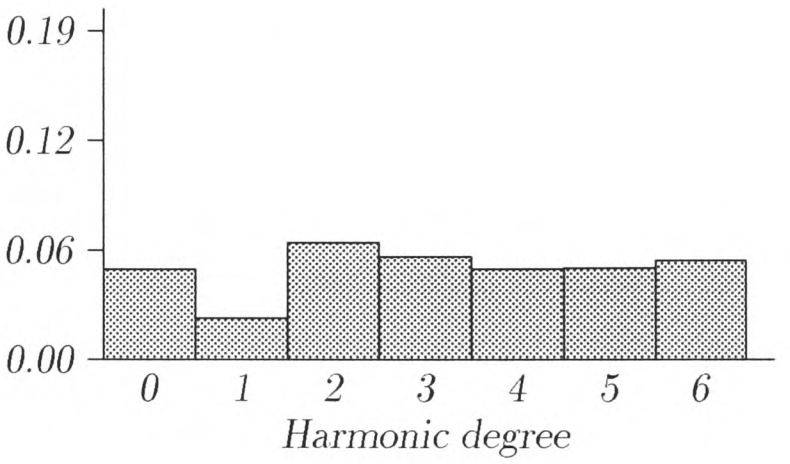


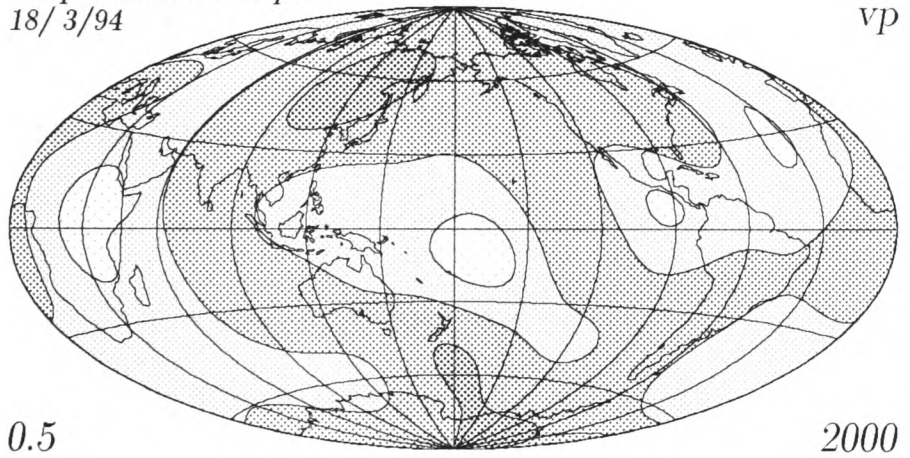
Figure 7.22: 6A P model truncated to $n = 4, l = 6$.

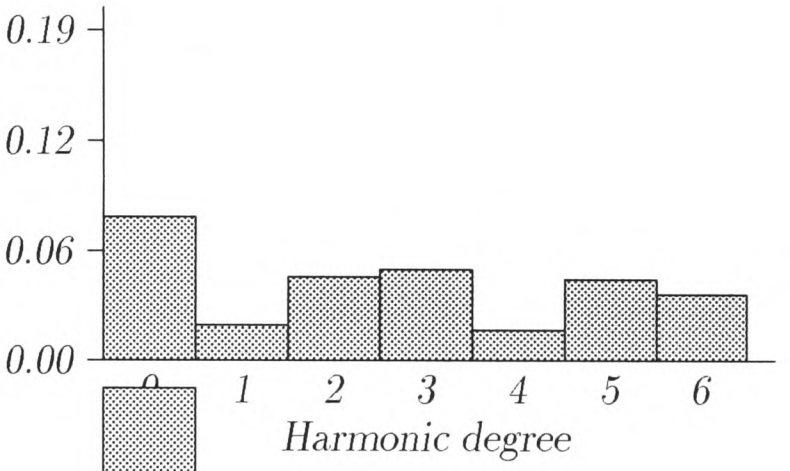


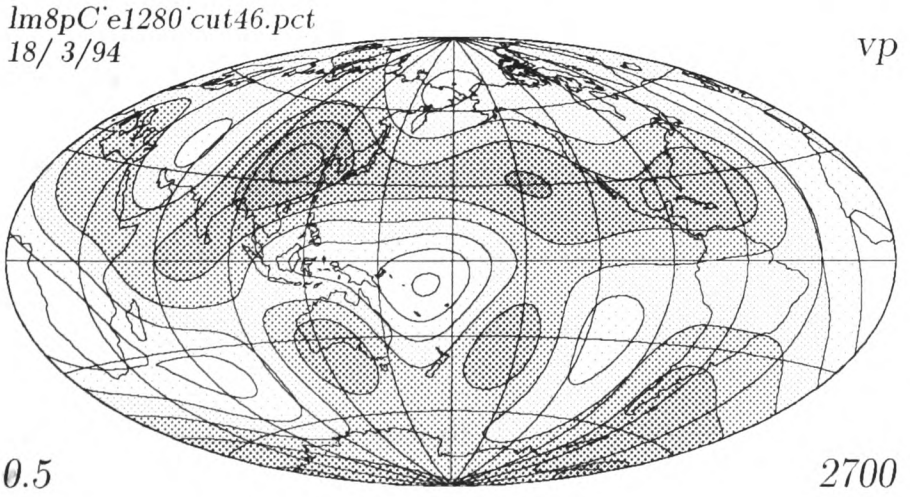












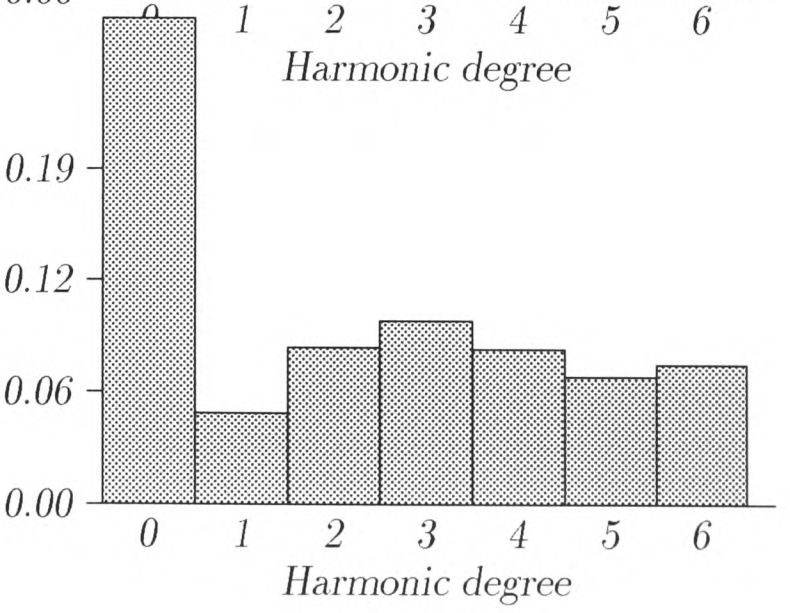


Figure 7.23: 8C P model truncated to $n = 4, l = 6$.

Chapter 8

Model analysis

In this chapter the P and S models that have been derived in this thesis will be compared to pre-existing mantle models. Not all studies that have been made will be included herein because numbers are quite large. Instead the examples chosen will be the most recent available and will be representative of the modeling techniques and parameterizations that have been used.

8.1 Pre-existing models

The models chosen are:

- P
  1. Dziewonski, 1984. **l02.56**
  2. Morelli & Dziewonski, 1991. **V3.i**
  3. Inoue *et al.*, 1990. denoted **IFTO**
- S
  1. Woodhouse & Dziewonski, 1986. **U84L85/SH**
  2. Tanimoto, 1990. **MDLSH**
  3. Woodward *et al.*, 1992. **SH8WM13**

A brief description of each of these follows:

- **l02.56**

  The method of this thesis is based largely on the theory detailed in this paper. Arrival times reported by the ISC between the years 1964 and 1979 were used to determine l02.56, a model of the lower mantle including D'', parameterized with 5 Legendre polynomials in depth and 7 spherical harmonics to represent the lateral heterogeneity. Hence the method of inversion and parameterization of this model is exactly the same as the P model in this study, and so

comparisons with this model should be free from effects caused by, for example, different resolution and parameters included in one inversion but not the other.

- **V3.i**

  One of the fundamental problems associated with mantle tomography is the trade–off between topographic features on boundaries and volumetric structures in their vicinity. Morelli & Dziewonski 1986, 1987a, 1987b have used ISC PcP and PKP to resolve this trade–off because the two phases have opposing effects from boundary perturbations. With the addition of P and PKIKP, Morelli & Dziewonski, 1991 have calculated simultaneously a lower mantle model V3.i parameterized in an identical way to l02.56, CMB topography to degree 4, and inner core heterogeneity also to degree 4.

  The inversion method involves splitting the earth into equal area cells and then forming *summary rays* which are bundles of rays from one source cell to a receiver cell. Their data element, a summary residual, is the average of all residuals within one bundle of rays and so the amount of data is drastically reduced. This enables the inversion for both the model coefficients and event locations to be carried out jointly.

- **IFTO**

  This model describes whole mantle P wave heterogeneity in terms of blocks and as a result it is parameterized in a completely different way to the models described above. The data used is ISC *e*P, *i*P, and P from the years 1964 to 1985. Lateral block sizes are 5.6° wide at the equator giving a maximum lateral resolution roughly equivalent to l_{MAX}=32. The sizes of the radial blocks are defined by a polynomial in such as way that the blocks at the CMB are far thicker than those at the surface representing the much smaller resolution that is expected to be obtained at this depth. With 11 layers, the total number of unknowns in this study is 32768.

  Similar studies have been carried out by Clayton & Comer, 1983 and Hager & Clayton, 1989. They use a different inversion algorithm (Simultaneous Iterative Reconstruction Technique) to the authors of IFTO (Conjugate Gradient) and some authors (Morelli & Dziewonski, 1991) have questioned the validity of its use with uneven datasets. However the main reason that these models are not used in this chapter is that IFTO represents the most recent block parameterized model derived from the largest compressional wave arrival time dataset.

In contrast to the compressional models described above, not one of the following models of S heterogeneity is derived from ISC arrival time data. Instead these models use a completely different technique pioneered in 1984 by Woodhouse & Dziewonski which requires digital seismograms and the calculation of a large number of partial derivative seismograms in a least squares fitting procedure. The dataset originates from several global seismometer networks – the Global Digital Seismograph Network (GDSN), the International Deployment of Accelerometers (IDA), and more recently the French operated GEOSCOPE program.

- **U84L85/SH**

  This model was first presented in Woodhouse & Dziewonski, 1986, and subsequently featured in Woodhouse & Dziewonski, 1989. It uses long period body waves ($f \leq \frac{1}{45}$Hz and *mantle waves* which are essentially Rayleigh and Love waves which follow great circle paths around the globe and sample the mantle to depths comparable to their wavelengths. The model consists of separate parameterizations for the upper and lower mantle in terms of spherical harmonics to degree 8, and radially to degrees 3 and 4 for the upper and lower mantles respectively.

- **MDLSH**

  Tanimoto, 1990 used similar types and roughly the same amounts of data that are used in U84L85/SH to derive this whole mantle model of S heterogeneity. However this model is discretized in depth, with 11 layers, and is expanded laterally in terms of spherical harmonics to degree 8.

- **SH8WM13**

  The latest 'Harvard' model of S heterogeneity is also parameterized throughout the entire mantle with no breaks at the upper/lower mantle boundary. It incorporates the widest range of data available with, in addition to the data types described above, several short period phases. These consist of two further subsets of data:

  1. absolute SS readings (Su & Dziewonski, 1991)
  2. differential PP-P, SS-S, ScS-S readings (Woodward & Masters, 1991a; Woodward & Masters, 1991b)

  Both datasets are highly accurate measurements obtained by waveform cross correlation techniques. The coverage of the SS dataset is excellent in both oceanic and continental regions and it has been shown that they are sensitive to upper mantle structure at the bounce point. Differential travel times are even more sensitive to bounce point structure because the ray paths of the two phases involved are most similar at the endpoints where heterogeneity is largest. Furthermore these readings are also less sensitive to source mislocation because it will affect both the reflected and the direct phases in exactly the same way. If this dataset is plotted at the bounce point, coverage is much more restricted than that for SS. The internal consistency of these phases is very good with clear correlations being observed between PP-P and SS-S, and with the tectonic province and lithospheric age at the bounce point (Woodward *et al.*, 1992).

  The authors have performed an inversion with the same dataset in which the upper and lower mantles are parameterized separately. The results show that correlation is high at 0.9 in all areas except the upper/lower mantle boundary at 670km depth where correlation drops to 0.7.

8.2 RMS amplitude

The derivation of the root mean square (RMS) amplitude for a model expanded in spherical harmonics at a specific depth is given in appendix 2. Only asymmetric terms are used in order to eliminate the significance of the starting spherically symmetric model and to concentrate on the heterogeneity that each model represents. The results for the four compressional models are shown in figure 8.1

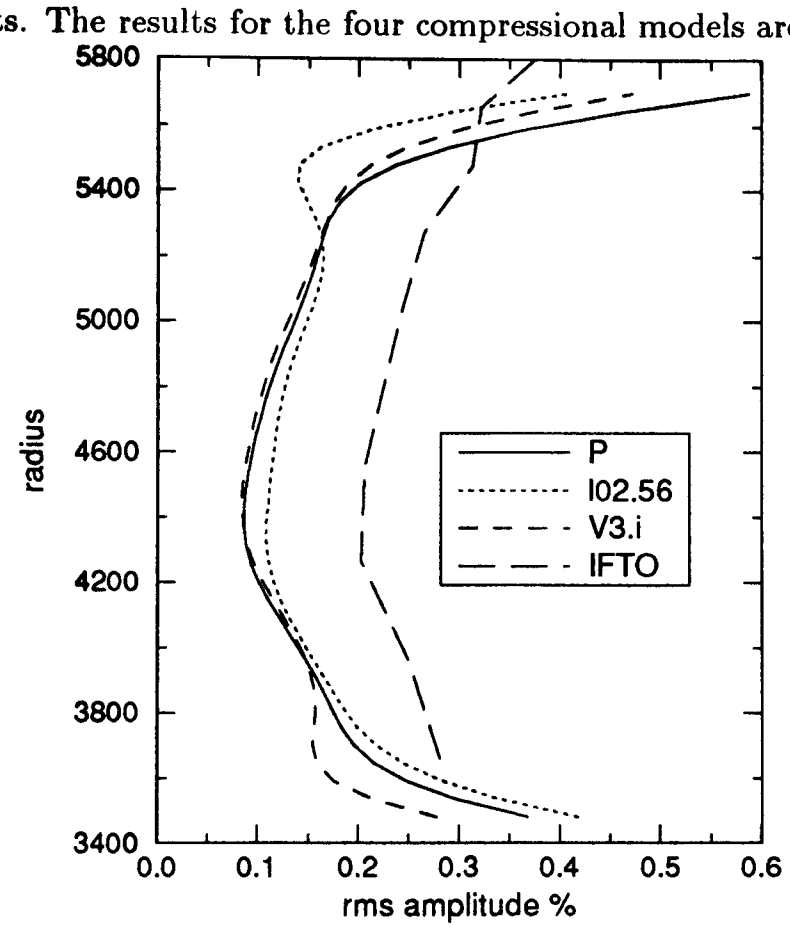


Figure 8.1: RMS amplitudes for the compressional models. Values for IFTO are plotted in the centre of each depth interval.

Model IFTO results are obtained from table 3 in Inoue *et al.*, 1990 and represent the RMS slowness perturbations. Their model is parameterized in terms of blocks and the results here are not smoothed to give results comparable to the resolution of the other three models. Hence it is only the general features of this RMS curve than can be considered, and not absolute values. Generally it is clear that all models have large amplitudes at the boundaries of the lower mantle and much smaller values in mid mantle regions, with the lowest values of ≈0.1% being obtained at a radius of 4400km (≈2000km depth). The three identically parameterized models, P, I02.56, and V3.i, have very similar amplitudes especially throughout mid mantle regions where data coverage is best.

At the top of the lower mantle, I02.56 is smaller than both P and V3.i and shows a local minimum at 5400km radius. This probably results from the use of azimuth dependent as opposed to static station corrections to represent upper mantle velocity heterogeneity. This allows a greater number of degrees of freedom in the inversion, but can lead to the incorporation of lower mantle signal in the station corrections. However it is difficult to know if this is in fact the explanation.

V3.i is much smaller at the CMB because of the additional degrees of freedom in the inversion created

by the inclusion of CMB topography and inner core heterogeneity.

Although only general comparisons with IFTO can be made, this model does seem to show a more even spread of heterogeneity throughout the lower mantle. At least in the upper regions, the inconsistencies can be attributed to differences in the parameterizations of the models – IFTO has no specified boundary at the upper/lower mantle interface whereas all the other compressional models presented hare are parameterizations of only the lower mantle, and so leakage of signal from the upper mantle into the lower mantle near the boundary is probable. Nevertheless this argument cannot be used to explain the differences at the CMB where IFTO does not show the same increase in size.

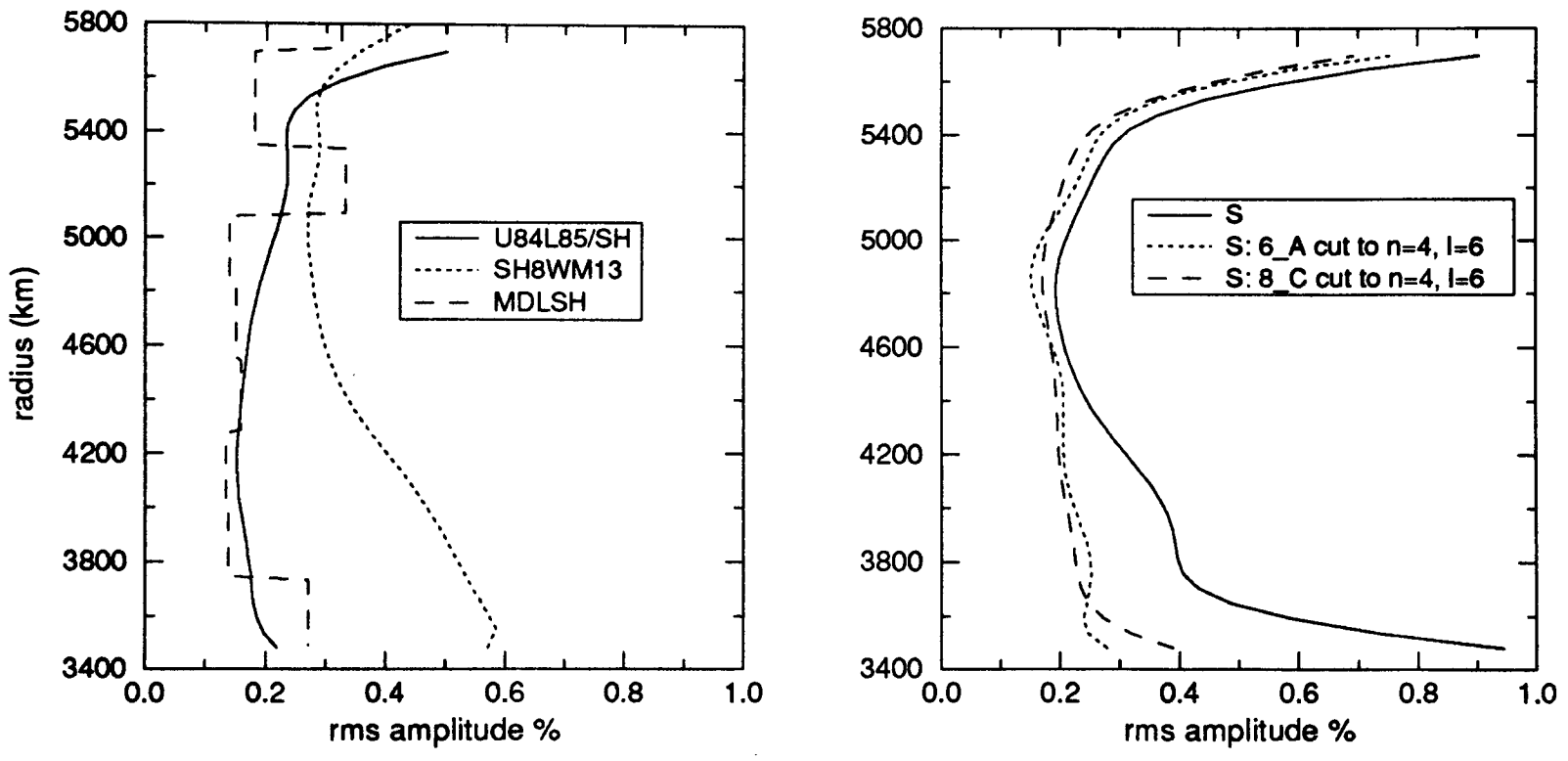


Figure 8.2: RMS amplitudes for the shear models. Spherically symmetric terms are not included.

Figure 8.2 shows the RMS velocity perturbations for the shear wave models. For clarity these are split up into two groups, with those models from this study plotted together in the right hand graph. Where models are expanded laterally with spherical harmonics, only the coefficients with $l \leq 6$ are included. Model SH8WM13 is expanded in terms of Chebyshev polynomials throughout the entire mantle and its nominal radial resolution is twice as great as U84L85/SH and the models of this study. As a result, the amplitude of this model is not directly comparable with the others, and in a similar way to the P models and IFTO, only qualitative comments can be made.

These plots show that compared to the P models, the S models do not show the same degree of similarity. Most models are largest at shallow depths, but not to the same degree, and at the CMB there are considerable discrepancies. It is only in mid mantle regions that all models share roughly the same amplitude of 0.2-0.3%, which is at least twice as large as the compressional models. Prior knowledge of the resolution of these models with depth should be used before any more specific can be made. U84L85/SH has relatively poor data coverage of the lowermost mantle and so amplitudes are determined largely by the degree of damping applied. Coverage at this depth in MDLSH is excellent

(see figure 6 in Tanimoto, 1990) but even accounting for possible differences in depth resolution it is still much smaller than SH8WM13 which has very accurate ScS-S differential travel time measurements as constraints. However it is possible that these shorter period measurements may be more sensitive to CMB topography which is not included in the derivation of this model.

Results from the models of this study are shown on the right hand plot of figure 8.2. They are in excellent agreement in the upper half of the lower mantle where data coverage is known to be good, but they show large discrepancies at depth principally because of the very small amount of possibly inaccurate data. The RMS amplitudes of the two truncated higher parameterized models shown as the dotted and dashed lines are very similar to eachother and to U84L85/SH and MDLSH.

8.3 Correlation coefficients

8.3.1 P

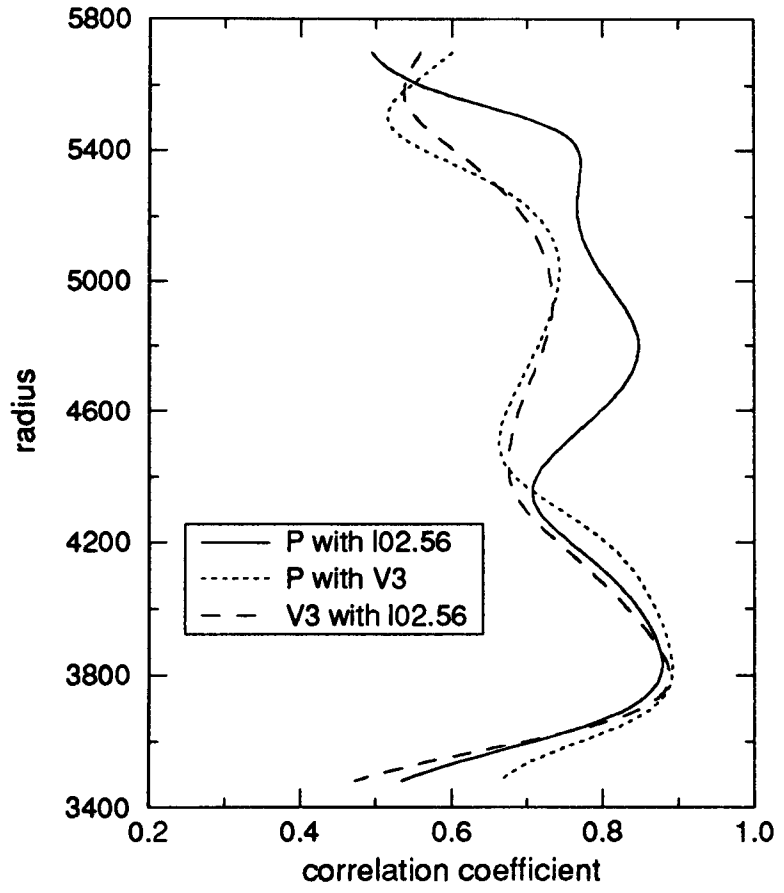


Figure 8.3: Correlation coefficients as a function of depth for the P models.

Correlation of one model with another is straightforward if the models are parameterized using the same basis functions. Most of the models considered here, whether they be whole or only lower mantle parameterizations, use spherical harmonics to describe lateral heterogeneity. Model IFTO is the exception, being parameterized in terms of blocks with varying sizes. Where there is data, the resolution of this model is far higher than that which is available from the spherical harmonic basis function models, so what is normally done is to smooth or fit spherical harmonics to the model so that the resolvable feature sizes are approximately the same. Unfortunately model IFTO has not been available in this form and as a result it is not included in this section.

Figure 8.3 shows that the correlation of all available P models is high, being on average 0.7 throughout the lower mantle, and peaking 300km above the CMB and in upper mid mantle regions for all three cases. The correlation coefficient of V3.i with the other two models at the CMB is lower than average as a result of the allowance for CMB topography in the inversion. However it is surprising that the correlation of the P model of this study with 102.56 is not higher in this region given the similarity of the modeling method. This observation is probably attributable to the inclusion of S in the relocations and will be discussed later in this section.

8.3.2 S

Although model MDLSH is discretized in depth, correlation coefficients with other models are computed continuously in order to investigate at which point in the layer the models are most similar. As a result those plots which involve MDLSH in figure 8.4 are not smoothly varying.

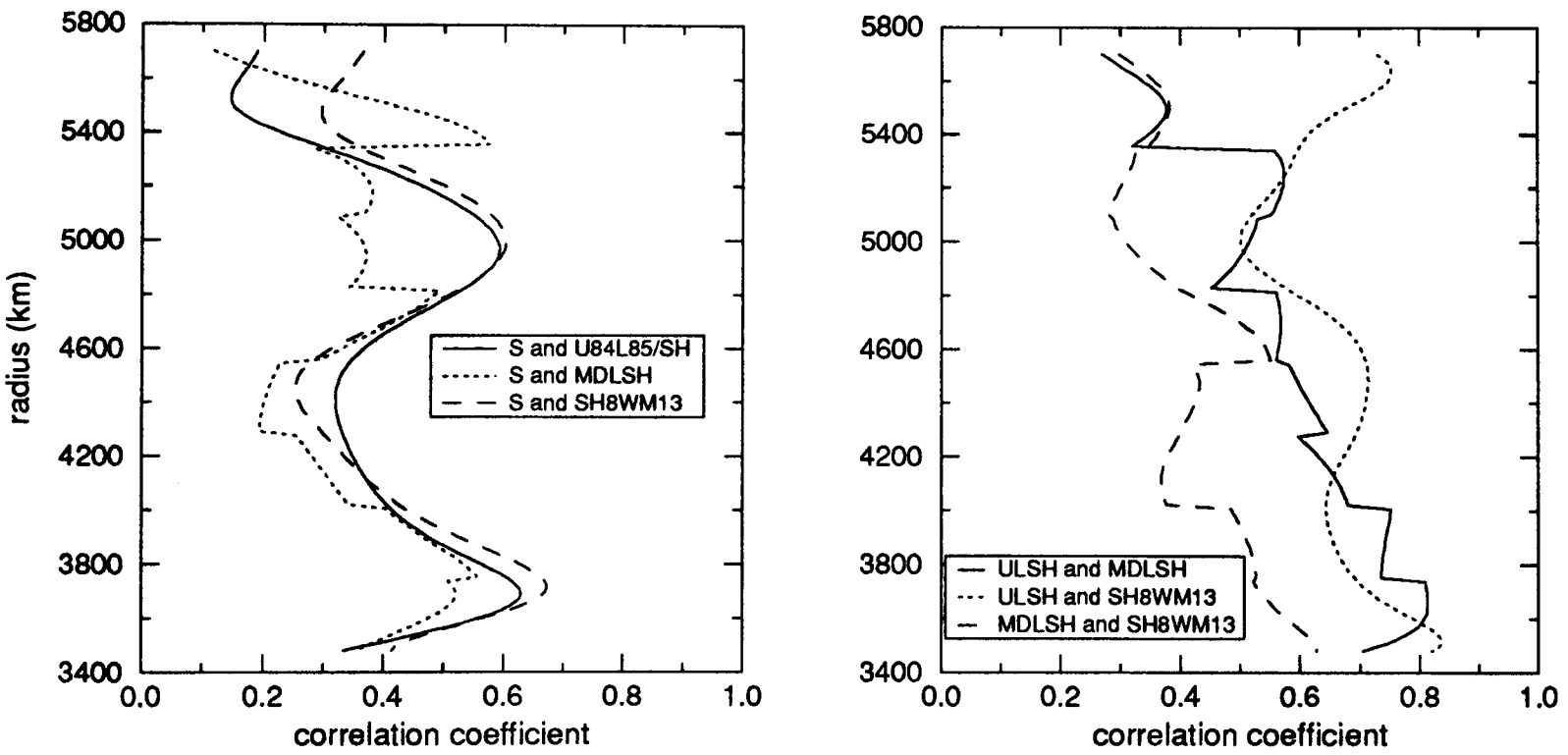


Figure 8.4: Shear wave model correlation coefficients. ULSH is short for U84L85/SH .

The left hand graph, which plots the depth dependent correlation coefficient between the S model of this study and pre-existing S models, shows that the correlation between models is far lower than what was observed with the compressional models. Averages for all three models are close to 0.4 with peaks occurring at approximately 1300km depth (≈5000km radius) and 300km above the CMB. It should be noted that these peaks correspond well to similar peaks in the correlation coefficients of the P models. The general nature of this plot is easily explained. At the upper/lower mantle boundary the S model in this study suffers from poor resolution in areas where there are no sources or receivers because of the vertical nature of the ray paths. The other models all use long period surface waves which are capable of resolving structure far better in these areas. The peak at 5000km is a significant factor because resolution of all models in mid mantle regions is good. Below this depth correlation with all models

decreases as the lack of data between 80° and 90° begins to affect the accuracy of the S model of this study. Proceeding deeper, the rise in the correlation coefficients is attributable to the reappearance of ray paths which bottom at this depth. Low correlation coefficients at the CMB have been a feature of all plots comparing the models in this study to others. It is likely that there have been misidentifications of other phases, probably SKS and S_{DIFF} as S at high epicentral distances, and because the amount of data here is small, this has affected the models and propagated through subsequent relocations. The observation in the previous section that, despite the almost identical methodology, I02.56 and the P model of this study do not correlate well near the CMB is further evidence for this hypothesis.

Correlation of U84L85/SH with MDLSH and SH8WM13 is plotted in the right hand graph of figure 8.4. Although both plots seem to be quite different, the inconsistencies are confined largely to the upper/lower mantle boundary, with the layer of MDLSH just under the boundary correlating poorly with U84L85/SH. At 5000km and 3700km radius (1300km and 2700km depth respectively) the sizes of the correlation coefficients agree quite closely with those of the left hand plot of this figure. This is a significant result because it implies that where the S model of this study is good, it correlates as well with other models as other models do with eachother. Correlation of U84L85/SH with MDLSH and SH8WM13 at the CMB is excellent, and probably results from the almost identical datasets used.

8.4 Comparison of features

Specific comparisons of the heterogeneity of lower mantle models can be made using the plots that have been used in this thesis so far *ie.* maps of heterogeneity at specific depths, or by taking cross sections of the earth through great circles. The latter approach is adopted when images of convection patterns are sought.

For the models whose coefficients have been obtained, figures 8.6 to 8.8 show maps of the three lower mantle P models at specific depths – 1300, 2000, and 2700km. Plots of S heterogeneity for the four models considered here are shown in figures 8.9 to 8.11. Their depths are 1400, 1950, and 2760km, which correspond to the centre of three layers within MDLSH. They are suitably similar to the depths of the P maps for both sets to be compared together. The S maps are plotted with twice the saturation contour levels of the P plots. Maps at 680km depth are not included because the models derived from arrival time data are unreliable at this depth. Where models are expanded beyond degree 6, only coefficients with $l \leq 6$ are used. In addition the depth resolution of the models is not the same, and so some differences in features may be attributable to this.

- 1300km depth

  Despite the fact that the harmonic spectra are not similar, the three P models share almost identical features, with differences being attributable mainly to changes in amplitude. All three

show fast features circumscribing the Pacific which, because of their existence from at least the transition zone (Inoue *et al.*, 1990), has been linked with the great subduction slabs of Tonga–Kermadec, Java, South America, and Japan–Izu (Woodhouse & Dziewonski, 1989; Creager & Jordan, 1986). It should be stated that the similarity in the P models may be attributable at least in part to the identical basis functions and model extents chosen. Nevertheless many of the major features are also exhibited in the S models of figure 8.9. In particular, all four plots show the same fast areas under southern Asia and the Caribbean. This latter feature has been reported by several regional studies (Jordan & Lynn, 1974; Lay, 1983; Grand, 1987, whose authors have suggested the same mechanism for its existence. Fast regions under the Tasman sea are seen in all P and S maps although the amplitudes are not the same.

All maps consistently show slow anomalies under southern Africa and Madagascar. Similarly the south central Pacific region is predominantly slow, although the size of this anomaly differs substantially. It is larger in all of the P models than any of the S models. This is not caused by the different plotting depths of the two sets of maps, but instead is probably a result of the poorer coverage of the mantle at this location by ray paths in the ISC P dataset (see figure 6.23).

- 2000km depth

The P models for this depth and 50km shallower for the S models show similar features to those discussed above. Amplitudes are smaller, but the pattern of high velocities around the Pacific are still evident. Low velocities underneath Africa are still observed, as are the slow anomalies in the central Pacific region. In this latter case, the S models are consistently larger than the P models. As was seen in the RMS amplitude plots of figure 8.2, model SH8WM13 does seem to be larger than the others, but this may result from its larger parameterization and proportionately higher resolution in depth. The S model of this study correlates poorly with the other models, but it shares several of the prominent features of the other maps.

- 2700km depth

Correlation of the plots at this depth is very good, and all show a strong degree two component of heterogeneity which describes the ring of high velocities circumscribing the Pacific. The authors of all of these models have noted that this feature extends throughout most of the lower mantle to the CMB. This feature is clearly seen in the S model of this study, which correlates with the other S models at this depth.

The degree of similarity that these models share at this depth is significant. Gudmundsson *et al.*, 1990 have suggested that models of lower mantle heterogeneity are heavily influenced by the much stronger heterogeneity in the upper mantle and that images of the core mantle boundary are completely obscured. Models SH8WM13 and MDLSH both include the upper mantle in their

formulation and are very similar to U84L85/SH , V3.i, l02.56, and the P model of this study, all of which are parameterized in the lower mantle only. However this still does not discount the possibility that all these models could be wrong since there is considerable small scale heterogeneity in the earth at shallow depths (Gudmundsson *et al.*, 1990; Davies *et al.*, 1992) and this is not included in any of these global models.

It is interesting to note that as well as the degree 2 signal, the P models additionally show large power in degree 3. This may be linked to the existence of a more pronounced fast feature in the compressional models, including IFTO, centring on 30° latitude in the Pacific region. The only shear wave model which shows an anomaly similar to this is SH8WM13. However, as has been stated earlier, the P wave models are constructed using the same parameterizations and similar inversion methods, and as a result it is not surprising that they show similar features.

Inoue *et al.*, 1990 report that IFTO has three major slow anomalies at this depth:- the East Pacific Rise, the subduction region in the southwest Pacific, and from the Southern Indian Ocean to southwestern Africa. These are evident in all of the compressional maps, in the S model of this study, and in SH8WM13. U84L85/SH and MDLSH do not show these anomalies quite so clearly. At least in the former case, this probably results from poor data coverage at this depth. Indeed this model is much smaller in size than any of the others, and this is a feature which has already been attributed to high damping.

8.5 Comparisons of further parameterized models

In this chapter only the comparisons of models with maximum parameterizations of $n = 4, l = 6$ have been considered, and this has included truncations of the 6A and 8C models. In this section, these models will be truncated to $l = 8$ and their maps and correlation coefficients will be compared with SH8WM13, which has a maximum expansion to the same lateral extent. The nominal resolution in depth of SH8WM13 is comparable to the 8C models, but it is almost twice as good as the 6A models.

The correlation coefficients of SH8WM13 with the 6A S model and the 8C P and S models are shown in figure 8.5.

In general the curves fluctuate between 0.2 and 0.6, with the highest value being obtained at 3700km radius (≈ 2700km depth). Highs have also been found here with the 4_6 models. At 1300km depth (≈ 5100km radius) all the curves are 'in phase' and have similar values of between 0.3 and 0.4. Considering that SH8WM13 not only has a completely different parameterization including the upper mantle, and uses different datasets, obtaining correlation coefficients such as those mentioned above is significant. Cross sections of all four of these models at 1300, 2000, and 2700km depth are shown in figures 8.12 to 8.14 respectively.

At 1300km depth the spectra from all four models are relatively flat with no dominance of any one

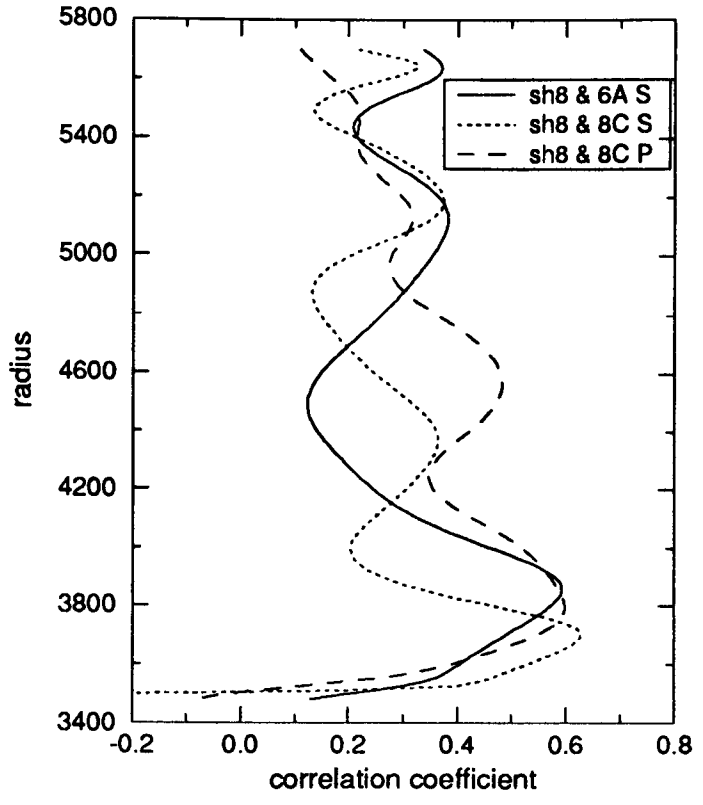


Figure 8.5: Correlation of SH8WM13 with the 6A S model and the P and S 8C models to degree 8.

term. All of these maps show strong positive anomalies under India and northern South America, and under the Tasman Sea. In addition, Madagascar and west Africa tend to be slow. However in other areas the models from this study are far more similar to eachother than to SH8WM13. There are large discrepancies in North America and in the Indian Ocean.

At 2000km depth the model spectra are far more similar, with degrees 2, 3, and 5 being prominent in all maps, although degree 2 dominates in SH8WM13 far more than in any of the others. Figure 8.5 shows that at this depth ($\approx$ 4400km) correlation of SH8WM13 with the 6A S model is poor, but it still has several of the key features in common with the other three. These include fast anomalies in the northern Pacific, eastern China, India, and southern South America, although this latter feature is displaced slightly west in the bottom P plot. The 'ring' circumscribing the Pacific is more evident in SH8WM13 than it is in the other plots, principally because of a positive anomaly from northern Canada through the Caribbean to the southern tip of South America. The large positive anomaly under western Africa that is seen clearly in the two S models of this study is not seen in SH8WM13. The degree of visual correlation of the 8C P and S models in these plots is excellent, despite their relatively low correlation coefficient at this depth (see figure 7.1).

Comparison of both the features and the harmonic spectra of the shear models at 2700km depth (figure 8.14) is excellent. The degree 2 component is almost a factor of two greater than any of the others, and this is seen in the very strong 'ring' of high velocity in the top three plots. Furthermore low velocities are seen in the central and Eastern Pacific regions, west Africa, Kamchatka, and the west coast of Canada. Visual correlation of the P model and SH8WM13 does not seem to be as impressive, but the correlation coefficient is very similar at $\approx$ 0.5. This may reflect its greater similarity to SH8WM13 compared to

the S models in certain regions, for example, Australia, northern Europe, and South Africa.

8.6 Discussion and conclusions

The nature of the power spectra can help to determine the type of convection that is occurring within the earth. For example, Jarvis, 1985; Jarvis & Peltier, 1986; Jarvis & Peltier, 1991 have shown that the boundary layers of a convection cell will tend to have heterogeneity concentrated in low order harmonics, termed a 'red' spectrum, whereas in the centre of a cell the power should be evenly distributed amongst all degrees – a 'white' spectrum.

Deterministic studies of mantle heterogeneity can only scratch the surface of convection issues because of their relatively low resolution and because models are normally poor at boundaries as a result of inadequacies of theories or data. Several authors (Woodward *et al.*, 1992; Inoue *et al.*, 1990; Woodward & Masters, 1991a; Woodward & Masters, 1991b) have found that the spectrum is red in both the upper and lower mantles, with power in degrees less than 6 being far greater that power beyond degree 6. The evidence from this chapter has been that although the features of the models may be similar, the harmonic spectra are often quite different (see for example figures 8.6 and 8.10). The effects of aliasing, considered by some authors (Trampert & Snieder, 1994) to be of great importance are not investigated (Woodward *et al.*, 1992), or done in a qualitative basis (Tanimoto, 1990). Stochastic models (Gudmundsson *et al.*, 1990; Davies & Clayton, 1986) overcome this latter problem because they incorporate degrees up to $l = 100$. Their power spectra are also concentrated in degrees 0 to 6 throughout the lower mantle (see figure 17 of Gudmundsson *et al.*, 1990), but even allowing for the Gaussian filter that is used to present these results, the spectrum is much more concentrated around degrees 0 to 4. Results from almost all of the map plots in this chapter do not agree with this, and nor do the complete spectra of SH8WM13.

Stochastic models estimate the characteristic scale length of heterogeneity in the lower mantle to be approximately 1200km, which corresponds to $l \approx 11$. Until deterministic models can be reliably expanded beyond this, and according to Su & Dziewonski, 1991 expansion up to $l = 20$ should be possible, the true nature of the heterogeneity spectrum will remain obscured.

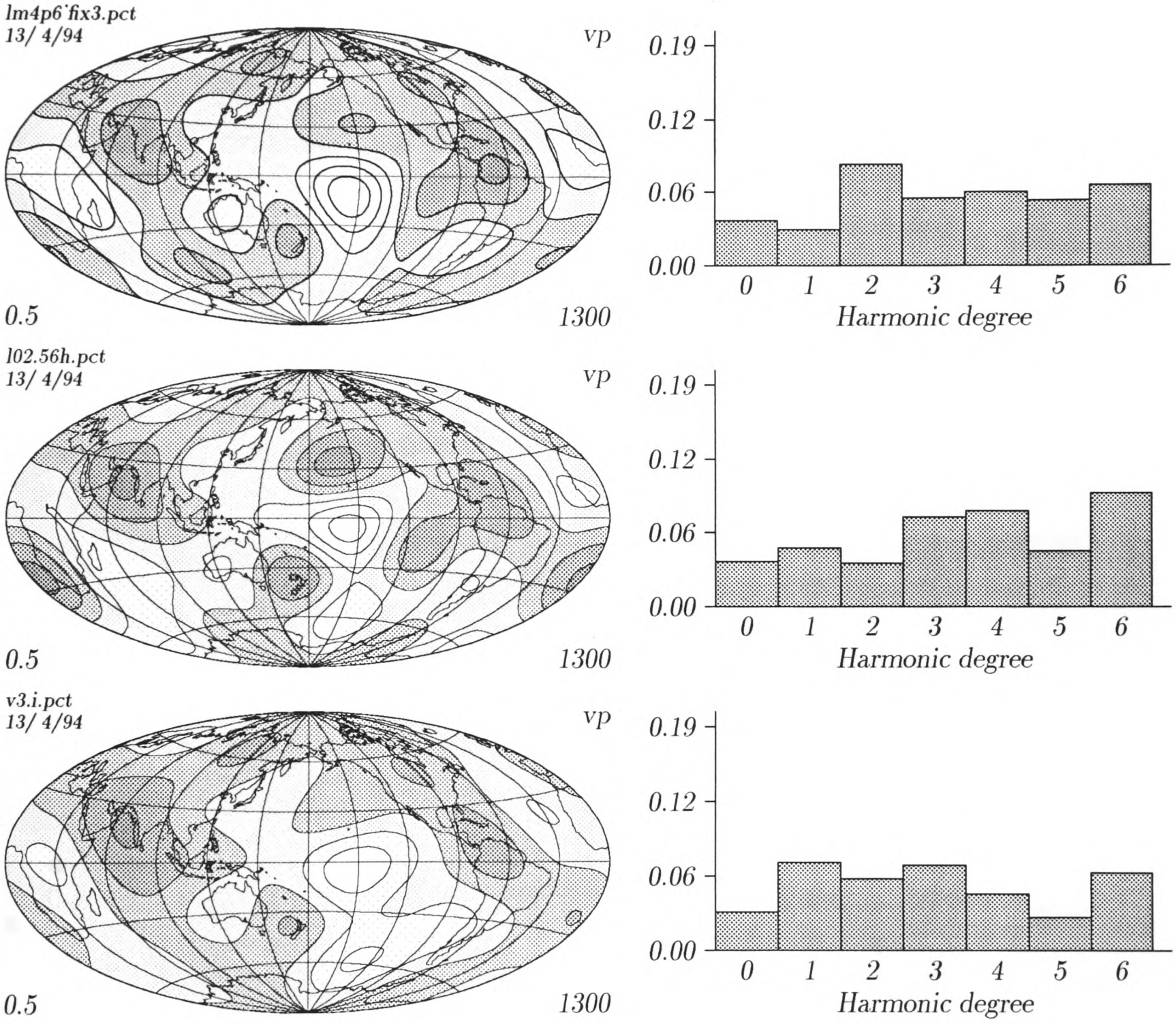


Figure 8.6: Maps of P, l02.56, and V3.i at 1300km depth.

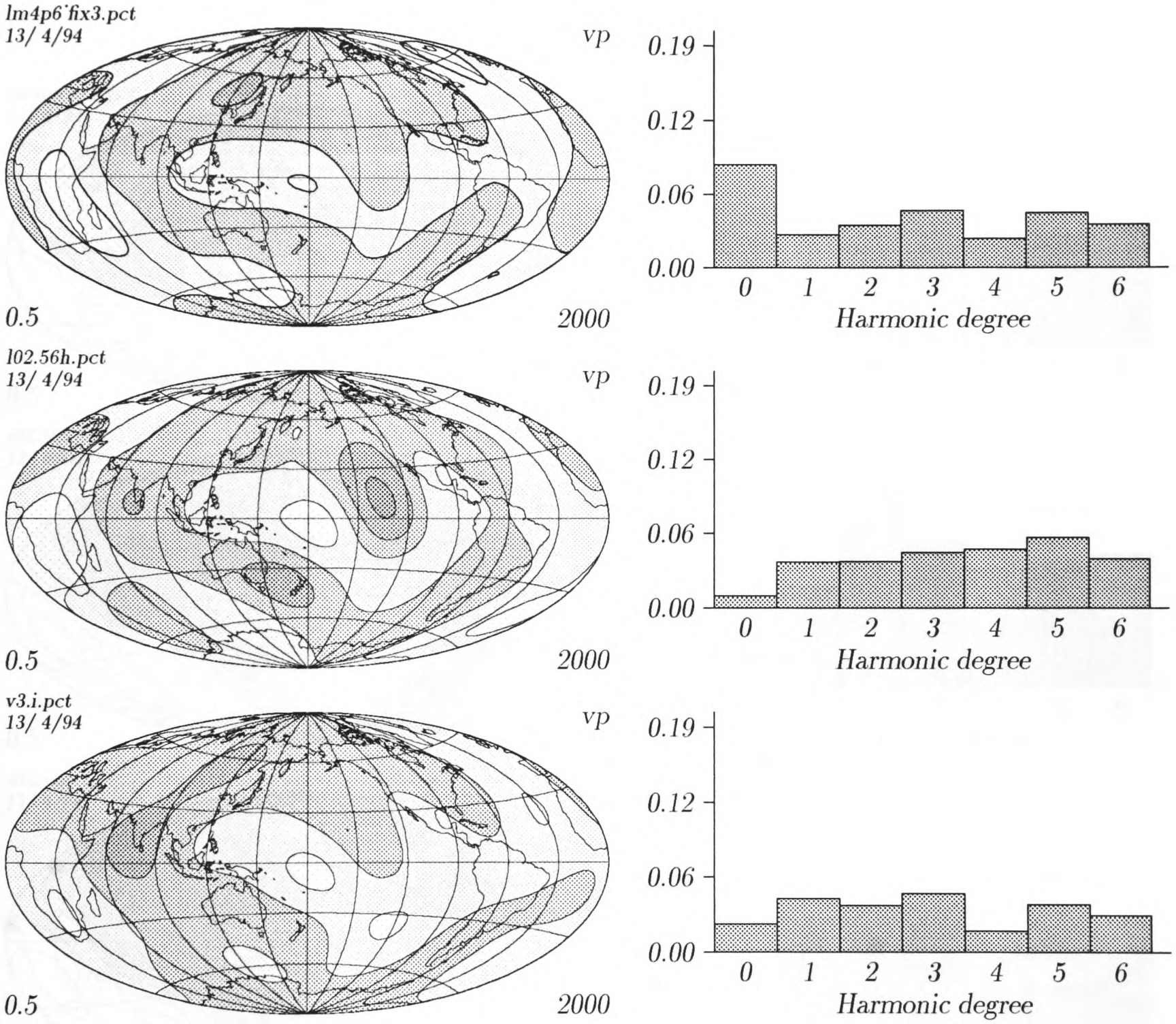


Figure 8.7: Maps of P, l02.56, and V3.i at 2000km depth.

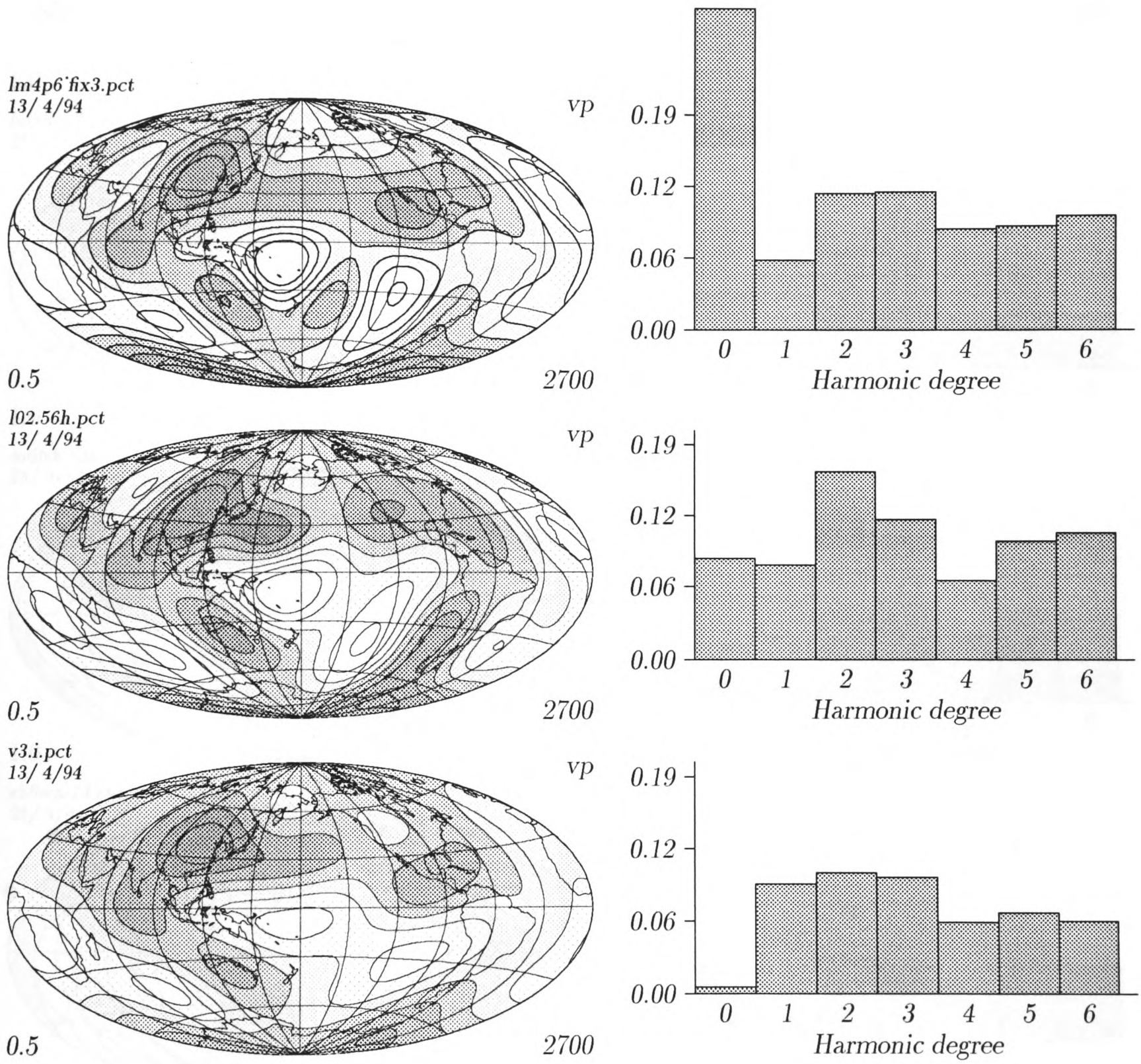


Figure 8.8: Maps of P, l02.56, and V3.i at 2700km depth.

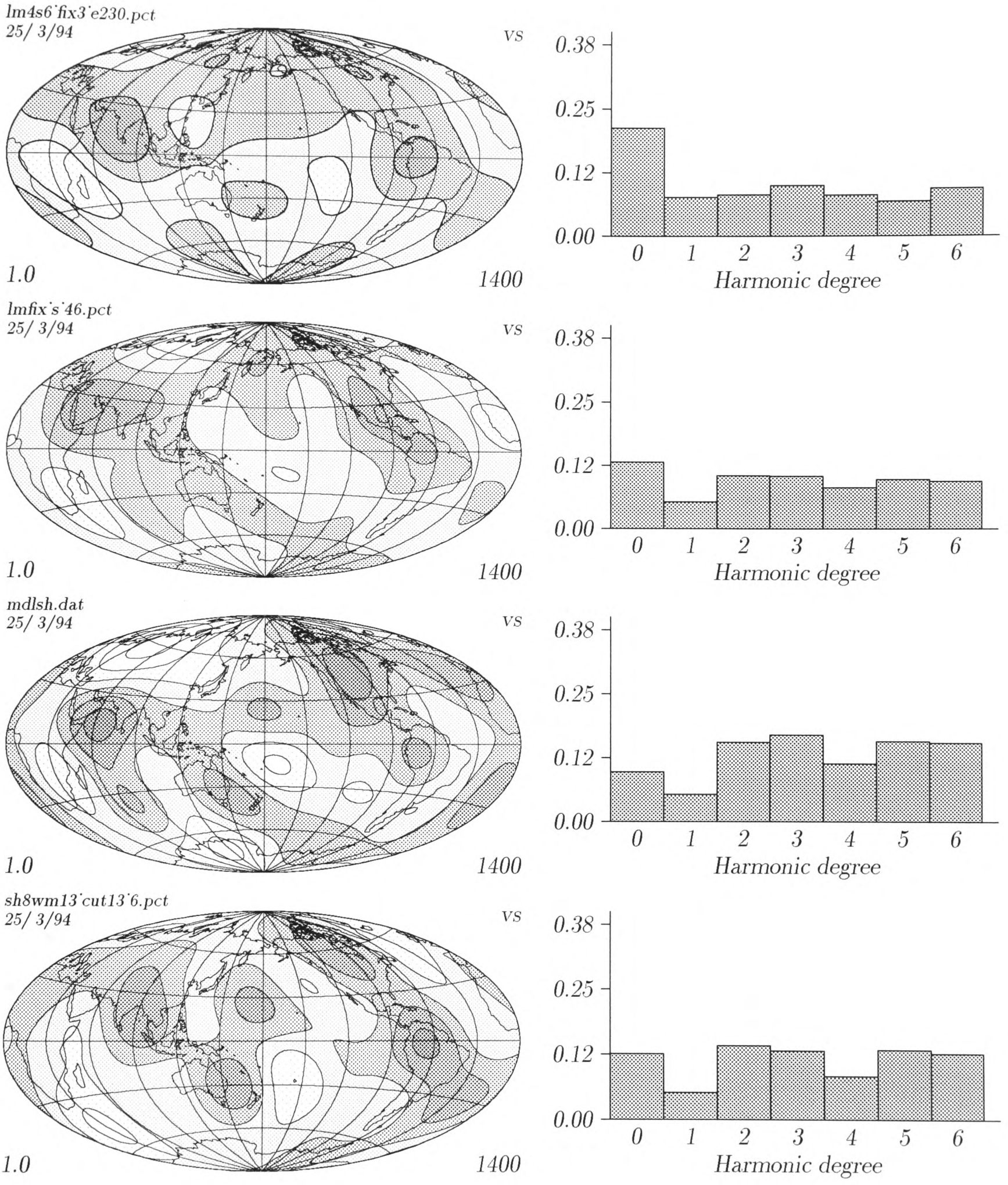


Figure 8.9: Maps of S, U84L85/SH , MDLSH, and SH8WM13 at 1400km depth.

Figure 8.10: Maps of S, U84L85/SH , MDLSH, and SH8WM13 at 1950km depth.

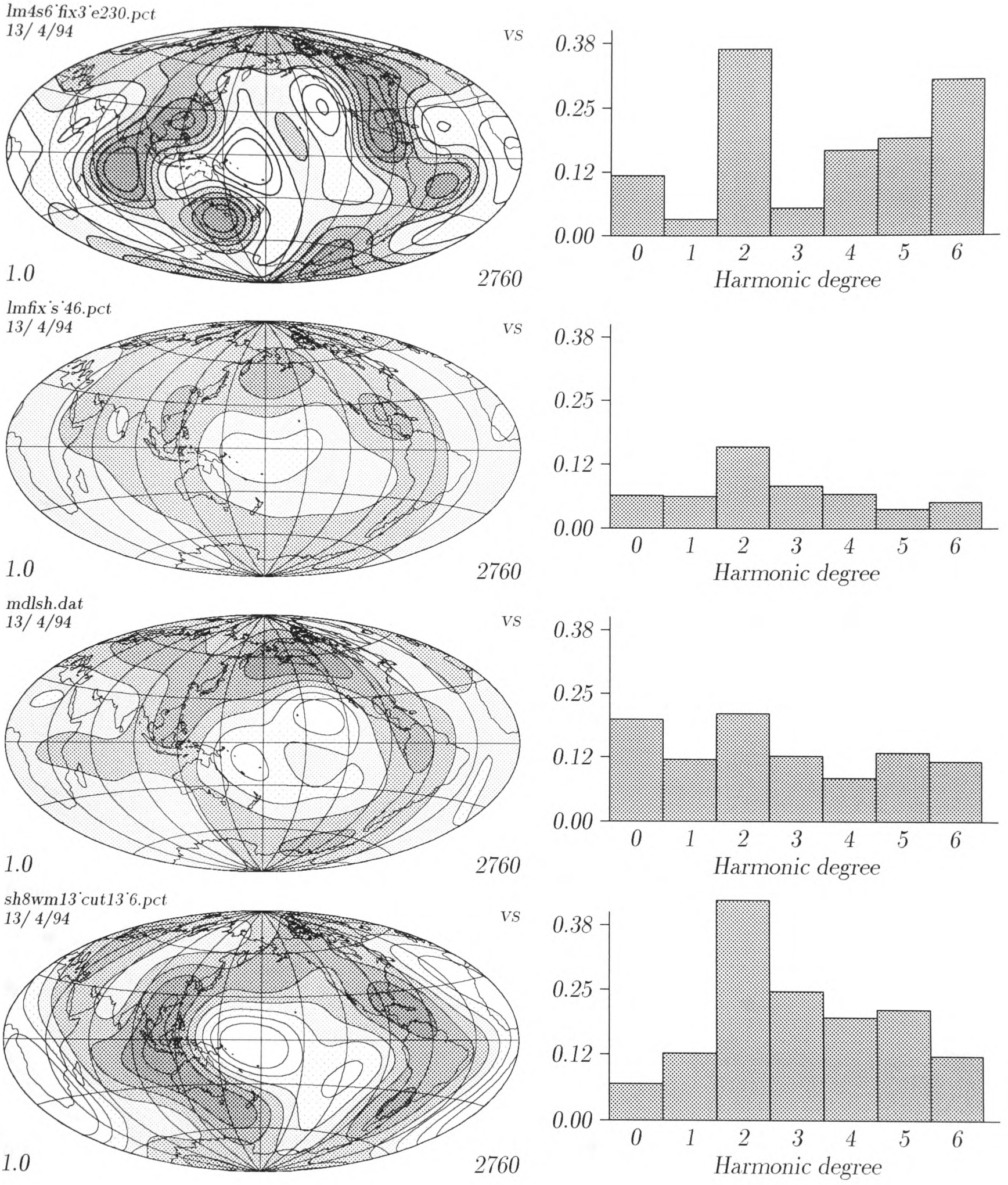


Figure 8.11: Maps of S, U84L85/SH , MDLSH, and SH8WM13 at 2760km depth.

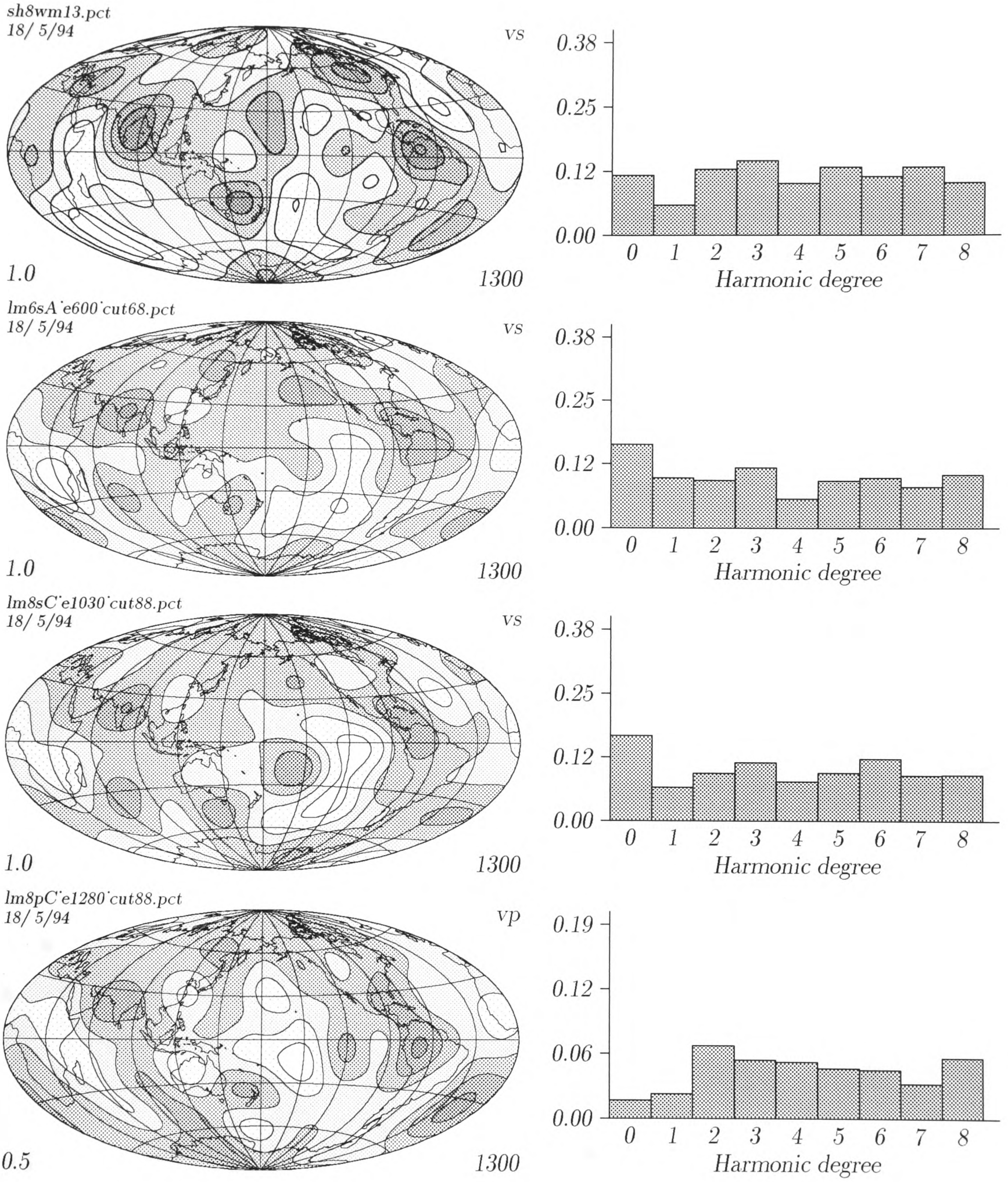
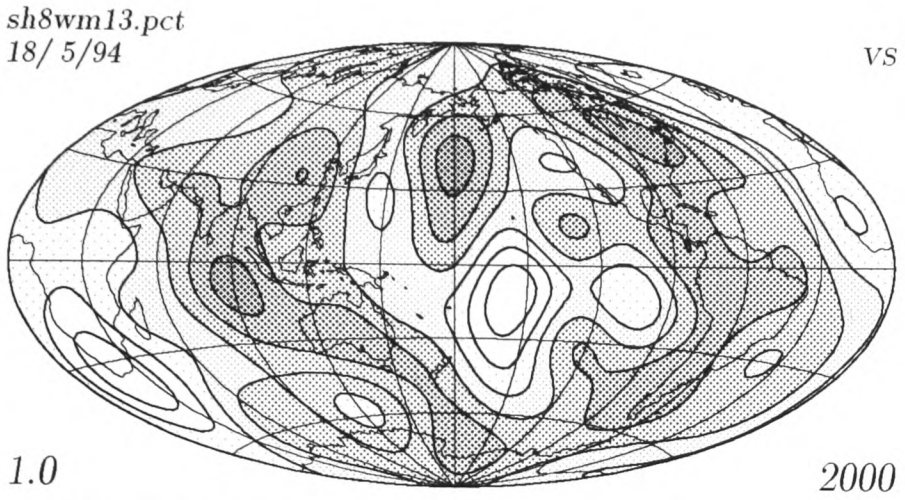
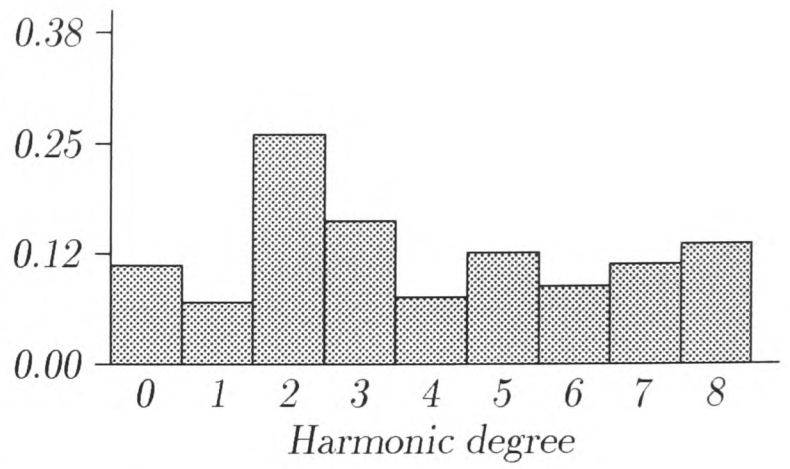
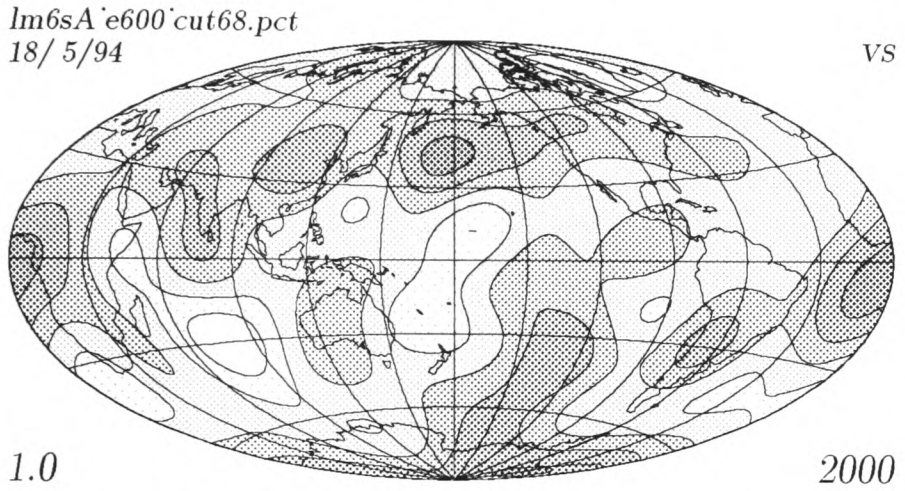
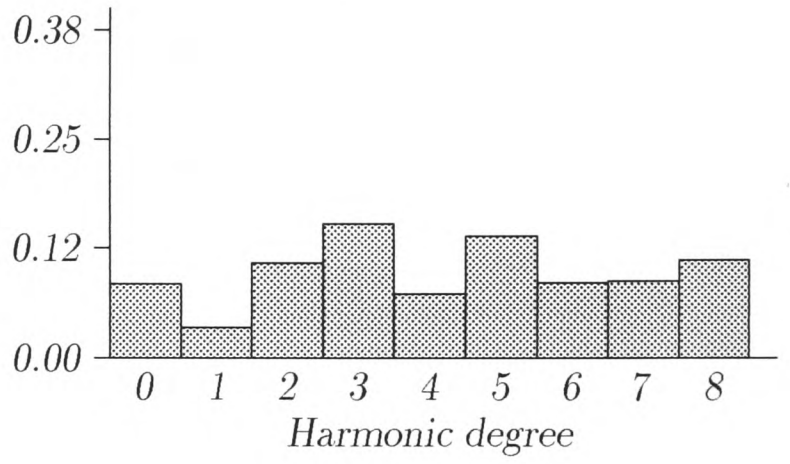


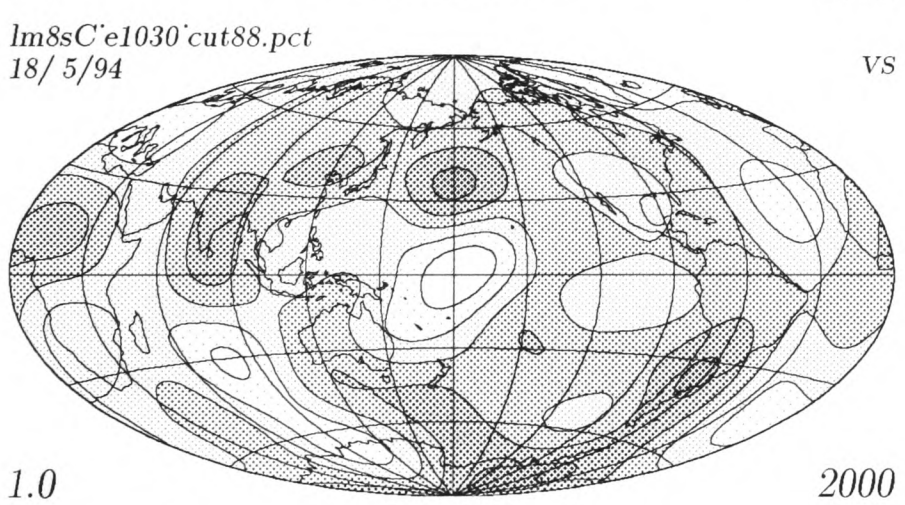
Figure 8.12: Maps of SH8WM13, 6A S model, and 8C S and P models at 1300km depth. Models with lateral parameterizations greater than l=8 have been truncated.

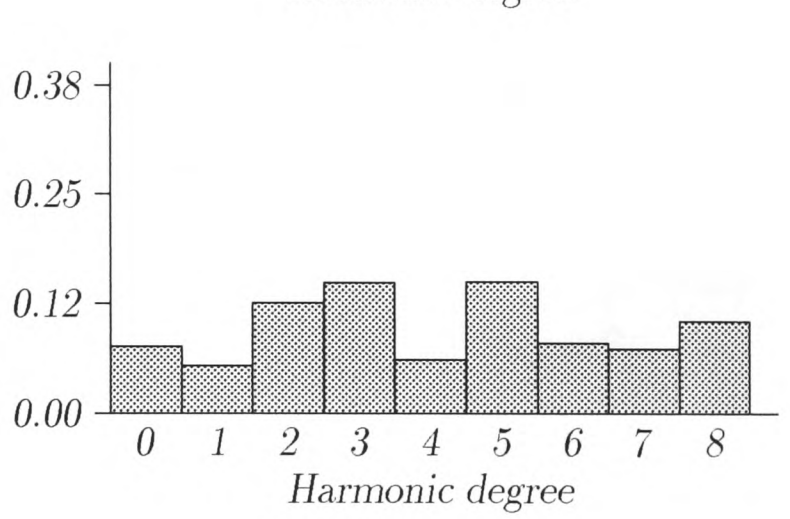


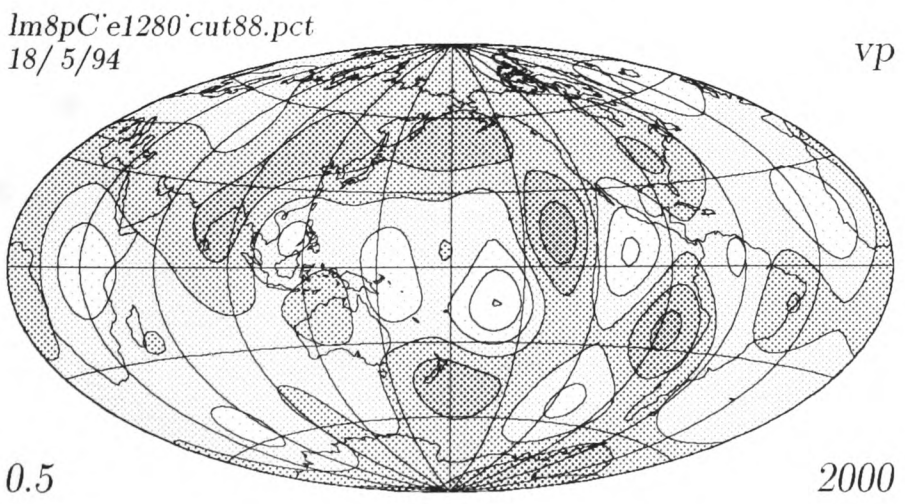












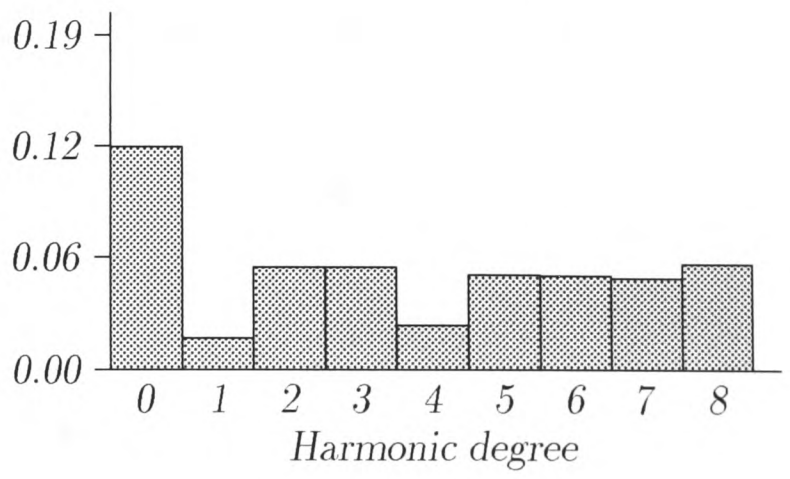


Figure 8.13: Maps of SH8WM13, 6A S model, and 8C S and P models at 2700km depth. Models with lateral parameterizations greater than l=8 have been truncated.

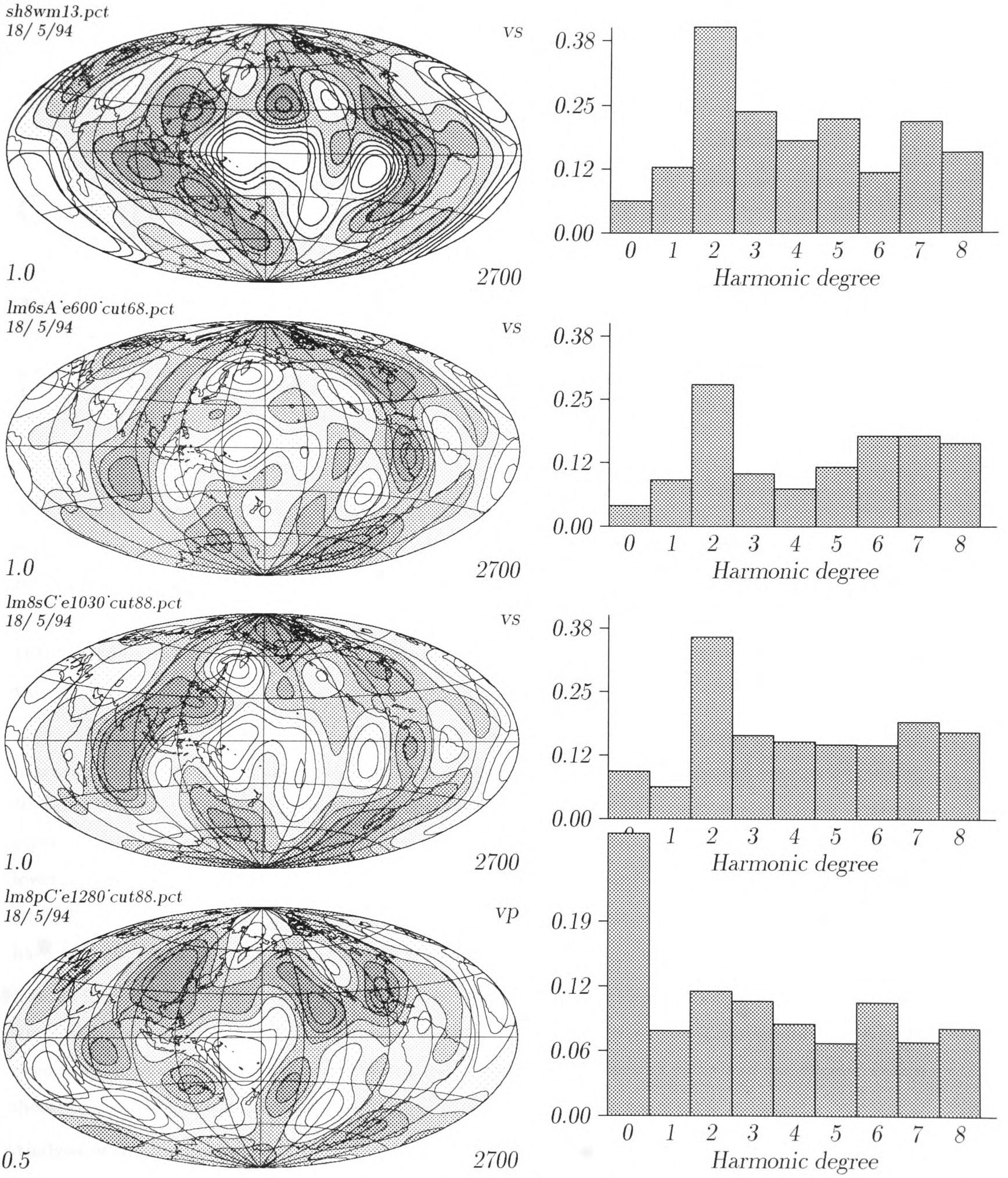


Figure 8.14: Maps of SH8WM13, 6A S model, and 8C S and P models at 2700km depth. Models with lateral parameterizations greater than l=8 have been truncated.

Chapter 9

Ratio of relative S to P model perturbations

There has been considerable debate in the literature over the size of the relative perturbations of shear and compressional velocities throughout the lower mantle. By extrapolation of measurements from rocks under laboratory conditions, Anderson *et al.*, 1968 argued that $\frac{d\ln v_s}{d\ln v_p} = 1.25$, and this value has been adopted by several studies *e.g.* Masters *et al.*, 1982; Forte & Peltier, 1987; Ritzwoller & Gilbert, 1988. In addition there is also a report in Davies *et al.*, 1992 of shock wave experiments giving similar values

Regional seismological studies using differential ScS-S and PcP-P travel times read from digitized seismograms (Lay, 1983) have shown this ratio to be much higher ($\approx$ 2) near in the lowermost mantle. However Pulver & Masters, 1990 have used the same phases derived by waveform correlation measurements to find that the ratio in the lowermost mantle is $\approx$1.7. The first global estimate of $\frac{d\ln v_s}{d\ln v_p}$ in the lower mantle is given in Giardini *et al.*, 1987, 1988 and is even larger at 2.5, although a more recent study by the same authors (Li *et al.*, 1991) obtain an optimum value of 2.27. Bolton & Masters, 1991 have also suggested that the ratio increases with depth.

Results from theoretical calculations also disagree. Agnon & Bukowinski, 1990 used molecular dynamic simulations at pressures and temperatures corresponding to the lower mantle and found that a large ratio of shear to compressional lateral velocity variations can be caused by compressional effects. Other theoretical calculations by Reynard & Price, 1992 disagree with this conclusion.

Analysis of the conflict between laboratory estimates and seismological observations by Anderson, 1987 led him to conclude that '...one cannot adopt laboratory values of temperature derivatives to estimate the effects of temperature on density and elastic wave velocities in slabs and in the deep mantle'.

At first sight it might appear that this parameter should be easily measured seismically because various models of both P and S perturbations exist in the lower mantle. However it is important that the compressional and shear models used are constructed from datasets of the same frequency. There are two main reasons for this:

1. The different seismic datasets all have different resolving powers. For example, the short period models in this study suffer from poor resolution at the top of the mantle whereas the SH body wave model of Woodhouse & Dziewonski, 1986 is relatively poor at the CMB (J. H. Woodhouse, personal communication).

2. The effects of frequency dependence and physical dispersion might cause differences in models constructed from datasets with different frequencies. Several authors (*e.g.* Dziewonski & Woodhouse, 1987; Davies *et al.*, 1992) have suggested that the ratio is not a strong function of seismic period. Nevertheless Li *et al.*, 1991 could not rule out the possibility that frequency dependent heterogeneity could reconcile the difference between their result and those produced in the laboratory.

To date, Davies & Clayton, 1986 is the only other study to derive a global model for S at body wave arrival time periods. Davies *et al.*, 1992 report that this study found the ratio to be approximately 2. Their study used ISC data between the years 1971 and 1980, and was parameterized in terms of blocks. In this study we use ISC data from the years 1969 to 1990 and construct simultaneously models of P and S heterogeneity using the same spherical harmonic expansion. As a result, the models will have very similar resolution operators and should be free of any of the complications detailed above. In addition, because of the parameterization used, comparison with more recent P and S models is easier.

9.1 Importance of the ratio

The ratio of relative S to P velocity heterogeneity is one of the few parameters that can be calculated from geopysical studies and used to constrain the physical properties of rocks in the lower mantle. Several studies (*e.g.* Woodward, 1990) use values obtained from different sources so that both compressional and shear data can be used together.

The most recent work on this subject using deterministic global seismic velocity models has been carried out by Li *et al.*, 1991. In this study the authors compute models of P and S heterogeneity by using splitting coefficients of normal modes sensitive to mantle structure. Not only do they compute a ratio from these models, but they try to incorporate the possible effects of frequency dependence by including factors which describe the over or underestimation of these models compared to pre-existing models derived from higher frequency data. This study confirms a high value of the ratio and confines it to be in the interval (1.67, 2.56) with 75% confidence. However the upper bound of this result is subject to the constraint that heterogeneity in bulk modulus is not negatively correlated with the heterogeneity in rigidity modulus, the seismic data alone giving a value much higher than this. The effect that this condition has on the ratio is derived below.

$$\frac{d\ln v_s}{d\ln v_p} = \frac{d\ln(v_s)^2}{d\ln(v_p)^2} = \frac{\frac{\delta v_s^2}{v_s^2}}{\frac{\delta v_p^2}{v_p^2}} \tag{9.1}$$

$$= \frac{\delta\mu}{\delta\kappa + \frac{4}{3}\delta\mu}\frac{v_p^2}{v_s^2} \tag{9.2}$$

For the limiting case of $\delta\kappa = 0$ therefore

$$\frac{d\ln v_s}{d\ln v_p} = \frac{3}{4}\frac{v_p^2}{v_s^2} = (2.36, 2.56, 2.67) \tag{9.3}$$

where (1.77, 1.84, 1.89) have been used to represent the minimum, average, and maximum values of $\frac{v_p}{v_s}$ in the lower mantle (see figure 9.1).

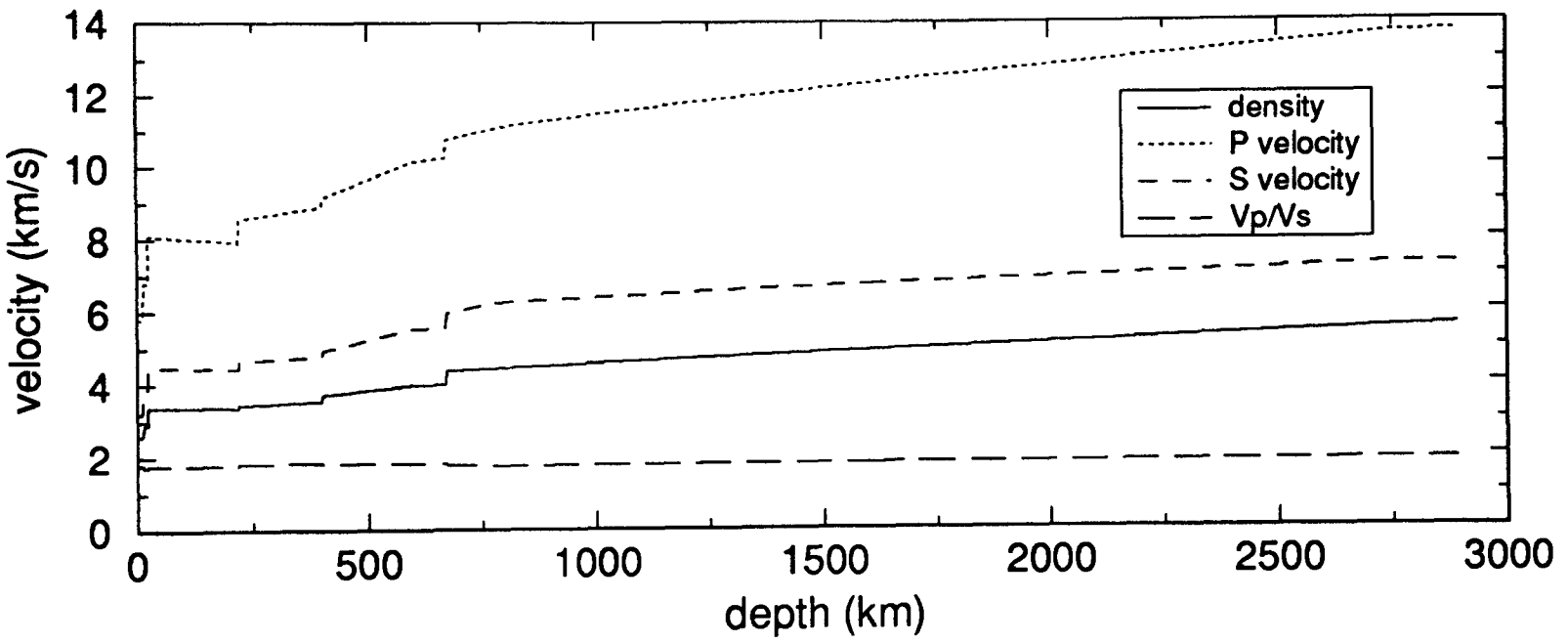


Figure 9.1: Distribution of seismic velocities and density within the spherically symmetric model PREM.

9.2 Chapter outline

Two experiments are performed in this chapter to estimate the ratio $\frac{d\ln v_s}{d\ln v_p}$.

1. Calculate the best fitting ratio assuming that the features of the P model give the most accurate representation of reality. Use the same dataset and station corrections used for the final S model, *ie.* the third iteration with the depths fixed.

2. Invert both P and S datasets simultaneously for a new P model and a ratio.

The second experiment is a nonlinear process because calculation of a ratio requires knowledge of a model for the S dataset. It is necessary therefore to perform the first experiment in order to compute starting models for experiment 2. In a similar way to the inversion method of chapter 5, this experiment is iterative because it involves the calculation of perturbations to both the starting model and the ratio.

Throughout this chapter the models of chapter 5 will be referred to as linear despite the fact that the calculation of these models involved iterations. The term reflects the inherent linearity of the problem, uncomplicated by practical considerations.

9.3 Experiment 1: Fixed P model

The main assumption in this experiment is that the S model takes the shape but not the size of the P model. Indeed Giardini *et al.*, 1987, 1988 suggested that the lateral variations in P and S velocity were proportional. Evidence from the previous chapters of this study has been that the P and S models are well correlated – in chapter 5 the correlation coefficient of the P and S models was found to be between 0.4 and 0.7, with the highest values in these bounds being found where both resolution is good and model variance is low (see section 6.3). This was also found to be the case with the higher parameterized models, which showed good correlation coefficients of 0.5 where data coverage was more complete.

In addition to the ratio, independent perturbations to the degree zero S model are calculated in the inversion. This is necessary because the degree zero terms in all models are dependent on the choice of spherically symmetric reference model, and this must not be included in the ratio of perturbations.

9.3.1 Methodology

Derivation of a set of equations relating the observed travel time residual to the ratio $\frac{d\ln v_s}{d\ln v_p}$ proceeds in a similar fashion to chapter 3. Using the same terminology equation 3.32 can be rewritten specifically for P waves as

$$\delta t_P = \sum_{k=0}^{K}\sum_{l=0}^{L}\sum_{m=-l}^{l} {}_kc_{Pl}^{m}\,{}_k\alpha_{Pl}^{m} \tag{9.4}$$

where ${}_kc_{Pl}^{m}$ are the P model coefficients and ${}_k\alpha_{Pl}^{m}$ involves the kernel functions generated from the spherically symmetric reference model and rotated spherical harmonics. If it is assumed that the shear wave heterogeneity is proportional to the compressional heterogeneity and depth dependent, then we have for the terms with $l > 0$:

$$\frac{\delta v_S}{v_S} = R(r)\frac{\delta v_P}{v_P} \tag{9.5}$$

$R(r)$, the depth dependent ratio can be expanded in terms of Legendre polynomials:

$$R(r) = \sum_{j=0}^{J} \chi_j f_j(r) \tag{9.6}$$

In equation 9.6 above, χ_j are the coefficients of the ratio parameterization. Expanding as before, for shear waves with $l > 0$:

$$ {}_k\delta t_l^m = {}_k c_P{}_l^m \int_{\mathbf{x_S}}^{\mathbf{x}_r} R(r)\frac{1}{v(r)} f_k(r) Y_l^m(\mathbf{x})\, d\mathbf{x} \tag{9.7} $$

$$ \text{Thus we define } {}_{jk}\delta t_l^m = {}_k c_P{}_l^m \chi_j \int_0^{\Delta} G(\xi) f_k(\xi) f_j(r) Y_l^m(\theta,\phi)\, d\xi \tag{9.8} $$

and rotating spherical harmonics this becomes

$$ {}_{jk}\delta t_l^m = {}_k c_P{}_l^m \chi_j e^{im\Phi} \sum_{n=-l}^{l} e^{in\Psi} Q_l^{mn}(\Theta) X_l^n(\tfrac{\pi}{2})\, {}_{jk}I_S^n(\Delta) \tag{9.9} $$

where

$$ {}_{jk}I_S^n(\Delta) = \int_0^{\Delta} G(\xi) f_k(\xi) f_j(\xi) e^{in\xi}\, d\xi \tag{9.10} $$

is a *perturbation integral* calculated from the spherically symmetric reference shear wave model. Concisely therefore, for shear waves with $l > 0$

$$ {}_{jk}\delta t_l^m = \chi_j\, {}_k c_P{}_l^m\, {}_{jk}\beta_l^m \tag{9.11} $$

where

$$ {}_{jk}\beta_l^m = e^{im\Phi} \sum_{n=-l}^{l} e^{in\Psi} Q_l^{mn}(\Theta) X_l^n(\tfrac{\pi}{2})\, {}_{jk}I_S^n(\Delta) \tag{9.12} $$

The δt term for the S arrival with $l = 0$ must be computed with the ${}_k\alpha_S{}_0^0$ calculated from the spherically symmetric shear model, *ie.* using I_S instead of I_P. Hence, using the same terminology as equation 3.32 we have

$$ \delta t_S = \left[\sum_{j=0}^{J} \chi_j \sum_{k=0}^{K} \sum_{l=1}^{L} \sum_{m=-l}^{l} {}_k c_P{}_l^m\, {}_{jk}\beta_l^m \right]_{m\neq 0} + \sum_{k=0}^{K} {}_k c_S{}_0^0\, {}_{0k}\alpha_S{}_0^0 \tag{9.13} $$

9.3.2 Synthetic experiments

A synthetic dataset has been generated using the ray geometries of the dataset that is used to compute the final S model of figure 5.39. The synthetic residuals are calculated from equation 3.32 using the final P model and a synthetic ratio model constructed from Legendre polynomials of degrees 0 and 1. The coefficients are 2 and -0.5, giving rise to the ratio profile shown as the solid line in figure 9.2 and is supposed to be representative (although this is not necessary) of the ratio within the lower mantle. Inverting this dataset for a ratio to degree 1 using the same P model as was used to generate the synthetic data gives the same ratio coefficients back, with 100% variance reduction. However in

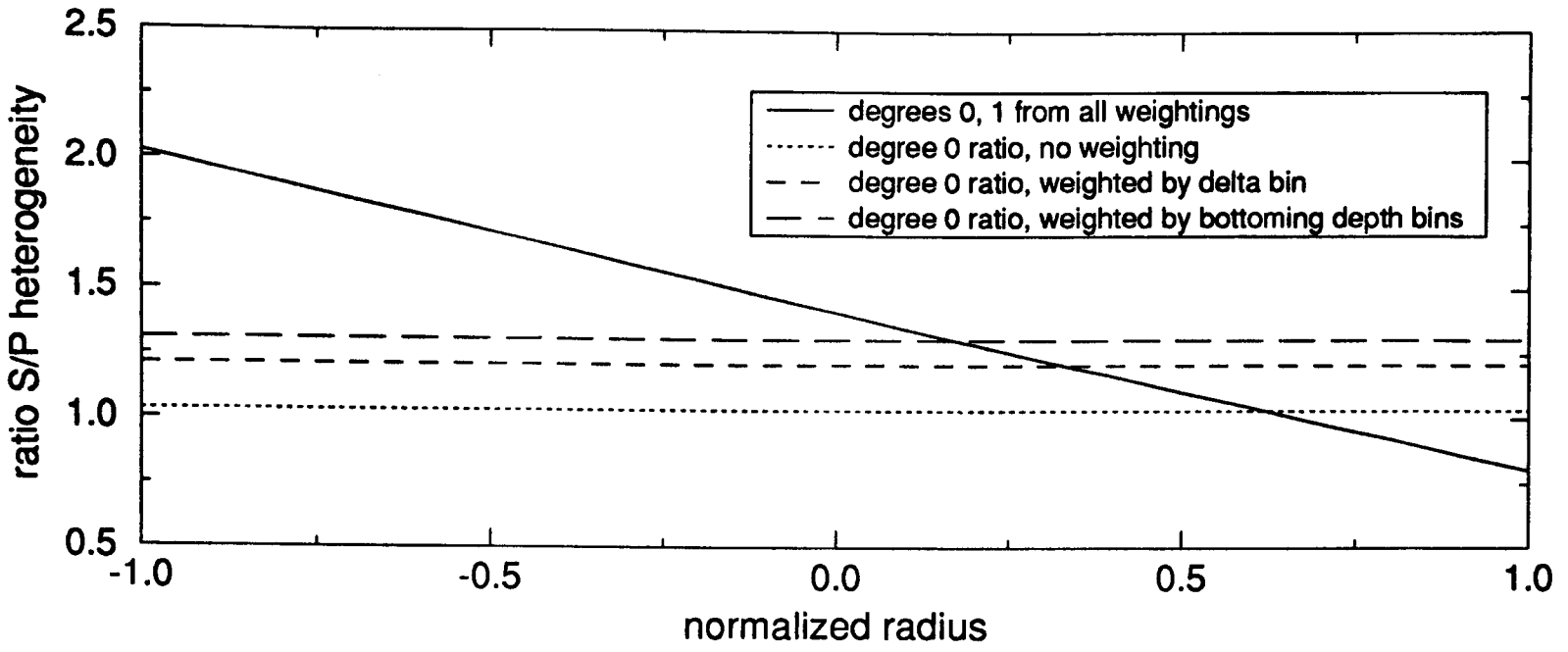


Figure 9.2: The results of the synthetic experiment to investigate the effects of weighting in the ratio inversion.

the inversion for only a degree zero term (*ie.* inversion for a constant ratio) the coefficient returned is 1.46, which corresponds to a ratio of 1.03 (the dotted line of figure 9.2). This is not the expected average ratio coefficient value of 2.0 because of the distribution of the data within the lower mantle. The comparatively small amount of data which penetrates to depths greater than ≈2000km is hardly contributing to the overall average lower mantle ratio resulting in a biased value.

Clearly some sort of weighting scheme is required to account for the considerable data bias in the upper regions of the lower mantle. Two schemes have been investigated.

1. Binning the data at equal epicentral angles and then weighting each residual with the inverse of the number of arrivals in that bin. The distribution of the data has already been shown in figure 6.6 in section 6.3.3.

2. Binning the data at equal bottoming depth intervals and then inversely weighting each residual with the number of arrivals in that bin[1]. The distribution of data from this criterion is shown in figure 9.3.

Comparison of these two figures quite clearly shows that the residuals at greater epicentral angles are going to be weighted higher in the second scheme than in the first. In both cases special care is taken to ensure that bins with very few arrivals do not give rise to very high path weights.

The results of the inversions for the average lower mantle ratio are shown as the dashed and long dashed lines in figure 9.2 for schemes 1 and 2 respectively. It is not surprising that the latter gives the more accurate result because the ratio is a function of depth and not epicentral angle. It should be noted that even with this weighting the depth independent ratio is still smaller than it should be by 7.4%

[1] In practice this means finding the relationship between bottoming depth and epicentral angle through PREM

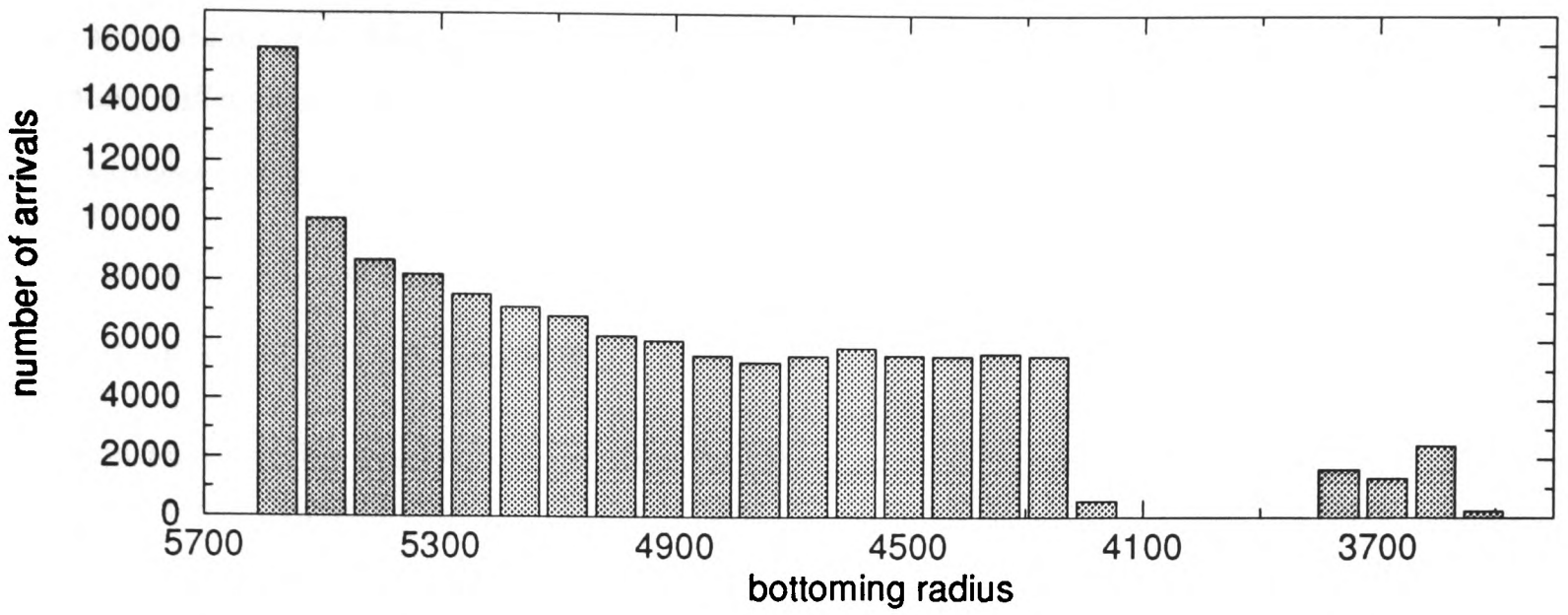


Figure 9.3: Number of S arrivals per bottoming depth bin for the dataset contributing towards the final S model, and the models of this section.

parameterization n l	*model*	*ratio*	*standard deviation*	*% variance reduction*
2 2	P	1.42	0.024	2.45
2 2	PS	1.35	0.022	2.73
4 2	P	1.46	0.023	3.20
4 2	PS	1.39	0.023	3.36
4 4	P	1.40	0.019	3.92
4 6	P	1.30	0.017	5.09
4 6	PS	1.07	0.015	5.07
4 6	V3.i	1.02	0.015	4.36

Table 9.1: Experiment 1: Results of the inversion for a constant S to P velocity heterogeneity ratio throughout the lower mantle.

because of the complete absense of data in 3 bins at large depths, which means that the ratio is slightly biased towards its value in the upper parts of the lower mantle. This will have to be taken into account in the analysis of the results of the actual experiment.

9.3.3 Results

Since the results of an inversion cannot be assumed to be independent of the parameterization used, several parameterizations and models have been tested. The results for the case in which only the degree zero or depth independent term in the ratio expansion is calculated are shown in table 9.1. All models apart from V3.i are derived from the dataset that is used to construct the chosen models of chapter 5.

It is clear that even taking into account the factor of 7.4% by which the synthetic experiments show the inversion results can differ from reality, the ratio is very low, and the spread over parameterizations is very large. This spread is an order of magnitude greater than the standard deviation associated with

each individual value. The results for the $n = 4, l = 6$ experiment are by far the most indecisive with the three different models used giving significantly different results.

The variance reductions obtained are less than half of those of chapter 5 which shows that either

- one term is not adequate to describe this ratio.
- the P model does not describe the heterogeneity well.

This question can be answered by inverting for higher parameterized ratios. The variance reductions obtained will undoubtedly be higher, but it is the amount by which this is true that will determine which of the two points listed above is correct. Only the $n = 4, l = 6$ parameterizations are used because it is invalid to compute a ratio whose number of parameters is comparable to the number of terms used in the depth expansions of the models. The results are shown graphically in figures 9.9, 9.10, and 9.11 for the P, PS , and V3.i (Morelli & Dziewonski, 1991) basis models respectively. The average value of all parameterizations for each of the models is approximately the same, which verifies the choice of weighting system.

Inverting for ratio coefficients $j = 0, 1$ shows that in two out of the three cases, P and V3.i, the ratio increases with depth, with the error bars being twice as large at the top and bottom of the lower mantle than they are in mid mantle regions. This behaviour is not shown in the PS case, figure 9.10, but it must be remembered that the data distribution at depth in this model is severely restricted.

When three coefficients are computed in the inversion, ratios derived using the P and V3.i starting models are again very similar in shape. Both have their lowest values at the upper/lower mantle boundary before rising to their maximum points at around 4000 to 5000km radius, and then falling slightly towards the CMB. Their general trends are the same, but the overall variations are different – the P ratio spans 0.8 to 1.6 whereas the V3.i ratio goes from 0.75 to 1.1. The PS ratio mimics this behaviour in the mid and upper lower mantle, but falls away rapidly towards the CMB. The final inversions for the ratio with four coefficients show rapid variations with depth in all three cases. This is probably because the ratio is over parameterized (see above). The variance reductions involved are shown in table 9.2

The variance reductions used in the table are derived by removing the contribution of the ratio, S_0 model, and compressional model from the S residuals. In the inversion procedure it is the residuals weighted according to dataset geometry (see section 5.1) and bottoming depth bins that are minimized. This is the reason for the decrease in the variance reduction for model V3.i as the number of parameters increases (a higher parameterized ratio inversion should never give a decrease in variance). The weighted variance reductions obtained from equation 5.7 do not decrease.

Table 9.2 also shows that the S_0 variance reductions for the basis model V3.i are far larger in magnitude than those of the models derived in this study. Similarly the variance reduction that results from the ratio only are very small. Since the S_0 variance reduction is large and negative while the total variance

model	*maximum ratio parameterization*	*total variance reduction %*	*ratio variance reduction %*	*S_0 variance reduction %*
P	0	5.09	2.79	-0.32
	1	5.10	2.94	-0.20
	2	5.12	2.80	-0.28
	3	5.13	2.82	-0.22
PS	0	5.02	3.38	0.17
	1	5.03	3.38	0.16
	2	5.09	3.33	0.09
	3	5.13	3.30	0.10
V3.i	0	4.36	0.09	-2.32
	1	4.21	0.33	-1.92
	2	4.14	0.21	-1.91
	3	4.28	0.60	-1.66

Table 9.2: Experiment 1: Results of the inversion for a depth dependent S to P velocity heterogeneity ratio throughout the lower mantle. All three models are parameterized with $n = 4, l = 6$.

reduction is positive, the ratio must be trading off with the S_0 model. This tends to imply that V3.i does not accurately represent the form of the S heterogeneity. Nevertheless, figure 9.4 shows that this is not the case – it correlates better with S than the compressional models of this study in several places and is worse only in the lower mid mantle region. Why these differences exist is not fully understood.

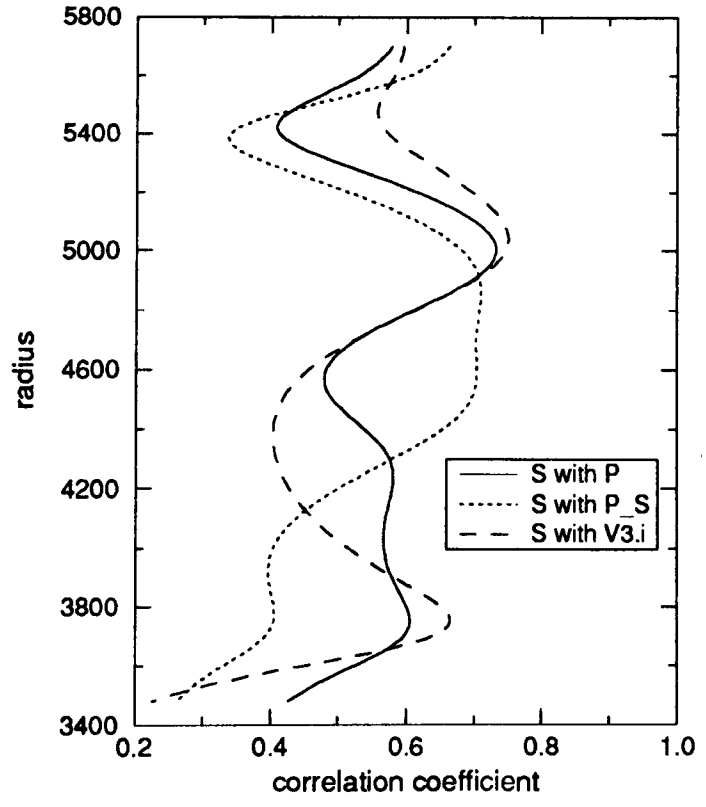


Figure 9.4: Correlation coefficients of the compressional models P, PS , and V3.i with the S model of this study.

The maximum variance reduction obtainable from this dataset is 8.93% – that which is obtained when the S model derived from it is removed (see table 5.5). In other words, this is the greatest amount of coherent lower mantle heterogeneity signal that can be recovered from this dataset using models of this parameterization. As a result, 8.93% is the maximum variance reduction that can be hoped to be

obtained from this experiment. In terms of these statistics, this means that the percentage improvement in one model over another is greater than the difference between their variance reductions. For example, the difference between the percentage variance reductions of the ratios to degree zero and one using the P model is 0.01%. This actually represents an improvement of $\frac{0.01 \cdot 100}{8.93}\% = 0.11\%$. Hence the percentage differences in variance reductions have to be multiplied by 11 to obtain the actual percentage potential improvement. This argument presumes that a variance reduction of 8.93% is obtainable from the technique of this experiment. This is almost definitely not going to be the case because the P models and the S model of chapter 5 are far from being identical.

Despite this argument, the improvements offered by the larger parameterized ratio inversions are very small, with the ratio to degree two offering hardly any improvement in real terms over the depth independent ratio. Better results should be obtained in the next experiment when changes to the event locations and station corrections are permitted

9.4 Experiment 2: Joint inversion of P and S datasets

Experiment 1 was far from conclusive in terms of determining the ratio of the relative perturbations in velocities. This is because it is far from an ideal experiment, principally because there is no allowance for changes to either the source or receiver terms (relocations or station corrections). Experiment 2 is intended to be far more rigorous than the first experiment, but it requires the output from it for its starting conditions.

As was discussed earlier in this chapter, a joint inversion of both datasets for a P model and a ratio is highly nonlinear. In order to calculate an S ratio it is necessary to know a starting P model, and in order to fit a model to the S data, it is necessary to have knowledge of a starting ratio. This is in addition to the slight nonlinearity involved in calculating the models on their own (which arises from the non simultaneous inversion of the hypocentral coordinates, the station corrections, and the model coefficients). For the same reasons as those given in section 9.3 an independent degree zero S model (S_0) is computed at the same time as the ratio. Hence the ratio is that of relative heterogeneities – the departure from the spherical average of the seismic velocities.

This experiment proceeds in an almost identical method to the one outlined in chapter 5. The steps involved are summarized below.

1. Relocate the raw PREM residuals using the P model derived from the third iteration of chapter 5 with the depths fixed, along with the ratio and S_0 model derived from experiment 1.
2. Calculate the station corrections.
3. Relocate again using the P model, ratio, S_0 model, and station corrections.
4. Select the best N events per 5° cell according to the criterion of section 5.1.

5. Invert both the P and S datasets resulting from item 4 above for perturbations to the P model, the ratio, and the S_0 model.

6. Add the perturbations to the starting models.

7. Repeat steps 5 and 6 until the perturbations are insignificant.

8. Repeat steps 1 to 7 until the process converges.

Unlike the calculation of the models in chapter 5, item 7 should lead to complete convergence because the models (P, ratio, and S_0) are the only parameters that are changing, and these are all included in the inversion. Both the hypocentral coordinates and the station corrections are fixed at this stage. The speed of convergence is dependent only on the accuracy of the starting models. Step 8, however, which involves the relocation of events, will suffer from the same lack of convergence problems that were evident in chapter 5.

9.4.1 Calculation of model perturbations

Allowance for changes to the models in the inversion can be made by perturbing equations 9.4 and 9.13. This gives:

$$\begin{aligned} \delta(\delta t_P) &= \sum_{klm} {}_k\delta c_{P\,l}^{\,m}\ {}_k\alpha_{P\,l}^{\,m} \\ \delta(\delta t_S) &= \sum_{jklm} [{}_k\delta c_{P\,l}^{\,m}\ \chi_j\ {}_{jk}\beta_l^m + {}_k c_{P\,l}^{\,m}\ \delta\chi_j\ {}_{jk}\beta_l^m]_{l\neq 0} + \sum_k {}_k c_{S\,0}^{\,0}\ {}_k\alpha_{S\,0}^{\,0} \end{aligned} \qquad (9.14)$$

9.4.2 Depth independent ratio

In a similar way to experiment 1, several different parameterizations of the model have been used in this experiment in order to estimate the dependence of the ratio on the parameterization used. Throughout experiment 2 the number of coefficients in the depth expansion of the models is kept as large as possible in order to minimize the effects of the depth parameterization on the ratio. In other words, the variation of heterogeneity with depth might not be fit well by very low order polynomial expansions. The same weightings that were described in section 9.3.2 for experiment 1 are used for the S data in this experiment. In order to make sure that this additional weighting does not severely overemphasize the importance of the P data in the inversion, both sets of residuals are normalized so that the sum of the weights of the P and S datasets are equal to the number of data that each contributes to the inversion. This effectively means that the compressional phase has six times the weighting of the shear phase. Although this seems large, it implements our belief that the P model more accurately represents the shape of the heterogeneity in the lower mantle. Furthermore in the deepest mantle the P

arrivals are far more likely to be reliable than S which has a higher probability of being contaminated by diffracted S or SKS.

All starting P models are derived from the dataset that was inverted to obtain the final P model, in other words, from the third iteration where the depths of the events were fixed after the second.

The first model parameterization used is $n_{MAX} = 4, l_{MAX} = 2$. Together with the ratio and the spherically symmetric model, there are only 51 coefficients in the inversion and so the whole iterative procedure takes a relatively small amount of time. In addition, eigenvalue analysis shows that damping of the models calculated within each iteration is not required and so results are independent of damping. As a result, and because of the small amount of CPU time involved, we take the opportunity to invert two sets of data:

1. 5 events per 5° cell
2. 15 events per 5° cell

model parameterization				*ratio*			*% variance reduction*	
n	*l*	*events*	*cell width°*	*it 1*	*it 2*	*it 3*	*S*	*P*
4	2	5	5	1.65	1.74	1.76	7.35	9.45
4	2	15	5	1.59	1.66	1.67	6.68	9.43

Table 9.3: Results for experiment 2 for a ratio of S to P heterogeneity which is independent of depth. The results in the three 'it' columns refer to the results of the third repeat of step 7 at the start of this section, when the changes to the ratio, model, and S_0 model become vanishingly small.

The results from table 9.3 show that the ratios are quite similar, as indeed is their behaviour throughout the iterations. The variance reductions are quite high, and in fact are comparable to the variance reductions derived from the higher parameterized inversions of chapter 5. This result means that the S data can be fit well by the procedure of this experiment. The ratios derived from these two datasets are much larger that those for the first experiment, and are comparable to several results in the literature at similar periods, *e.g.* Pulver & Masters, 1990. A proper analysis of what differences are occurring to the P model will be deferred until the 4_6 parameterization model has been calculated since this result will be directly comparable with the corresponding plots of the linear models in chapter 5.

Damping of the model when higher parameterizations are used becomes an important issue. Unlike the inversions in previous chapters, the coefficients that are calculated here are not all of the same size. Spherical harmonic coefficients are typically $\approx 10^{-3}$ in magnitude. The ratio coefficients are typically three orders of magnitude larger than this. Consequently there will be big differences in the rows and columns of the inner product matrix elements in the least squares inversion procedure which in turn will make some eigenvalues much larger than others. No longer are the sizes of the eigenvalues all proportional to the accuracy with which the eigenvector is known, and so the eigenvector analysis model norm and variance plots cannot be used in the same way as before.

The choice of which coefficients to damp is also one which has to be made. For example the ratio should be constrained by every S arrival and therefore should be well known. However in the linear inversions of chapter 5 it was found that the P model continued to become larger at each iteration in places where the model was poorly constrained, and although the eigenvalue analysis plots showed that damping was unnecessary, a small amount of damping may have prevented this. As a result the formulation below is used so that a degree of damping can be applied only to the perturbations of the P model.

The set of equations 9.14 can be written symbolically as:

$$\mathbf{Ax} + \mathbf{By} = \mathbf{d} \tag{9.15}$$

where $\mathbf{x}$ is a vector of P model coefficients and $\mathbf{y}$ is a vector of ratio and S_0 model coefficients. This has effectively split the coefficients into parts which might not be well constrained and those which should be well constrained. Application of the least squares procedure to this gives

$$\begin{bmatrix} \mathbf{A^T A} & \mathbf{A^T B} \\ \mathbf{B^T A} & \mathbf{B^T B} \end{bmatrix} \begin{bmatrix} \mathbf{x} \\ \mathbf{y} \end{bmatrix} = \begin{bmatrix} \mathbf{A^T d} \\ \mathbf{B^T d} \end{bmatrix} \tag{9.16}$$

or

$$\mathbf{A^T Ax} + \mathbf{A^T By} = \mathbf{A^T d} \tag{9.17}$$

$$\mathbf{B^T Ax} + \mathbf{B^T By} = \mathbf{B^T d} \tag{9.18}$$

Substituting $\mathbf{y}$ from equation 9.18 into 9.17 gives

$$[\mathbf{A^T A} - \mathbf{A^T B}(\mathbf{B^T B})^{-1}\mathbf{B^T A}]\mathbf{x} = \mathbf{A^T d} - \mathbf{A^T B}(\mathbf{B^T B})^{-1}\mathbf{B^T d} \tag{9.19}$$

This equation is in a form which can be solved in an identical way to previous inversions. Once the eigenvalue analysis has been performed and the solution $\mathbf{x_g}$ found, equation 9.18 can be rewritten

$$\Rightarrow \mathbf{y} = (\mathbf{B^T B})^{-1}[\mathbf{B^T d} - \mathbf{B^T A x_g}] \tag{9.20}$$

Figure 9.12 shows the eigenvalue analysis for the inversion for $\mathbf{x}$ in equation 9.19 for models parameterized to $l_{MAX} = 4$ and $l_{MAX} = 6$. The most noticeable point about these plots compared with the previous examples is that the scales of the y axes are much smaller because the inversion is for model coefficient perturbations, not the model itself.

The plots for both the 4_4 and 4_6 cases show a feature which has not been apparent in previous eigenvalue analysis plots – the model norms become much bigger while the variance reductions continue to decrease at the same rate. This makes the choice of truncation point quite difficult. Indeed damping may not even be required because no damping was used for the P model in chapter 5, and this model has contributing to it additionally the S dataset. However section 7.5.1 showed that the final S model of chapter 5 is probably underdamped. Furthermore, the starting models for these iterations are already

larger than they should be (see section 5.7.1) and so damping is probably going to be required. With cutoffs chosen at 85 and 180 for the 4_4 and 4_6 cases respectively, the model norm squares are cut by more than two thirds while the variance reductions are only cut by around 20%.

The statistics obtained when this damping is used in the inversions throughout the iterations are tabulated in table 9.4.

					before inversion		after inversion		
parameterization n l	events/cell	*phase type*	*iteration number*	*ratio*	*mean*	*one step variance*	*mean*	*variance*	*unw. variance reduction (%)*
4 4	15 5	P	1	1.66	0.038	1.616	-0.018	1.447	10.59
			2	1.77	0.034	1.634	-0.018	1.445	11.68
			3	1.81	0.031	1.652	-0.018	1.444	12.63
		S	1		0.231	13.875	-0.133	13.063	5.85
			2		0.365	14.059	-0.123	13.014	7.43
			3		0.488	14.215	-0.120	12.994	8.59
4 6	15 5	P	1	1.58	0.032	1.621	-0.016	1.433	11.67
			2	1.81	0.026	1.637	-0.016	1.432	12.57
			3	1.89	0.020	1.652	-0.016	1.432	13.34
		S	1		0.228	13.906	-0.125	12.959	6.81
			2		0.353	14.130	-0.116	12.934	8.42
			3		0.467	14.337	-0.115	12.914	9.93

Table 9.4: Iteration statistics for the joint inversion of the P and S datasets for a depth independent ratio.

The ratios for these parameterizations agree well, but both are higher than those for the 4_2 cases in table 9.3. The results here are probably more accurate because the true nature of heterogeneity in the earth may not be described very well by spherical harmonic expansions to degree 2 only. A discussion of the variation in ratios derived in this study will be presented in section 9.4.3.

The inversions show clear signs of convergence, with changes in the ratios and the variance of the P dataset becoming increasingly small with each iteration. In section 5.9 it was stated that the iterative procedure probably would not converge because of the different weightings in the relocations and the inversions, and because of the trade–off problem. Hence these iterations are terminated at 3 to avoid compounding these effects. The ratios have not quite converged but they are close. As was observed in chapter 5, the variance of the S dataset is slower to converge because it is less dominant in the inversion. Indeed the variances of both the P and S datasets are larger than they were in chapter 5. This is understandable because there are fewer degrees of freedom involved in the inversion for a P model and a ratio and spherically symmetric model to describe S heterogeneity, as opposed to completely independent P and S models in the linear case.

Since the P arrivals outnumber the S arrivals by a factor of six, there is the possibility that the iterations could be dominated by the compressional data with changes to the model and the ratio from the shear wave data occurring only slowly. Figure 9.5 attempts to show that this has not been the case. The left hand plot shows the size of the changes to the model within the first iteration (step 7 in section 9.4).

It is clear that the first change is large, being approximately 40% of the size of the model itself, but subsequent changes are very small, being on average 0.01%. The right hand plot shows the first change to the model after the relocation stage in each iteration. The solid curve in this graph is exactly the same as the solid curve in the left hand graph. Again it is only the first iteration that is large, with subsequent iterations becoming much smaller. Both these plots show that the principal changes are happening at the boundaries to the lower mantle, with the greatest change of 0.2%, which is almost half the size of the model, occurring at the CMB. This is not a surprising result because the correlation of the S model with the P model falls very rapidly towards the CMB. This may or may not be a reflection on the quality of the P or the S model. Instead it is quite possible that compressional and shear velocities are not correlated because this region, D'', is thought to be a chemical as well as a thermal boundary layer, and chemical heterogeneity could cause the shear modulus to behave in a different way to the bulk modulus. Nevertheless the changes to the starting model are restricted to within 200km of the lower mantle boundaries which is smaller than the resolution of the model, so no firm conclusions about the physical significance of this result can be made.

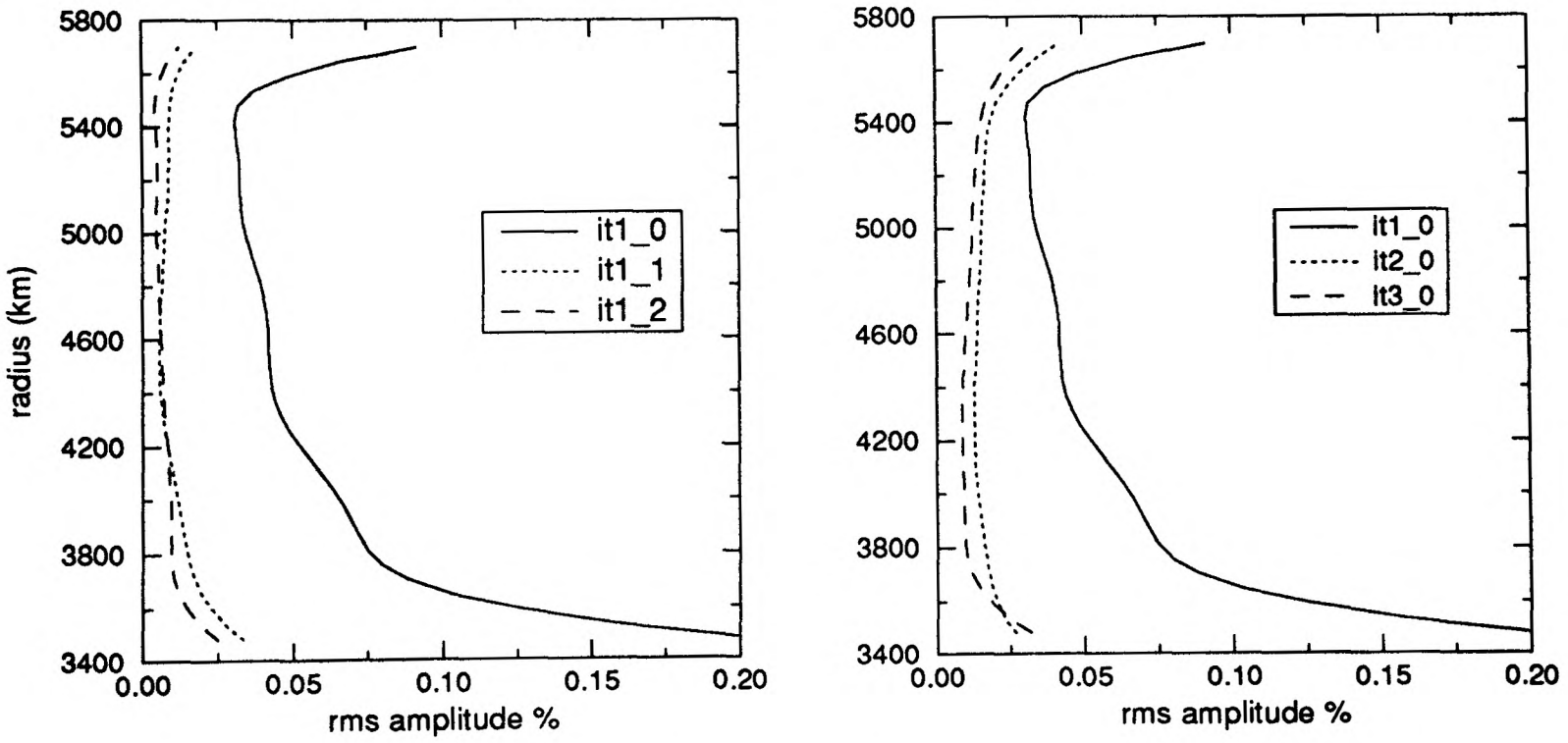


Figure 9.5: Comparison of the RMS amplitudes of the model perturbations throughout the joint inversion of the P and S datasets.

The model itself is shown in figure 9.13. It is clear that it is very similar to the P model of this study, figure 5.38, with the largest differences occurring in the bottom two maps. At 2000km depth, despite the similarities in the harmonic spectra, this model has additional high velocity anomalies on the coast of Chile down to Antarctica, and in the mid Atlantic. The former feature is also partly evident in MDLSH and SH8WM13 (see figure 8.10), whereas the Atlantic feature is not seen on any other S models. A slow anomaly is more evident over the East Pacific Rise, and this is also seen quite clearly in MDLSH. At 2700km depth the changes are largest, with the growth of a fast anomaly in the Indian Ocean, and the disappearance of the fast anomaly at 30° latitude in the central Pacific which was described

in section 8.4. This is a significant point because this feature was one of the main differences between the compressional and the shear models at this depth. As a result of its disappearance, the degree 2 component of the heterogeneity has become more pronounced. Despite the existence of a strong fast anomaly in the S model of this study, the joint P model does not show linkage of the ring of fast velocities circumscribing the Pacific under northern South America, which was a feature common to all of the shear models (see figure 8.11). Further analysis of this joint model will be performed in the next section.

Event depth analysis

The depths of the events in this joint inversion are shown in figure 9.14. In addition, figure 9.15 shows the changes in the average depth of the events in one 5° by 5° cell relative to the third iteration of the linear models without fixed depths or fixed station corrections. In general the depths of the events are consistent with what would be expected from the tectonic regions in which they exist. For example, mid ocean ridge events are shallow, *e.g.* East Pacific Rise, north Atlantic, and events in subduction areas penetrate to the cut off depth of 50km. However the Indian Ocean triple junction does show anomalously deep events averaging greater than 25km. Even accounting for the fact that these depths are not supposed to be the most accurate that can be obtained because arrivals from local stations are not used (see section 4.3) this is very deep. Figure 9.15 shows that these events and most of the events near Eurasia are much deeper than those in the linear case. Some of this increase is attributable to the continued increase of depth with increasing iterations. Figures 9.16 and 9.17 show the changes in event depth between iterations 1 and 2, and 2 and 3 respectively. It is clear that almost all of the events become deeper at each stage, with the amount by which they are becoming deeper only decreasing slightly as the iterations proceed. This is indeed the same behaviour that was observed with the linear models in chapter 5, and in the same way this is interpreted as being a trade–off with the top of the model. This will be investigated in the next section.

In chapter 5 it was found that the changes in depths were closely linked to changes in the top of the model and that the S model was more sensitive to depth changes than the P model. Hence comparison of the linear S model and the P model from this joint inversion should show differences in regions where there are large depth changes. Analysis of figures 9.13 and 5.39 does indeed show this to be the case:

1. In the southern Atlantic the S model shows a large low velocity anomaly which is a fast anomaly in the joint P model. In figure 9.15 there are corresponding large negative changes in depth.

2. The joint P model shows a large negative anomaly under the Indian Ocean triple junction which is not seen in the linear S model. There are corresponding large increases in the depth of the events in this region.

3. The fast anomaly under Japan is not as evident in the P model as the S model, and large changes

in depth are seen here.

4. The low velocity feature under Arabia is much larger in figure 9.13 than in figure 5.39, and again the depth changes are large.

It should be noted that the sign of the changes in depth are consistent throughout the examples. When the P model shows a larger negative anomaly the change in depth is positive, and when the P model has a larger fast anomaly, the change in depth is negative.

Station corrections

Figures 9.18 and 9.19 show the P and S station corrections for the joint inversion. Correlation of the two does not appear to be significantly better than the correlation in the linear case (see figures 5.4 and 5.5). Both sets of station corrections show the same relation to tectonic setting – generally fast in shield areas and slow in tectonically active regions (see section 5.5.2). The most striking differences become apparent when the changes in station corrections between those derived in this joint inversion and those of the linear inversions are examined. These are shown in figures 9.20 and 9.21 for the P and S cases respectively. The third iteration results where no depths were fixed have been chosen to represent the linear case.

In a similar way to the example described in the previous section, allowance has to be made for the gradual change of the station corrections with each iteration that is a consequence of the trade–off problem. The size of this effect has been estimated by calculating the change in the station corrections between the first and the third iteration of this joint inversion. Differences in the P corrections are negligible and are not plotted. The S changes between iterations 2 and 3 are shown in figure 9.22. It is clear that these are also very small, being largest at $\approx$0.4s under Hawaii, and as a result it can be concluded that any trade–off between the model and the station corrections is negligible.

The most noticeable aspect of the comparison of figures 9.20 and 9.21 is that, despite the different scales, the changes to the S corrections are far larger than the P corrections. In many cases do the S corrections exceed 1.0s whereas it is very rare for the P changes to exceed 0.5s. Furthermore the changes do not seem to be correlated. These results reflect the consequences of the relocation algorithm using a ratio S model which is quite different in some places to the linear S model. It might be argued that the changes to the S station corrections are larger than the P corrections because P dominates the inversion. However it has already been shown (see figure 9.5) that the changes to the joint P model occur quite quickly, and not in a long slow process which would indicate that the S data cannot accommodate the new parameterization with which the heterogeneity is being described.

Relocation vectors

The lateral changes in the hypocentral coordinates relative to the positions of the events in the third iteration of the linear models are shown in figure 9.23. These are quite small with the average vector length being 1.8km and the largest vectors only 7km long. The general trend of the vectors around the Pacific to point to the centre of the Pacific has been noted already and attributed to the increasing size of the unconstrained negative velocity anomaly in the models under Hawaii. However those seen in, for example, figure 5.21 are far smaller than the arrows presented here, so it is unlikely that this is the sole reason for their existence. Furthermore the size of the Pacific anomaly in the joint model is no bigger than that in the linear model

9.4.3 Depth independent ratio with fixed depths

Analysis of the statistics in table 9.4 shows that in the same way as before the one step variance at each stage continues to increase with each iteration by a greater amount than the variance after the inversion decreases. Again this causes the variance reductions to increase while the final variances have actually converged (see the P variance statistics for both the 4_4 and 4_6 cases). The reasons for this are the same as those discussed in section 5.7.1, namely

- The different weighting schemes of the P and S phases involved in the relocations and the inversions.
- Trade offs between different variables within the iterative inversion procedure.

In chapter 5 a great deal of time was spent trying to discover which parameters were involved in trade–offs with the model. Although not all combinations were tested, it was established that there are complex interactions involved with all of the variables. These interactions predominantly affected the top of the model which is poorly constrained because of the geometry of the ray paths in the uppermost parts of the lower mantle. The S model that was chosen from chapter 5 was generated from the third iteration of the relocation/inversion procedure with the depths of the events fixed at the end of the first iteration because it was found that it converged best under these conditions. However, fixing the depths of the events resulted in a slightly larger P model than the one derived without depth fixing. The optimum (in the sense that convergence was closest) P model was the one in which the station corrections were fixed at the end of the first iteration.

There is no 'correct' choice of P and S model from the trade–off experiments of chapter 5. From the evidence above, fixing a parameter which is beneficial to one is often detrimental to the other. Tradeoffs exist, and the consequences of trying to deal with them may be as bad as ignoring them, especially if the models are going to be used together. Nevertheless it is important to know their effect on a result. In this section it has already been shown that there is an increase in the depths of the events at the end

of each iteration by an amount that is only slowly decreasing, and this has been attributed to the same depth trade–off problem. Contrary to the results of chapter 5, the changes to the station corrections, especially P, hardly change, and so it is concluded that a trade–off with the station corrections is less of a problem in this case than it was in the linear inversion. This may be a result of the higher damping applied to the perturbations of the model.

In order to investigate the effects on the ratio of the possible depth trade–off problem, iteration 3 from the previous experiment has been reperformed keeping the depths of the events the same as they are at the end of the second iteration. These depths were chosen because the changes in depth between the final locations in chapter 5 were quite different from those at the end of iteration 1 in this joint experiment. Consequently it is not unreasonable to expect some genuine changes in the depths of the events at the end of the next iteration to compensate for the first order linear depth change assumptions that are made in the relocation process. The results are shown in table 9.5.

				before inversion		after inversion		
parameterization n l events/cell	*phase type*	*iteration number*	*ratio*	*mean*	*one step variance*	*mean*	*variance*	*unw. variance reduction (%)*
4 6 15 5	P	3	1.81	0.023	1.650	-0.016	1.432	13.21
	S	3		0.462	14.198	-0.089	12.891	9.21

Table 9.5: Statistics for the joint inversion of the P and S datasets for a depth independent ratio with fixed event depths at the end of the second iteration.

As a consequence of fixing the depths, the value of the ratio has not changed from what it was at the end of the second iteration. The statistics of the P dataset are almost exactly the same as those in the previous section showing that the effects of depth fixing are being accommodated elsewhere. Changes to the S statistics are more obvious with the one step and the final variance being lower than those given in table 9.4. However the variance reduction is down by 0.7%.

The new model, figure 9.24, is almost identical to the reference joint inversion model, figure 9.13. This reflects the almost identical statistics. Figure 9.6 shows the RMS amplitudes and correlation coefficients for the two joint inversion P models computed in this chapter, and the linear P model from chapter 5. It is clear that there is practically no change to the joint P model caused by fixing the event depths after the second iteration since the correlation coefficient between the two is indistinguishable from 1. The joint models also agree well with the linear P model. The RMS amplitude curves are very similar with the largest differences occurring in lower mid mantle regions where the joint model is around 10% larger. However the correlation coefficient is high here at over 0.85, indicating that the features agree.

Hypocentre locations

The lateral change in the event locations caused by fixing the depths at the end of the second iteration are too small to be plotted at the same scale as previous diagrams. This result is in agreement with

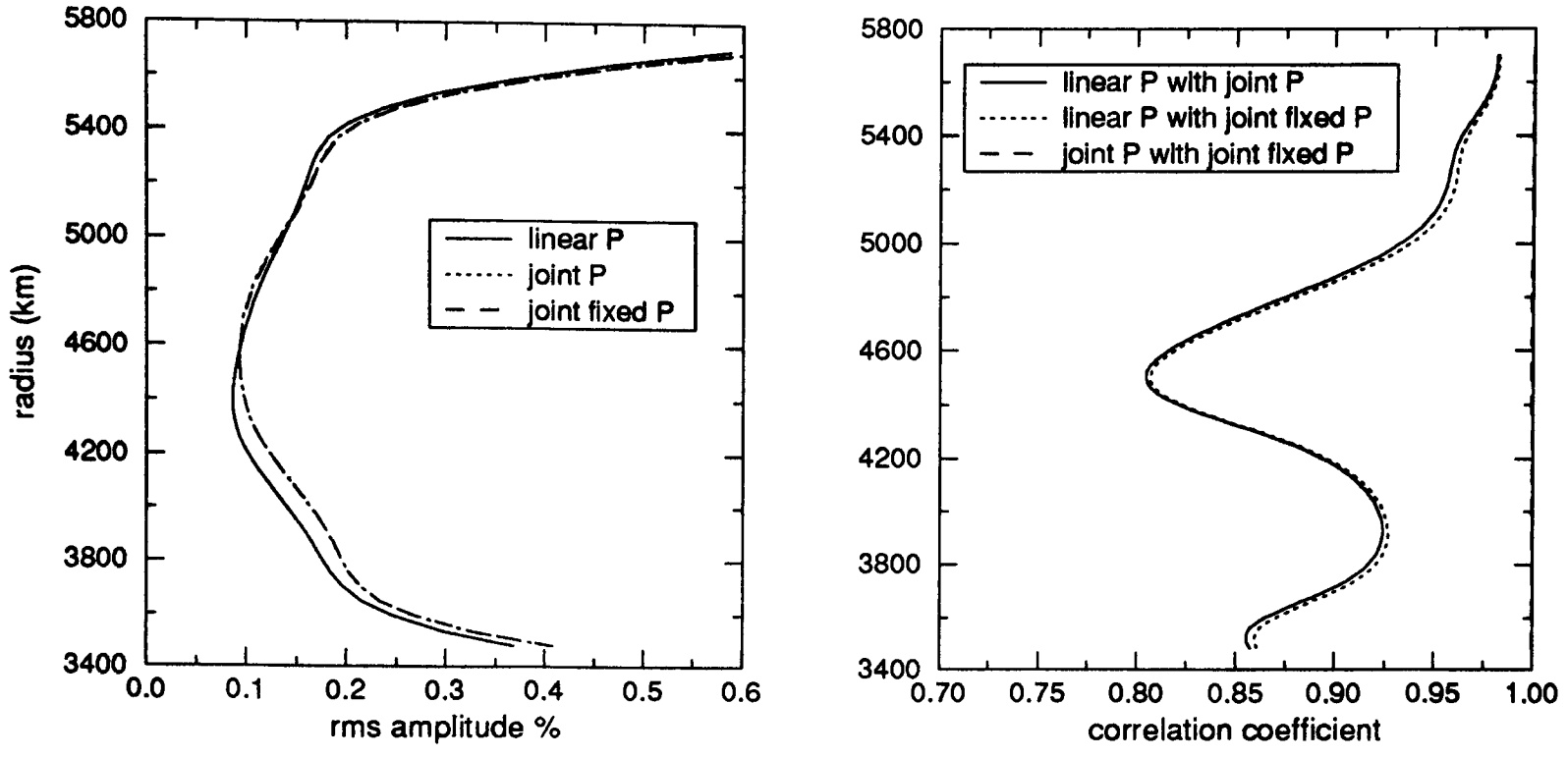


Figure 9.6: Comparison of the depth independent ratio models with the linear P model.

the observation that the P models are almost identical because it is the compressional phases which dominate the relocations.

Station corrections

Examination of the changes in station corrections can reveal whether there is also a trade–off between the depth and the station corrections. In the P case these changes are too small to be plotted, but there are changes to the S corrections (see figure 9.25). As was explained in chapter 5, fixing the depths of the events can be accommodated by changes in the origin times of the events. These changes are determined largely by the P dataset because they are weighted higher and they outnumber S by approximately a factor of six in the relocations. As a result the necessary changes to the S dataset caused by fixing the event depths have to be accommodated elsewhere, and this figure shows that, at least in part, this is happening with the station corrections. It has already been established that the S model also changes when the depths are fixed because the third iteration ratios have changed while the P models are almost identical.

Conclusion

This experiment has shown that fixing the depth of the events can account for any changes to the ratio between the second and third iterations of the joint inversion. However the results are far from conclusive. It is probable that a different conclusion could have been drawn if there had been as much S data available as P data. In this case the dominance of P in the inversion would not be so great and as a result changes to the P model could also have occurred. In this scenario it is also possible that the

depth trade-off problem itself would be minimal. The physical system that is being modelled here is extremely complex and interactions between the different parameters are difficult to separate.

9.4.4 Depth dependent ratio

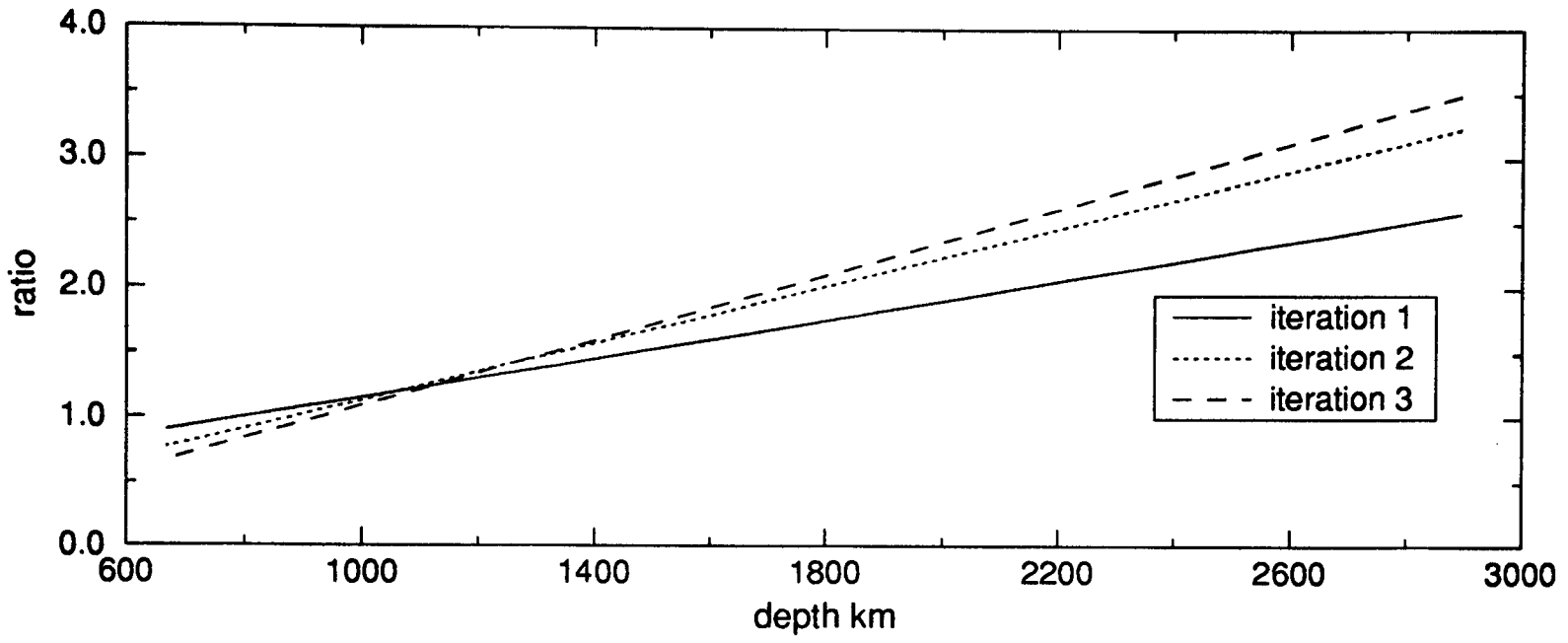


Figure 9.7: Values of the depth dependent ratio from the joint inversion of the P and S datasets at the end of each iteration.

The same inversion has been performed on the P and S datasets with the ratio parameterized with two terms instead of one. Hence the ratio of S to P heterogeneity can vary linearly throughout the lower mantle. Figure 9.7 shows the ratios at the end of each iteration.

It is clear that the ratio increases with depth and is converging, but as yet it has not converged. Furthermore the ratio at the base of the lower mantle is already 3.5 and would probably be nearer to 4 if more iterations were performed. This is too high to be physical because it means that the shear and bulk moduli are uncorrelated (see section 9.1). It is probable that the relatively small amount of possibly innaccurate S arrivals at large epicentral distances which are given high weights in the inversion are causing this effect. Furthermore these arrivals bottom in the region D'', at the base of the lower mantle as it is modeled here, and it has already been stated that chemical heterogeneity could well cause large differences in shear and compressional velocity heterogeneity, to the extent that they may not be proportional.

Examination of the P model from this experiment, figure 9.26, shows remarkable consistency with the model from the depth independent ratio experiment. The features are almost identical, but the amplitudes differ. The top of the model is far bigger than before, with increases to the dominant degrees 2, 3, and 5. The 1300km maps are almost identical. At greater depths this model becomes progressively smaller than the depth independent P model. At 2700km, there is a loss of around 15% in degrees 1, 2, and 6, with smaller increases in the others. This description fits well with the size of

the ratio throughout the lower mantle, with the ratio being smaller than average at the 670km depth discontinuity and larger than average at the CMB. At the depth in which the depth dependent ratio is the same as the depth independent ratio, approximately 1200km, the models are almost the same.

These observations are clearly seen in the left hand plot of figure 9.8, which shows the variation in RMS amplitude of the various P models with depth. Notwithstanding the difficulties encountered in this experiment, the depth dependent ratio model correlates extremely well with the joint depth independent ratio model, and its correlation coefficient with the linear P model is rarely less than 0.8. Given the discussion above, it is not surprising that this value decreases with depth.

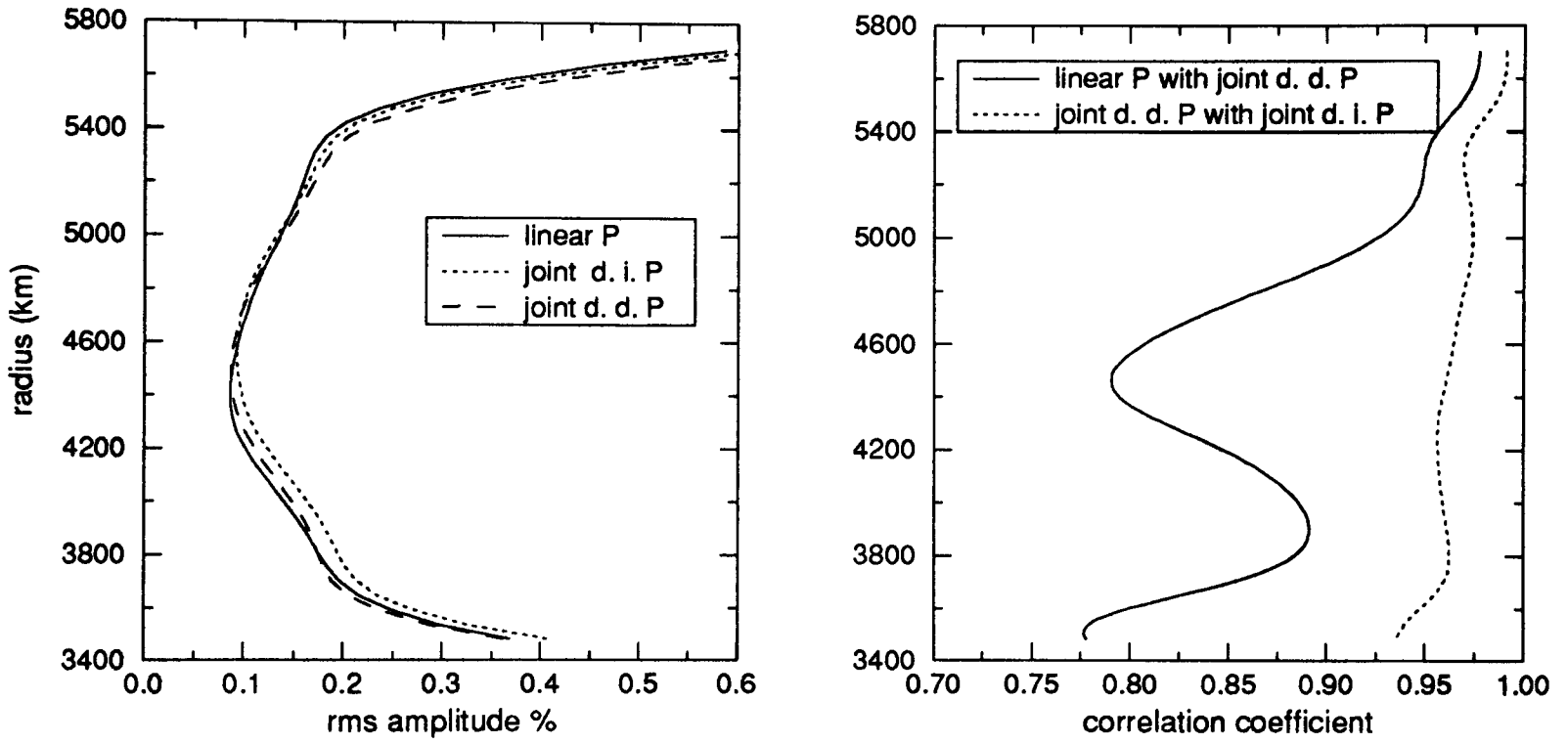


Figure 9.8: Comparison of the depth dependent ratio joint P model with the depth independent ratio joint P model and the linear P model.

9.5 Discussion and conclusions

Experiment 2, which involves the joint inversion of the P and S datasets has been the only experiment to produce reliable estimates of the ratio between P and S heterogeneity in the lower mantle. This ratio has been calculated under the assumption that the forms of the compressional and shear velocity perturbations are the same, and that they differ only in amplitude.

Since the largest errors in the method are thought to be in the parameterization of the models rather than in the errors associated with the ratio derived from analysis of the least squares solution to the inverse problem, the experiment has been repeated for different distributions of data and different parameterizations of the model. The results for both the P and S datasets give variance reductions which are comparable to those in the derivation of the linear models in chapter 5. However the final variances of the datasets are higher. This may simply reflect the reduced number of degrees of freedom in this

inversion and hence does not prove that the assumption of proportionality of the P and S heterogeneity is invalid. The joint P model also correlates well with the linear P model, with a correlation coefficient averaging $\approx$ 0.85 throughout the lower mantle. Any perturbations to the P model from both the P and the S datasets occur very quickly showing that the necessary changes to the S model can be accommodated by other parameters in the inversion.

The results for a depth independent ratio lie in the range (1.67, 1.89). The lower value is derived from a model which is expanded to degree 2 laterally and may be subject to large errors if the earth is not represented well by this very low order expansion. When this lateral parameterization is increased the ratio increases to 1.81 for the 4_4 and 1.89 for the 4_6 case. When experiments are performed to investigate the effects of trade–offs within the inversion it is found that the ratio, at least for the 4_6 case, is reduced to 1.81. However there is no conclusive proof that a trade–off problem exists – it is only a continued increase in depth of the events after the second iteration and experience gained from the linear inversions that requires its investigation. Furthermore, investigations into depth trade–offs are severely affected by the dominance of P waves in the earthquake relocations which, from evidence in chapter 5, tends to decrease the size of S heterogeneity and reduce the size of the ratio. Hence it is possible that this latter result could be more biased than the original result. From these considerations alone it would seem that the ratio lies in the interval (1.8,1.9).

When an inversion for a depth dependent ratio is performed it is found that the ratio increases with depth but becomes unrealistically large in the lowermost mantle. This is attributed to the large weightings of possibly inaccurate data arriving at large epicentral distances which bottom close to the CMB. This has the effect of decreasing the size of the P model at the CMB and increasing it at the 670km discontinuity.

Even though the resultant ratio is deemed unreliable, there is evidence that the ratio does in fact increase with depth. As well as the depth dependent joint inversion, this was found in the synthetic tests of experiment 1 which showed that if the S data was not weighted to make the sum of weights in the bottoming depth bin the same, then the result was biased by the ratio of heterogeneity in the uppermost regions of the lower mantle. Without this weighting the ratio was found to be around 1.1 – 1.2, which is lower than than the value of $\approx$1.35 that was found in section 9.3. Hence, in agreement with Bolton & Masters, 1991 it would seem that the ratio does increase with depth.

The synthetic experiment also showed that if the ratio does increase with depth, then even accounting for the poor distribution of data by giving each bottoming depth bin the same weight in the inversion, the resultant value of the depth dependent ratio is lower than it should be. For the gradient of the depth dependency used in section 9.3.2 the derived ratio was underestimated by 7.4%. Clearly it is not known whether the ratio does vary linearly with depth, and even if it does, the gradient is unknown. If a linear relationship is assumed then an intuitive guess at the maximum gradient can be found as follows.

If the bulk and shear moduli are forced to be positively correlated, then the ratio can be at most 2.67

at the CMB (see equation 9.3). From joint experiments without bottoming depth bin weightings, the ratio is found to be ≈ 1.35, which from the dotted line in figure 9.2 should correspond to a normalized radius of 0.65, *ie.* 1100km depth.

Hence the maximum gradient of the ratio is $\frac{2.67-1.35}{2891-1100} = 7.4 * 10^{-4}\text{km}^{-1}$.

The gradient of the ratio in the synthetic experiment was $\frac{2.05-0.5}{2221} = 5.6 * 10^{-4}\text{km}^{-1}$.

From the synthetic experiment in which the weighting of the rays according to bottoming depth bins was introduced, it was found that the ratio was underpredicted by 7.4% . Hence, under the assumption that the underprediction is proportional to the gradient of the ratio, for the maximum gradient estimated above the experiment 2 ratio should be underpredicted by $\frac{7.4}{5.6} * 7.4 = 9.8\%$. This changes the bounds on the depth dependent ratio to the interval (2.0,2.1).

Clearly several assumptions have had to be made here, and these are not all compatible with observations in the literature. For example Pulver & Masters, 1990 constrain the ratio to be ≈ 1.7 with 68% confidence at the CMB. However this study uses differential travel times which record perturbations in very localized regions. This result may be specific to depths very near the CMB and hence not be compatible with the very large scale average value of the ratio being derived here.

In conclusion, the results of this study would indicate that the depth dependent ratio of P to S heterogeneity assuming proportionality throughout the lower mantle is greater than 1.8 and less than 2.1, with emphasis on larger values within these bounds, which is based on the belief that the ratio increases with depth. This result agrees well with previous work with similar data (Davies & Clayton, 1986) and is also comparable with the optimum value of 2.27 obtained by Li *et al.*, 1991 from normal mode data. Since these results are derived from datasets of vastly different frequencies it would seem that the heterogeneity within the earth is at most only weakly dependent on frequency.

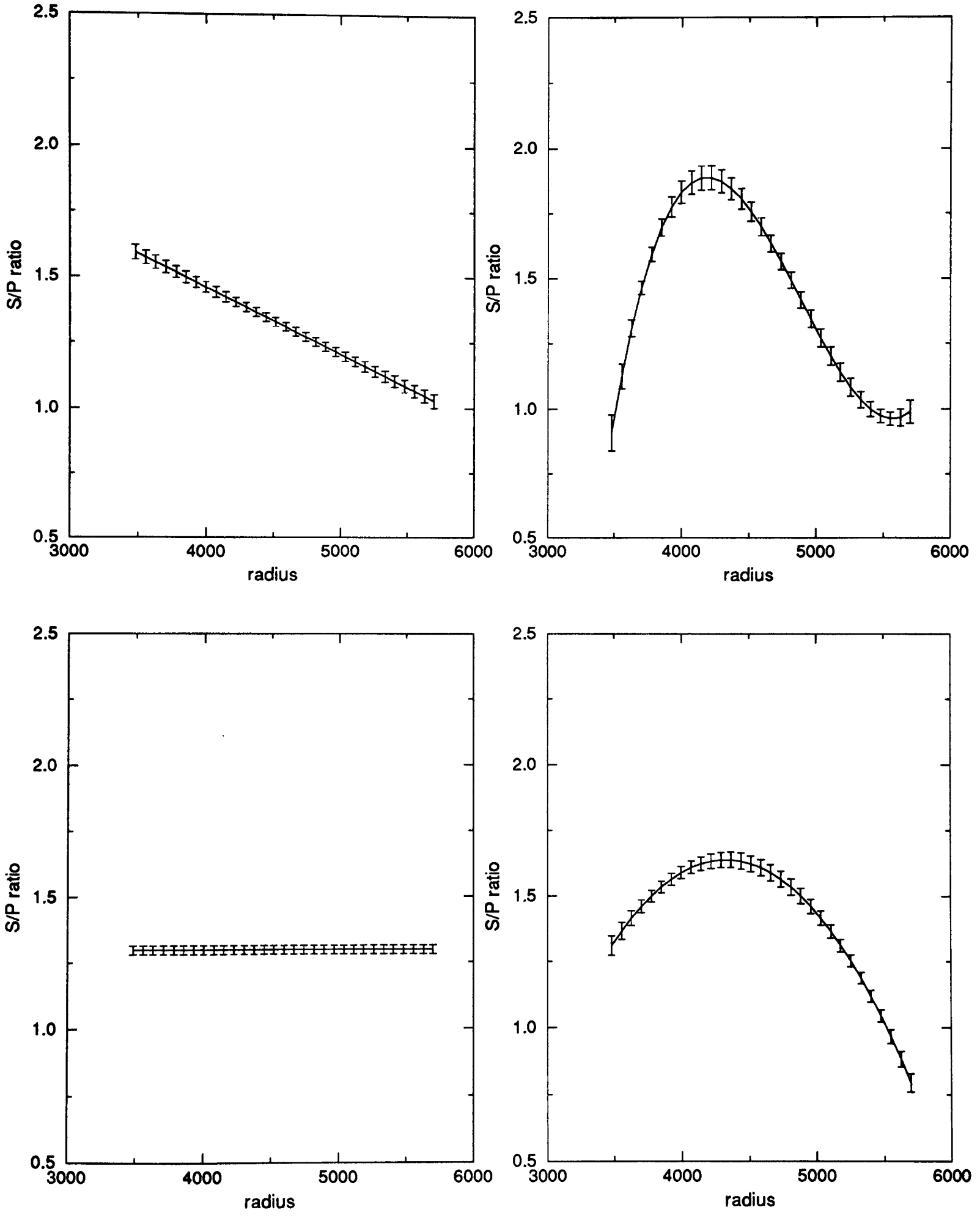


Figure 9.9: The ratio of S to P heterogeneity assuming the form of the final P model, parameterized to $n = 4, l = 6$. Clockwise from bottom left, these represent a total of 1, 2, 3, and 4 terms in the ratio expansion respectively. The error bars are one standard deviation.

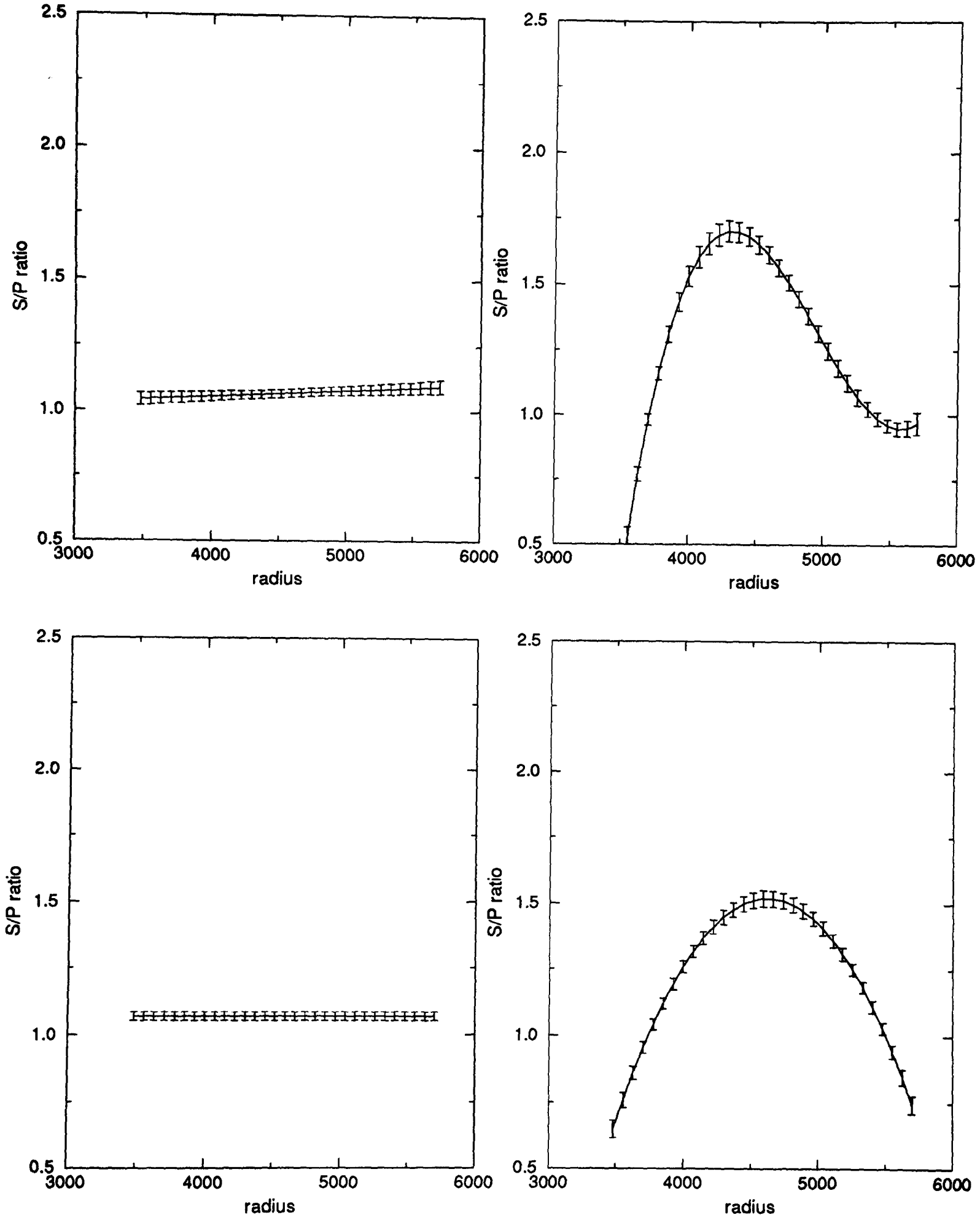


Figure 9.10: The ratio of S to P heterogeneity assuming the form of the PS model, parameterized to $n = 4, l = 6$. Clockwise from bottom left, these represent a total of 1, 2, 3, and 4 terms in the ratio expansion respectively. The error bars are one standard deviation.

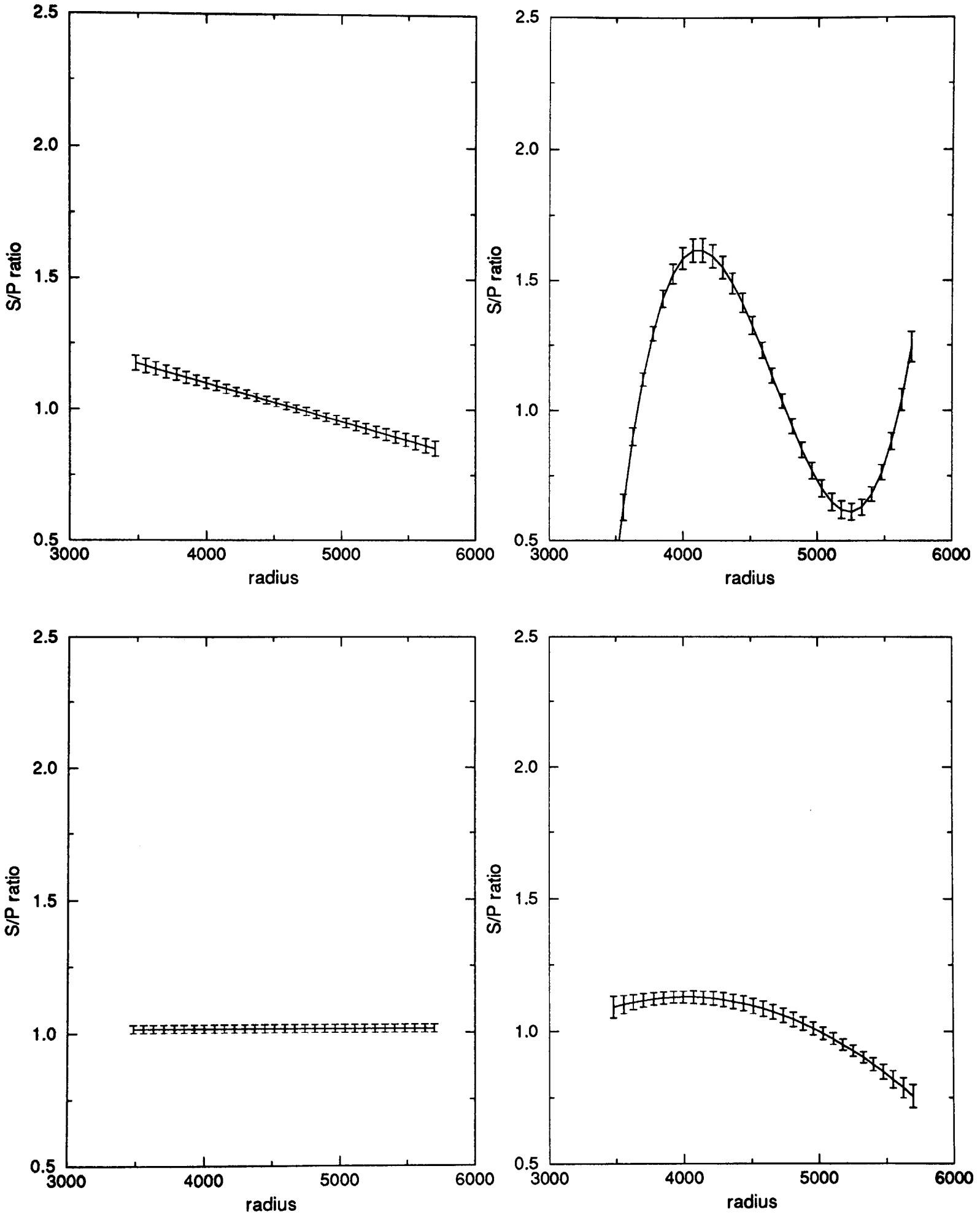
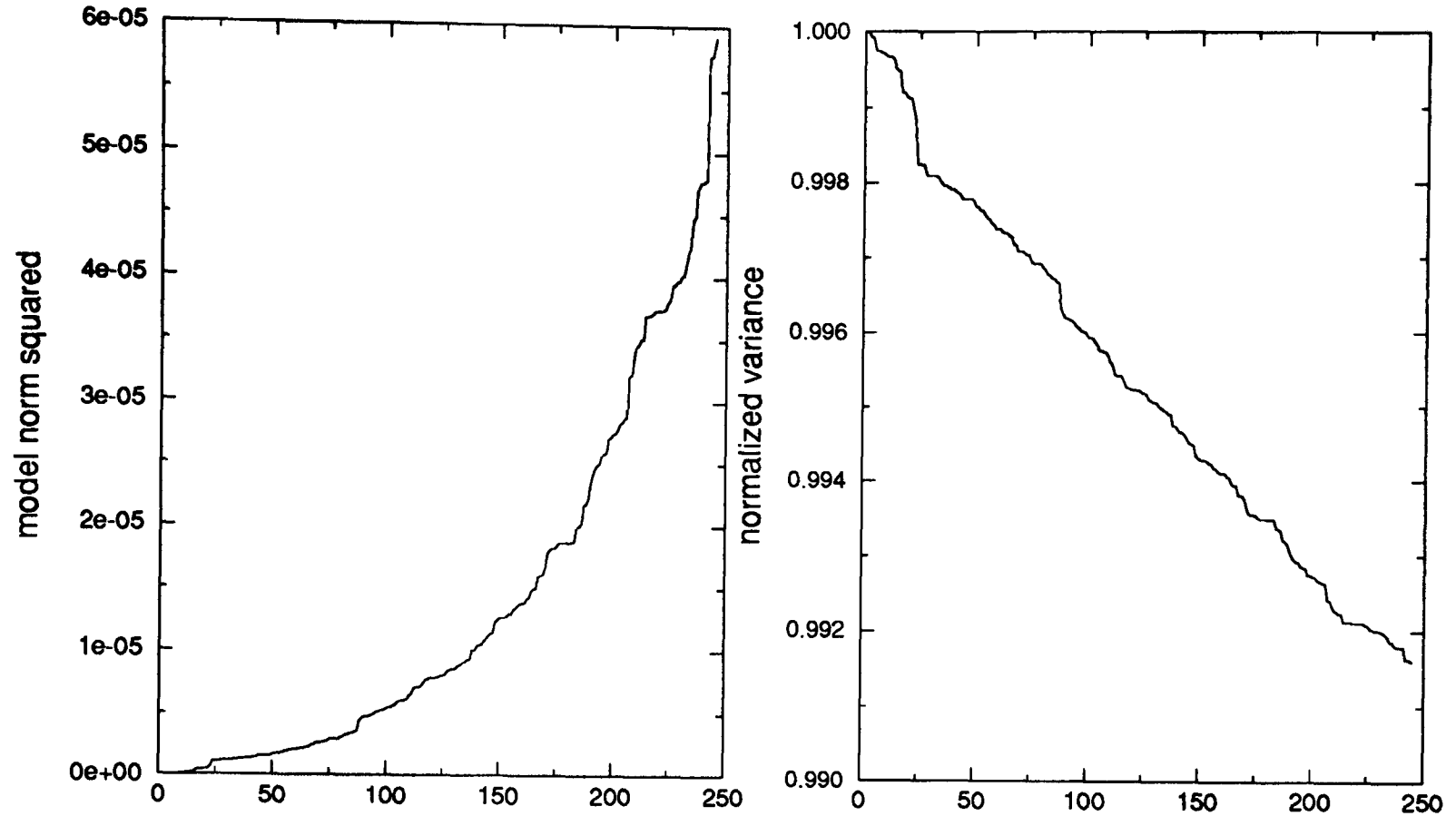


Figure 9.11: The ratio of S to P heterogeneity assuming the form of model V3.i, parameterized to $n = 4, l = 6$. Clockwise from bottom left, these represent a total of 1, 2, 3, and 4 terms in the ratio expansion respectively. The error bars are one standard deviation.



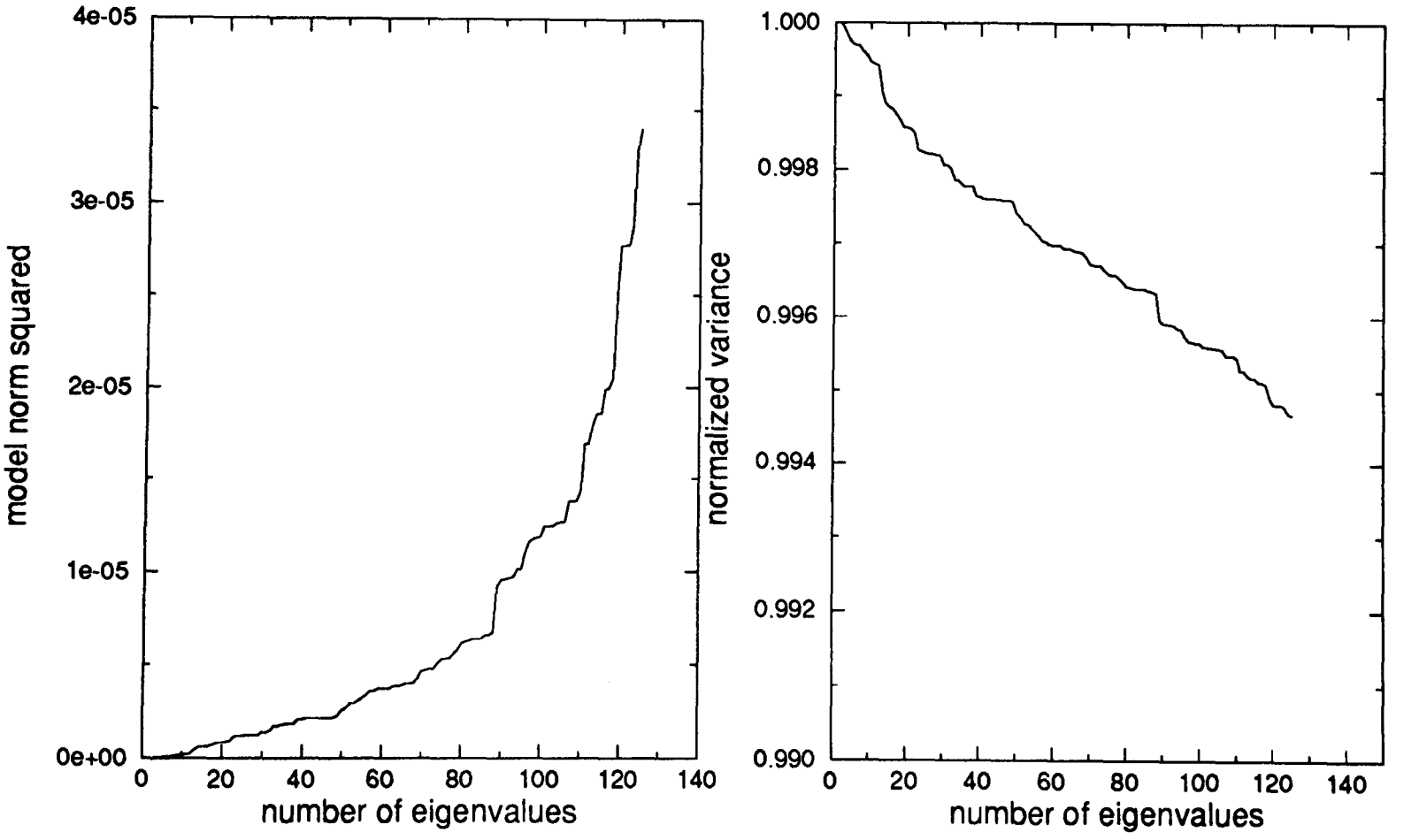


Figure 9.12: Model norm and variance plots after the first inversion of the first iteration for the 4_4 (bottom) and 4_6 (top) parameterized P model.

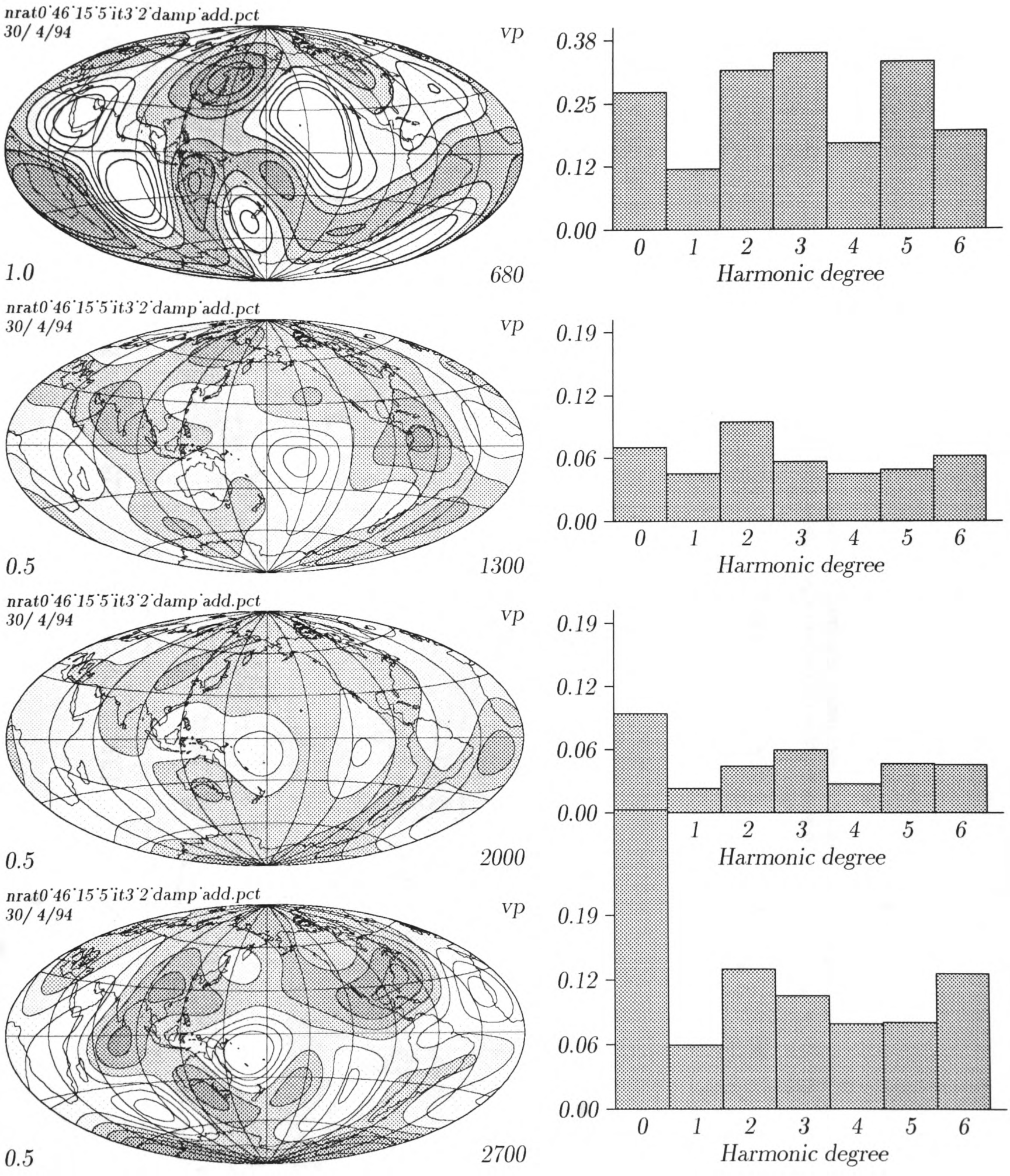


Figure 9.13: The third iteration joint inversion P model.

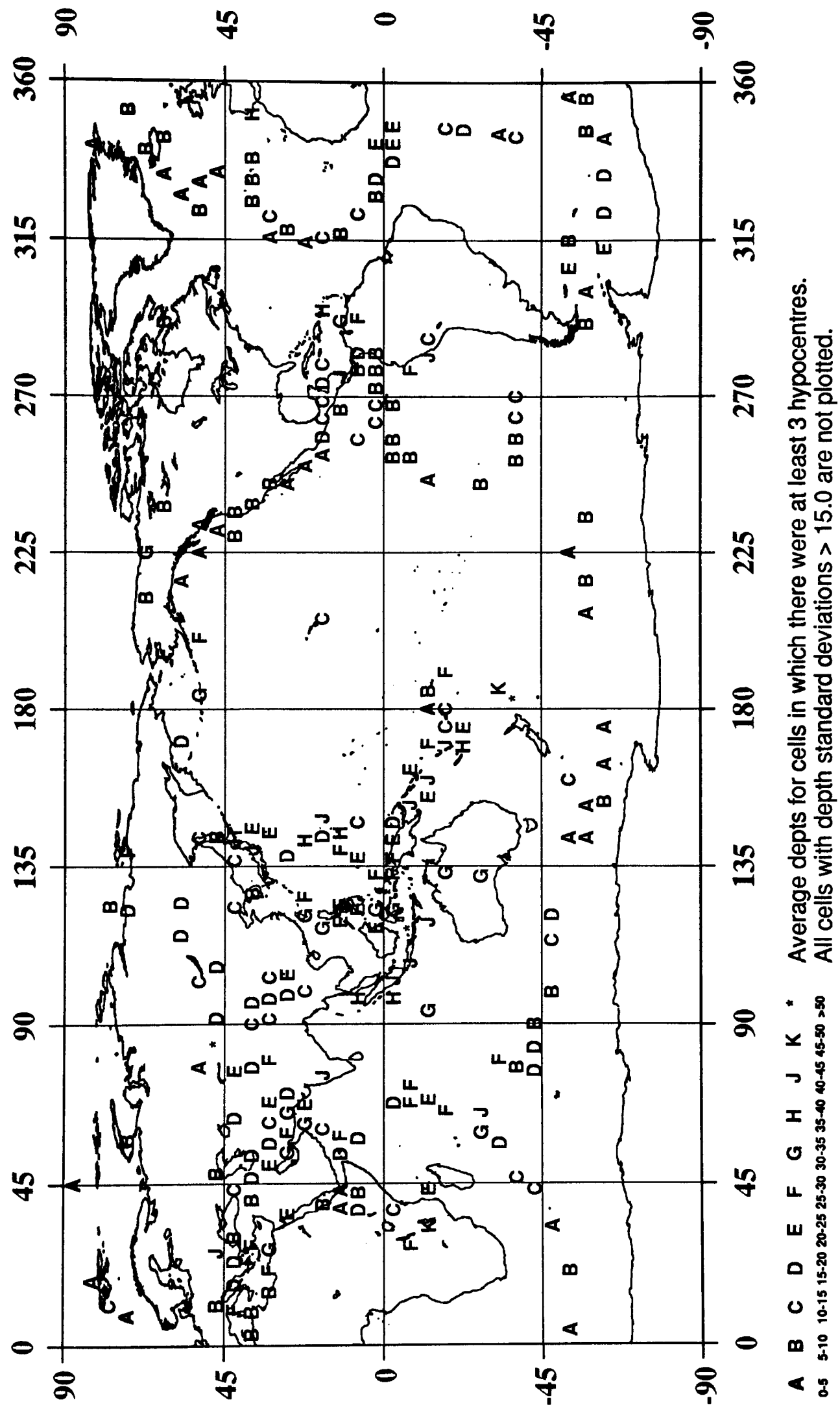


Figure 9.14: Binned depths for the relocated events contributing to the third iteration of the joint inversion.

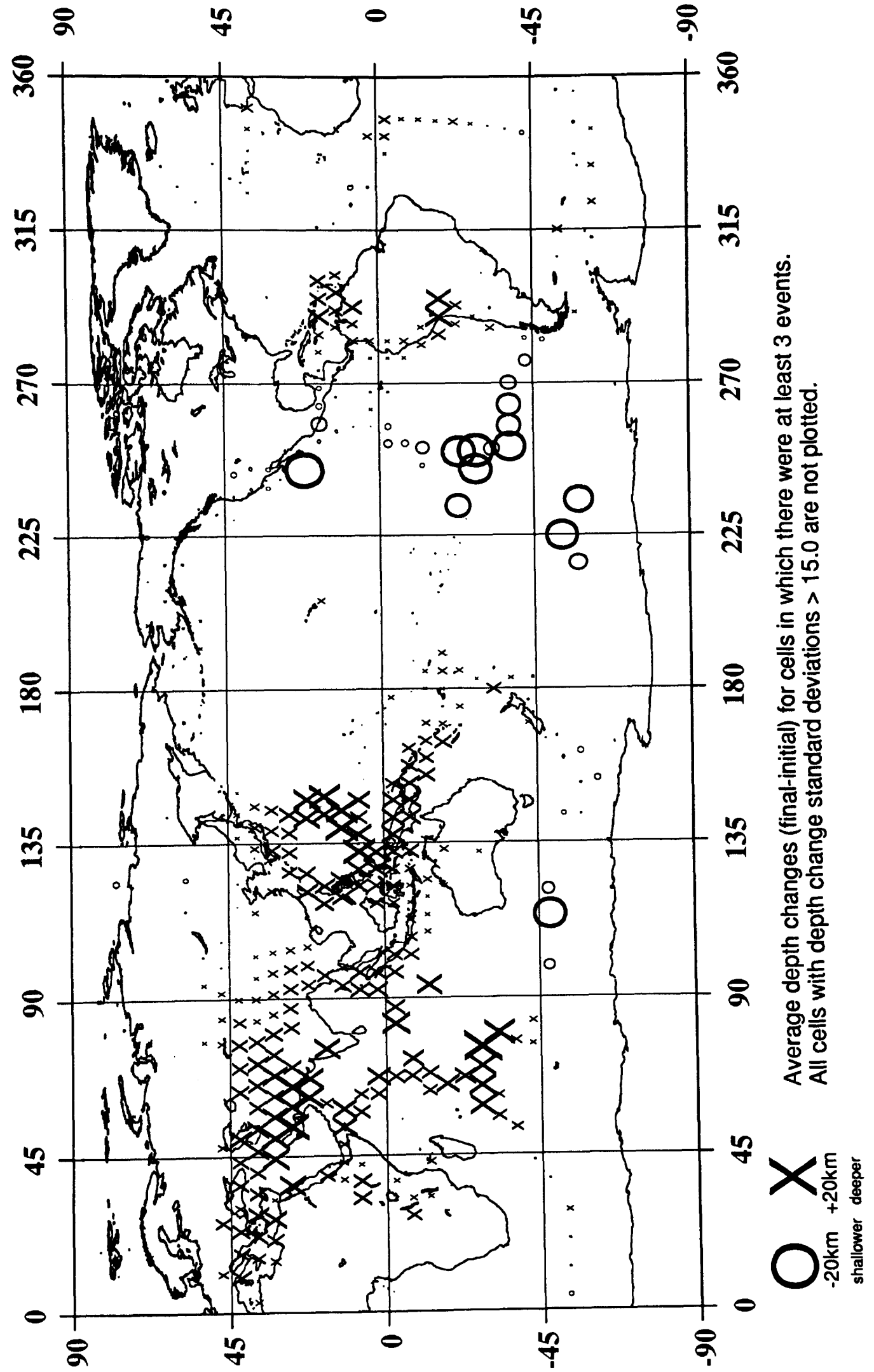


Figure 9.15: Average depth changes for events per 5° cell between the third iteration of the linear inversion and the third iteration of the joint inversion.

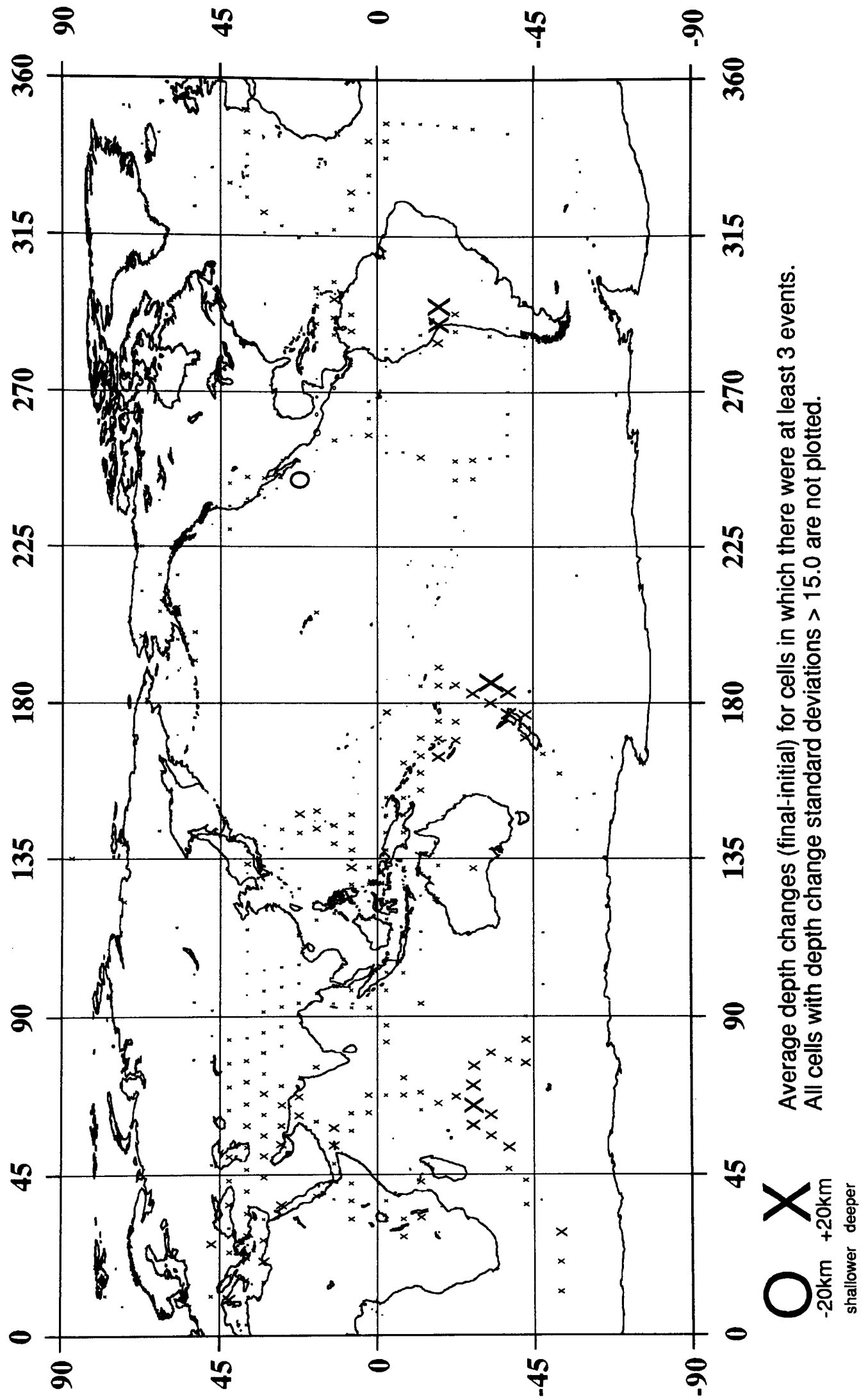


Figure 9.16: Average depth changes for events per 5° cell between the first and second iterations of the joint inversion.

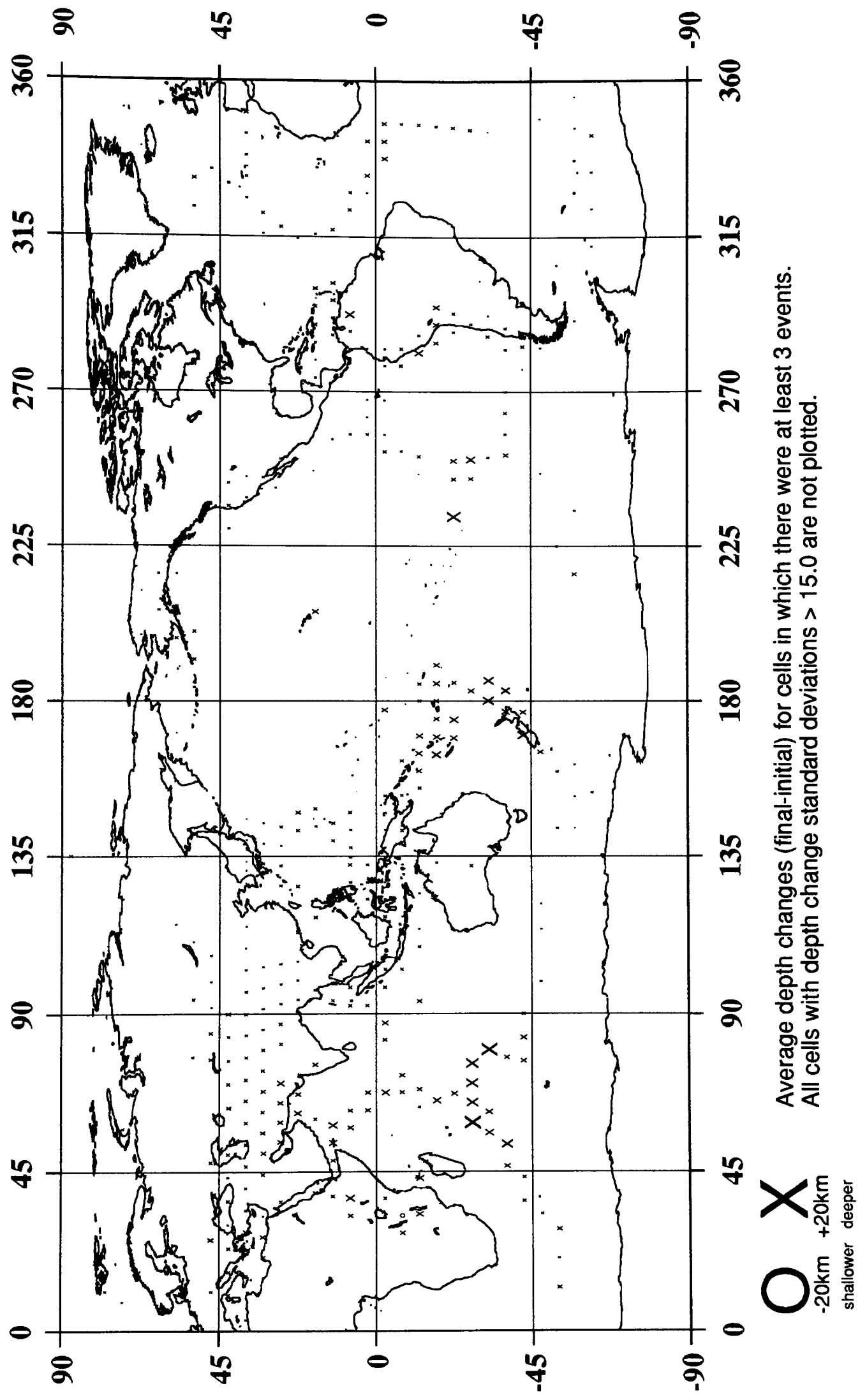


Figure 9.17: Average depth changes for events per 5° cell between the second and third iterations of the joint inversion.

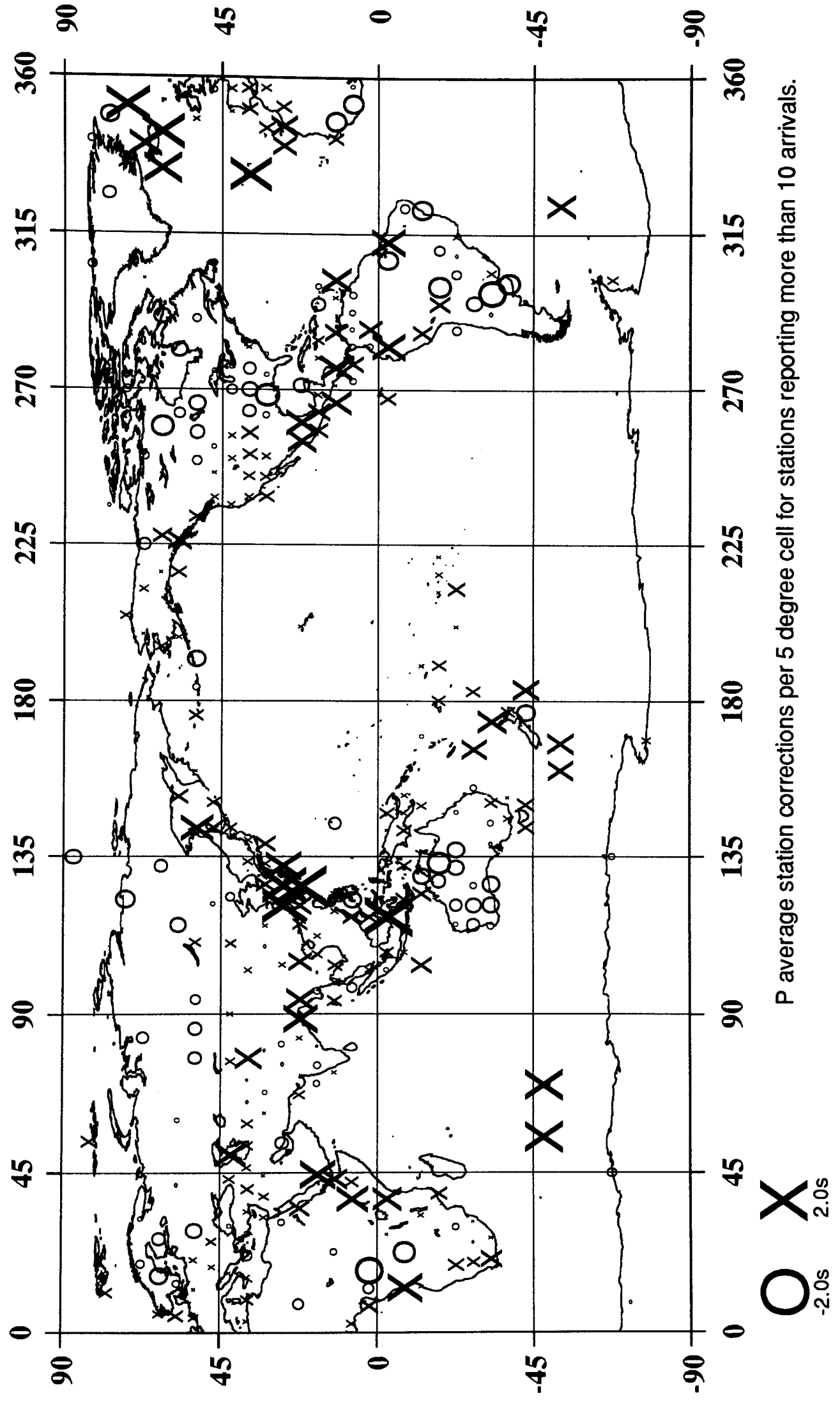


Figure 9.18: P station corrections in the nonlinear joint inversion.

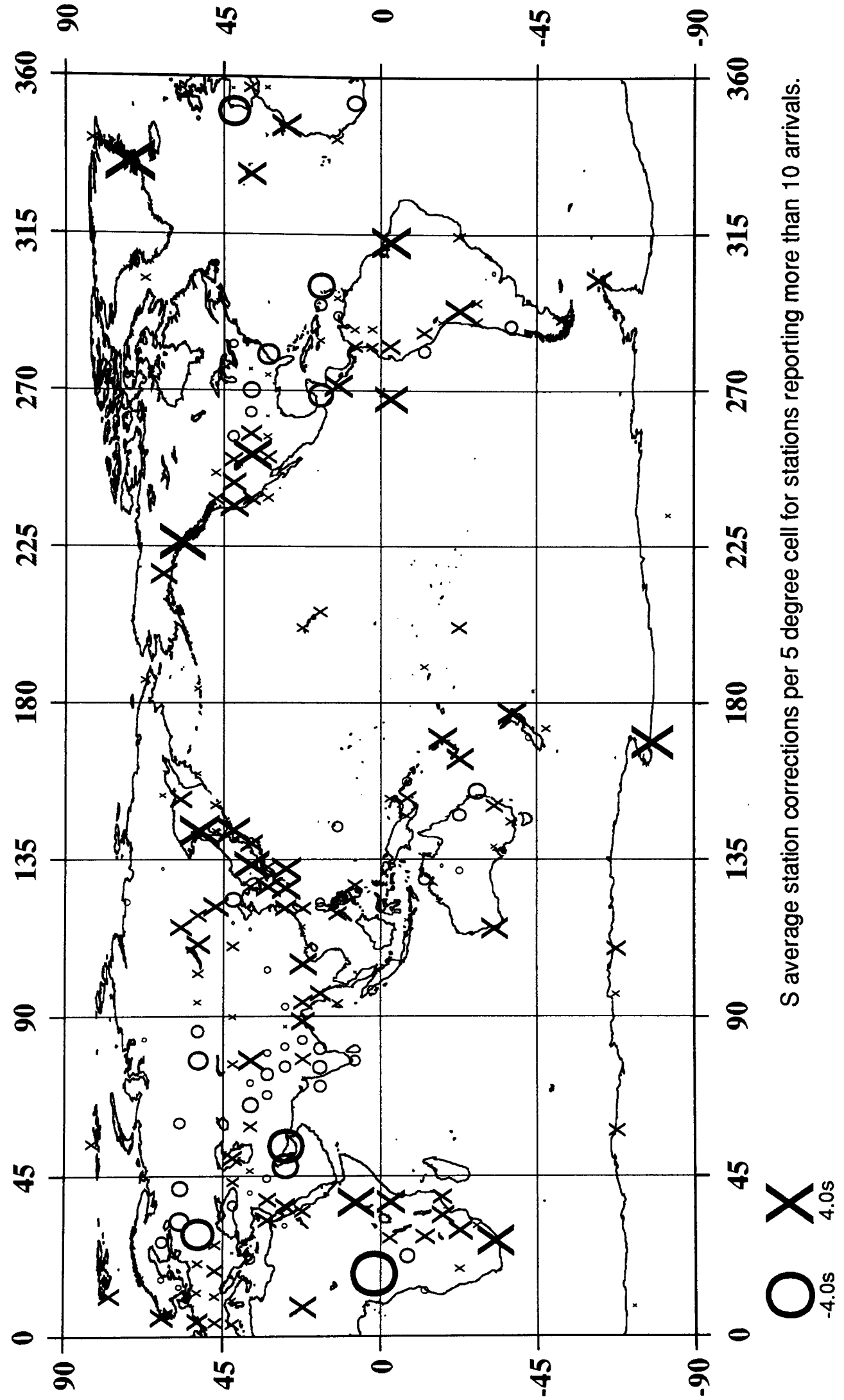


Figure 9.19: S station corrections in the nonlinear joint inversion.

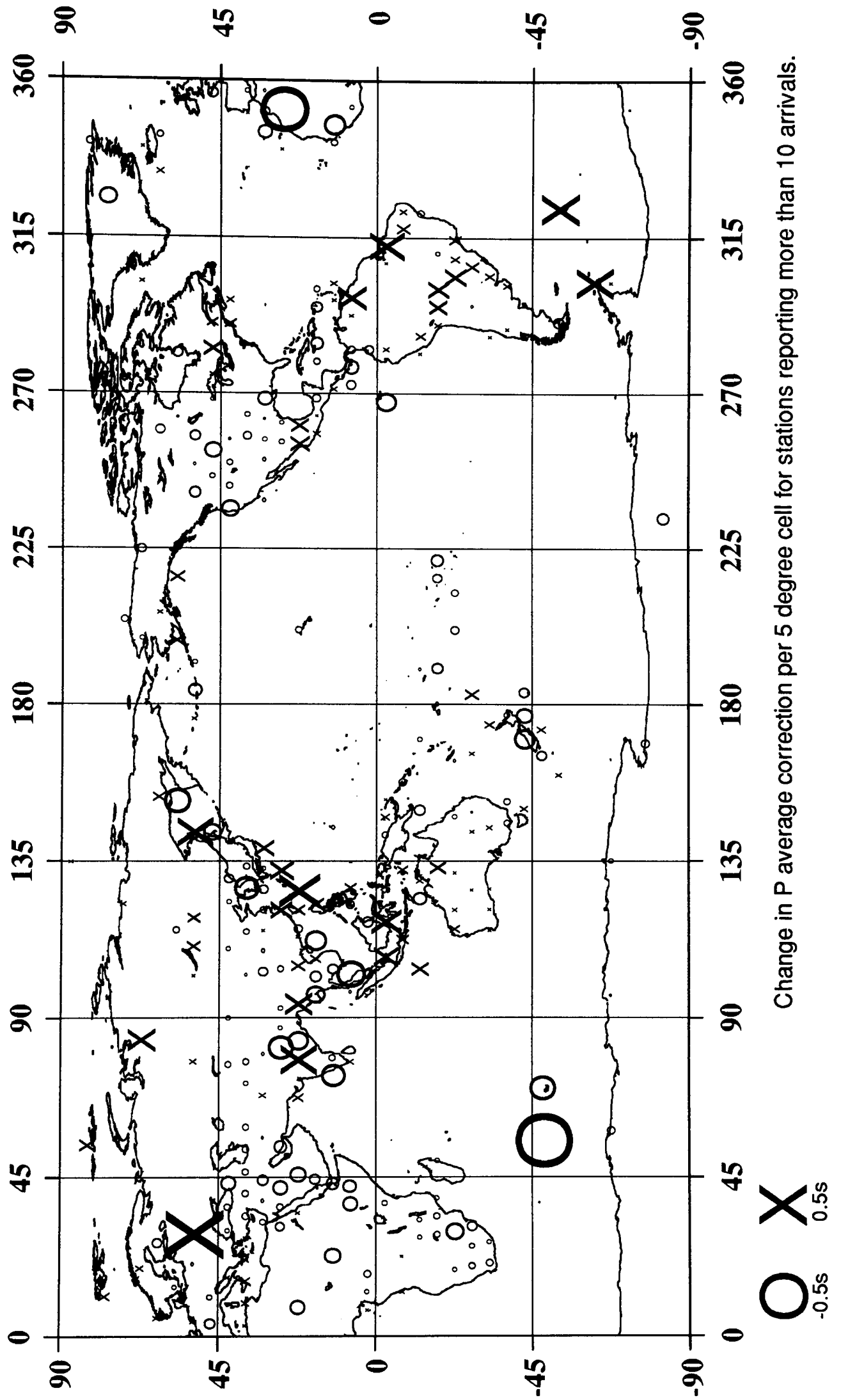


Figure 9.20: Change in the P station corrections between the nonlinear joint inversion and the linear inversion of chapter 5.

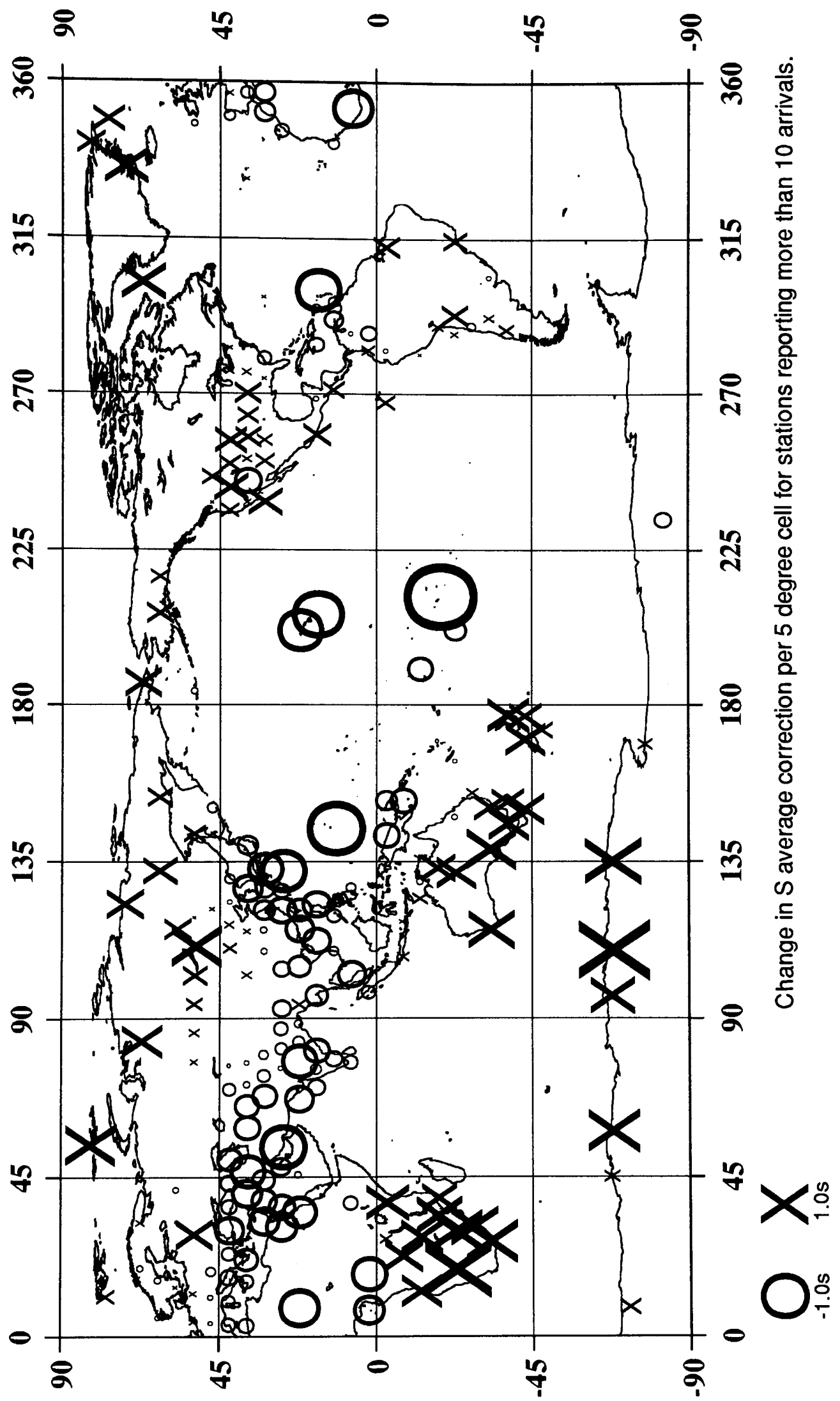


Figure 9.21: Change in the S station corrections between the nonlinear joint inversion and the linear inversion of chapter 5.

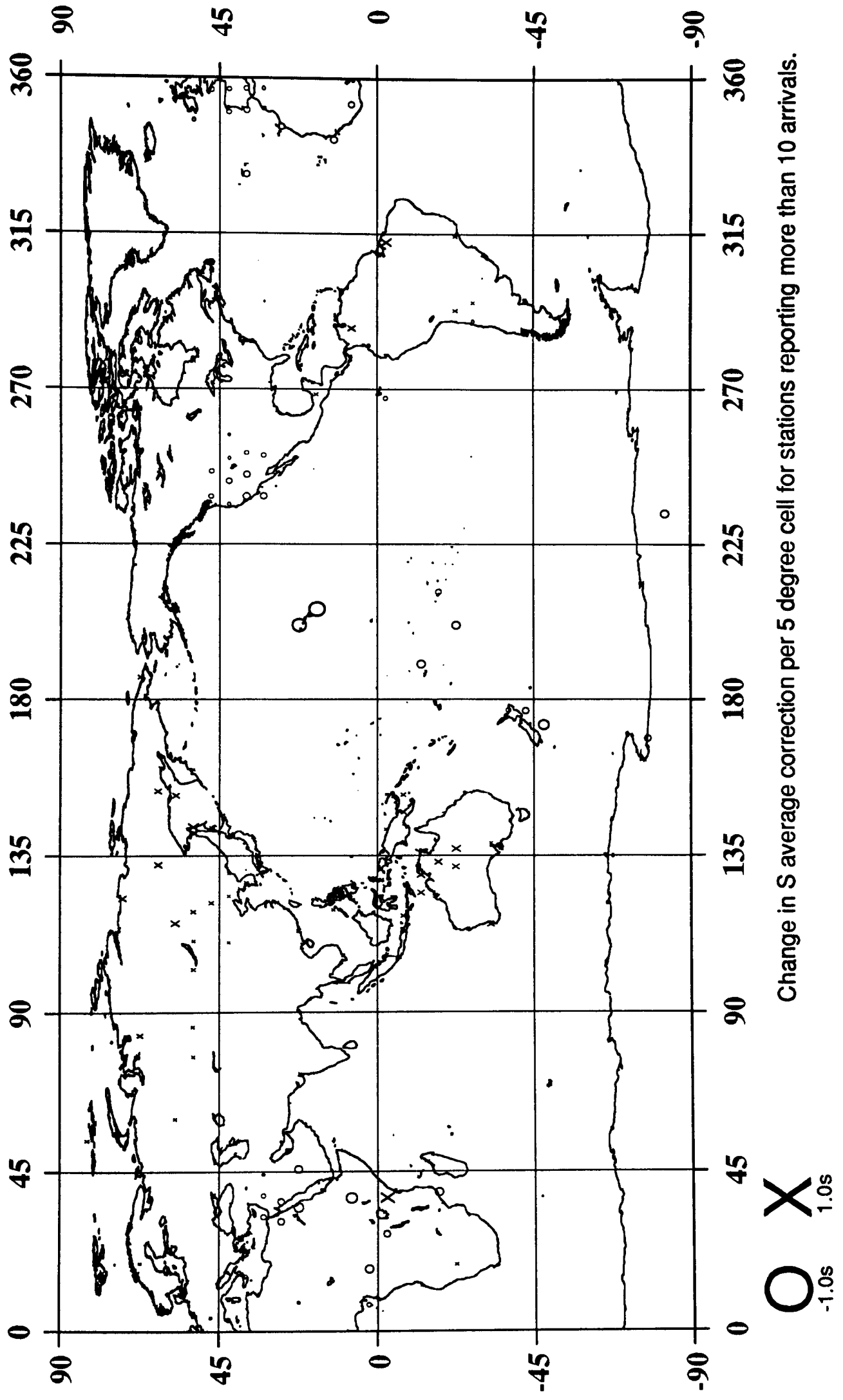


Figure 9.22: Change in the S station corrections between iterations 2 and 3 of the nonlinear joint inversion.

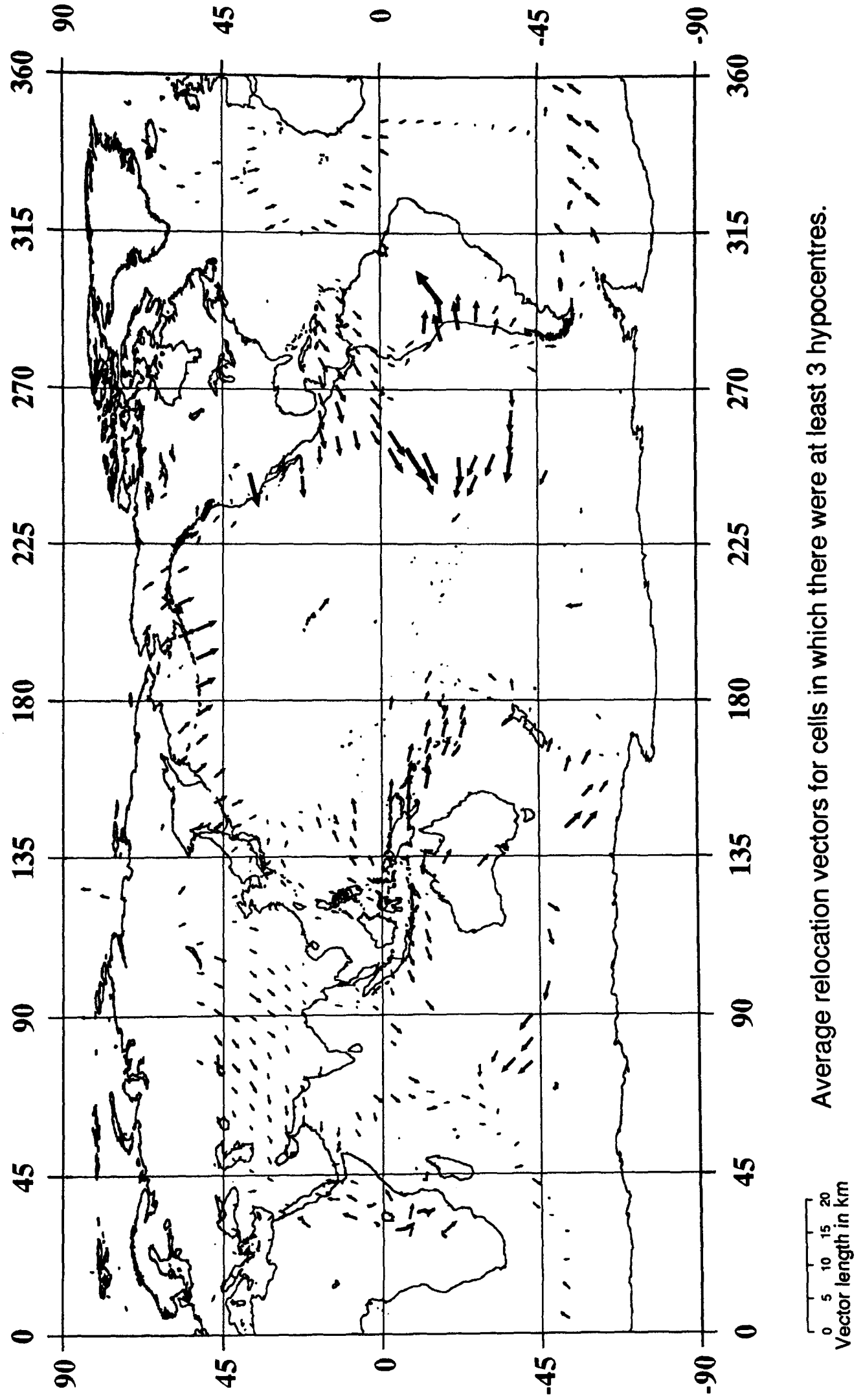


Figure 9.23: Relocation vectors between the hypocentral coordinates of the nonlinear inversion and those of the third iteration of the linear inversion in chapter 5.

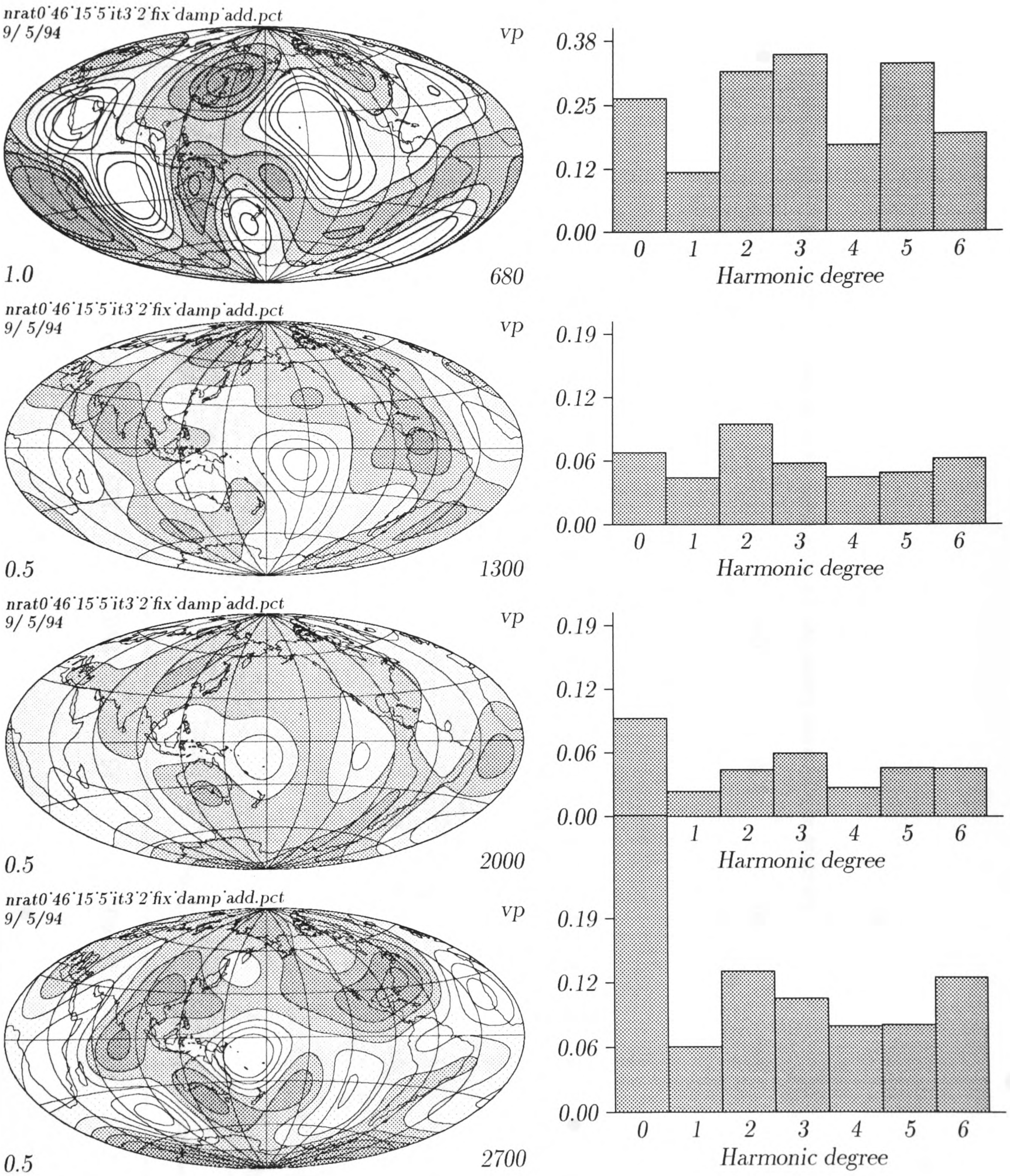


Figure 9.24: The third iteration joint inversion P model in which the depths were kept fixed to the same as those in the dataset from which the fixed depth linear models were derived.

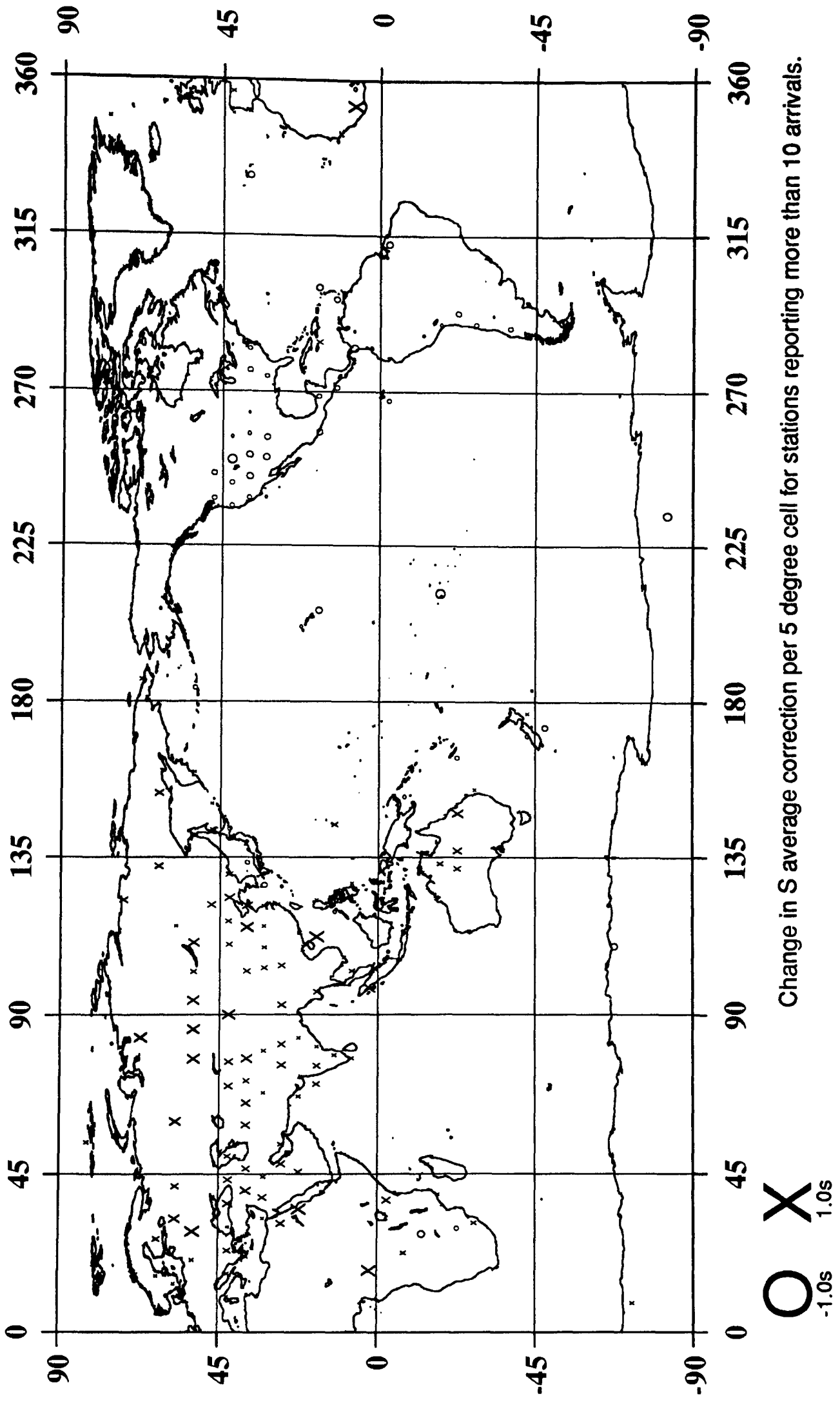


Figure 9.25: Average change in the S station corrections between the third iterations of the reference joint inversion and the joint inversion in which the depths of the events were fixed after the second iteration.

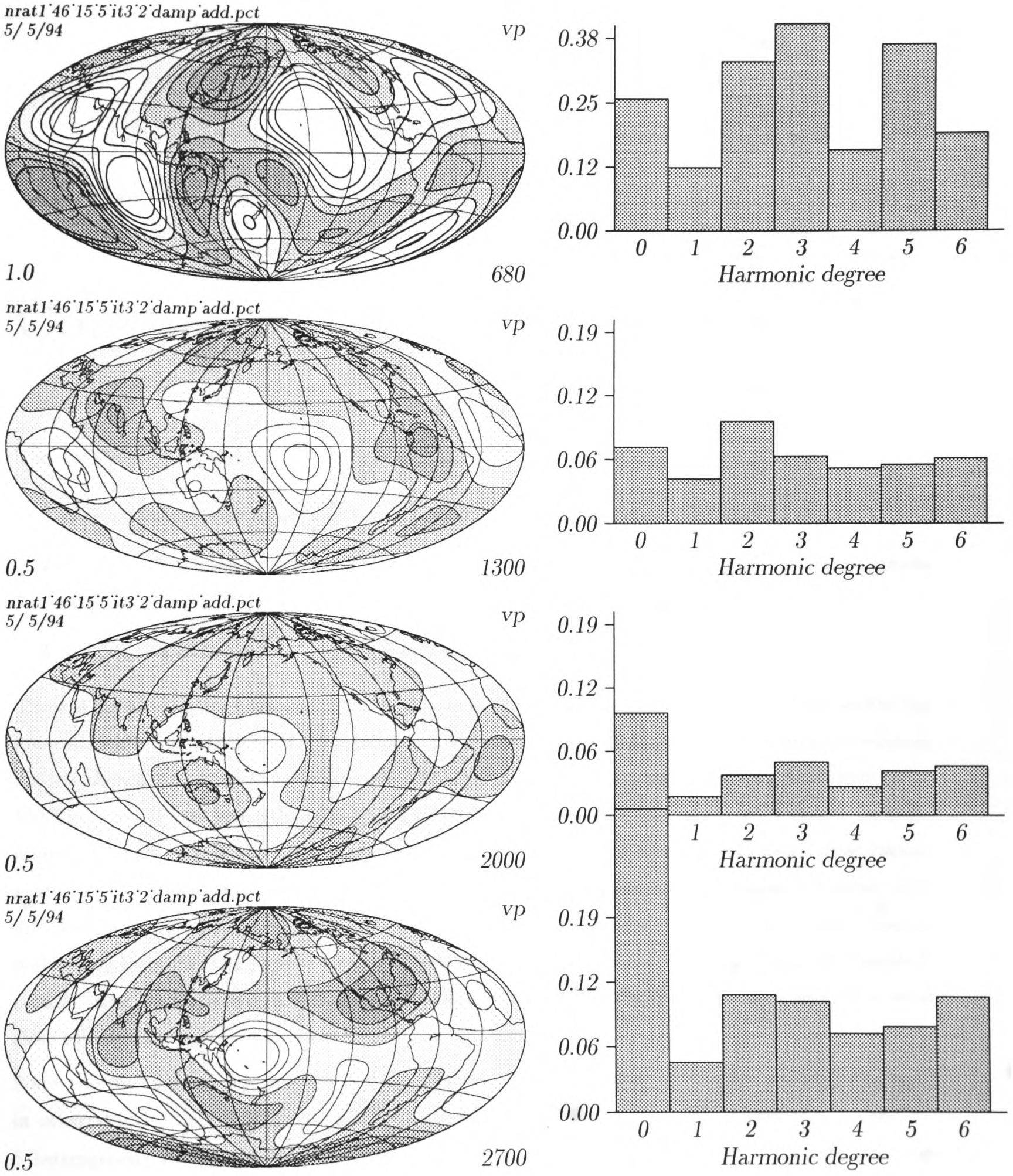


Figure 9.26: The third iteration joint inversion P model for a depth dependent ratio.

Chapter 10

Conclusions and further work

The work reported in this thesis has been conducted in three stages:

1. Calculation of three dimensional models of shear wave heterogeneity in the lower mantle.
2. Comparison of these models with themselves and with existing models using different datasets and parameterizations.
3. Calculation of the ratio of relative S to P heterogeneity.

Three different parameterizations of both the shear and compressional velocity variations within the lower mantle have been derived. Comparison of the S model expanded to $n = 4, l = 6$ with pre–existing models shows that correlation is good in places where the data coverage is good. Furthermore, at 1300km depth it was found that the S model correlates as well with any of the other models as these models do with each other. This significant result means that this short period shear wave dataset contains information about the interior of the earth which is consistent with other seismic datasets with different coverages and resolving powers, and opens up possibilities for their joint use in the future to make more accurate tomographic models. Correlation of the 4_6 P model with existing lower mantle P models using the same parameterization is excellent, averaging over 0.7, and having a maximum value close to 0.9 in the lowermost mantle.

Since the ISC dataset has much better coverage at mid mantle depths than the datasets employed in other studies, the models reported here are expected to provide the best information to date on S heterogeneity in this region. Furthermore, the measure of agreement between models derived here and other models constructed using very different kinds of data, none of them incorporating significant information on direct S, provides information of the validity of the various techniques which have been employed.

Not only do each of the P and S models share many similar features, but these can be identified in more and more detail as the number of parameters in the inversion increases. Hence it has been shown

that the inferred large scale structure of the earth is, to the extent expected, independent of the model parameterization. Correlation coefficients of the S and P models derived throughout this study are high, but in almost all cases correlation is best at 1300km and 2700km depth. These are regions in which the data coverage of the lower mantle is most dense. The 4_6 models correlate better together than the other parameterizations, averaging around 0.6. Considering the number of parameters involved in the inversion for 6A and 8C models, the average correlation coefficient of between 0.3 and 0.4 is also significant.

The size of the correlation coefficients alone is evidence of proportionality of the P and S heterogeneity, but the similarity of features in areas where data coverage is most dense, particularly under the continents in the northern hemisphere, provides further strong evidence for proportionality. It is undoubtedly true that if the ray coverage in the lower mantle was better the correlation coefficients would be higher.

The conclusion that the P and S velocity heterogeneities in the lower mantle are proportional is significant because it means that the calculation of a ratio between them is valid. The results from experiment 2 in chapter 9 also verifies the proportionality because they show that there are only minor changes to the P model resulting from the inclusion of S in the inversion, and variance reductions are similar to those when the P and S models are calculated independently.

The synthetic experiment in section 9.3.2 has proved to be invaluable. It shows that the ratio obtained in the inversion is strongly dependent on the distribution of the data, and if this is not taken into account, the result can be severely biased. This experiment has been used not only to decide the weighting of the arrivals, but also to determine how much the final estimate of the lower mantle mean ratio is an underprediction of reality.

10.1 Further work

In chapter 3 it was stated that the validity of using the iterative time term inversion approach as opposed to a simultaneous inversion would be determined if convergence of the model was obtained. The largest problem encountered in this study has been with the lack of convergence of the models. However evidence has been presented that this is attributable to two other factors, and not to the inversion method itself.

- The different weighting schemes of the P and S phases involved in the relocations and the inversions.
- Trade offs between different variables within the iterative inversion procedure.

In order to overcome these problems, the method of joint determination of lateral heterogeneity and hypocentre location (Morelli & Dziewonski, 1991) may represent a better approach to the tomographic

inverse problem. In this technique the earth is divided up into equal area cells and averages are taken from all rays traveling between two cells in order to obtain a representative or *summary* ray. Similarly a summary earthquake is defined as an event, initially with zero origin time, located at the centre of a source cell whose travel times are those computed for summary paths. As a result the number of 'events' contributing to the model is governed only by the size of the cell chosen. This greatly reduces the number of parameters, and enables the inversion for both hypocentre locations and model to be done simultaneously, thus eliminating the need for iterations.

By far the largest improvements to the results of this study can be obtained by improving not the method but the distribution of data. For tomography in general the resolution can only be improved when seismic observatories are placed in areas where coverage is at present sparse, which means the installation of ocean bottom seismometers. In this study the most significant improvement would involve obtaining readings of arrival times between 80° and 90° epicentral distance, where the ISC dataset is badly contaminated by other phases. This would involve the cross correlation of synthetic S seismograms with the original seismograms. Clearly the time required to do this would be substantial, but since few other datasets adequately sample the mantle at depths greater than 2000km, the effort should be worthwhile. In addition to the improvements to the model, this should not only help to remove the cause of the underestimation of the depth independent S to P ratio, but it should constrain far better its variation with depth.

References

Agnon, A., & Bukowinski, M. S. T. 1990. δ_S at high pressure and $d \ln V_S / d \ln V_P$ in the lower mantle. *Geophys. Res. Lett.*, **17**, 1149–1152.

Anderson, D. L. 1987. A seismic equation of state II. Shear properties and thermodynamics of the lower mantle. *Phys. Earth Planet. Inter.*, **45**, 307–323.

Anderson, O. L., Schreiber, E., Liebermann, R. C., & Soga, M. 1968. Some elastic constant data on minerals relevant to geophysics. *Rev. Geophys.*, **6**, 491–524.

Backus, G. E. 1964. Geographical interpretation of measurements of average phase velocities of surface waves over great circular and great semi-circular paths. *Bull. Seismol. Soc. Am.*, **54**, 571–610.

Backus, G. E., & Gilbert, F. 1970. Uniqueness in the inversion of inaccurate gross earth data. *Phil. Trans R. Soc. Lond. A*, **266**, 123–192.

Benioff, H. 1958. Long waves observed in the Kamchatka earthquake of Nov 4 1952. *J. Geophys. Res.*, **63**, 589–593.

Bolton, H., & Masters, G. 1991. Long period absolute P times and lower mantle structures. *Eos Trans. AGU. Un*, **72**, 339.

Bott. 1980. *The Interior of the Earth.* San Francicso, California: W. H. Freeman and Company.

Chapman, S., & Bartels, J. 1940, 1951. *Geomagnetism.* Clarendon Press.

Clayton, R. W., & Comer, R. P. 1983. A tomographic analysis of mantle heterogeneities from body wave travel time data. *Eos Trans. AGU. Un*, **64**, 776.

Cleary, J. R., & Hales, A. L. 1966. An analysis of the travel times of P waves to North American stations in the distance range 30° to 100°. *Bull. Seismol. Soc. Am.*, **56**, 467–489.

Creager, K. C., & Jordan, T. H. 1986. Slab penetration into the lower mantle beneath the Mariana and other Island Arcs of the Northwest Pacific. *J. Geophys. Res.*, **91**, 3573–3589.

Dahlen, F. A. 1968. The normal modes of a rotating, elliptical earth. *Geophys. J. R. Astron. Soc.*, **16**, 329–367.

Darragh, R. B. 1985. Mapping of upper mantle structure from differential *PP–P* travel time residuals. *Phys. Earth Planet. Inter.*, **41**, 6–17.

Davies, D., & McKenzie, D. P. 1969. Seismic travel-time residuals and plates. *Geophys. J. R. Astron. Soc.*, **18**, 51–63.

Davies, D., & Sheppard, R. M. 1972. Lateral heterogeneity in the Earth's mantle. *Nature*, **239**, 318–323.

Davies, J. H., & Clayton, R. W. 1986. Lower mantle S wave tomography. *Eos Trans. AGU. Un*, **67**, 1099.

Davies, J. H., Gudmundsson, O., & Clayton, R. W. 1992. Spectra of mantle shear wave velocity structure. *Geophys. J. Int.*, **108**, 865–882.

Dewey, James W. 1971. *Seismic studies with the method of joint hypocenter determination.* Ph.D. thesis, Berkeley, University of California.

Duda, S. J. 1971. Travel times and body wave magnitude. *Pure and Applied Geophysics*, **87**, 13–37.

Dziewonski, A. M. 1984. Mapping the lower mantle: Determination of lateral heterogeneity in P velocity up to degree and order 6. *J. Geophys. Res.*, **89**, 5929–5952.

Dziewonski, A. M., & Anderson, D. L. 1981. Preliminary Reference Earth Model. *Phys. Earth Planet. Inter.*, **25**, 297–356.

Dziewonski, A. M., & Anderson, D. L. 1983. Travel times and station corrections for *P*-waves at teleseismic distances. *J. Geophys. Res.*, **88**, 3295–3314.

Dziewonski, A. M., & Woodhouse, J. H. 1987. Global images of the Earth's interior. *Science*, **236**, 37–48.

Dziewonski, A.M., & Gilbert, F. 1976. The effect of small, aspherical perturbations on travel times and re-examination of the corrections for ellipticity. *Geophys. J. R. Astron. Soc.*, **44**, 7–18.

Dziewonski, A.M., Hager, B. H., & O'Connell, R. J. 1977. Large scale heterogeneity in the lower mantle. *J. Geophys. Res.*, **82**, 239–255.

Forte, A. M., & Peltier, W. R. 1987. Mantle convection and core-mantle boundary topography: Explanations and implications. *J. Geophys. Res.*, **92**, 3645–3679.

Garland, G. D. 1971. *Introduction to Geophysics - Mantle, Core, and Crust.* W. B. Saunders Company.

Giardini, D., Li, X., & Woodhouse, J. H. 1987. Three dimensional structure of the Earth from splitting in free oscillation spectra. *Nature*, **325**, 405–411.

Giardini, D., Li, X., & Woodhouse, J. H. 1988. The splitting functions of long period normal modes of the Earth. *J. Geophys. Res.*, **93**, 13716–13742.

Grand, S. P. 1987. Tomographic inversions for shear structure beneath the North American plate. *J. Geophys. Res.*, **92**, 14065–14090.

Grand, S. P. 1990. A possible station bias in travel time measurements reported to ISC. *Geophys. Res. Lett.*, **17**, 17–20.

Gudmundsson, O., Davies, J. H., & Clayton, R. W. 1990. Stochastic analysis of global traveltime data: mantle heterogeneity and random error in the ISC data. *Geophys. J. Int.*, **102**, 25–43.

Gutenberg, B. 1953. Travel times of longitudinal waves from surface foci. *Proc. Natl. Acad. Sci*, **39**, 849–853.

Hager, B. H., & Clayton, R. W. 1989. Constraints on the structure of mantle convection using seismic observations, flow models and the geoid. *Pages 657–763 of:* Peltier, W. R. (ed), *Mantle Convection.* Gordon Breach, New York.

Herrin, E., & Taggart, J. 1962. Regional variations in P_n velocity and their effects on the location of epicenters. *Bull. Seismol. Soc. Am.*, **52**, 1037–1046.

Hwang, & Solomon. 1988. Centroid Depths of Mid-Ocean Ridge Earthquakes. Dependence on Spreading Rate. *J. Geophys. Res.*, **93**, 13445–13467.

Inoue, H., Fukao, Y., Tanabe, K., & Ogata, Y. 1990. Whole mantle P-wave travel time tomography. *Phys. Earth Planet. Inter.*, 90, 294–328.

Jarvis, G. T. 1985. The long wavelength component of mantle convection. *Phys. Earth Planet. Inter.*, **40**, 24–42.

Jarvis, G. T., & Peltier, W. R. 1986. Lateral heterogeneity in the convecting mantle. *J. Geophys. Res.*, **91**, 435–451.

Jarvis, G. T., & Peltier, W. R. 1991. Joint determination of lateral heterogeneity and earthquake location. *Pages 579–594 of:* Sabadini, K. Lambeck, & Boschi, E. (eds), *Glacial Isostasy, Sea-Level and Mantle Rheology.* NATO ASI Series, Kluwer, Boston.

Jeffreys, H., & Bullen, K. E. 1940. Seismological Tables. *British Association, London.*

Jordan, T. H., & Lynn, W. S. 1974. A velocity anomaly in the lower mantle. *J. Geophys. Res.*, **79**, 2679–2685.

Julian, B. R., & Sengupta, M. K. 1973. Seismic travel time evidence for lateral inhomogeneity in the deep mantle. *Nature*, **242**, 443.

Lay, T. 1983. Localized velocity anomalies in the lower mantle. *Geophys. J. R. Astron. Soc.*, **72**, 483–516.

Li, X.-D., Giardini, D., & Woodhouse, J. H. 1991. The relative amplitudes of mantle heterogeneity in P-velocity, S-velocity and density from free oscillation data. *Geophys. J. Int.*, **105**, 649–657.

Masters, G., Jordan, T. H., Silver, P. G., & Gilbert, F. 1982. Aspherical earth structure from fundamental spheroidal mode data. *Nature*, **298**, 609–613.

Morelli, A., & Dziewonski, A. M. 1986. Topography of the core-mantle boundary determined with reflected and refracted rays. *Eos Trans. AGU. Un*, **67**, 1099.

Morelli, A., & Dziewonski, A. M. 1987a. 3D structure of the Earth's core inferred from travel time residuals. *Eos Trans. AGU. Un*, **67**, 311.

Morelli, A., & Dziewonski, A. M. 1987b. Topography of the core-mantle boundary and lateral homogeneity of the liquid core. *Nature*, **325**, 678–683.

Morelli, A., & Dziewonski, A. M. 1991. Joint determination of lateral heterogeneity and earthquake location. *Pages 515–534 of:* Sabadini, K. Lambeck, & Boschi, E. (eds), *Glacial Isostasy, Sea-Level and Mantle Rheology.* NATO ASI Series, Kluwer, Boston.

Nolet, G. 1987. Wave propagation and seismic tomography. *Pages 1–23 of:* Nolet, G. (ed), *Seismic Tomography.* D. Reidel, Dordrecht.

Press, W. H., Flannery, B. P., Teukolsky, S. A., & Vetterling, W. T. 1986. *Numerical Methods.* Cambridge University Press.

Pulver, S., & Masters, G. 1990. PcP - P travel times and the ratio of S to P velocity variations in the lower mantle. *Eos Trans. AGU. Un*, **71**, 1464.

Reynard, B., & Price, G. D. 1992. Thermal expansion of mantle minerals at high pressures – a theoretical study. *Geophys. Res. Lett.*, **17**, 689–692.

Ritzwoller, M., G. Masters, & Gilbert, F. 1988. Constraining aspherical structure with low frequency interaction coefficients: Application to uncoupled multiplets. *J. Geophys. Res.*, **93**, 6369–6396.

Sengupta, M., & Toksoz, M. N. 1976. Three dimensional model of seismic velocity variation. *Geophys. Res. Lett.*, **3**, 84–86.

Souriau, A., & Woodhouse, J. H. 1987. A worldwide comparison of predicted S wave delays from a three-dimensional upper mantle model with P wave station corrections. *Phys. Earth Planet. Inter.*, **39**, 75–88.

Su, W.-J., & Dziewonski, A. M. 1991. Predominance of long wavelength heterogeneity in the mantle. *Nature*, **352**, 121–126.

Tanimoto, T. 1990. Long wavelength S-velocity structure throughout the mantle. *Geophys. J. R. Astron. Soc.*, **100**, 327–336.

Tarantola, A., & Valette, B. 1982. Inverse problems = quest for information. *J. Geophys,*, **50**, 159–170.

Toksoz, M. N., Chinnery, M. A., & Anderson, D. L. 1967. Inhomogeneities in the earth's mantle. *Geophys. J. R. Astron. Soc.*, **13**, 31–59.

Trampert, J., & Snieder, R. 1994. Spectral leakage and seismic tomography. *IASPEI meeting, Wellington, New Zealand.*

Wiggins, R. A. 1972. The general linear inverse problem: Implications of surface waves and free oscillations for earth structure. *Rev. Geophys. Space Phys.*, **10**, 251–285.

Woodhouse, J. H., & Dahlen, F. A. 1978. The effect of a general aspherical perturbation on the free oscillations of the Earth. *Geophys. J. R. Astron. Soc.*, **53**, 335–354.

Woodhouse, J. H., & Dziewonski, A. M. 1984. Mapping the upper mantle: Three dimensional modelling of Earth structure by inversion of seismic waveforms. *J. Geophys. Res.*, **89**, 5953–5986.

Woodhouse, J. H., & Dziewonski, A. M. 1986. Three dimensional mantle models based on mantle wave and long period body wave data. *Eos Trans. AGU. Un*, **67**, 307.

Woodhouse, J. H., & Dziewonski, A. M. 1989. Seismic modelling of the Earth's large scale three-dimensional structure. *Phil. Trans R. Soc. Lond. A*, **328**, 291–308.

Woodhouse, J. H., & Giardini, D. 1985. Inversion for the splitting function of isolated low order normal mode multiplets. *Eos Trans. AGU. Un*, **66**, 300.

Woodhouse, J. H., & Girnius, T. P. 1982. Surface waves and free oscillations in a regionalized Earth model. *Geophys. J. R. Astron. Soc.*, **68**, 653–673.

Woodhouse, J. H., Dziewonski, A. M., Giardini, D., Li, X.-D., & Morelli, A. 1986. Anisotropy of the inner core inferred from splitting in normal mode spectra and from PKIKP travel times. *Eos Trans. AGU. Un*, **67**, 1100.

Woodward, R. L., & Masters, G. 1991a. Global upper mantle structure from long-period differential travel times. *J. Geophys. Res.*, **96**, 6351–6377.

Woodward, R. L., & Masters, G. 1991b. Lower mantle structure from ScS-S differential travel times. *Nature*, **352**, 231–233.

Woodward, R. L., Forte, A. M., Su, W.-J., & Dziewonski, A. M. 1992. Constraints on the large-scale structure of the Earth's mantle. *In: et al.* , Takahashi (ed), *Chemical Evolution of the Earth and Planets.* in press.

Woodward, Robert L. 1990. *Structure of the Earth's Upper Mantle from Long Period Seismic data.* Ph.D. thesis, University of California, San Diego.

Zhang, Y.-S., & Tanimoto, T. 1991. Global Love wave phase velocity variation and its significance to plate tectonics. ***Phys.** Earth Planet. Inter.*, **66**, 160–202.

Appendix A

Transformation of model coefficients

Equation 3.17 can be rewritten without the depth dependency for one specific l value as shown below. To be more concise the notation $\Re\{Y_l^m(\mathbf{x})\} = Y_l^{mR}(\mathbf{x})$ and $\Im\{Y_l^m(\mathbf{x})\} = Y_l^{mI}(\mathbf{x})$ are used.

$$
\begin{aligned}
\left(\frac{\delta v}{v}\right)_l(\mathbf{x}) &= \sum_{m=-l}^{l} c_l^m Y_l^m(\mathbf{x}) \\
&= \sum_{m=-l}^{l} c_l^{mR}\{Y_l^{mR}(\mathbf{x}) + iY_l^{mI}(\mathbf{x})\} + i[c_l^{mI}\{Y_l^{mR}(\mathbf{x}) + iY_l^{mI}(\mathbf{x})\}] \\
&= \sum_{m=-l}^{l} c_l^{mR}Y_l^{mR}(\mathbf{x}) - c_l^{mI}Y_l^{mI}(\mathbf{x}) + i[\cdots] \\
\Re\left(\frac{\delta v}{v}\right)_l(\mathbf{x}) &= c_l^{0R}Y_l^{0R}(\mathbf{x}) + \sum_{m=1}^{l}[c_l^{mR}Y_l^{mR}(\mathbf{x}) - c_l^{mI}Y_l^{mI}(\mathbf{x}) + \\
&\quad c_l^{-mR}Y_l^{-mR}(\mathbf{x}) - c_l^{-mI}Y_l^{-mI}(\mathbf{x})] \\
&= c_l^{0R}Y_l^{0R}(\mathbf{x}) + \sum_{m=1}^{l} c_l^{mR}Y_l^{mR}(\mathbf{x}) - c_l^{mI}Y_l^{mI}(\mathbf{x}) + \\
&\quad (-1)^m[c_l^{-mR}Y_l^{mR}(\mathbf{x}) + c_l^{-mI}Y_l^{mI}(\mathbf{x})]
\end{aligned}
$$

For this last line the substitution $Y_l^{-m}(\mathbf{x}) = (-1)^m[Y_l^m(\mathbf{x})]^*$ has been used. It follows that $c_l^{-m} = (-1)^m c_l^{m*}$, so the above equation becomes

$$
\begin{aligned}
\Re\left(\frac{\delta v}{v}\right)_l(\mathbf{x}) &= c_l^{0R}Y_l^{0R}(\mathbf{x}) + \sum_{m=1}^{l} c_l^{mR}Y_l^{mR}(\mathbf{x}) - c_l^{mI}Y_l^{mI}(\mathbf{x}) + c_l^{mR}Y_l^{mR}(\mathbf{x}) - c_l^{mI}Y_l^{mI}(\mathbf{x}) \quad \text{(A.1)} \\
&= c_l^{0R}Y_l^{0R}(\mathbf{x}) + 2\sum_{m=1}^{l} c_l^{mR}Y_l^{mR}(\mathbf{x}) - c_l^{mI}Y_l^{mI}(\mathbf{x}) \quad \text{(A.2)}
\end{aligned}
$$

Comparing equations A.2 and 3.41, and re-introducing the depth index k, the relationship between the real and complex model coefficients is

$$ {}_kc_l^m = {}_ka_l^m \qquad m = 0 \tag{A.3} $$

$$ {}_kc_l^m = \frac{1}{2}({}_ka_l^m - i\,{}_kb_l^m) \qquad m \neq 0 \tag{A.4} $$

Appendix B

Derivation of mean square amplitude

The mean square of the amplitude of the model at a certain radius is given by

$$\frac{1}{4\pi r^2}\int\left(\frac{\delta v}{v}\right)^2 dA = \frac{1}{4\pi r^2}\int_0^{\pi}\int_0^{2\pi}\|\sum_{l=0}^{L}\sum_{m=-l}^{l}c_l^m Y_l^m(\theta,\phi)\|^2 r^2 sin\theta d\theta d\phi \qquad \text{(B.1)}$$

$$= \frac{1}{4\pi}\sum_{l=0}^{L}\sum_{m=-l}^{l}\|c_l^m\|^2 \qquad \text{(B.2)}$$

Using the equations of Appendix A

$$\|c_l^m\|^2 = \begin{cases} a_l^{m\,2} & \text{if } m = 0 \\ \frac{1}{4}(a_l^{m\,2} + b_l^{m\,2}) & \text{if } m \neq 0 \end{cases}$$

Substituting this into equation B.2 we have

$$\text{mean square amplitude} = \frac{1}{4\pi}\sum_{l=0}^{L}\left[a_l^{0\,2} + \frac{1}{2}\sum_{m=1}^{l} a_l^{m\,2} + b_l^{m\,2}\right] \qquad \text{(B.3)}$$

Appendix C

Model coefficients

The following tables give the coefficients a and b, multiplied by 1000, from equation 3.41

		k=0		*k=1*		*k=2*		*k=3*		*k=4*	
l	m	*a*	*b*	*a*	*b*	*a*	*b*	*a*	*b*	*a*	*b*
0	0	-4.410		-3.745		3.308		1.443		3.788	
1	0	1.672		0.447		-0.563		-1.361		-0.896	
	1	-0.673	-0.129	-1.118	-2.814	-1.616	-2.833	-0.557	0.664	-0.123	-1.281
2	0	1.956		-2.255		0.765		-0.116		0.770	
	1	1.866	-2.459	1.592	0.009	1.359	0.821	0.743	-2.369	-2.180	-0.013
	2	-5.299	-3.615	6.583	-2.193	-2.296	-3.288	3.990	1.309	0.211	-0.202
3	0	-2.191		1.541		2.098		-0.409		0.861	
	1	1.611	-0.692	-0.363	-1.850	-1.975	-0.708	0.890	-1.019	2.021	-0.714
	2	-1.435	1.583	-1.852	-0.571	-1.404	-2.212	1.075	-1.173	-1.508	-1.799
	3	-0.260	0.932	0.050	-2.075	-0.561	-1.681	-2.851	0.105	-2.023	0.177
4	0	0.650		-0.524		-0.429		0.994		-1.530	
	1	1.571	0.894	2.170	1.082	-0.101	-0.674	1.558	0.071	0.235	1.282
	2	0.324	-2.035	0.083	2.841	0.942	-1.345	-1.920	-0.385	0.146	-0.255
	3	0.070	-1.175	-1.794	-0.483	-4.246	-1.430	-0.506	0.028	-1.969	-1.681
	4	0.743	2.735	1.164	1.213	0.856	2.612	-2.889	1.563	1.284	0.265
5	0	-0.823		-0.831		-0.681		-0.967		-1.194	
	1	-0.746	0.986	3.176	-0.217	0.981	1.619	-1.214	-0.494	0.381	1.015
	2	0.789	0.336	2.350	-0.622	1.570	1.680	1.130	1.752	0.396	-0.078
	3	1.512	-2.553	0.579	1.034	-0.351	-2.336	2.791	0.312	-0.601	-0.756
	4	4.049	-0.347	-2.794	-1.772	0.979	0.086	3.162	-1.738	-0.504	-1.429
	5	-3.855	-0.388	-1.737	-1.239	-0.852	0.515	-1.682	-1.315	-2.766	0.250
6	0	0.159		-0.089		-0.531		-0.126		-0.108	
	1	1.991	-1.505	-3.350	0.552	1.599	-0.065	-1.680	0.684	0.196	-0.977
	2	-1.703	0.486	-0.540	-2.320	0.134	-0.349	3.332	1.185	-0.834	-1.846
	3	-0.319	2.089	-0.787	-2.868	3.176	0.382	-2.336	0.206	4.067	-1.579
	4	-0.979	1.892	0.951	-0.533	1.022	-0.418	-1.443	1.091	0.724	0.964
	5	1.022	1.895	-3.979	-2.044	-0.796	1.464	-0.112	0.521	0.744	-0.361
	6	-0.353	0.937	0.785	-0.542	-1.269	2.476	1.130	-1.694	-1.463	1.631

Table C.1: The coefficients of the 4_6 S model.

		k=0		*k=1*		*k=2*		*k=3*		*k=4*	
l	m	*a*	*b*	*a*	*b*	*a*	*b*	*a*	*b*	*a*	*b*
0	0	-4.466		5.641		-0.433		1.133		1.048	
1	0	0.322		-1.127		-0.373		-1.248		0.230	
	1	0.404	-0.262	-2.422	-0.063	-0.634	-0.900	0.523	-0.565	-0.490	0.131
2	0	2.182		0.399		1.233		0.959		-0.485	
	1	1.953	-0.828	0.133	0.009	1.211	-0.452	-0.153	-1.219	-0.058	-0.216
	2	-2.731	-2.126	1.941	-2.383	0.638	-2.051	2.659	-1.255	1.332	0.035
3	0	-1.203		2.145		0.085		0.416		1.458	
	1	1.840	-0.575	1.209	0.099	-0.242	-0.338	1.300	0.955	-0.211	-0.589
	2	-1.620	0.906	-0.074	-1.505	-1.534	-1.787	0.700	-1.017	-1.057	-1.461
	3	-0.385	-0.800	-0.258	-3.462	-0.802	-1.841	-0.654	-0.970	-0.938	0.045
4	0	-0.849		-0.141		-0.254		0.396		-0.442	
	1	0.054	-0.097	-0.028	1.219	-0.355	0.029	0.384	0.058	-0.076	0.150
	2	0.803	-0.079	-0.752	2.196	-0.096	0.145	-0.957	0.329	-1.489	0.487
	3	0.135	0.246	0.690	1.360	-0.427	-0.084	-0.346	0.561	-0.518	-0.047
	4	1.162	0.510	1.363	-0.573	-0.188	1.472	-0.172	1.079	0.482	-0.101
5	0	0.156		-0.411		-0.162		-0.774		-0.532	
	1	-1.204	-0.058	1.679	-0.447	-1.178	-0.318	-0.327	-0.836	0.555	1.048
	2	-0.093	-0.826	2.083	-0.463	0.905	0.186	0.652	-0.004	0.941	-0.475
	3	-0.763	-1.214	-0.883	-0.131	-1.193	-0.693	-0.542	-0.351	-0.431	-1.662
	4	0.475	-0.542	0.384	-0.644	1.632	-2.213	1.051	-1.083	0.385	-1.386
	5	-0.694	-0.549	0.930	-0.862	1.228	0.472	0.114	0.153	0.014	0.797
6	0	0.356		-0.438		-0.275		0.253		-0.350	
	1	1.054	0.112	-0.661	0.123	-0.189	1.079	-0.187	0.788	-0.193	-0.183
	2	-1.191	-0.304	-1.433	-1.180	0.030	-0.087	0.310	0.540	0.450	0.471
	3	-0.554	-0.285	0.158	-1.484	0.553	0.011	0.000	-0.285	0.430	-0.168
	4	0.666	1.179	-0.301	-1.156	-0.237	1.452	-0.337	-0.184	0.438	0.918
	5	-0.313	-0.348	-1.400	1.193	0.430	-1.433	-0.102	0.102	0.281	-0.600
	6	0.715	0.249	1.030	-0.041	0.236	1.059	0.215	-0.473	0.066	0.549

Table C.2: The coefficients of the 4_6 P model.